Title
Next-generation Electrode Materials for Na- and Li-ion Batteries

Author
Butts, Danielle

Publication Date
2022

Peer reviewed|Thesis/dissertation

UNIVERSITY OF CALIFORNIA

Los Angeles

Next-generation Electrode Materials for Na- and Li-ion Batteries

A dissertation submitted in partial satisfaction of the

requirements for the degree Doctor of Philosophy

in Materials Science and Engineering

by

Danielle Butts

2022

ABSTRACT OF THE DISSERTATION

Next-generation Electrode Materials for Na- and Li-ion Batteries

by

Danielle Butts

Doctor of Philosophy in Materials Science and Engineering

University of California, Los Angeles, 2022

Professor Bruce Dunn, Chair

With climate change upon us, the development of energy storage technologies to increase the integration of renewable energy systems is critical. Thus, a variety of energy storage systems are required to meet the wide array of demands from grid-level storage to high-power, fast-charging electric vehicles. This dissertation presents the introduction of novel Li- and Na-ion chemistries and materials systems for energy storage (Chapter 3 and 5) and demonstrates further development of full-cell chemistries for industrial applications (Chapter 4). In Chapter 3, we present a method for high-power electrode development from high ionic conductivity solid-state electrolytes in a model Na-ion system: Na-β alumina (NBA). The substitution of a redox active ion, Fe, for Al within the NBA structure enabled development of a high-power Na-ion battery electrode with 75% capacity retention at a 20C-rate. This work demonstrates a new avenue for materials research development in high-power materials design and improved interface compatibility of electrodes with solid state electrolytes. In Chapter 4, we present high-power Li-

ion devices, which can deliver charge in a matter of minutes instead of hours, that could transform the electric vehicle market as well as consumer electronics and 'internet-of-things' (IOT) devices. The Nb_2O_5-based devices demonstrate the advantage of pseudocapacitive materials, those with capacitor-like kinetics, in full-cell battery systems. Energy storage devices with the demonstrated power-density capabilities are necessary to realize the clean energy goals of the upcoming decades and mark a significant step from lab-scale to practical applications. Finally, in Chapter 5, a combination of high-power and high-energy is demonstrated in amorphous sulfides: *a*-WS_x and *a*-TaS_y. This is the first demonstration to date of high-power, amorphous materials for energy storage with evidence of multielectron, anionic redox. The development of amorphous sulfide materials highlights the advantage of amorphous over crystalline structures for multielectron, anionic redox reversibility as well as the importance of local atomic ordering compared with long-range order for fast charging capabilities. Taken together, the work presented here delivers pathways for future materials development and design in Na- and Li-ion battery systems from fundamental materials properties for high energy and high power to full-cell, prototype devices.

The dissertation of Danielle Butts is approved.

Jane P. Chang

Aaswath Raman

Philippe Sautet

Bruce Dunn, Committee Chair

University of California, Los Angeles

2022

To my family,

especially Tom,

who showed me the joy in relentless intellectual curiosity,

even in the toughest of times.

Table of Contents

Table of Figures

Acknowledgements

First and foremost, I would like to thank Professor Bruce Dunn for helping me learn and grow as a scientist throughout my time at UCLA. He has taught me the importance of maintaining a scientific curiosity throughout life and the value of community engagement for the scientific community worldwide. He has also fostered a community of collaboration within his lab that I have enjoyed working in and hope to emulate in future scientific spaces.

I would also like to thank the many Dunn lab members who have helped me immensely along the way: Jonathan Lau, David Ashby, Qiulong Wei, Ryan DeBlock, Dean Cheikh, Jürgen Schoiber, Matt Lai, Grace Whang and mostly importantly, Christopher Choi, who spent countless hours helping me to understand electrochemistry. This dissertation was made possible by the help of these members and their generosity in passing down knowledge. I would like to thank Alexander Cheikh, Yunkai Luo, Bintao Hu, Winny Hsieh, Patricia McNeil, and Maggie Fox for being great friends and colleagues throughout graduate school. I would also like to thank my collaborators in the Women Supporting Women in the Sciences project, Julie Fornaciari, Jill Wenderott, Joyce Elisadiki, Cecilia China, Gloriana Monko, and Professor Sossina Haile. These women have helped me appreciate the importance of women in science and to provide opportunities for women to pursue science careers worldwide.

Finally, I would like to thank my committee members, Professors Jane Chang, Philippe Sautet and Aaswath Raman, for their collaboration, comments, and constructive criticism on this work.

Chapter three is a version of **Butts, D.**; Schoiber, J.; Choi, C.; Redhammer, G. J.; Hüsing, N.; Donne, S.; Dunn, B. Fe-Substituted Sodium B″-Al_2O_3 as a High-Rate Na-Ion Electrode. *Chem. Mater.* **2021**, *33* (15), 6136–6145. https://doi.org/10.1021/acs.chemmater.1c01680.

Chapter Four is a version of a manuscript in preparation with Chun-Han (Matt) Lai, Yiyi Yao, Christopher S. Choi, Victoria M. Basile, David Grant, Rogerio M. Ribas, Robson S. Monteiro, Sarah, Tolbert and Bruce, Dunn, in collaboration with Battery Streak Inc.

Chapter Five is a version of a manuscript in preparation with Ziyang Wei, Molleigh Preefer, Grace Whang, Rebecca Vincent, Jue Liu, Daniel Olds, Johanna Nelson Weker, Phillipe Sautet and Bruce Dunn. Synchrotron experiments for this work were performed at the Stanford Synchrotron Radiation Lightsource (SSRL), Oak Ridge National Lab (ORNL) and Brookhaven National Lab (BNL).

Appendix A is a version of Sheil, R.; **Butts, D.**; Jungjohann, K.; Yoo, J.; Dunn, B.; Chang, J. P. Plasma Enhanced Atomic Layer Deposition of Thin Film $Li_{1+x}Mn_{2-x}O_4$ for Realization of All Solid-State 3D Lithium-Ion Microbatteries. *Journal of Vacuum Science & Technology A* **2021**, *39* (1), 012408. https://doi.org/10.1116/6.0000644.

Vita

2012–2016 Bachelor of Science, Materials Science and Engineering, Northwestern University

Select Publications and Patents

Butts, D.; Schoiber, J.; Choi, C.; Redhammer, G. J.; Hüsing, N.; Donne, S.; Dunn, B. Fe-Substituted Sodium B″-Al $_2$ O $_3$ as a High-Rate Na-Ion Electrode. *Chem. Mater.* **2021**, *33* (15), 6136–6145. https://doi.org/10.1021/acs.chemmater.1c01680.

Butts, D. M.; McNeil, P. E.; Marszewski, M.; Lan, E.; Galy, T.; Li, M.; Kang, J. S.; Ashby, D.; King, S.; Tolbert, S. H.; Hu, Y.; Pilon, L.; Dunn, B. S. Engineering Mesoporous Silica for Superior Optical and Thermal Properties. *MRS Energy & Sustainability* **2020**, *7* (1), 39. https://doi.org/10.1557/mre.2020.40.

Sheil, R.*; **Butts, D.***; Jungjohann, K.; Yoo, J.; Dunn, B.; Chang, J. P. Plasma Enhanced Atomic Layer Deposition of Thin Film Li $_{1+x}$ Mn $_{2–x}$ O $_4$ for Realization of All Solid-State 3D Lithium-Ion Microbatteries. *Journal of Vacuum Science & Technology A* **2021**, *39* (1), 012408. https://doi.org/10.1116/6.0000644.

Choi, C.*; Ashby, D. S.*; **Butts, D. M.***; DeBlock, R. H.; Wei, Q.; Lau, J.; Dunn, B. Achieving High Energy Density and High Power Density with Pseudocapacitive Materials. *Nat Rev Mater* **2020**, *5* (1), 5–19. https://doi.org/10.1038/s41578-019-0142-z.

Marszewski, M.; **Butts, D.**; Lan, E.; Yan, Y.; King, S. C.; McNeil, P. E.; Galy, T.; Dunn, B.; Tolbert, S. H.; Hu, Y.; Pilon, L. Effect of Surface Hydroxyl Groups on Heat Capacity of Mesoporous Silica. *Appl. Phys. Lett.* **2018**, *112* (20), 201903. https://doi.org/10.1063/1.5027080.

Baek, S. W.; Wyckoff, K. E.; **Butts, D. M.;** Bienz, J.; Likitchatchawankun, A.; Preefer, M. B.; Frajnkovič, M.; Dunn, B. S.; Seshadri, R.; Pilon, L. Operando Calorimetry Informs the Origin of Rapid Rate Performance in Microwave-Prepared TiNb 2 O 7 Electrodes. *Journal of Power Sources*

2021, *490*, 229537. https://doi.org/10.1016/j.jpowsour.2021.229537.

Wei, Q.; DeBlock, R. H.; **Butts, D. M.**; Choi, C.; Dunn, B. Pseudocapacitive Vanadium-based Materials toward High-Rate Sodium-Ion Storage. *Energy Environ. Mater.* **2020**, *3* (3), 221–234. https://doi.org/10.1002/eem2.12131.

Lau, J.; DeBlock, R. H.; **Butts, D. M.**; Ashby, D. S.; Choi, C. S.; Dunn, B. S. Sulfide Solid Electrolytes for Lithium Battery Applications. *Adv. Energy Mater.* **2018**, *8* (27), 1800933. https://doi.org/10.1002/aenm.201800933.

Pilon, L.; Dunn, B.; Tolbert, S.; Marszewski, M.; Yan, Y.; Sophia, K.; Esther, L.; **Butts, D**.; McNeil, P. Optically-Transparent Thermally-Insulating Manoporous Coatings and Monoliths. US 2021/0207428 A1.

Presentations

Butts, D., Dunn, B., Engineering Mesoporous Silica for Superior Optical and Thermal Properties. Presented at the 14th Pacific Rim Conference on Ceramic and Glass Technology. Vancouver, CA. (2021) (Invited)

Butts, **D.**, Schöiber J., Dunn, B., Transforming an Electrolyte into an Electrode: Fe Substituted Na β"-Al_2O_3. Presented at the Materials Research Society Fall Meeting. Boston, MA, USA. (2020).

Butts, D., Dunn, B., Engineering Mesoporous Silica for Superior Optical and Thermal Properties. Presented at the TMS2020 Meeting. San Diego, CA, USA. (2020)

Butts, D., Fornaciari, J., China, C., Increasing girl's participation in higher education through girl-centered science laboratories. Presented at the African Materials Research Society Meeting. Arusha, Tanzania. (2019)

Butts, D., Dunn, B., Engineering Mesoporous Silica for Superior Optical and Thermal Properties. Presented at the IMMS18 Meeting. Los Angeles, CA, USA. (2018)

1. Chapter 1. Introduction and Motivation

Energy storage for various technologies from consumer electronics and electric vehicles to stationary grid-level storage is becoming increasingly important with the integration of intermittent renewable energy systems.[1] Given such a wide range of potential applications, the development of a variety of energy storage solutions is necessary to meet the demands in energy-density, power-density, flexibility, etc. Over the past decade, Li-ion battery technology has garnered significant momentum in research and development to improve materials systems, resulting in practical volumetric and gravimetric energy densities of 733 Wh/l and 264 Wh/kg, respectively (**Figure 1-1**). [2] However, Li-ion batteries are not expected to be economically viable in all instances such as at the grid-storage level, and other technologies such as sodium-ion batteries and lithium sulfur batteries may prove more promising for certain applications. Thus, Li- and Na-ion batteries can serve in complementary roles to meet demands and the advancement of multiple material technologies enables an efficient spreading of resources.[3]

Throughout the past decade, progress has been made toward designing Li-ion battery materials for high power-density devices, which are needed to achieve widespread adoption of electric vehicles (EV). Achieving high-power density without sacrificing substantial energy density is made possible by surface-limited charge storage materials.[4] That is, materials which are not limited by diffusion through the material but by transport at the surface. Surface-limited charge storage materials, such as Nb_2O_5 and nano-structured fast-battery materials, are promising in the development of next generation fast charging devices.[4] However, these materials cannot be directly implemented as Na-ion battery analogues due to the larger ionic radius and higher reduction potential of Na compared to that of Li (0.7 vs 1.08 Å and 0 vs 0.3 V vs Li/Li^+ for Li and

Na, respectively).[3] For this reason, materials for high-power Na-ion batteries must be designed specifically for Na-ion systems to achieve the desired performance.

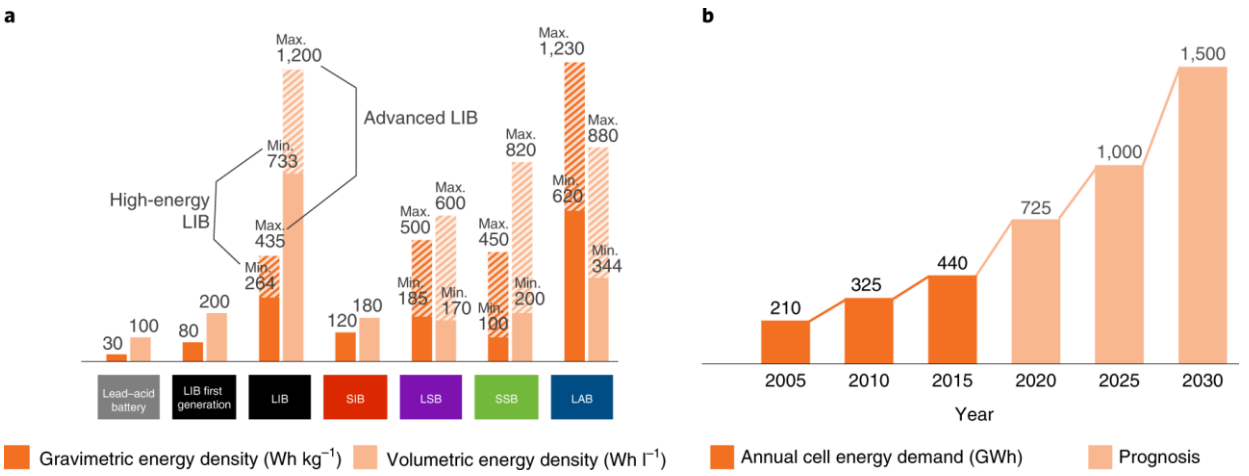

Figure 1-1. **a)** Gravimetric energy density and volumetric energy density of various battery technologies at the cell level indicating the maximum (next generation) and minimum (current technology) for each technology. **b)** Past and predicted trends in battery demand from 2005 to 2030, with more than 50% of the market expected to be dominated by LIB in 2030. LIB = Li-ion battery, SIB = sodium-ion battery, LSB = Li-S battery, SSB = solid-state battery, LAB = Li-air battery.[2] Reprinted with permission from Springer Nature.

In addition to high-power density materials development, high-energy density materials have been a large focus of research development. While higher energy densities can be achieved by more efficient packaging and electrode architectures, it is important to design materials with multielectron redox processes to achieve more than incremental improvements.[5] If commercialized, multielectron redox materials would change the landscape of Li-ion battery energy storage compared with that of the ≤ 1 electron redox in commercial battery materials today.[6]

One method to achieve multielectron charge transfer is through Li-metal anodes, alloying materials, or conversion materials.[6] However, cycling each of these materials is accompanied by limitations such as large volume change, cycling instabilities, and Li-dendrite growth which can lead to safety concerns and a low cycle life. An alternative is to design new intercalation-based materials which can store more than one Li per transition metal while avoiding full conversion.[7,8] Intercalation electrode materials, typically transition metal oxides and sulfides, offer improved stability and cycling life, but existing materials have been optimized such that most improvements are incremental.[6] Achieving new multielectron redox electrode materials requires exploring fundamentally new materials systems.

1.1 References

1. Ding, Y., Cano, Z. P., Yu, A., Lu, J. & Chen, Z. Automotive Li-Ion Batteries: Current Status and Future Perspectives. *Electrochem. Energy Rev.* **2**, 1–28 (2019).
2. Duffner, F. *et al.* Post-lithium-ion battery cell production and its compatibility with lithium-ion cell production infrastructure. *Nat. Energy* **6**, 123–134 (2021).
3. Tarascon, J.-M. Na-ion versus Li-ion Batteries: Complementarity Rather than Competitiveness. *Joule* (2020) doi:10.1016/j.joule.2020.06.003.
4. Choi, C. *et al.* Achieving high energy density and high power density with pseudocapacitive materials. *Nat. Rev. Mater.* **5**, 5–19 (2020).
5. Chen, R., Luo, R., Huang, Y., Wu, F. & Li, L. Advanced High Energy Density Secondary Batteries with Multi-Electron Reaction Materials. *Adv. Sci.* **3**, 1600051 (2016).

6. Gao, X.-P. & Yang, H.-X. Multi-electron reaction materials for high energy density batteries. *Energy Env. Sci* **3**, 174–189 (2010).
7. Preefer, M. B. *et al.* Multielectron Redox and Insulator-to-Metal Transition upon Lithium Insertion in the Fast-Charging, Wadsley-Roth Phase PNb_9O_{25}. *Chem. Mater.* **32**, 4553–4563 (2020).
8. Doan-Nguyen, V. V. T. *et al.* Molybdenum polysulfide chalcogels as high-capacity, anion-redox-driven electrode materials for Li-ion batteries. *Chem. Mater.* **28**, 8357–8365 (2016).

2. Background on Electrochemical Energy Storage Systems

2.1 Principles of traditional Li-ion batteries

Li-ion batteries store energy by converting electrical energy into chemical energy. The Li-ion battery consists of two electrodes, an anode (the negative electrode) and a cathode (the positive electrode).[1] The anode and cathode are separated by a porous separator saturated with electrically insulating but ionically conducting liquid electrolyte. The liquid electrolyte works to move ions back and forth from the cathode to the anode upon charge and from the anode to the cathode upon discharge [**Figure 2-1**].[2] Upon charge, the Li-ions are removed from the cathode, with a concurrent oxidation of metal cations within the cathode, and are inserted into the anode material, with a concurrent reduction of metal cations within the anode to maintain charge balance. This creates an electrical current which runs through an external circuit from the cathode to the anode. Upon discharge, the reverse reaction occurs with an electrical current flowing from the anode to the cathode through the external circuit.[3]

The electrode materials of the anode and cathode must be chosen such that both ionic and electrical conduction can take place within the material to quickly move both ions and electrons through the electrodes. The energy density *E* of a Li-ion battery may be calculated as

Equation 2-1

$$E = \frac{nF}{MW}\Delta V \text{ [Wh/g]}$$

where *n* is the number of electrons transferred [mol], *F* is Faraday's constant [C/mol], *MW* is the molecular weight of the material [kg/mol], and ΔV is the operating voltage range between the anode and cathode.[3] In traditional Li-ion battery materials, the number of electrons transferred *n* is limited to ~1 per transition metal. This is due to the charge storage mechanism in traditional Li-

ion battery materials being cationic redox and charge transfer. For example, $LiFePO_4$ (LFP) cathode material undergoes Fe^{2+}/ Fe^{3+} redox to compensate for Li-insertion and deinsertion as:

$$LiFe^{2+}PO_4 \leftrightarrow Fe^{3+}PO_4 + Li^+ + e^-.[4]$$

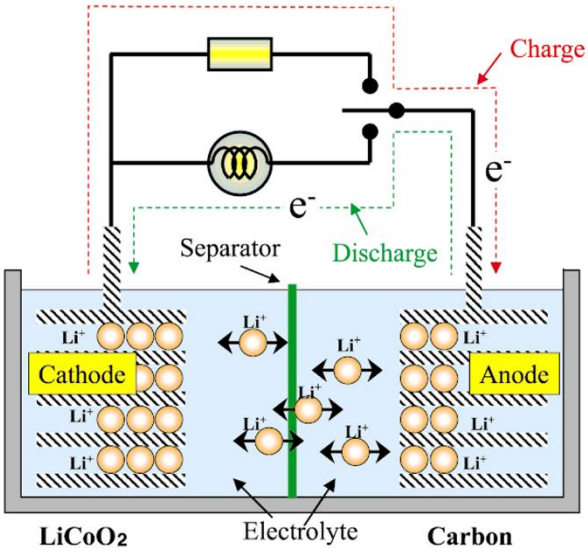

Figure 2-1. Li-ion battery operating during discharge consisting of an anode, cathode, and electrolyte where Li-ions move back and forth through the ionically conducting liquid electrolyte and electrons move between the electrodes through external circuit.[2] Reprinted with permission from Wiley.

2.2 Electrochemical signatures of traditional battery materials

In electrochemical testing of Li-ion battery materials, there are electrochemical signatures that signify physical phenomena and that can be corroborated with in-situ or ex-situ characterization techniques. Traditional Li-ion battery materials display galvanostatic charge-discharge curves where charge is incrementally added at a constant potential, resulting in a voltage plateau. Thus, the energy stored in a battery material can be calculated as $E = QV$, where Q is the stored charge and V is the redox voltage.[5] For example, in a commonly used Li-ion battery cathode material $LiFePO_4$ (LFP), the Fe undergoes redox at ~3.8 V vs Li^+/Li [**Figure 2-2**].[6] This can be

seen in the half-cell (vs Li-metal) galvanostatic measurement where a constant current is applied and resulting voltage response is measured. The observed voltage plateau (**Figure 2-2**a-b) is characteristic of a two-phase region and a phase change in the active material, kinetically limited by diffusion processes.

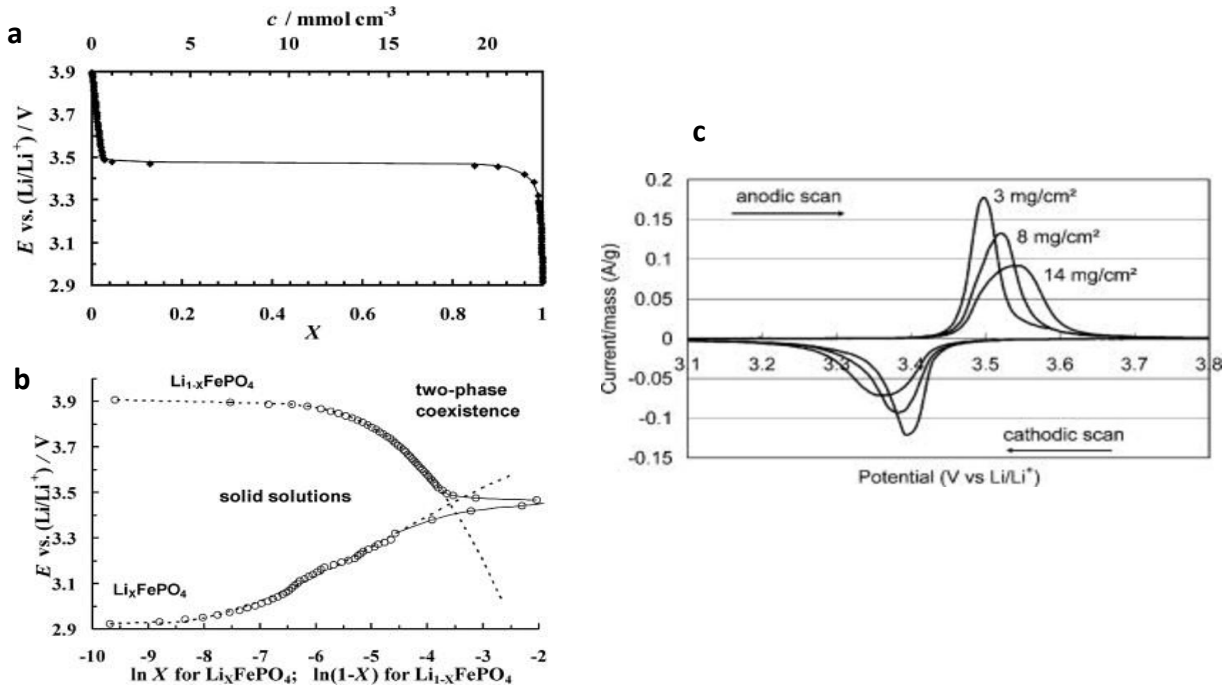

Figure 2-2. Electrochemical signatures of traditional Li-ion battery material $LiFePO_4$ highlighting **a-b)** the voltage plateau upon galvanostatic cycling indicating a region of two-phase coexistence.[6] Reproduced with permission from ECS. **c)** The sharp redox peak in cyclic voltammetry is also characteristic of a battery-like material that is diffusion limited.[7] Reproduced with permission from ECS.

In cyclic voltammetry, where the voltage is changed at a constant rate and the current response is measured, the electrochemical signature of a traditional battery material consists of a sharp redox peak upon oxidation and reduction where the majority of the current response occurs in a narrow voltage range (**Figure 2-2**c**)**. However, polarization of the system during high mass loading or high current operation due to sluggish kinetics and diffusion limitations lead to larger

peak separations and a decrease in energy efficiency.[5] In devices, this clearly defined redox voltage is helpful in that the voltage difference between the anode and cathode is constant during both charge and discharge. However, the existence of a phase change during cycling leads to limitations in high-power capabilities.[8] In cyclic voltammetry, this can be observed in the relationship between the peak current i_p and sweep rate υ according to the Randles-Sevcik equation

Equation 2-2

$$i_p = 0.4463nFAcD^{1/2}\upsilon^{1/2}\left(\frac{\alpha nF}{RT}\right)^{1/2}$$

where c is the surface concentration of the electrode material, α is the transfer coefficient, and D is the diffusion coefficient.[9] Thus, the peak current increases as $i_p \propto \upsilon^{1/2}$ in a battery-like material indicating a diffusion-controlled faradaic-redox process. One tool to qualitatively identify this relationship is the *b*-value analysis where the power law relationship

Equation 2-3

$$i(\upsilon) = a \times \upsilon^b$$

can be used to identify the nature of the reaction (*a* is a constant and *b* is the power-law exponent). In a diffusion-controlled, battery-like reaction, $b = 0.5$ according to **Equation 2-2**.

2.3 Challenges of high-power operation

Fast-charging is desirable in Li-ion battery systems due to the desire to charge portable electronics in shorter timeframes and the need to charge electric-vehicles in times comparable to that of refueling an internal combustion engine, ~ 8 minutes.[10] Current Li-ion battery electrode materials, however, are not equipped for fast-charging operation due to the high currents needed and the inherent, diffusion-limited material properties. The phase change that occurs upon lithium insertion into many transition metal oxides is diffusion-limited and faster charging leads to a

dramatic decrease in energy-density due to high polarization [**Figure 2-3a**].[11] Additionally, higher currents can lead to detrimental side reactions and material and electrolyte breakdown due to increased Joule heating.[5,8] This excess heating can lead to safety concerns such as thermal runaway and catastrophic failure resulting in fires and explosions of pressurized cells [**Figure 2-3b**].[12] The most commonly used Li-ion anode material, graphite, is rate-limited by the eventual plating of lithium on top of the graphite above a critical current density.[13] Lithium plating then leads to eventual Li dendrite formation which can grow through the separator, shorting the cell with the risk of safety concerns such as fires. Thus, it is desirable to design materials which avoid sluggish phase transformations upon lithium (de)insertion and remain stable under high-rate operation.

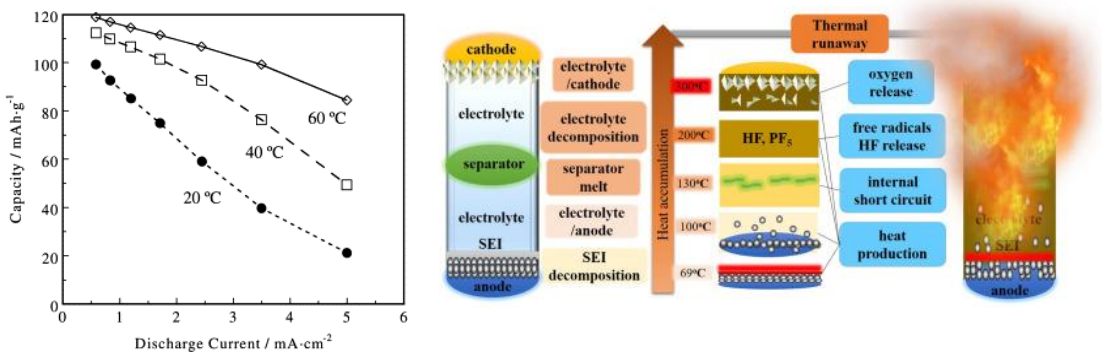

Figure 2-3 a) Gravimetric discharge capacity as a function of discharge current density in $LiFePO_4$ cathodes, highlighting the poor capacity retention with increasing rate.[11] Reproduced with permission from Elsevier. **b)** Process of thermal runaway in Li-ion batteries which can be exacerbated by high-power operation.[12] Reproduced with permission from Elsevier.

2.4 Pseudocapacitive materials and electrochemical signatures

Pseudocapacitive materials offer a potential solution to the challenges of high-rate operation in traditional Li-ion battery electrode materials. Pseudocapacitive materials undergo a faradaic-redox charge-storage mechanism like battery materials, but display the electrochemical

signatures similar to that of electrical double-layer capacitor (EDLC) materials. In EDLCs, the galvanostatic curve is linear (dQ/dV = 1) such that charge storage occurs over the entire voltage range as ions are adsorbed onto the surface of the electrode. As opposed to battery-like materials (Equation 2-1), the energy stored in a capacitor-like material can be calculated as $E = \frac{1}{2}CV^2 = \frac{1}{2}QV$ where C is the capacitance [F/g].[5] In cyclic voltammetry, this results in a box-shaped curve and a linear increase in current with increasing sweep rate υ according to

Equation 2-4

$$i_p = \upsilon CA$$

where i_p is the peak current and A is the surface area of the electrode. Thus, the *b*-value [**Equation 2-3**] of ELDC materials is 1, indicating a surface-limited, as opposed to diffusion limited, charge storage mechanism.[5] Pseudocapacitive materials are similar in that the charge is stored over a wide voltage range resulting a linear (or nearly linear) change in capacity with voltage in the galvanostatic curve. However, instead of EDLC charge storage, pseudocapacitive materials undergo faradic-redox and gradual insertion of lithium into the material.[5] The capacitor-like electrochemical signatures of pseudocapacitive materials are due to the avoidance of a phase change upon lithium insertion and fast Li-ion diffusion through the electrode material that leads to the surface reaction instead of the diffusion within the material being the limiting component. One example of a pseudocapacitive material in Li-ion systems is Nb_2O_5 which displays a box-like cyclic voltammogram where the *b*-value = 1 and a nearly linear galvanostatic curve.[14] This enables high-rate capabilities without significant Joule heating or side reactions and the possibility of safe fast-charging. Qualitatively, the b-value can be used to indicate the limiting factor in the electrochemical reaction as being more diffusion-controlled or more surface-limited and can help to guide the design of materials with surface-limited kinetics.

2.5 Designing high energy-density materials

In general, the energy density of materials can be raised by examining the energy density *E* equation for battery materials shown in (Equation 2-5). First, the redox voltage of the material can be raised or lowered to increase the voltage difference between a given cathode and anode. Second, the molecular weight of the active material can me minimized by using light elements and focusing on 3*d* transition metals or light semimetals for conversion electrodes. Finally, the number of electrons transferred can be maximized by designing multielectron redox materials which has been observed with conversion electrodes,[15] and insertion materials such as in some Wadsley-Roth phase materials[16] and anionic redox materials.[17] Conversion electrodes offer high energy densities but with significant drawbacks including poor reversibility, cyclability, and typically slow kinetic performance due to the formation of entirely new products upon lithaiton.[18] In addition, the complex electrochemical reaction pathways in conversion materials are notoriously difficult to study making it difficult to optimize and improve conversion chemistries. Conversely, Li-ion insertion materials avoid conversion to elemental metals resulting in higher reversibility and cyclability and therefore, increased practicality for industrial applications. Thus, attaining multielectron redox in Li-ion insertion materials offers an exciting pathway toward higher energies in Li-ion battery systems.

2.6 References

1. Dunn, B., Kamath, H. & Tarascon, J.-M. Electrical Energy Storage for the Grid: A Battery of Choices. *Science* **334**, 928–935 (2011).
2. Nishi, Y. The development of lithium ion secondary batteries. *Chem. Rec.* **1**, 406–413 (2001).
3. Deng, D. Li-ion batteries: basics, progress, and challenges. *Energy Sci. Eng.* **3**, 385–418 (2015).

4. Love, C. T. *et al.* Review of LiFePO $_4$ Phase Transition Mechanisms and New Observations from X-ray Absorption Spectroscopy. *J. Electrochem. Soc.* **160**, A3153–A3161 (2013).
5. Choi, C. *et al.* Achieving high energy density and high power density with pseudocapacitive materials. *Nat. Rev. Mater.* **5**, 5–19 (2020).
6. Churikov, A. V. *et al.* Determination of lithium diffusion coefficient in LiFePO4 electrode by galvanostatic and potentiostatic intermittent titration techniques. *Electrochimica Acta* **55**, 2939–2950 (2010).
7. Yu, D. Y. W. *et al.* Study of LiFePO[sub 4] by Cyclic Voltammetry. *J. Electrochem. Soc.* **154**, A253 (2007).
8. Dubarry, M., Truchot, C. & Liaw, B. Y. Cell degradation in commercial LiFePO4 cells with high-power and high-energy designs. *J. Power Sources* **258**, 408–419 (2014).
9. Bard, A. J. & Faulkner, L. R. *Electrochemical methods: fundamentals and applications*. (Wiley, 2001).
10. Tu, H., Feng, H., Srdic, S. & Lukic, S. Extreme Fast Charging of Electric Vehicles: A Technology Overview. *IEEE Trans. Transp. Electrification* **5**, 861–878 (2019).
11. Takahashi, M. Reaction behavior of LiFePO4 as a cathode material for rechargeable lithium batteries. *Solid State Ion.* **148**, 283–289 (2002).
12. Wang, Q., Jiang, L., Yu, Y. & Sun, J. Progress of enhancing the safety of lithium ion battery from the electrolyte aspect. *Nano Energy* **55**, 93–114 (2019).
13. Wandt, J., Jakes, P., Granwehr, J., Eichel, R.-A. & Gasteiger, H. A. Quantitative and time-resolved detection of lithium plating on graphite anodes in lithium ion batteries. *Mater. Today* **21**, 231–240 (2018).

14. Augustyn, V. *et al.* High-rate electrochemical energy storage through Li+ intercalation pseudocapacitance. *Nat. Mater.* **12**, 518–522 (2013).
15. Gao, X.-P. & Yang, H.-X. Multi-electron reaction materials for high energy density batteries. *Energy Env. Sci* **3**, 174–189 (2010).
16. Preefer, M. B. *et al.* Multielectron Redox and Insulator-to-Metal Transition upon Lithium Insertion in the Fast-Charging, Wadsley-Roth Phase PNb_9O_{25}. *Chem. Mater.* **32**, 4553–4563 (2020).
17. Hansen, C. J. *et al.* Multielectron, Cation and Anion Redox in Lithium-Rich Iron Sulfide Cathodes. *J. Am. Chem. Soc.* **142**, 6737–6749 (2020).
18. Yu, S.-H., Feng, X., Zhang, N., Seok, J. & Abruña, H. D. Understanding Conversion-Type Electrodes for Lithium Rechargeable Batteries. *Acc. Chem. Res.* **51**, 273–281 (2018).

3. Chapter 3. Fe-substituted Na-beta alumina as a high-rate Na-ion electrode

3.1 Introduction

The desired energy-density and power-density goals of next-generation energy-storage devices must be met with next-generation battery materials. The looming effects of climate change demand new materials derived from new chemistries which will enable increased use of electric vehicles and decreased reliance on a fossil-fuel-powered grid. Despite the dominance of Li-ion batteries, especially for mobile power, alternative battery technologies are being pursued because of potential advantages in terms of energy and power density as well as providing greener and more sustainable approaches.[1] Na-ion batteries present a promising alternative to existing Li-ion battery technology due to the low cost and abundance of sodium raw materials, the ability to leverage Li-ion battery materials and the potential for high-power Na-ion electrodes.[1,2] However, the larger size of Na^+ compared to that of Li^+ as well as the lower operating potential, can limit the direct extension of Li-ion chemistries into Na-ion analogues. For this reason, Na-ion battery electrode material design presents a promising opportunity for innovation.

Here, we demonstrate the design of Na-ion electrode materials by converting a well-known fast sodium-ion conductor into a mixed electron-ion conductor. Although solid-state electrolyte materials are known for their high levels of ionic conductivity, negligible levels of electronic conductivity disqualify solid-state electrolytes as candidates for electrode materials which require both ionic and electronic conduction. However, by deliberately modifying the fast ion conductor to produce electronic conduction without altering their defect structure, we demonstrate that high ionic conductivity, which is rarely achieved in Na-ion battery electrodes, can be preserved. Such an electrolyte-based material design method takes advantage of not only the inherently fast ionic

conduction within the material but also the possibility of having a more continuous chemical potential across the electrode-electrolyte interface, leading to increased interfacial stability.

The prospect of converting a fast ion conductor into an electrode material has received limited attention. The sodium-ion conductor known as NASICON ($Na_{1+x}Zr_2P_{3-x}Si_xO_{12}$ with $0 \leq x \leq 3$), which was developed as a 3D Na-ion conductor to replace Na β"-Al_2O_3, has a room temperature conductivity of 6.7×10^{-4} S cm^{-1}.[3] NASICON structures, of general formula $Na_xMM'(XO_4)_3$ have been the subject of a few studies aimed at developing mixed ionic-electronic conduction in electrode materials.[4,5,6] Substitution of M and M' for redox active transition metals such as Ti, V, and Fe, creates redox centers for charge transfer upon Na insertion and de-insertion while maintaining the NASICON structure.[5,7] However, the low electronic conductivity of mixed-conducting NASICON materials necessitates nano-structuring as well as surface treatments or coatings for stable high-rate performance.[8] Additionally, Na insertion or de-insertion in NASICON electrodes is accompanied by a phase transition, which can lead to problems in capacity retention with long-term cycling.[1,7] For the most part, NASICON-based electrode materials have been of limited importance in the field. In addition to NASICON structures, one other solid-state electrolyte that has been investigated as a battery electrode material is the Li-ion conductor Li_3N. The conversion of Li_3N into $Li_{3-x}M_xN$ where M = Co, Ni, Fe has been reported, however, even with moderate levels of transition metal substitution, lithium insertion induces a phase transition at lower voltages, severely limiting performance.[9,10] Taken together, these prior studies that used either Na or Li high-conductivity solid electrolytes as the parent material have achieved limited success in creating battery electrode materials.

In the present paper, we use a model system in which to develop design rules for converting a fast Na-ion conducting solid electrolyte into a mixed electron-ion conductor that can serve as an electrode in Na-ion batteries. Na β"-Al_2O_3 (typically stabilized as $Na_{1.67}Li_{0.33}Al_{11}O_{17}$) has an exceptional ionic conductivity (1 x 10^{-3} S cm^{-1} at 25 °C)[11], higher than that of NASICON type $Na_3Zr_2Si_2PO_{12}$ and Na-tetra thiophosphate Na_3PS_4.[12,13] In addition, the fast ion conduction and high interfacial stability against Na-metal enables Na β"-Al_2O_3 to be used in commercial Na-S and Zebra ($NiCl_2$/Na) batteries as a solid-state electrolyte.[14]

The unit cell of the β" phase, $Na_2O{\cdot}5.5(Al_2O_3)$, is comprised of three spinel-like blocks of aluminum and close packed oxygen layers separated by 2D conduction planes for Na-ion transport.[15] The β" phase has a higher concentration of Na in the conduction planes compared to the β phase, $Na_2O{\cdot}11(Al_2O_3)$. The Na-ion conduction mechanism involves two sodium-ion sites in the conduction plane: the Beevers-Ross regular lattice site (BR) and the mid-oxygen site (mO).[15,16] These two sites allow for Na-ions to move rapidly throughout the 2D lattice under an applied electric field as the number of vacant sites is comparable to the number of mobile Na^+ cations.[17] The higher availability of Na-ions and Na-ion sites in the β" phase compared to the β phase leads to its superior ionic conductivity.

Over the past decades, a few attempts have been made to substitute various ions for Al in the spinel block of the Na β"-Al_2O_3 structure to either improve the stability of the β" phase (i.e., Li^+ and Mg^{2+}) or to promote electronic conductivity (i.e., Fe^{3+} and Ni^{2+}).[18,19,20,21] The most promising candidate for transition metal substitution into the spinel-like block is Fe^{3+} due to γ-Fe_2O_3 and γ-Al_2O_3 being isostructural as well as the wide range of compositions forming a spinel solid solution.[22] In the 1970s, Kennedy *et al.* explored this approach with mild success, demonstrating a sodium metal galvanic cell with an Fe-substituted Na β-Al_2O_3 electrode.[23]

However, solid state synthesis methods could not achieve higher than ~35 mol% Fe doping without producing a secondary iron oxide phase.[23–25] In the 1990s, Fe-substitution in the β" phase, $Na_{1+y}(Al_{1-x}Fe_x)_{11}O_{17}$, was explored using sol-gel synthesis and substitution up to x = 0.54 was achieved.[26,27] This study, which investigated fundamental thermodynamic properties and not transport, provided evidence that Fe can be substituted to substantial amounts into the pure β" phase by using sol-gel processes.

The present paper shows it is possible to substitute up to 75 % Fe for Al in Na β"-Al_2O_3 using sol-gel synthesis. We employ X-ray diffraction and Mössbauer spectroscopy to characterize the spinel block occupancy for Fe and determine its role in creating electronic conduction. By retaining the β"-Al_2O_3 structure, the resulting ion conductivity is comparable to that of unsubstituted Na β"-Al_2O_3. The various Fe – substituted Na β"-Al_2O_3 compositions exhibit mixed electronic-ionic conduction which enables the material to function as a high-rate negative electrode for Na-ion battery.

3.2 Experimental methods

Material synthesis

Fe-substituted sodium β" alumina powders were prepared by sol-gel methods using stoichiometric amounts of $FeSO_4 \cdot 6H_2O$ (Sigma, 99.9%), $NaNO_3$ (Sigma, 99.9%), and $AlNO_3 \cdot 9H_2O$ (Sigma, 99.9%, reagent grade, ≥ 98%). The target compositions for NAFO-0.52 and NAFO-0.75 powders were $Na_2Al_7Fe_7O_{17}$ and $Na_2Al_{2.3}Fe_{11.2}O_{17}$, respectively. The precursors were first dissolved in 40 mL DI water with 1:1 molar ratio of citric acid monohydrate (Alfa Aesar, 99.5+%): metal-ions and stirred at 25 °C until completely dissolved. The water in the solution was then evaporated at 80 °C overnight before heating to 900 °C at a rate of 5 °C min^{-1} for 1 hr in an alumina

crucible. The resulting powder (typically ~1g) was then collected and pressed into a 1 cm diameter pellet. The amount of powder used to make the pellet did not affect the outcome of the synthesis. The pellet was heated for a second time to 1400 °C at a rate of 3 °C min^{-1} for 2 hrs in a closed platinum crucible. The pellet was completely submerged in a bed of excess Na β" alumina powder (~ 1g) made in the same manner, but without Fe-substitution. The resulting pellet is expected to contain predominantly oxidized iron in the 3+ state due to the high temperatures in air. After the second heat treatment, the pellet was immediately submerged in a bed of excess Na_2CO_3 (Fisher, anhydrous, 99.8%) (~500 mg) and heated at 500 °C for ~8h to promote Na diffusion to replace any sodium lost at high temperature with a corresponding reduction of Fe^{3+} to Fe^{2+} to maintain charge balance. The pellet was then removed from the furnace at ~300 °C and immediately brought into an Ar-filled glove box, where the materials remained for storage and use. Inside the Ar-filled glove box, the pellet was crushed in diethylene glycol dimethyl ether (Diglyme) (Sigma, anhydrous, 99.5%) solvent with a mortar and pestle, resulting in a dark red (NAFO-0.52) or black (NAFO-0.75) powder for electrode preparation. Scanning electron microscopy (SEM) images taken on a Nova 230 Nano SEM were used to determine particle size and morphology after grinding. Various compositions in the range of 10 to 80 mol% Fe for Al were successfully synthesized, but two are discussed here for simplicity. For conductivity testing, the sintered pellet, ~ 85% dense, was coated on both sides with a thin layer of conductive silver paint (Ted Pella) directly after synthesis. Pellet density was determined by bulk density and the calculated theoretical density by Rietveld refinement.

Powder X-ray diffraction

Powder X-ray diffraction (PXRD) measurements ($5° \leq 2\Theta \leq 95°$, continuous scan) were carried out in reflection-mode on a BRUKER D8 DaVinci Design diffractometer using CuKα

radiation, fixed 0.3° divergence slit, primary and secondary slit 0.04 rad Soller slits, anti-scatter slit 4.0° and a Lynxeye detector (opening angle 2.95°). The Rietveld refinement was done using the FULLPROF-suite of programs.[28] The pseudo-Voigt function was chosen to model peak shape, all atoms were refined using isotropic atomic displacement parameters (and fixed values from literature). Starting values for the refinement of PXRD data were taken from the literature.[28]

Inductively coupled plasma mass spectroscopy

Inductively coupled plasma mass spectroscopy (ICP-MS) measurements were performed on a NexION 2000 (PerkinElmer) instrument. The as synthesized powders were digested in phosphoric acid at 180 °C for ~1h using a microwave digestion unit (Titan MPS, PerkinElmer). No precipitates were observed in the digested solution.

Mössbauer Spectroscopy

Transmission ^{57}Fe Mössbauer spectra were collected using a Mössbauer apparatus (Halder Electronics, Germany) in horizontal arrangement (^{57}Co/Rh single line thin source, constant acceleration mode, symmetric saw tooth velocity shape, multi-channel analyzer with 1024 channels, velocity scale calibrated to α-iron). For Mössbauer – absorber preparation, samples were carefully ground under ethanol, filled into Cu-rings (inner diameter 10 mm and covered with a high-purity Al-foil on one side), and mixed with epoxy resin to fix the sample. The folded spectra were analyzed using both a classical full static Hamiltonian site analysis (using Lorentzian shaped doublets) and a Voigt-based hyperfine field distribution method as implemented in the program RECOIL.[29,30]

Electrochemical characterization

Electrodes were prepared by mixing the active material with carbon black (Ketjenblack, > 99%) and polyvinylidene fluoride (Sigma, 99%) binder in N-Methyl-2-pyrrolidone (Sigma,

anhydrous 99.5%), solvent in weight ratio of 75:15:10, respectively. The slurry was then cast onto a copper or carbon-coated aluminum foil current collector, yielding an active material loading of ~1-2 mg cm^{-2}. The electrolyte was prepared using 1M $NaPF_6$ salt (Alfa, 99%) in Diglyme solvent. Coin cells (CR2035) used the active material as the working electrode, sodium metal foil (Sigma, 99%) as the counter electrode with a 24 μm, polyethylene coated Targray (Quebec, Canada) separator and ~100 μL 1M $NaPF_6$ Diglyme electrolyte. This arrangement was used in all experiments unless otherwise noted and at least three cells were tested for each experiment to confirm repeatability. All electrochemical testing was performed on a Biologic VMP3. Electrochemical impedance spectroscopy (EIS) measurements were performed at open circuit voltage with a sinusoidal signal in a frequency range from 100 kHz to 10 mHz at an amplitude of 10 mV. The simulation of the EIS experiments was carried out using ZFit software on EC-Lab (Biologic) using an equivalent circuit model of R1+Q2/R2+Q3/R3+Q3 for coin cell impedance and L+R1(C1+Q2/R2+Q3/R3)+W for a pellet of NAFO-0.52 with silver blocking electrodes (a cylinder with dimensions of 0.7 mm by 0.8 cm^2 after sintering). Step potential electrochemical spectroscopy analysis (SPECS) was carried out using methods described in previous works.[31–33] Briefly, a 10-mV potential step was applied and held for an equilibration period of 300 s, during which time the current response was measured (See Supplemental Information for a complete description). Energy dispersive x-ray (EDX) analysis taken on a Phenom G2 Pro desktop SEM was used to characterize the change in Na-content ex-situ composite electrodes.

3.3 Results

Fe-substitution into the β" alumina structure has been difficult to achieve through solid-state synthesis methods.[34] This is due to diffusion limitations of ions into the spinel block caused by the inconvenient balance needed between high temperature crystallization (> 1500 °C) and the inevitable soda loss above ~1000 °C. Thus, it is desirable to create short diffusion distances through excellent cation mixing and to form nanoparticles which can lower the required crystallization temperature.[35,36] In this work, adequate cation mixing is achieved with aqueous solutions of Al-nitrate, Na-nitrate, and Fe-sulfate chelated by 1:1 citric acid: metal ions. After pre-firing of the sol at 900 °C, 200 nm particles are realized (Figure 3-1**a**), enabling the formation of a densely packed pellet for high temperature firing at 1400 °C. This crystallization temperature is much lower than that of traditional solid-state synthesis methods (1540 - 1600 °C),[24] preventing excess soda loss and enabling facile stabilization of the high temperature β" phase.

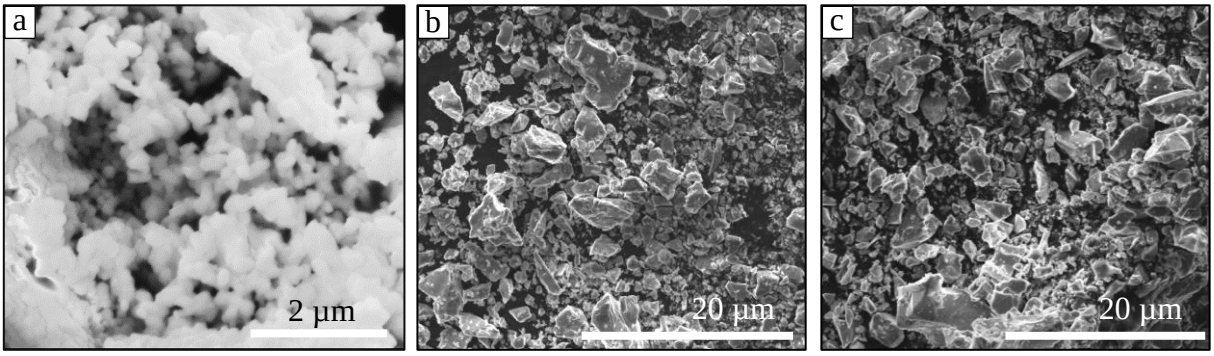

Figure 3-1. Scanning electron microscopy (SEM) images of a) NAFO-0.75 900 °C precursor powder and 1400 °C fully crystallized powders of b) NAFO-0.52 and c) NAFO-0.75, highlighting the larger particle size and inhomogeneous character after 1400 °C heat treatment.

The two Fe-substituted Na-β" Al_2O_3 compositions examined in this paper are 52 mol% Fe-substituted $Na_{1+x}(Al_{0.48}Fe_{0.52})_{11}O_{17}$ and 75 mol% Fe-substituted $Na_{1+x}(Al_{0.25}Fe_{0.75})_{11}O_{17}$, referred to as NAFO-0.52 and NAFO-0.75 hereafter, respectively. The high temperature firing process at

1400 °C required for Fe-substitution and β" phase formation resulted an ~85% dense pellet and micron-sized particles after grinding. The final powders used for electrochemical analysis are shown in the SEM images in Figure 3-1**b** and **c**, displaying inhomogeneous 1 - 10 μm sized particles after mortar and pestle grinding.

3.3.1 Crystal structure determination

The Fe-substituted β"-Al_2O_3 structure was determined through Rietveld refinement of X-ray diffraction (XRD) patterns. The XRD patterns displayed in Figure 3-3**a** indicate an $R\bar{3}m$ space group, confirming β" phase formation in both the NAFO-0.52 and NAFO-0.75 compositions. There was no evidence of Fe_2O_3 or Fe_3O_4 phase formation in either sample, although there was evidence of a small amount of the β phase formed in NAFO-0.75, as indicated by a small peak at ~32° 2θ. Rietveld refinement of the observed XRD patterns (Figure 3-2) confirms the formation of a solid solution of Fe and Al within the alumina spinel block and indicates Fe is occupying both tetrahedral and octahedral sites with a slight preference for octahedral site coordination. The site occupancy for each atom is outlined in **Table *3-1***. Inductively coupled plasma mass spectroscopy (ICP-MS) measurements confirmed the Fe: Al molar ratio to be within ± 3% of those calculated by Rietveld refinement (**Table *3-3***).

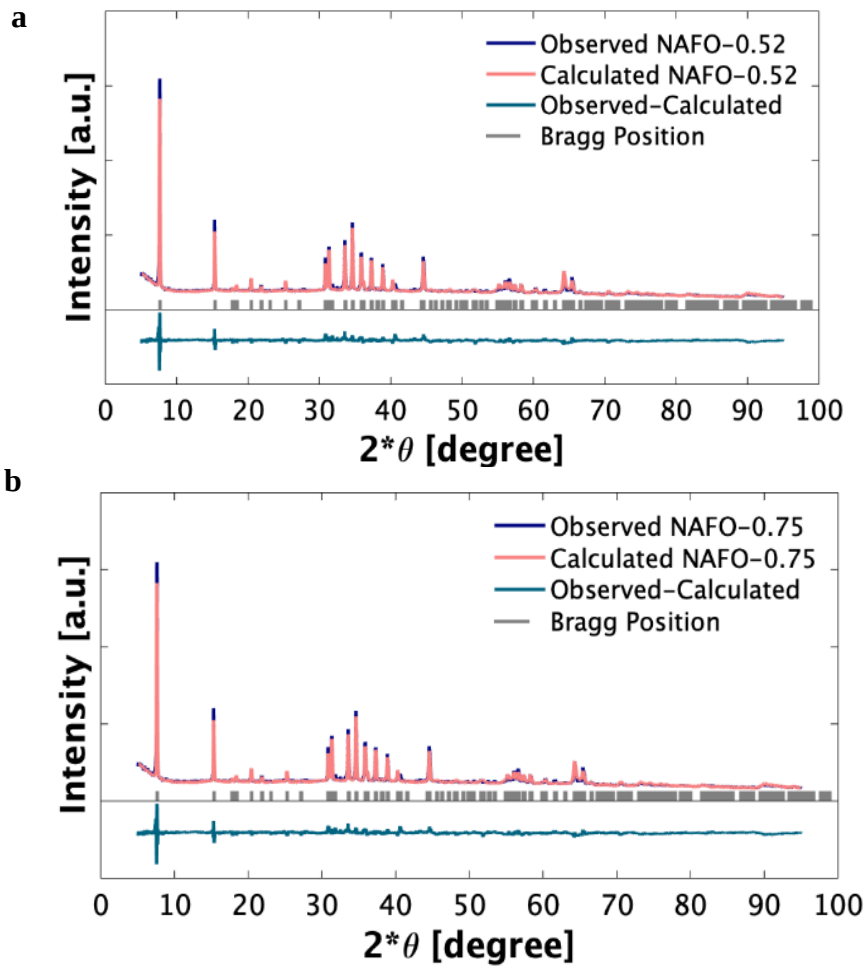

Figure 3-2. Rietveld refinements of **a)** NAFO-0.52 and **b)** NAFO-0.75 powder diffractograms shown here are used to calculate the Fe site occupancy.

The *a*(*b*)- and *c*- axis lattice parameters calculated from XRD were found to increase with increasing Fe doping levels and are consistent with those of similar compositions obtained in previous transition metal doping studies.[26] The NAFO-0.52 structure and Fe-site occupancy is shown in Figure 3-3**b** and **c**, highlighting the partial occupancy of Fe-ions (red) across all available Al (blue) sites along with the 2D conduction planes for Na-ion diffusion. In Figure 3-3c the BR (yellow diamonds) sites are the lattice sites Na can occupy at equilibrium (2 per formula unit). The

mO sites (yellow triangles) act as temporary Na sites during Na^+ conduction through the *a*-*b* plane (3 per formula unit). Although the *c*-axis lattice parameter did increase slightly with Fe substitution, the thickness of the Na-ion conduction plane decreased with increasing Fe doping (5.1 Å for Li-stabilized β", 4.9 Å for NAFO-0.52 and 4.8 Å for NAFO-0.75) to compensate for the larger Fe-ions in the spinel block (**Error! Reference source not found.**).[19] Thus, although the high ionic conductivity β" phase was formed, sodium ion conductivities in NAFO-0.52 and NAFO-0.75 should differ slightly from that of the undoped phase due to subtle structural differences.

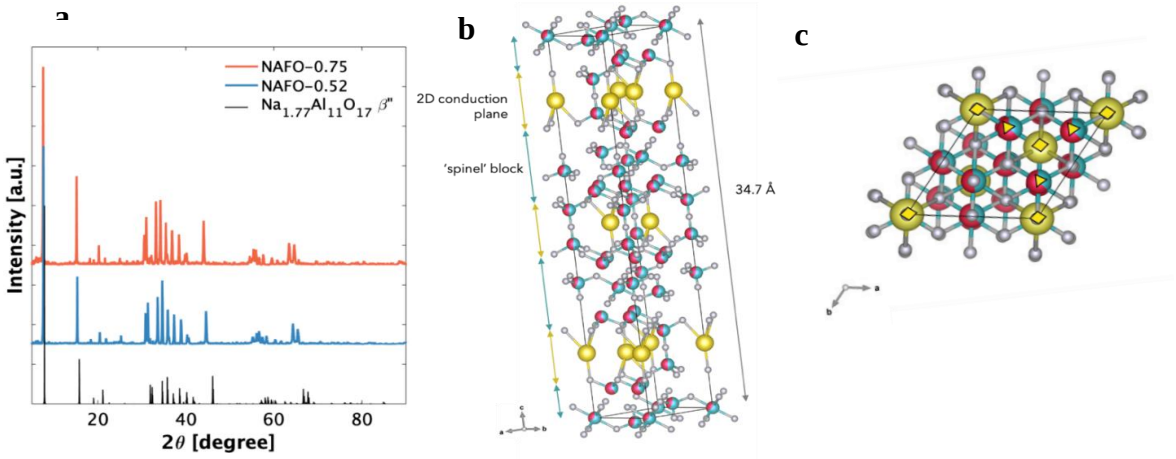

Figure 3-3. a) X-ray diffraction patterns for NAFO-0.52 and NAFO-0.75 with an un-doped β" pattern for reference.[29] The absence of peaks from a Fe-oxide phase confirms the complete substitution of Fe into the β" structure and slight shifts to lower 2θ indicates an increasing lattice constant with the substitution of Fe for Al **b)** Crystal structure of NAFO-0.52 as determined by Rietveld refinement of the powder X-ray diffraction pattern, showing full occupancy of Na-ions. Na (yellow), O (gray), Al (blue), Fe (red). The β" structure with $R\bar{3}m$ space group consists of three 'spinel'-like blocks of $(Fe,Al)_2O_3$ and three 2D conduction planes for Na-ion diffusion. **c)** The Na-ion sites can be seen more clearly from the c-axis view. The Beevers-Ross (BR) sites are indicated by the yellow diamonds and the mid-oxygen (mO) sites are indicated by yellow triangles. These two lattice sites allow for Na-ions to rapidly migrate along the a-b conduction plane.

Table 3-1. Site occupancy and lattice parameters from Rietveld refinement of X-ray diffraction pattern.

		$Na_{1+x}(Al_{0.25}Fe_{0.75})_{11}O_{17}$		$Na_{1+x}(Al_{0.48}Fe_{0.52})_{11}O_{17}$		$Na_{1.77}Al_{11}O_{17}$[a]
	Site (coordination)[b]	**Al**	**Fe**	**Al**	**Fe**	**Al**
Occupancy	1 (O)	0.83	5.17	2.43	3.57	6
	2 (T)	0.78	1.22	1.17	0.83	2
	3 (T)	0.80	1.20	1.00	1.00	2
	4 (O)	0.37	0.63	0.66	0.34	1
Lattice parameters	*a* [Å]	5.86		5.79		5.604
	c [Å]	35.06		34.66		33.62
	V [Å^3]	1044		1007		914.3
	Conduction plane thickness [Å][c]	4.82		4.88		5.07

a. From single crystal measurements[28]

b. Coordination is either octahedral (O) or tetrahedral (T) for Al and Fe sites.

c. Calculated from 2 x (O3-Na) bond distance. See Figure 3-4 and Table 3-2.

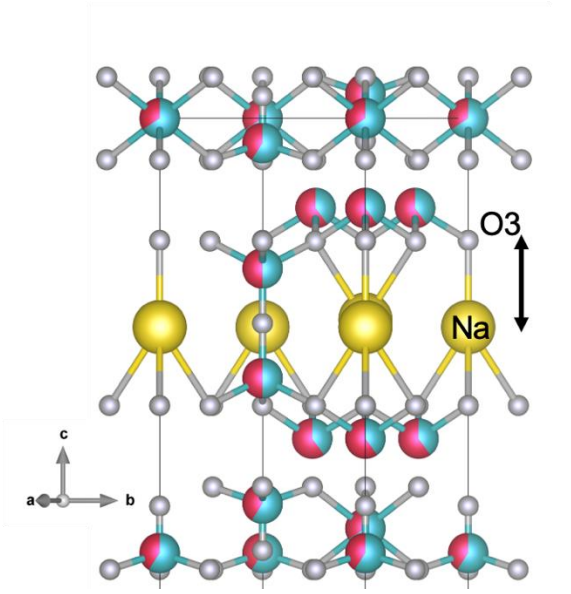

Figure 3-4. a*-axis view of NAFO-0.52, showing the O3-Na bond used to calculate the conduction plane thickness. The calculated bond distances are outlined in **Table 3-2**. [Na (yellow), O (gray) Al (blue) Fe (red)]

Table 3-2. Bond lengths from O3 on the edge of the spinel block to Na in the center of the conduction plane (**Figure 3-4**) for NAFO-0.52, NAFO-0.75, and undoped $Na_{1.77}Al_{11}O_{17}$ for reference.

Composition	**O3 to Na1 bond length [Å]**
$Na_{1.77}Al_{11}O_{17}$ [a]	2.54
NAFO-0.52	2.44
NAFO-0.75	2.14

[a] from single crystal measurements [28]

Table 3-3. Inductively coupled plasma mass spectrometry (ICP-MS) measurements on NAFO-0.52 and NAFO-0.75 highlighting the similar Fe: Al molar ratios to those calculated through Rietveld refinement (**Table 3-1**).

Sample	**Iron [wt. %]**		**Aluminum [wt. %]**		**Average Fe_xAl_y molar ratio**	
	Average*	**stdev**	**Average***	**stdev**	**x**	**Y**
NAFO-0.52	31.32	1.44	15.91	0.87	0.49	0.51
NAFO-0.75	47.92	1.03	6.55	0.27	0.78	0.22

**Each sample was done in triplicated measurements with background correction.*

The site occupancy of Fe was confirmed by employing ^{57}Fe Mössbauer spectroscopy. Figure 3-5 displays the Mössbauer spectrum of NAFO-0.52 powder, which can be characterized by a broad, asymmetric doublet with a slight shoulder at the inner part of the high velocity resonance absorption peak. Peak fitting for this structure is only possible with 4 subcomponents which reveal isomer shift values that are typical for high spin Fe^{3+} in octahedral (around 0.3 – 0.4 mm s^{-1}) and tetrahedral (around 0.15 – 0.25 mm s^{-1}) oxygen coordination.[37] The site occupancy obtained through Mössbauer spectroscopy of NAFO-0.52 is included in
Table *3-4* and corroborates the Rietveld refinement results within experimental error. The main component of the NAFO-0.52 Mössbauer spectrum (Figure 3-5) corresponds to Fe^{3+} in a regular octahedral coordination, site 1(O) in
Table ***3-4***, based on the quadrupole splitting value of ~ 0.6 mm s^{-1}. The second octahedral component, site 4(O) in
Table ***3-4***, with a distinctly lower occupancy has a somewhat more distorted local distortion environment. On the two tetrahedral sites, site 2 and 3 in **Error! Reference source not found.**, both have lower Fe^{3+} occupancy than the octahedral sites with a larger locally distorted environment for site 2(T) than site 3(T). Thus, a fairly good agreement between iron site population by Mössbauer spectroscopy (
Table ***3-4*****Error! Reference source not found.**) and Rietveld refinement (**Table 3-1**) is obtained despite the errors associated with the large overlap of individual components in the Mössbauer spectrum.

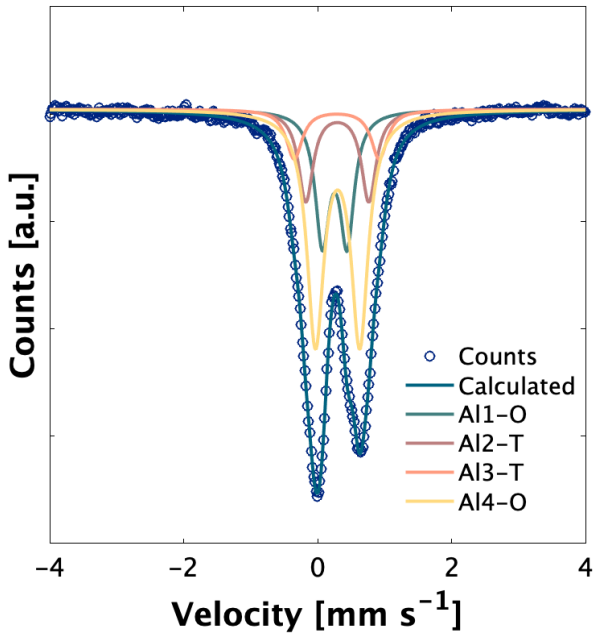

Figure 3-5. ^{57}Fe Mössbauer spectrum of NAFO-0.52, recorded at 298 K and evaluated with 4 Lorentzian shaped doublets. The Fe occupancy obtained from Mössbauer fitting closely matches Fe occupancy obtained through Rietveld refinement and suggests that Fe is in the 3+ valence state after synthesis.

Table 3-4. Fe site occupancy of NAFO-0.52 as determined by Mössbauer spectroscopy.

Site (coordination)[a]	**Isomer Shift [mm s^{-1}]**	**Quadrupole Splitting [mm s^{-1}]**	**Amount [%]**
1 (O)	0.299	0.661	50
2 (T)	0.286	1.270	10
3 (T)	0.295	0.941	17
4 (O)	0.256	0.369	23

[a] Coordination is either octahedral (O) or tetrahedral (T) for Fe sites.

Although there are no indications of the presence of ferrous iron (Fe^{2+}) in the obtained Mössbauer spectra, it is likely that Fe^{2+} exists in small amounts on octahedral sites in the both the NAFO-0.52 and NAFO-0.75 β" compositions. This is due to the dark color of the powders (deep red for NAFO-0.52 and black for NAFO-0.75), as typically seen in Fe^{2+} containing materials, as well as the ability to measure electronic conduction in the as-synthesized pellet (*vide supra*) which requires Fe^{2+} to be present in the structure. The lack of Fe^{2+} detection is consistent with previous studies of Fe substitution into K- β"-ferrite which were also not able measure the presence of Fe^{2+}. The authors of that study suggested this is not unexpected as Fe^{2+} content is low and, due to fast electron hopping between Fe^{2+}/Fe^{3+} ions, peak overlap in the Mössbauer spectra is likely, as shown in magnetite.[38,39,40]

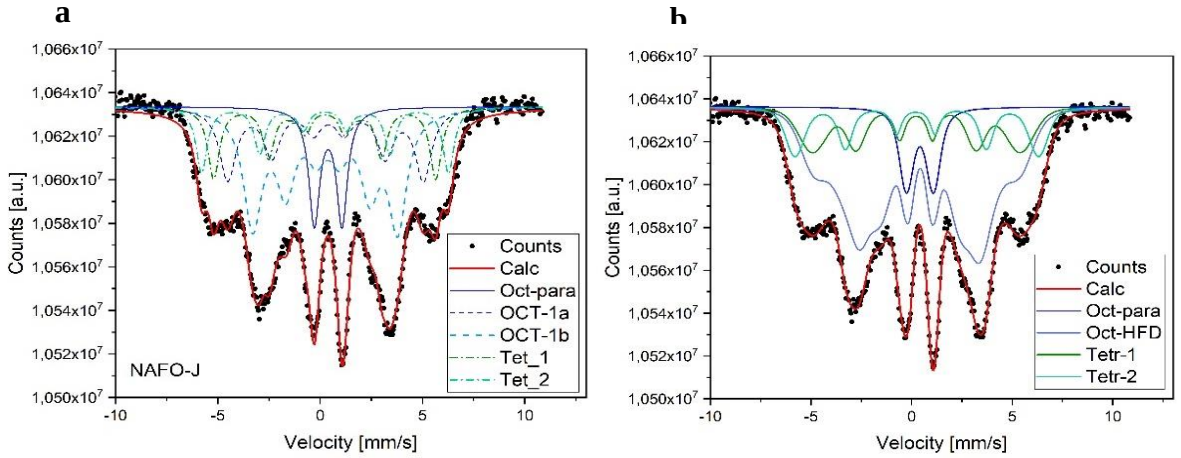

Figure 3-6. a) ^{57}Fe Mössbauer spectrum of NAFO-0.75 powder, recorded at 298 K and evaluated with an exact line shape full static Hamiltonian approach and b) and a hyperfine field distribution approach. The fittings utilized 5 components: one paramagnetic doublet octahedral site (Oct-para), two identical octahedral sties with hyperfine field distributions (Oct-HFD), and two tetrahedral sites (Tet-1 and Tet-2). Due to the low resolution of the spectra and the complicated nature of magnetic interactions within the structure, site occupancy calculations were not possible.

The higher Fe content NAFO-0.75 displays a much more complicated ^{57}Fe Mössbauer spectrum due to the observed magnetic hyperfine interactions at room temperature. Figure 3-6 displays the two attempted fittings of the NAFO-0.75 Mössbauer spectrum based on a classical Hamiltonian approach with Lorentzian shaped lines and a hyperfine field distribution approach. Adequate refinements were achieved using four magnetic split sextets for Fe^{3+} (two ascribed to the octahedral and two to the tetrahedral sites based on the Mössbauer parameters). Additionally, one paramagnetic doublet, which is low in relative area fraction, is ascribed to Fe^{3+} in octahedral coordination. There is no firm evidence for the presence of Fe^{2+}. As only four sites are available in the structure, but a minimum of 5 components are needed for adequate refinement, it was assumed that two of the magnetic split components both belong to Fe^{3+} in the same octahedral site. The paramagnetic doublet site is ascribed to the other octahedral site which shows mainly an occupation with Al^{3+}. Due to the low Fe content at this site, the magnetic super-exchange is most likely hindered. For the two remaining magnetic components, the refined isomer shift clearly indicates tetrahedral coordination although the quadrupole splitting is high. This may suggest that there is a distorted Fe tetrahedral site, but also may be due to an artefact because of the high correlation between the internal magnetic field $H_{f,eq}$. Based on the low resolution and magnetic hyperfine distribution effects, observed in the broad resonance absorption lines, more detailed refinement and site occupancy calculations were not possible.

3.3.2 Electronic conduction through Fe-sites

Due to the β" 'spinel' block structure, analysis of transition metal substitution for Al to promote electronic conduction has focused on the question of octahedral site occupancy. Appreciable electronic conduction has been difficult to achieve in the β" structure due to the

preferential doping into tetrahedral (T) sites over octahedral (O) sites.[34] The short bond distances between Al T sites and tetrahedrally coordinated oxygen atoms as well as the large bond distances between Al T-T sites render Fe^{3+} reduction to Fe^{2+} and subsequent electronic conduction through T sites unlikely. Electronic conduction by electron hopping through transitions from Fe^{2+} to Fe^{3+} is favored in structures where the possibility of charge transfer occurs within one equivalent lattice site to maintain equilibrium throughout the crystal. One example is Fe_3O_4 where electronic conduction occurs between Fe^{3+}/Fe^{2+} on octahedral sites only.[40] Thus, it has been theorized that if an appreciable amount of mixed valence Fe can be doped into octahedral sites, ~26 % based on Kagomé lattice percolation threshold modeling, electronic conduction should occur through the spinel block in an electron hopping mechanism similar to multivalent conductive spinel ferrites such as $NiFe_2O_4$ and $ZnFe_2O_4$.[41]

In the synthesized NAFO-0.52 and NAFO-0.75 materials, Fe substitution into octahedral sites was found to be higher than into tetrahedral sites (Table 3-1). The high octahedral site occupancy by Fe, ~60% NAFO-0.52 and ~83% for NAFO-0.75, may result from the chelation of metal ions in the sol, leading to homogeneous gel-formation and sustained Al/Fe mixing throughout synthesis. As this degree of octahedral Fe occupancy is higher than the calculated percolation threshold, electronic conduction is expected.

Electrochemical impedance spectroscopy (EIS) measurements carried out on an 86% dense NAFO-0.52 sintered pellet were used to characterize electronic conductivity and ionic conductivity contributions in the Fe-substituted Na β"-Al_2O_3 material. The EIS measurement is shown in Figure 3-7 with the modeled equivalent circuit illustrated in the inset. The ionic conductivity can be split into bulk ionic conductivity $\sigma_{b,Na+}$ and grain boundary conductivity $\sigma_{gb,Na+}$, which are measured to be 1.7×10^{-3} S cm^{-1} and 1.2×10^{-7} S cm^{-1}, respectively. A bulk

ionic conductivity on the order of 10^{-3} S cm^{-1} is of the same order of magnitude as that of the un-doped polycrystalline[11] Na β"-Al_2O_3 structure at room temperature, indicating that 52 % Fe for Al substitution into the β"-Al_2O_3 structure maintains the conduction plane structure which enables rapid Na^+ transport. The bulk ionic conductivity of NAFO-0.52 is also an order of magnitude larger than that of NASICON type solid electrolyte $Na_{1+x}Zr_2P_{3-x}Si_xO_{12}$ ($0 \leq x \leq 3$) (~10^{-4} S cm^{-1}) [3] and several orders of magnitude larger than transition metal substituted NASICON type $Na_3V_2(PO_4)_3$ (~$10^{-6.5}$ S cm^{-1}) [42] and $Na_{1+x}Ti_{2-x}Al_x(PO_4)_3$ (x = 0.6 – 0.9) (~10^{-7} S cm^{-1}) [43] at room temperature.

The diffusion coefficient was calculated from the ionic conductivity to compare the diffusion coefficient of NAFO-0.52 to other high-rate electrode materials. The Nernst-Einstein relation can be used to calculate a Na^+ diffusion coefficient through the bulk of the material as[44]

$$D_{Na^+} = \frac{\sigma_{b,Na^+} RT}{c_{Na^+} F^2} \qquad \text{Eq. S1}$$

where R is the gas constant, T is temperature, c_{Na^+} is the molar concentration of Na^+ per unit volume obtained from Rietveld refinement, and F is Faraday's constant The diffusion coefficient of Na^+ in NAFO-0.52 is calculated to be 9 x 10^{-8} cm^2 s^{-1}, well surpassing the diffusion coefficient of ~10^{-10} cm^2 s^{-1} typically observed in NASICON type materials[5] (for $Na_3V_2(PO_4)_3$, D_{Na^+} ≈10^{-10} cm^2 s^{-1} [REF 45] and for $NaTi_2(PO_4)_3$, D_{Na^+} ≈ 10^{-12}- 10^{-13} cm^2 s^{-1} [REF 46]). based on the modeled electronic resistance from EIS data is 1.5 x 10^{-7} S cm^{-1}. While sufficient to achieve mixed electronic-ionic conduction, electronic conductivity on this order of magnitude is lower than that of pseudocapacitive, high-power electrode materials for Li-ion batteries such as T-Nb_2O_5 (~ 10^{-5} S cm^{-1}) [47] and TiO_2(B) (~ 10^{-5} S cm^{-1}).[48] (See Table 3-5 for a summary of materials properties discussed.)

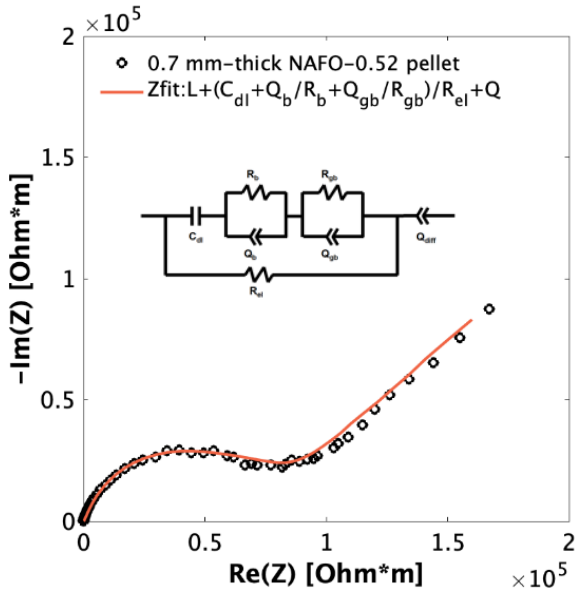

Figure 3-7. Electronic σ_{el}, bulk ionic $\sigma_{b,Na+}$ and grain boundary $\sigma_{gb,Na+}$ conductivities of a NAFO-0.52 sintered pellet with silver blocking electrodes were determined by electrochemical impedance spectroscopy (EIS). The EIS data was fit to the equivalent circuit shown in the inset giving $\sigma_{b,Na+}$ = 1.7 x 10^{-3} S cm^{-1}, σ_{gb} = 1.2 x 10^{-7} S cm^{-1}, and σ_{el} = 1.5 x 10^{-7} S cm^{-1}.

Table 3-5. Conductivities and diffusion coefficients of materials discussed throughout Chapter 3.

Material	Conductivity [S cm^{-1}]		Diffusion Coefficient [cm^2 s^{-1}]	Test environment, technique	Electrolyte, Electrode	REF
	Ionic	Electronic				
$Na_3V_2(PO_4)_3$@C/G	---	---	4.59 x 10^{-10}	25 °C; 1 M $NaClO_4$ in EC/DEC (1:2; v/v) with 2 vol.% FEC, EIS	Electrode	[45]
P2-$Na_{2/3}Ni_{1/3}Mn_{1/3}Ti_{1/3}O_2$	---	---	10^{-10} - 10^{-9}	RT, 1M $NaClO_4$ in EC/DEC (1:1; v/v) with 5 vol.% FEC, GITT	Electrode	[49]
$Na_3V_2(PO_4)_3$	~$10^{-6.5}$	---	6×10^{-13} – 2×10^{-15} cm^2 s^{-1}	- Polycrystalline, RT, EIS - RT, 1 M $NaPF_6$ in propylene carbonate (PC), GITT	Electrode	[42,50]
$Na_3Fe_2(PO_4)_3$	---	---	2.4 × 10^{-8} cm^2 s^{-1}	RT, 1M $NaClO_4$ in EC/DMC (1:1; v/v), CV	Electrode	[51]
$Na_3Fe_2(PO_4)P_2O_7$@ RGO	---	---	1 × 10^{-11} – 5 × 10^{-10} cm^2 s^{-1}	RT, 1M $NaClO_4$ in EC/DEC (1:1; v/v) 5% FEC, GITT	Electrode	[52]
$NaTi_2(PO_4)_3$	---	---	~4 × 10^{-15} cm^2 s^{-1}	RT, 1M $NaClO_4$ in EC/DMC (1:1; v/v), CV	Electrode	[53]
T-Nb_2O_5	---	3 x 10^{-5}	---	Polycrystalline 300K, four-point probe	Electrode	[47]
TiO_2(B)	---	8 x 10^{-5}	---	Polycrystalline, Room Temperature	Electrode	[48]
$Na_{1+x}Ti_{2-x}Al_x(PO_4)_3$ x = 0.6 – 0.9	1.3 x 10^{-7}	---	---	Polycrystalline, RT	Electrolyte	[43]
$Na_{1+x}Zr_2P_{3-x}Si_xO_{12}$ $0 \le x \le 3$	6.7 × 10^{-4}	---	---	Polycrystalline, Room Temperature, EIS	Electrolyte	[3]

$Na_{3.1}Zr_{1.95}Mg_{0.05}Si_2PO_{12}$	~3.5 × 10^{-3}	---	~5 × 10^{-8}	Polycrystalline, Room Temperature, EIS, CV	Electrolyte	[54]
Li_3N	6.6 x 10^{-4}	---	---	Polycrystalline at 25 °C, EIS	Electrolyte	[55]
$Na_{1.67}Li_{0.33}Al_{11}O_{17}$	1 x 10^{-3}	---	---	Polycrystalline β" at 25 °C	Electrolyte	[11]
NAFO-0.52	1.7 x 10^{-3}	1.2 x 10^{-7}	9 x 10^{-8}	Polycrystalline 25 °C, EIS	Electrode	This work

3.3.3 Sodium charge-storage properties of Fe- substituted beta" alumina

The combination of a high bulk ionic conductivity and a sufficient level of electronic conduction led us to characterize the charge storage properties of Fe-substituted Na β"-Al_2O_3 as a Na-ion electrode material. Galvanostatic (GV) measurements provide insight regarding the attainable capacity and the maximum number of Na-ions that can be reversibly cycled into the material (Figure 3-8**)**. Due to the partially filled sodium sites in the pristine material, the open circuit voltage is typically in the range of 2.3 - 2.5 V vs Na/Na^+. Notably, GV cycling demonstrates that at a 0.5C rate, the capacity of NAFO-0.52 and NAFO-0.75 are nearly equal at 66 mAh g^{-1} (1.9 mol Na^+) and 61 mAh g^{-1} (1.9 mol Na^+) respectively. In both cases, the capacity from conductive carbon has been subtracted. The similar gravimetric capacities and close to 2 mol Na^+ inserted at slow C-rates implies that the capacity of NAFO compounds is not limited by the amount of $Fe^{2+/3+}$ within the structure but is instead limited by the number of sodium sites available. In the β" structure, Na^+ can occupy BR sites (Figure 3-3c), resulting in 2 Na^+ per site per formula unit (6 per unit cell) and a theoretical capacity of ~69 mAh g^{-1} regardless of excess $Fe^{2+/3+}$ substitution or the amount of Fe on octahedral sites. The proposed reaction mechanism for sodium intercalation into NAFO-0.52 is:

Equation 3-1

$$Na_{2-x}(Al_{0.48}Fe_{0.52})_{11}O_{17} + xNa^{+} + xe^{-} \leftrightarrow Na_{2}(Al_{0.48}Fe_{0.52})_{11}O_{17}$$

where $x \lesssim 2$ and Fe^{2+}/ Fe^{3+} is responsible for charge storage. To confirm the GV experiments indicating that ~1.9 mols Na^{+} are removed per NAFO-0.52 formula unit, energy dispersive x-ray (EDX) analysis was performed on ex-situ NAFO-0.52 electrodes cycled to the upper and lower voltage window limits (0.2 and 2.5 V vs Na/Na^{+}). In this way it is possible to estimate the change in sodium concentration upon complete charge and discharge. The Na:Fe ratio for each electrode was identified (**Table 3-6)**; an estimated 1.7 mol Na^{+} were inserted per formula unit throughout

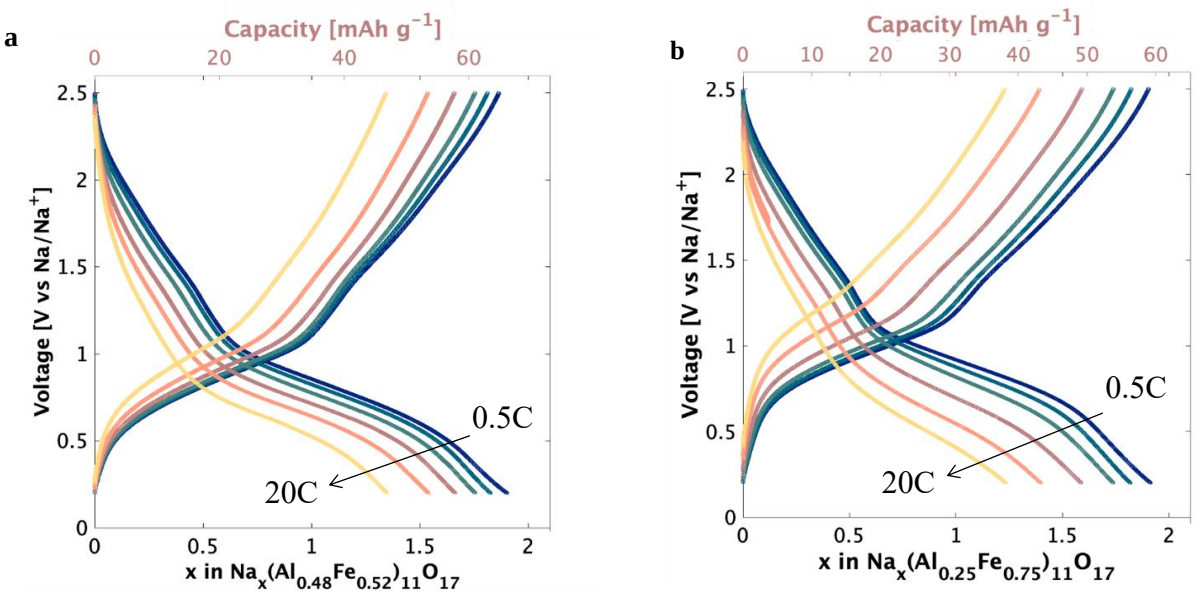

Figure 3-8. Galvanostatic cycling from 2.5 to 0.2 V vs Na/Na^{+} of **a)** NAFO-0.52 and **b)** NAFO-0.75 composite electrodes at charge-discharge rates of 0.5C, 1C, 2C, 5C, 10C and 20C demonstrating high-rate capability and similar Na-ion insertion at slow rates (1.9 mol Na^{+}, 66 mAh g^{-1} for NAFO-0.52 and 61 mAh g^{-1}, 1.9 mol Na^{+} for NAFO-0.75). The capacity attributed to sodiation of 15 wt% conductive carbon in the composite electrode has been subtracted and the displayed capacity is normalized to the active material only. The 1C-rate is defined as the integrated capacity from a 0.1 mV s^{-1} cyclic voltammogram.

the voltage window based on the difference in Na-ion content in the ex-situ electrodes. Thus, the EDX results suggest that $x \lesssim 2$ is a reasonable assumption in Equation 3-1.

Table 3-6. Na and Fe atom % determined by energy dispersive X-ray analysis on ex-situ NAFO-0.52 electrodes (pristine, cycled to 2.5 V, and cycled to 0.2 V). Electrodes were soaked in DMC and dried in an Ar atmosphere prior to measurements. Average atom % is used to calculate an average Na:Fe ratio for each electrode. The difference between the Na:Fe ratio in the electrode cycled to 2.5 V and 0.2 V is used to calculate the mol Na inserted per formula unit into NAFO-0.52 with 5.72 mol Fe per formula unit. The amount of Na in the pristine electrode is calculated for comparison.

		Pristine	**Cycled to 2.5 V**	**Cycled to 0.2 V**
EDX Map #*	**Element**	**Atom %**		
Map 1	Fe	5.15	1.77	4.71
	Na	1.83	5.92	12.03
Map 2	Fe	5.01	1.31	3.59
	Na	1.86	3.91	11.25
Map 3	Fe	3.86	1.64	3.49
	Na	1.66	4.85	12.11
Map 4	Fe	4.81	2.64	--
	Na	1.72	7.96	--
Map 5	Fe	--	3.29	--
	Na	--	9.51	--
Map 6	Fe	--	3.29	--
	Na	--	10.2	--
Map 7	Fe	--	4..93	--
	Na	--	8.70	--
Average Na: Fe		0.37	2.71	3.00
Calculated mol Na inserted based on 5.72 Fe per formula unit		2.13	1.67	

*each map represents various sections of the electrode surface

The GV cycling also demonstrates the excellent capacity retention from a rate of 0.5C to 20C (71 % and 65 % for NAFO-0.52 and NAFO-0.75, respectively) and underscores the slightly superior rate capability of NAFO-0.52 compared to that of NAFO-0.75. The galvanostatic charge-discharge curves do not display any obvious voltage plateaus throughout the voltage window, suggesting that the β" structure does not undergo a phase transition upon sodiation or desodiation. Comparison of the ex-situ XRD patterns of a pristine, a fully sodiated (1^{st} cycle) and fully desodiated (10^{th} cycle) NAFO-0.52 electrode (Figure 3-9) confirms that the integrity of the β" structure was maintained upon full sodiation to 0.2 V vs Na/Na^+ and conversion to Fe^0 is avoided. Similarly, the β" structure is maintained upon sodium removal to 2.5 V vs Na/Na^+. Rietveld refinement on an NAFO-0.52 electrode after 10 cycles at 1C confirms that the lattice parameters did not change significantly (**Table 3-7**), further indicating that the β" structure shows stable behavior during cycling despite removing nearly all the Na^+ ($x \lesssim 2$) on each cycle. Additional evidence of active material stability was demonstrated through EIS of NAFO-0.52 vs Na-metal at various voltages during charge and discharge, starting from open circuit voltage after pre-cycling at 1.9 V vs Na/Na^+. Cell resistance R_Ω and charge transfer resistance R_{CT} were found to be nearly constant throughout the voltage window (Figure 3-10), highlighting β" phase stability and the avoidance of interfacial reactions. Cycling stability of NAFO-0.52 was also confirmed by demonstrating 95% capacity retention at 1C over 50 cycles while maintaining a coulombic efficiency over 99.3% (Figure 3-11).

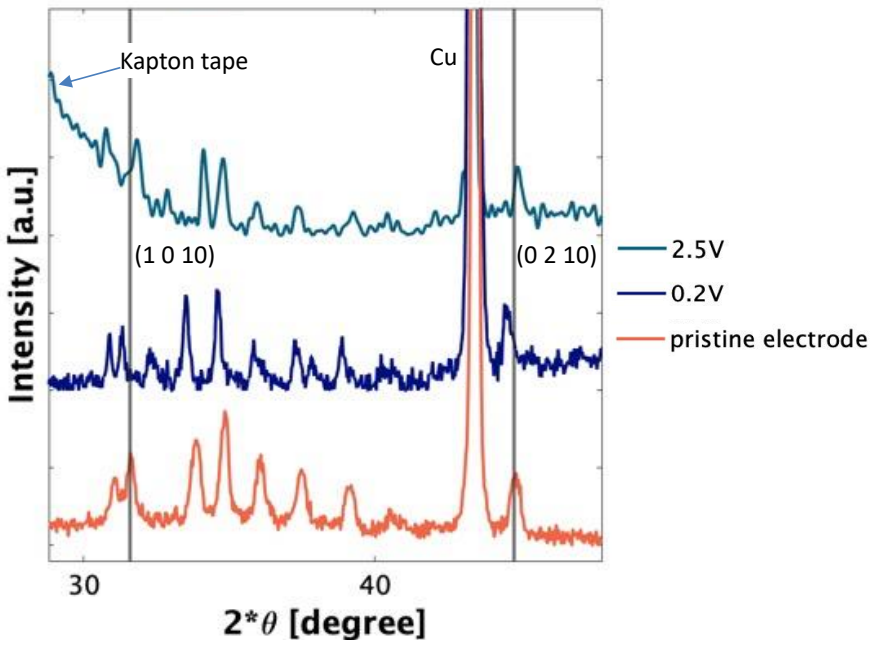

Figure 3-9. Comparison of the X-ray diffraction pattern of a pristine, uncycled electrode and electrodes galvanostatically cycled to 0.2 V (1st cycle) and 2.5 V vs Na/Na^+ (10th cycle). The shifts in peak positions indicate a compression of the unit cell upon Na removal to 2.5 V and expansion of the unit cell upon Na insertion to 0.2 V, highlighted by the vertical lines at the (1 0 10) and (0 2 10) reflections and corresponding shifts of the 0.2 and 2.5 V reflections. The 0.2 V diffraction pattern demonstrates that there is no obvious structural breakdown or conversion reaction that occurs at low voltages such as the formation of Fe_2O_3 or Na-metal. The small peak at ~32° 2θ reveals that a small amount of the β" phase has been converted to the β phase, which does not appear to significantly affect cycling behavior due to the capacity retention and high Coulombic efficiency (Figure 3-11).

Table 3-7. Lattice parameters of NAFO-0.52 before cycling and after 10 cycles at 1C, highlighting the structural stability after sodium insertion and de-insertion.

Lattice Parameter	Pristine	10 cycles at 1C
a [Å]	5.79	5.79
c [Å]	34.66	34.75
V [Å³]	1007.32	1007.51

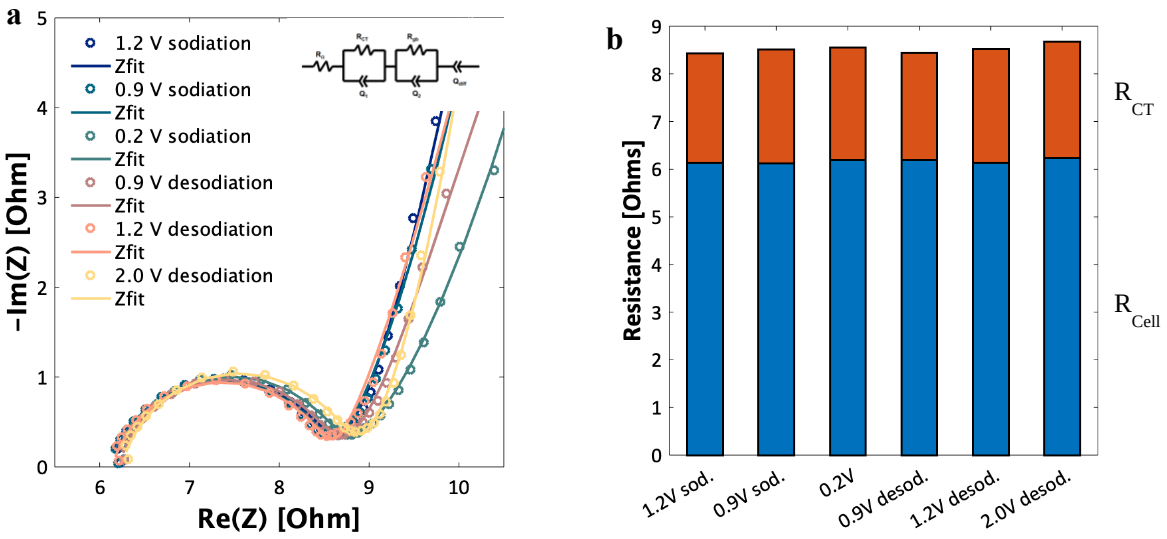

Figure 3-10. a) Electrochemical impedance spectroscopy (EIS) of an NAFO-0.52 vs Na metal coin-cell with corresponding equivalent circuit fitting (shown in the inset). EIS spectra were obtained after holding for 30 min at the indicated voltage to reach an equilibrium state. Throughout cycling, the cell resistance R_{cell} and charge transfer resistance R_{CT} remain stable (b), suggesting the absence of interfacial reactions or secondary phase formation.

The fundamental kinetic properties of NAFO-0.52 and NAFO-0.75 composite electrodes were determined using cyclic voltammetry (CV) measurements. The CV measurements between 2.5 and 0.2 V vs Na/Na^+ at rates from 0.1 to 1.0 mV s^{-1}, shown in Figure 3-12**a and b**, are highly

reversible producing one broad redox peak centered at ~0.7 V vs Na/Na^+ and a broad tail from ~1.2 to 2.5 V vs Na/Na^+. This demonstrated reversibility and low-voltage stability are contrary to behavior observed in CV measurements of Fe-oxide materials Fe_2O_3 and Fe_3O_4 where a high capacity Fe conversion peak is observed at low voltages upon sodiation (or lithiation) and the corresponding desodiation is polarized by as much as ~1 V.[56,45] Although a similar Fe-oxide structure exists in the spinel block of the β" material, there is no evidence of any conversion to Fe^0 upon sodium insertion into either NAFO-0.52 or NAFO-0.75.

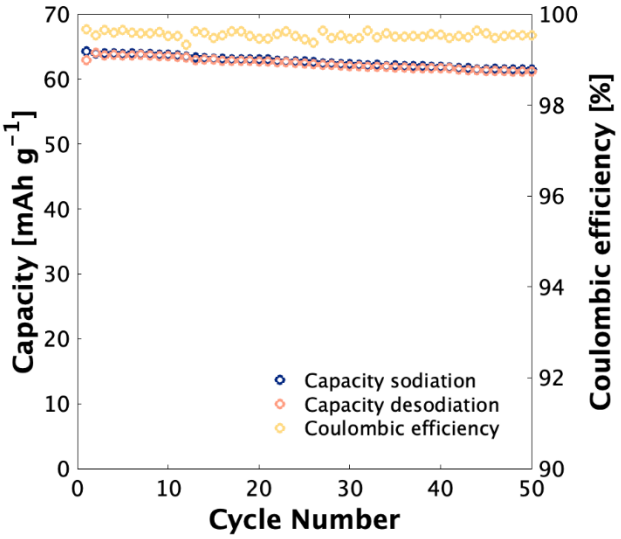

Figure 3-11. NAFO-0.52 galvanostatic cycling sodiation (blue) and desodiation (pink) capacity at a 1C-rate (after galvanostatic rate cycling shown in Figure 3-5a) with corresponding Coulombic efficiency (yellow), indicating > 95 % capacity retention over 50 cycles and > 99 % efficiency.

The broad nature of the NAFO-0.52 and NAFO-0.75 redox peaks in addition to the lack of substantial peak polarization suggest a capacitor-like charge storage mechanism for the Fe^{2+}/Fe^{3+} redox process.[57] Pseudocapacitance, a redox-based charge storage mechanism that occurs on

timescales similar to that of electrical double layer capacitors (EDLCs), is typically demonstrated in nano-sized particles due to the ample availability of surface storage sites.[58] The combination of such broad redox peaks and fast charge storage kinetics exhibited with *micron sized* particles of the NAFO materials is thus highly unusual and was investigated further.

The starting point for the kinetic studies is to determine the power-law relationship between current (i) and sweep rate (v):[57]

Equation 3-2

$$i(v) = av^b$$

where a is a constant and b is the power-law exponent. This analysis can be used to determine the qualitative nature of a redox reaction such that a diffusion limited redox reaction gives b = 0.5 based on the sweep rate dependence of the Randles-Sevcik equation whereas a surface-controlled redox reaction gives b = 1, similar to EDLC charge storage mechanisms.[57,59] Analysis of peak

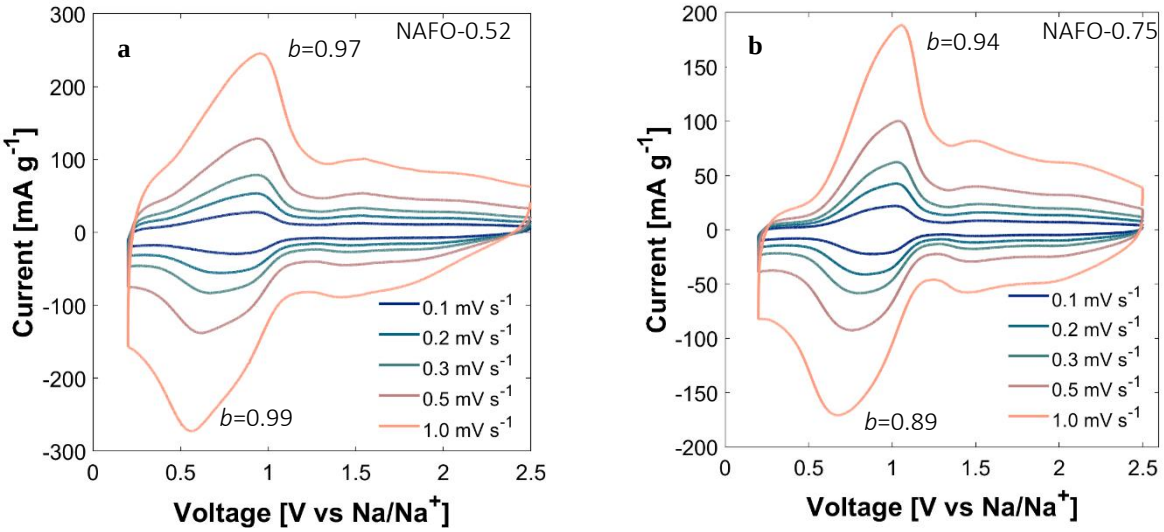

Figure 3-12. Cyclic voltammetry from 0.1 mv s^{-1} to 1.0 mV s^{-1} of **a)** NAFO-0.52 and **b)** NAFO-0.75 electrodes vs Na metal foil in a two-electrode coin cell configuration. The broad nature of the peaks and the peak current *b*-value determination, as indicated next to the peaks, suggest a capacitor-like charge storage mechanism.

currents from sweep rates of 0.1 to 1.0 mV s^{-1} resulted in *b*-values of 0.97 and 0.99 for NAFO-0.52 cathodic and anodic peaks, respectively, indicating a surface-controlled charge storage mechanism. The *b*-values of 0.94 and 0.89 determined for cathodic and anodic peaks, respectively, for NAFO-0.75 peak currents suggested that charge storage kinetics are dominated by a similar surface-controlled process as that for NAFO-0.52.

We also used step potential electrochemical spectroscopy (SPECS) to gain more quantitative insight into the nature of the capacitor-like vs. diffusion-controlled currents during NAFO-0.52 cycling.[60,61] In this method, a 10-mV potential step is applied and the current response is measured while holding at that potential for an equilibration period of 300 seconds. This is repeated throughout the entire potential window such that each potential step can be taken as a jump in voltage from an equilibrium current value. The current response can then be modeled using two capacitive current models, a diffusion-limited current model, and a residual current based on the small but non-zero current value after 300 seconds. The two modeled capacitive currents represent the geometric capacitive current i_g [A g^{-1}] (from the electrode-electrolyte surface) and the porous capacitive current i_p [A g^{-1}] (from the internal interfaces of the electrode)

Equation 3-3

$$i_g = \frac{\Delta E}{R_1} \exp\left(-\frac{t}{R_1 C_1}\right),$$

Equation 3-4

$$i_p = \frac{\Delta E}{R_2} \exp\left(-\frac{t}{R_2 C_2}\right),$$

where ΔE is the voltage step size [V], R is resistance [$\Omega \cdot g$], C is capacitance [F g^{-1}], and t is time [s]. The diffusion-controlled current can be modeled from the Cottrell equation for semi-infinite planar diffusion[31]:

Equation 3-5

$$i_d = \frac{B}{t^{1/2}} [\text{A g}^{-1}]$$

where *B* is a fitting parameter. The total current at each voltage step can then be taken as

Equation 3-6

$$i_{Total} = i_g + i_p + i_d + i_r,$$

where i_r [A g^{-1}] is the residual current. Given this model of a time-dependent current response throughout the voltage window, the current response can then be reevaluated at an assumed sweep rate to give a calculated cyclic voltammogram.[32] The reconstructed CV of NAFO-0.52 at 0.01 mV s^{-1} is shown in Figure 3-13, demonstrating the high values of i_p (the capacitive current within the electrode) throughout the redox process from 0.5 to 1.2 V vs Na/Na^+. Comparing the calculated SPECS voltammogram at 0.001 mV s^{-1} and the experimental data collected at a sweep rate of 0.1 mV s^{-1}, the SPECS analysis does an excellent job of capturing the electrochemical features of the Fe^{3+}/Fe^{2+} redox. An example of a modeled current response is shown in Figure 3-13**b and c**.

Now, with experimental CV measurements at sweep rates from 0.1 to 1.0 mV s^{-1} (**Figure 3-12**a), k_1/k_2 analysis was performed to compare the percentage of surface controlled vs. diffusion controlled current responses in NAFO-0.52.[57,62] In k_1/k_2 analysis, the relationship between current i and sweep rate v in surface- ($i \propto v$) and diffusion-controlled ($i \propto v^{1/2}$) mechanisms are qualitatively compared through the proportionality constants k_1 and k_2 as:[57]

Equation 3-7

$$i(v) = k_1 v + k_2 v^{1/2}.$$

Similarly, for reconstructed CVs from SPECS analysis at 0.01 and 0.1 mV s^{-1}, modeled capacitive currents (Figure 3-13) were taken throughout the voltage window as the capacitive percentage of the total current i_{Total}:

Equation 3-8

$$\% \text{ surface-controlled} = \frac{i_g + i_p}{i_{Total}},$$

where i_g is the geometric capacitive current and i_p is the porous capacitive current. The breakdown of contributions of diffusion and capacitive controlled currents are shown in Figure 3-14**a,** ranging from 81% capacitive-current at 0.01 mV s^{-1} from SPECS analysis to 94% capacitive-current at 1.0 mV s^{-1} from k_1/k_2 analysis. The % capacitive current obtained from SPECS analysis at 0.1 mV s^{-1} corresponds relatively well to that obtained from cyclic voltammetry at the same rate (91 vs 83%, respectively). The corresponding CV at 1.0 mV s^{-1} with the capacitive current region, $k_1 v$, shaded is displayed in Figure 3-14**b**. SPECS analysis allows for reconstruction of CVs at sweep rates slower than practically obtained though CV. Thus at 0.01 mV s^{-1}, an 81% capacitive current is close to that of an of intrinsic material property without limitations in charge storage that occur when fast sweep rates inflate the capacitive contribution.

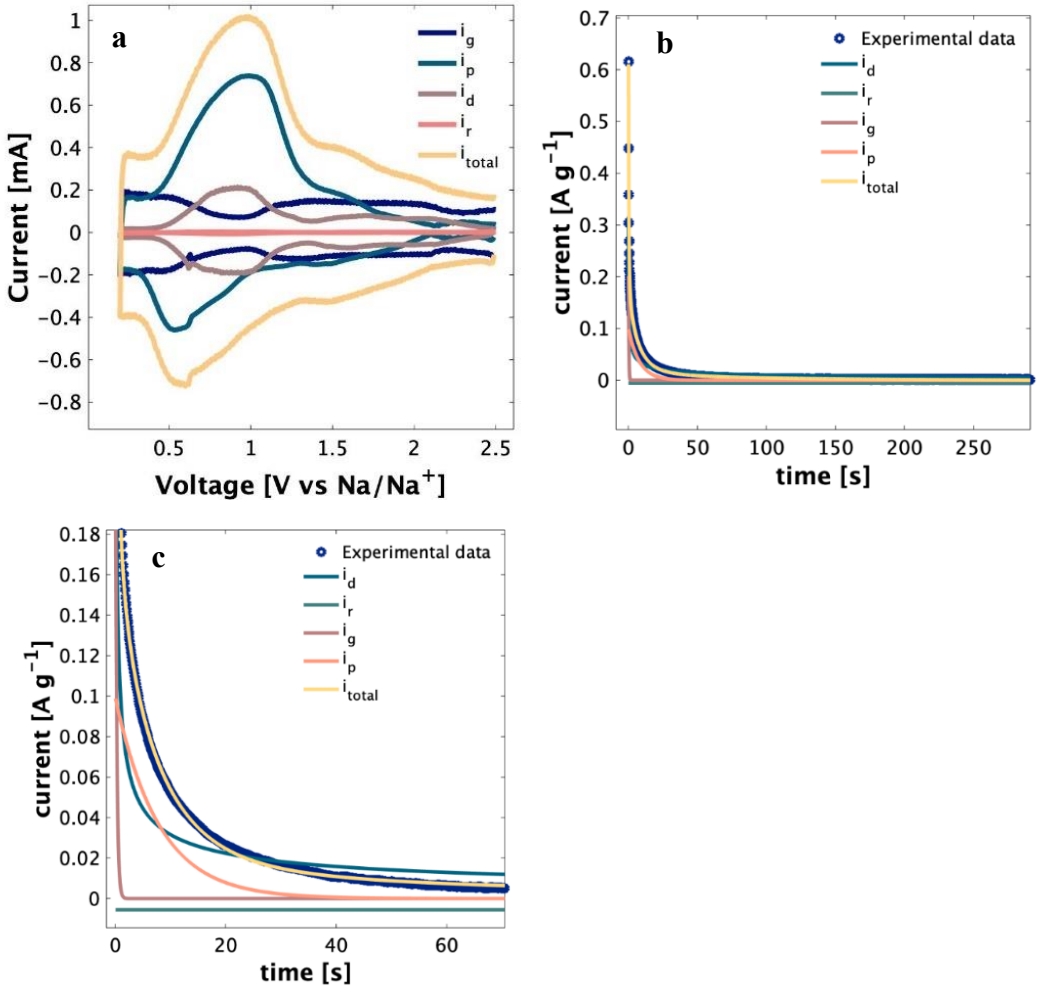

Figure 3-13. a.) Reconstruction of cyclic voltammetry currents at 0.01 mV s^{-1} based on step-potential electrochemical spectroscopy (SPECS) analysis where i_g is the geometric capacitance current, i_p is the porous capacitance current, i_d is the diffusion controlled current and i_r is the residual current. The high calculated current values of porous capacitance within the redox active voltage region (~0.3-1.2 V vs Na/Na^+) confirms the pseudocapacitive nature of the redox process. b) Current decay profile over 300s after a 10 mV voltage step to hold at 0.84 V vs Na/Na^+. Currents from SPECS fitting model are shown where i_g is the geometric capacitive current, i_p is the porous capacitive current, i_d is the diffusion-controlled current, i_r is the residual current, and i_{total} is the sum of the modeled currents. c) A zoomed-in view of the first 50 seconds displaying the short response time for capacitive currents, < 5 s for i_g and < 30 s for i_p, compared to the longer response times for the diffusion controlled current.

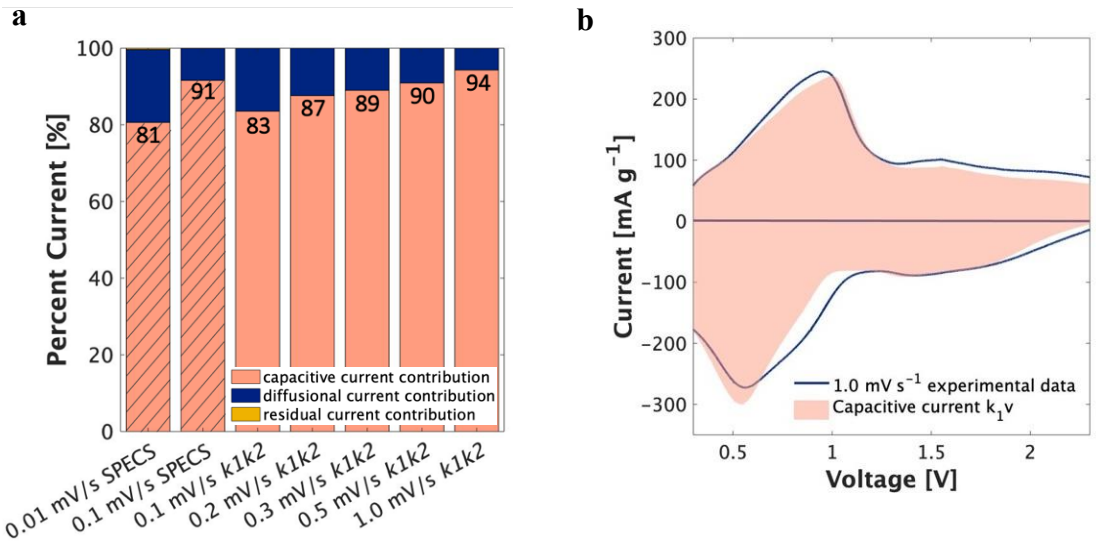

Figure 3-14. a) Percent capacitive, diffusional, and residual currents of a NAFO-0.52 composite electrode as determined by SPECS and k_1/k_2 analysis. **b)** k_1/k_2 analysis of NAFO-0.52 results in a 94% capacitive current at a scan rate of 1.0 mV s^{-1}.

3.4 Discussion

Due to the relatively low electronic conductivity, 1-10 μm particle size, and low electrochemical surface area available for surface charge storage in the Fe-substituted β" material, it is unexpected that the electrochemical kinetics of the Fe^{2+}/Fe^{3+} redox process in NAFO-0.52 have capacitor-like electrochemical signatures. However, the high Na-ion conductivity retained in the Fe-substituted structure enables high-rate performance and capacitor-like electrochemical signatures are indeed observed. Moreover, the avoidance of a conversion reaction at low potentials (0.2 V vs Na/Na^+) highlights the useful properties that can arise from electrodes designed from the modification of thermodynamically stable solid electrolytes. In order to compare the rate performance of NAFO-0.52 to other high-rate electrodes reported to date, it is helpful to consider the relative capacity of the electrode material as a function of C-rate. In this analysis, the capacity

for a given material is normalized by its theoretical capacity and a value of 1 indicates the material is operating at its theoretical capacity. This normalized capacity for various Na-ion electrode materials in nonaqueous electrolyte half cells is plotted as a function of C-rate in Figure 3-15. A particularly useful feature of this plot is that it indicates the C-rate where the capacity begins to exhibit a significant decrease.

The capacity of NAFO-0.52 is close to theoretical at a 0.5C rate and its capacity retention at high rate is comparable to the best performing high-rate nonaqueous electrodes such as P2-phase substituted oxides.[49,63] **Figure 3-15** also demonstrates the superior rate retention of NAFO-0.52 compared to that of bulk NASICON-type cathode materials $Na_3V_2(PO_4)_3$,[50] $Na_3Fe_2(PO_4)(P_2O_7)$,[52] and $Na_3(VO)_2(PO_4)_2F$ [64] and that of an anode material $NaTi_2(PO_4)_3$.[53] The relatively sluggish high-rate kinetics of NASICON-type materials doped with redox active transition-metal ions investigated to date can be explained by the phase transition that is triggered by the insertion/de-insertion of Na.[5,64,65] Achieving good charge storage retention at high rates has been difficult with Na-ion analogues to Li-ion materials due to the larger size of the Na-ion compared to the Li-ion. Thus, the Fe-doped Na-β" alumina electrode presented here represents a viable alternative to existing high-power, low-voltage anodes for Na-ion batteries and Na-ion capacitors.[66,67]

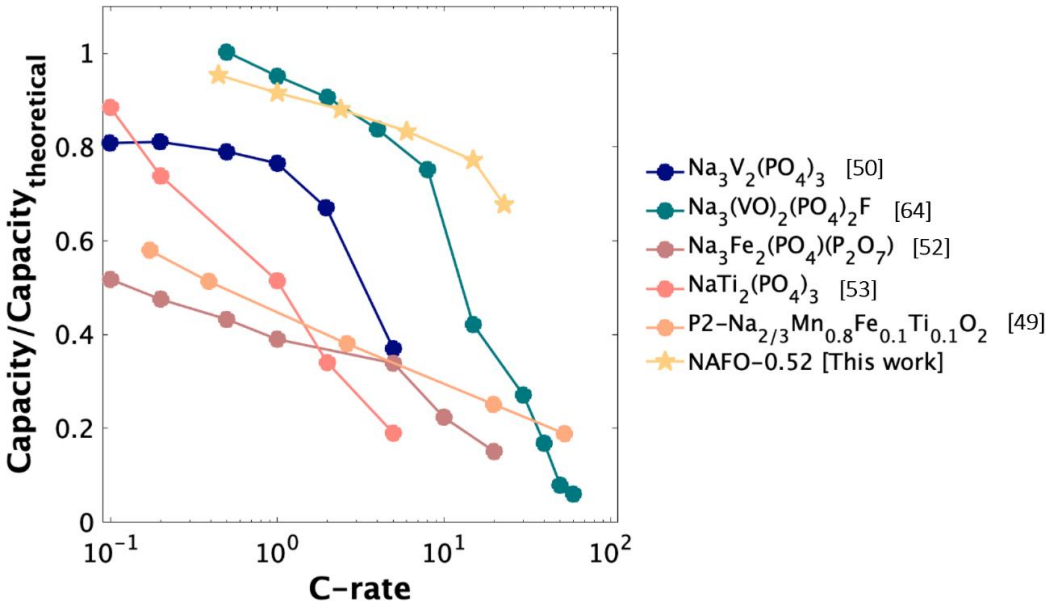

Figure 3-15. Comparison of normalized capacity of high-rate Na-ion battery electrode materials vs metal foil as a function of *log*C-rate. This data highlights the superior capacity retention of NAFO-0.52 compared to NASICON-type materials and comparable rate performance with the best performing high-rate Na-ion electrodes to date. [49,50,52,53,64] The C-rates of presented materials have been recalculated from reported data to represent time to charge (1C = 1 hour). Only materials tested without carbon matrix composites or coatings, or highly nanostructured arrays are included to illustrate fundamental materials properties. Each material was tested with an active material loading between 1 and 4 mg cm^{-2}.

In addition to its potential use as a negative electrode for Na-ion batteries, the Fe-doped Na-β" alumina electrode represents a model system which enables us to establish a set of design rules to guide the development of electrode materials that are based on solid electrolytes. First, a redox-active ion should be substituted that does not significantly affect the electrolyte crystal structure such that ion insertion does not induce a phase transition in the host material. If minimal structural changes are introduced by substituting a redox active transition metal, the high ionic conductivity of the parent solid electrolyte may be preserved. The change in structure upon

transition metal substitution may explain why NASICON-type materials have limited stability, cycle life and rate-performance. This behavior can also be seen in the slightly lower effective Na^+ diffusion coefficient of the mixed-ion-electron conducting NASICON-type materials (10^{-10}–10^{-14} cm^2 s^{-1}) compared to that of the parent solid-electrolyte phase (10^{-8} cm^2 s^{-1}) (see Table 3-5).[5] Second, it is helpful to start with a sodiated (or lithiated) electrolyte structure to provide a reasonable guarantee that stable insertion-ion lattice sites and fast diffusion pathways are present in the starting material. Third, the selected electrolyte material should have an insertion ion (i.e., Na^+) to redox-active ion (TM) ratio greater than 1. If the Na^+/TM ratio is less than one, as demonstrated here, the gravimetric capacity will be too low for the material to be practically useful. Finally, there needs to be a conductive scaffold, such as reduced graphene oxide or carbon coating, to enhance the electronic conductivity in the electrode composite. This is to offset the small polaron conduction mechanism for 3*d* transition metals which results in low electronic conductivity and limits the rate capability despite a high ionic conductivity. One class of materials which may provide opportunities to meet these design requirements is the superionic conductor Na_3PnX_4 (Pn = P,Sb; X = S, Se) due to having the insertion ion to transition metal ratio being >1 and the many options for transition metal substitution.[68,69,70,71]

3.5 Conclusion

The research reported here has demonstrated the successful modification of a solid electrolyte, Na- β" alumina, into an Fe-redox electrode material for sodium-ion batteries. The characteristic conduction plane for Na^+ transport is retained, and the ionic conductivity is comparable to the parent material. Electrode materials containing the 1-10 μm sized particles achieve nearly theoretical capacity for sodium storage at 0.5C and retain more than 70% of theoretical capacity up to a charge-discharge rate of 20C. In contrast to NASICON-type materials,

the fast, reversible kinetics of the Fe-substituted Na β" alumina indicates that the material overcomes the kinetic limitations associated with sodium ion transport processes by maintaining its structure for fast ion conduction. This approach demonstrates that superionic conductors can be modified into high-power electrodes that take advantage of the intrinsically high ionic conductivity, although insertion ion sites and structural properties must be taken into consideration for practical material design. In this way, Fe–substituted β"–Al_2O_3 offers a promising direction for designing high-rate redox electrodes from solid-state electrolytes.

3.6 References

(1) Tarascon, J.-M. Na-Ion versus Li-Ion Batteries: Complementarity Rather than Competitiveness. *Joule* **2020**. https://doi.org/10.1016/j.joule.2020.06.003.

(2) Ellis, B. L.; Nazar, L. F. Sodium and Sodium-Ion Energy Storage Batteries. *Curr. Opin. Solid State Mater. Sci.* **2012**, *16* (4), 168–177. https://doi.org/10.1016/j.cossms.2012.04.002.

(3) Goodenough, J. B.; Hong, H. Y.-P.; Kafalas, J. A. Fast Na+-Ion Transport in Skeleton Structures. *Mater. Res. Bull.* **1976**, *11* (2), 203–220. https://doi.org/10.1016/0025-5408(76)90077-5.

(4) Senguttuvan, P.; Rousse, G.; Arroyo y de Dompablo, M. E.; Vezin, H.; Tarascon, J.-M.; Palacín, M. R. Low-Potential Sodium Insertion in a NASICON-Type Structure through the Ti(III)/Ti(II) Redox Couple. *J. Am. Chem. Soc.* **2013**, *135* (10), 3897–3903. https://doi.org/10.1021/ja311044t.

(5) Chen, S.; Wu, C.; Shen, L.; Zhu, C.; Huang, Y.; Xi, K.; Maier, J.; Yu, Y. Challenges and Perspectives for NASICON-Type Electrode Materials for Advanced Sodium-Ion Batteries. *Adv. Mater.* **2017**, *29* (48), 1700431. https://doi.org/10.1002/adma.201700431.

(6) Delmas, C.; Cherkaoui, F.; Nadiri, A.; Hagenmuller, P. A Nasicon-Type Phase as Intercalation Electrode: NaTi2(PO4)3. *Mater. Res. Bull.* **1987**, *22* (5), 631–639. https://doi.org/10.1016/0025-5408(87)90112-7.

(7) Jian, Z.; Hu, Y.-S.; Ji, X.; Chen, W. NASICON-Structured Materials for Energy Storage. *Adv. Mater.* **2017**, *29* (20), 1601925. https://doi.org/10.1002/adma.201601925.

(8) Nguyen, V.; Liu, Y.; Yang, X.; Chen, W. Fe2(MoO4)3/Nanosilver Composite as a Cathode for Sodium-Ion Batteries. *ECS Electrochem. Lett.* **2014**, *4* (3), A29–A32. https://doi.org/10.1149/2.0021503eel.

(9) Shodai, T. Study of Li3 $minus; XMxN (M: Co, Ni or Cu) System for Use as Anode Material in Lithium Rechargeable Cells. *Solid State Ion.* **1996**, *86–88*, 785–789. https://doi.org/10.1016/0167-2738(96)00174-9.

(10) Rowsell, J. L. C.; Pralong, V.; Nazar, L. F. Layered Lithium Iron Nitride: A Promising Anode Material for Li-Ion Batteries. *J. Am. Chem. Soc.* **2001**, *123* (35), 8598–8599. https://doi.org/10.1021/ja0112745.

(11) Properties of Ionotec beta"-auminas http://www.ionotec.com/pdfs/NaKbetaceramics.pdf.

(12) Hueso, K. B.; Armand, M.; Rojo, T. High Temperature Sodium Batteries: Status, Challenges and Future Trends. *Energy Environ. Sci.* **2013**, *6* (3), 734. https://doi.org/10.1039/c3ee24086j.

(13) Lu, X.; Lemmon, J. P.; Sprenkle, V.; Yang, Z. Sodium-Beta Alumina Batteries: Status and Challenges. *JOM* **2010**, *62* (9), 31–36. https://doi.org/10.1007/s11837-010-0132-5.

(14) Lu, X.; Xia, G.; Lemmon, J. P.; Yang, Z. Advanced Materials for Sodium-Beta Alumina Batteries: Status, Challenges and Perspectives. *J. Power Sources* **2010**, *195* (9), 2431–2442. https://doi.org/10.1016/j.jpowsour.2009.11.120.

(15) Stevens, R.; Binner, J. G. P. Structure, Properties and Production of β-Alumina. *J. Mater. Sci.* **1984**, *19* (3), 695–715. https://doi.org/10.1007/BF00540440.

(16) Boilot, J. P.; Collin, G.; Colomban, Ph.; Comes, R. X-Ray-Scattering Study of the Fast-Ion Conductor β ′ ′ -Alumina. *Phys. Rev. B* **1980**, *22* (12), 5912–5923. https://doi.org/10.1103/PhysRevB.22.5912.

(17) Dunn, B.; Farrington, G. C.; Thomas, J. O. Frontiers in B″-Alumina Research. *MRS Bull.* **1989**, *14* (9), 22–30. https://doi.org/10.1557/S0883769400061704.

(18) Kennedy, J. H.; Akridge, J. R.; Kleitz, M. Complex Plane Analysis of the Impedance and Admittance of Polycrystalline Sodium-β-Alumina Doped with Transition Metal Ions. *Electrochimica Acta* **1979**, *24* (7), 781–787. https://doi.org/10.1016/0013-4686(79)80009-2.

(19) Dunn, B.; Schwarz, B. B.; Thomas, J. O.; Morgan, P. E. D. Preparation and Structure of Li-Stabilized Na+ Beta"-Alumina Single Crystals.

(20) Roth, W.; Benenson, R.; Tikku, V.; Briant, J.; Dunn, B. Li and Mg Stabilized Beta Aluminas. *Solid State Ion.* **1981**, *5*, 163–166. https://doi.org/10.1016/0167-2738(81)90218-6.

(21) Yang, L.-P.; Shan, S.; Wei, X.; Liu, X.; Yang, H.; Shen, X. The Mechanical and Electrical Properties of ZrO2–TiO2–Na-β/B″-Alumina Composite Electrolyte Synthesized via a Citrate Sol–Gel Method. *Ceram. Int.* **2014**, *40* (7), 9055–9060. https://doi.org/10.1016/j.ceramint.2014.01.118.

(22) Muan, A.; Gee, C. L. Phase Equilibrium Studies in the System Iron Oxide- A12O3 in Air and at 1 Atm. O2 Pressure. *J. Am. Ceram. Soc.* **1956**, *39* (6), 207–214. https://doi.org/10.1111/j.1151-2916.1956.tb15647.x.

(23) Kennedy, J. H.; Sammells, A. F. Galvanic Cells Containing Cathodes of Iron-Doped Beta-Alumina. *J. Electrochem. Soc.* **1974**, *121* (1), 1. https://doi.org/10.1149/1.2396820.

(24) Kennedy, J. Electrical and Structural Properties of Iron-Doped β-Alumina. *Solid State Ion.* **1983**, *8* (4), 323–331. https://doi.org/10.1016/0167-2738(83)90008-5.

(25) Kennedy, J. H. Conductivity of Beta-Alumina Highly Doped with Iron. *J. Electrochem. Soc.* **1981**, *128* (11), 2303. https://doi.org/10.1149/1.2127239.

(26) Roland, J. P.; Tseng, T. Y.; Vest, R. W. Stability of the Beta"-Alumina Phase in the System Na-Al-Fe-O. *J. Am. Ceram. Soc.* **1979**, *62* (11–12), 567–570. https://doi.org/10.1111/j.1151-2916.1979.tb12732.x.

(27) Tseng, T. Y.; Vest, R. W. Thermodynamic Properties of Iron Doped Beta-Alumina by e.m.f. Measurements with Beta-Alumina Electrolytes. *J. Mater. Sci.* **1988**, *23* (7), 2387–2393. https://doi.org/10.1007/BF01111893.

(28) Pearson, W. H.; Lomax, J. F. X-Ray Crystal Diffraction Study of Zr,Na-β-Alumina. *MRS Proc.* **1992**, *293*. https://doi.org/10.1557/PROC-293-315.

(29) Lagarec, K.; Rancourt, D. G. Extended Voigt-Based Analytic Lineshape Method for Determining N-Dimensional Correlated Hyperfine Parameter Distributions in Mössbauer Spectroscopy. *Nucl. Instrum. Methods Phys. Res. Sect. B Beam Interact. Mater. At.* **1997**, *129* (2), 266–280. https://doi.org/10.1016/S0168-583X(97)00284-X.

(30) Rancourt, D. G.; Ping, J. Y. Voigt-Based Methods for Arbitrary-Shape Static Hyperfine Parameter Distributions in Mössbauer Spectroscopy. *Nucl. Instrum. Methods Phys. Res. Sect. B Beam Interact. Mater. At.* **1991**, *58* (1), 85–97. https://doi.org/10.1016/0168-583X(91)95681-3.

(31) Dupont, M. F.; Donne, S. W. Electrolytic Manganese Dioxide Structural and Morphological Effects on Capacitive Performance. *Electrochimica Acta* **2016**, *191*, 479–490. https://doi.org/10.1016/j.electacta.2016.01.050.

(32) Forghani, M.; Donne, S. W. Modification of the Step Potential Electrochemical Spectroscopy Analysis Protocol to Improve Outcomes. *J. Electrochem. Soc.* **2019**, *166* (13), A2727–A2735. https://doi.org/10.1149/2.0091913jes.

(33) Forghani, M.; Donne, S. W. Method Comparison for Deconvoluting Capacitive and Pseudo-Capacitive Contributions to Electrochemical Capacitor Electrode Behavior. *J. Electrochem. Soc.* **2018**, *165* (3), A664–A673. https://doi.org/10.1149/2.0931803jes.

(34) Zhu, W.; Akbar, S. A. Mixed Conduction in β-Alumina Type Materials: A Critical Review. *J. Mater. Process. Technol.* **1993**, *38* (1–2), 15–27. https://doi.org/10.1016/0924-0136(93)90182-6.

(35) Mali, A.; Petric, A. Synthesis of Sodium B″-Alumina Powder by Sol–Gel Combustion. *J. Eur. Ceram. Soc.* **2012**, *32* (6), 1229–1234. https://doi.org/10.1016/j.jeurceramsoc.2011.11.004.

(36) Sartori, S.; Martucci, A.; Muffato, A.; Guglielmi, M. Sol-Gel Synthesis of Na+ Beta-Al2O3 Powders. *J. Eur. Ceram. Soc.* **2004**, *24* (6), 911–914. https://doi.org/10.1016/S0955-2219(03)00513-2.

(37) Longworth, G.; Long, G. J. *Mössbauer Spectroscopy Applied to Inorganic Chemistry.*; Plenum Press, New York, 1984; Vol. 1.

(38) Dudley, G. J.; Steele, B. C. H.; Howe, A. T. Studies of Potassium Ferrite K1+xFe11O17. I. Electronic Conductivity and Defect Structure. *J. Solid State Chem.* **1976**, *18* (2), 141–147. https://doi.org/10.1016/0022-4596(76)90088-8.

(39) Howe, A. T.; Dudley, G. J. Studies of Potassium Ferrite, K1+xFe11O17. II. Mössbauer Effect and Spin Flopping. *J. Solid State Chem.* **1976**, *18* (2), 149–153. https://doi.org/10.1016/0022-4596(76)90089-X.

(40) Kündig, W.; Steven Hargrove, R. Electron Hopping in Magnetite. *Solid State Commun.* **1969**, *7* (1), 223–227. https://doi.org/10.1016/0038-1098(69)90729-7.

(41) Sankararaman, M.; Kikuchi, R.; Sato, H. Percolation Threshold for Electronic Conduction in β-Alumina-Type Compounds. *J. Solid State Chem.* **1990**, *88* (1), 239–246. https://doi.org/10.1016/0022-4596(90)90220-R.

(42) Lalère, F.; Leriche, J. B.; Courty, M.; Boulineau, S.; Viallet, V.; Masquelier, C.; Seznec, V. An All-Solid State NASICON Sodium Battery Operating at 200 °C. *J. Power Sources* **2014**, *247*, 975–980. https://doi.org/10.1016/j.jpowsour.2013.09.051.

(43) Mouahid, F. E.; Bettach, M.; Zahir, M.; Maldonado-Manso, P.; Bruque, S.; Losilla, E. R.; Aranda, M. A. G. Crystal Chemistry and Ion Conductivity of the Na1 + XTi2 − XAlx(PO4)3 ($0 \leq x \leq 0.9$) NASICON Series. *J. Mater. Chem.* **2000**, *10* (12), 2748–2757. https://doi.org/10.1039/b004837m.

(44) Bruce, P.; Lisowskaoleksiak, A.; Saidi, M.; Vincent, C. Vacancy Diffusion in the Intercalation Electrode Li1−xNiO2. *Solid State Ion.* **1992**, *57* (3–4), 353–358. https://doi.org/10.1016/0167-2738(92)90169-P.

(45) Zhang, N.; Han, X.; Liu, Y.; Hu, X.; Zhao, Q.; Chen, J. 3D Porous γ-Fe_2O_3@C Nanocomposite as High-Performance Anode Material of Na-Ion Batteries. *Adv. Energy Mater.* **2015**, *5* (5), 1401123. https://doi.org/10.1002/aenm.201401123.

(46) Niu, Y.; Xu, M.; Zhang, Y.; Han, J.; Wang, Y.; Li, C. M. Detailed Investigation of a $NaTi_2(PO_4)_3$ Anode Prepared by Pyro-Synthesis for Na-Ion Batteries. *RSC Adv.* **2016**, *6* (51), 45605–45611. https://doi.org/10.1039/C6RA06533C.

(47) Cava, R. J.; Batlogg, B.; Krajewski, J. J.; Poulsen, H. F.; Gammel, P.; Peck, W. F.; Rupp, L. W. Electrical and Magnetic Properties of Nb 2 O 5 − δ Crystallographic Shear Structures. *Phys. Rev. B* **1991**, *44* (13), 6973–6981. https://doi.org/10.1103/PhysRevB.44.6973.

(48) Zachauchristiansen, B. Lithium Insertion in Different TiO2 Modifications. *Solid State Ion.* **1988**, *28–30*, 1176–1182. https://doi.org/10.1016/0167-2738(88)90352-9.

(49) Wang, P.-F.; Yao, H.-R.; Liu, X.-Y.; Yin, Y.-X.; Zhang, J.-N.; Wen, Y.; Yu, X.; Gu, L.; Guo, Y.-G. Na $^{+}$ /Vacancy Disordering Promises High-Rate Na-Ion Batteries. *Sci. Adv.* **2018**, *4* (3), eaar6018. https://doi.org/10.1126/sciadv.aar6018.

(50) Böckenfeld, N.; Balducci, A. Determination of Sodium Ion Diffusion Coefficients in Sodium Vanadium Phosphate. *J. Solid State Electrochem.* **2014**, *18* (4), 959–964. https://doi.org/10.1007/s10008-013-2342-6.

(51) Liu, Y.; Zhou, Y.; Zhang, J.; Xia, Y.; Chen, T.; Zhang, S. Monoclinic Phase $Na_3Fe_2(PO_4)_3$: Synthesis, Structure, and Electrochemical Performance as Cathode Material in Sodium-Ion Batteries. *ACS Sustain. Chem. Eng.* **2017**, *5* (2), 1306–1314. https://doi.org/10.1021/acssuschemeng.6b01536.

(52) Cao, Y.; Yang, C.; Liu, Y.; Xia, X.; Zhao, D.; Cao, Y.; Yang, H.; Zhang, J.; Lu, J.; Xia, Y. A New Polyanion $Na_3Fe_2(PO_4)P_2O_7$ Cathode with High Electrochemical Performance for Sodium-Ion Batteries. *ACS Energy Lett.* **2020**, *5* (12), 3788–3796. https://doi.org/10.1021/acsenergylett.0c01902.

(53) Roh, H.-K.; Kim, H.-K.; Kim, M.-S.; Kim, D.-H.; Chung, K. Y.; Roh, K. C.; Kim, K.-B. In Situ Synthesis of Chemically Bonded NaTi2(PO4)3/RGO 2D Nanocomposite for High-Rate Sodium-Ion Batteries. *Nano Res.* **2016**, *9* (6), 1844–1855. https://doi.org/10.1007/s12274-016-1077-y.

(54) Song, S.; Duong, H. M.; Korsunsky, A. M.; Hu, N.; Lu, L. A Na+ Superionic Conductor for Room-Temperature Sodium Batteries. *Sci. Rep.* **2016**, *6* (1), 32330. https://doi.org/10.1038/srep32330.

(55) Boukamp, B. A.; Huggins, R. A. Fast Ionic Conductivity in Lithium Nitride. *Mater. Res. Bull.* **1978**, *13* (1), 23–32. https://doi.org/10.1016/0025-5408(78)90023-5.

(56) Kumar, P. R.; Jung, Y. H.; Bharathi, K. K.; Lim, C. H.; Kim, D. K. High Capacity and Low Cost Spinel Fe 3 O 4 for the Na-Ion Battery Negative Electrode Materials. *Electrochimica Acta* **2014**, *146*, 503–510. https://doi.org/10.1016/j.electacta.2014.09.081.

(57) Choi, C.; Ashby, D. S.; Butts, D. M.; DeBlock, R. H.; Wei, Q.; Lau, J.; Dunn, B. Achieving High Energy Density and High Power Density with Pseudocapacitive Materials. *Nat. Rev. Mater.* **2020**, *5* (1), 5–19. https://doi.org/10.1038/s41578-019-0142-z.

(58) Costentin, C.; Porter, T. R.; Savéant, J.-M. How Do Pseudocapacitors Store Energy? Theoretical Analysis and Experimental Illustration. *ACS Appl. Mater. Interfaces* **2017**, *9* (10), 8649–8658. https://doi.org/10.1021/acsami.6b14100.

(59) Conway, B. E. *Electrochemical Supercapacitors: Scientific Fundamentals and Technological Applications*; Springer US: Boston, MA, 1999.

(60) Forghani, M.; Mavroudis, H.; McCarthy, J.; Donne, S. W. Electroanalytical Characterization of Electrochemical Capacitor Systems Using Step Potential Electrochemical Spectroscopy. *Electrochimica Acta* **2020**, *332*, 135508. https://doi.org/10.1016/j.electacta.2019.135508.

(61) Dupont, M. F.; Donne, S. W. Charge Storage Mechanisms in Electrochemical Capacitors: Effects of Electrode Properties on Performance. *J. Power Sources* **2016**, *326*, 613–623. https://doi.org/10.1016/j.jpowsour.2016.03.073.

(62) Liu, T.-C. Behavior of Molybdenum Nitrides as Materials for Electrochemical Capacitors. *J. Electrochem. Soc.* **1998**, *145* (6), 1882. https://doi.org/10.1149/1.1838571.

(63) Han, M. H.; Gonzalo, E.; Sharma, N.; López del Amo, J. M.; Armand, M.; Avdeev, M.; Saiz Garitaonandia, J. J.; Rojo, T. High-Performance P2-Phase $Na_{2/3}Mn_{0.8}Fe_{0.1}Ti_{0.1}O_2$ Cathode Material for Ambient-Temperature Sodium-Ion Batteries. *Chem. Mater.* **2016**, *28* (1), 106–116. https://doi.org/10.1021/acs.chemmater.5b03276.

(64) Chao, D.; Lai, C.-H. M.; Liang, P.; Wei, Q.; Wang, Y.-S.; Zhu, C. R.; Deng, G.; Doan-Nguyen, V. V. T.; Lin, J.; Mai, L.; Fan, H. J.; Dunn, B.; Shen, Z. X. Sodium Vanadium Fluorophosphates (NVOPF) Array Cathode Designed for High-Rate Full Sodium Ion Storage Device. *Adv. Energy Mater.* **2018**, *8* (16), 1800058. https://doi.org/10.1002/aenm.201800058.

(65) Zhang, X.; Rui, X.; Chen, D.; Tan, H.; Yang, D.; Huang, S.; Yu, Y. $Na_3V_2(PO_4)_3$: An Advanced Cathode for Sodium-Ion Batteries. *Nanoscale* **2019**, *11* (6), 2556–2576. https://doi.org/10.1039/C8NR09391A.

(66) Zhang, Y.; Jiang, J.; An, Y.; Wu, L.; Dou, H.; Zhang, J.; Zhang, Y.; Wu, S.; Dong, M.; Zhang, X.; Guo, Z. Sodium-ion Capacitors: Materials, Mechanism, and Challenges. *ChemSusChem* **2020**, *13* (10), 2522–2539. https://doi.org/10.1002/cssc.201903440.

(67) Yang, C.; Xin, S.; Mai, L.; You, Y. Materials Design for High-Safety Sodium-Ion Battery. *Adv. Energy Mater.* **2021**, *11* (2), 2000974. https://doi.org/10.1002/aenm.202000974.

(68) Fuchs, T.; Culver, S. P.; Till, P.; Zeier, W. G. Defect-Mediated Conductivity Enhancements in $Na_{3-x}Pn_{1-x}W_xS_4$ (Pn = P, Sb) Using Aliovalent Substitutions. *ACS Energy Lett.* **2020**, *5* (1), 146–151. https://doi.org/10.1021/acsenergylett.9b02537.

(69) Yubuchi, S.; Ito, A.; Masuzawa, N.; Sakuda, A.; Hayashi, A.; Tatsumisago, M. Aqueous Solution Synthesis of Na_3SbS_4–Na_2WS_4 Superionic Conductors. *J. Mater. Chem. A* **2020**, *8* (4), 1947–1954. https://doi.org/10.1039/C9TA02246E.

(70) Rao, R. P.; Chen, H.; Wong, L. L.; Adams, S. $Na_{3+x}M_xP_{1-x}S_4$ ($M = Ge^{4+}$, Ti^{4+}, Sn^{4+}) Enables High Rate All-Solid-State Na-Ion Batteries $Na_{2+2\delta}Fe_{2-\delta}(SO_4)_3$ |$Na_{3+x}M_xP_{1-x}S_4$ |$Na_2Ti_3O_7$. *J. Mater. Chem. A* **2017**, *5* (7), 3377–3388. https://doi.org/10.1039/C6TA09809F.

(71) Wang, N.; Yang, K.; Zhang, L.; Yan, X.; Wang, L.; Xu, B. Improvement in Ion Transport in Na3PSe4–Na3SbSe4 by Sb Substitution. *J. Mater. Sci.* **2018**, *53* (3), 1987–1994. https://doi.org/10.1007/s10853-017-1618-0.

4. Chapter 4. High-rate, Nb_2O_5-based Li-ion battery full-cell devices

4.1 Introduction

Fast charging batteries have received considerable attention because of the rapidly growing interest in renewable technologies and electric vehicles (EV).[1-3] The batteries used for such applications require not only high power density but also high stability, life span, and most importantly, safety.[4-6] Traditional batteries based on graphite and lithium cobalt oxide (LCO) electrodes have found difficulty in meeting these high power requirements with serious safety concerns.[7-9] Despite the low cost, graphite anodes have faced many fundamental challenges including slow Li-ion de-solvation and potential Li dendrite formation with subsequent thermal runaway upon overcharging. Additionally, a highly resistive solid electrolyte interphase (SEI) layer on graphite has caused slow charge transfer across the anode/electrolyte interface and crystallographic tortuosity contributes to the sluggish bulk diffusion of Li^+ in graphite due to the anisotropic nature of the graphite layer.[9] Therefore, researchers have been incorporating new chemistries that enable fast charging/discharging, such as using lithium titanate (LTO) or niobium titanium oxide (TNO) in place of graphite and replacing lithium cobalt oxide (LCO) with lithium iron phosphate (LFP) or lithium manganese oxide (LMO).[10-13] These electrode materials, either with three-dimensional open crystal channels or in nanoparticle form of concurrent intercalation pathways, provide facile lithium transport and a stable surface chemistry that ensures thermal stability and high-rate cyclability.[14,15]

T-phase Nb_2O_5 is attractive as a negative electrode material due to its ability to store Li-ions through rapid pseudocapacitance (surface-limited Faradaic reactions) and its potential scalability for commercialization.[16-21] The charge-discharge profile shows a linear slope storing charge within a stable potential region that avoids electrolyte breakdown and lithium plating. What

makes Nb_2O_5 especially interesting is its pseudocapacitive charge storage mechanism, which offers the prospect of charging high-power devices in seconds rather than hours.[16,17] With well-designed nanostructures, researchers have used Nb_2O_5 to demonstrate several impressive energy storage features, such as rapid charging/discharging (170 mAh g^{-1} in 1 min),[18] electrodes of high volumetric capacity (962 F cm^{-3} at 1C),[19] and great capacity retention with high mass loading (11 mg cm^{-2} at 10C).[20] One tradeoff for the reliable high-power operation resulting in long cycle life, less resistive SEI formation, and good thermal stability is the moderate energy due to the ~1.6 V redox potential.[21,22] Most recently, carbide-derived Nb_2O_5 has achieved a high gravimetric capacity of 300 mAh g^{-1} over 500 cycles with a three-electron charge transfer process,[23] indicating Nb_2O_5 can potentially provide comparable energy with existing commercial batteries. In addition, a hybrid device configuration of Nb_2O_5 vs carbon has been widely used for high energy capacitors to achieve fast charge/discharge.[24-26] The fact that Nb_2O_5 can deliver greater power and a longer lifespan than that of traditional battery materials has also make hybrid devices using Nb_2O_5 an attractive approach for achieving high power batteries.

Construction of a fast-charging device requires several design considerations to enable reliable cell operation with increased safety.[27-31] First, the basic requirement of full cell construction is to pair positive and negative electrodes with equivalent capacity.[27,28] This ensures that all active materials can be accessed efficiently during the storage process and enables a reasonable amount of charge to shuttle between the electrodes. A mismatched capacity cell design can cause irreversible cell failure and, in extreme cases, lead to permanent electrode damage or electrolyte shortage caused by over-charge or –discharge, frequently seen as over-grown SEI or lithium plating on a graphite electrode upon fast charging.[29,30] Second, selecting a cell voltage range is important for reliable operation. Electrolyte solvents, such as ethylene carbonate (EC),

dimethyl carbonate (DMC), propylene carbonate (PC), could potentially breakdown during fast charging operation[31-34] and a capacity mismatch could cause the cell voltage window to shift away from a stable potential range. Once the cell operation voltage falls outside of the stable range of the electrolyte, the full cell can undergo chemical breakdown, leading to capacity fade and self-heating. Finally, in building an Nb_2O_5-based full-cell, choosing a cathode with comparable kinetics is especially crucial since the device capacity at high rate is likely to be limited by whichever electrode has the slower kinetics.[29]

With these design considerations, we have developed four different types of Nb_2O_5-based 3 V full cell chemistries (LMO//Nb_2O_5, LFP//Nb_2O_5, LCO//Nb_2O_5, and NCA//Nb_2O_5) that are each evaluated under charge/discharge protocols at rates faster than 10C. Given the new storage chemistries, kinetic analysis was used to understand the charge storage mechanism at different states-of-charge (*SOC*) and how these materials can safely maintain fast-charging operation. Since the NCA//Nb_2O_5 chemistry retained the highest capacity under rapid charging conditions, these electrodes were further developed into a 1.2 Ah prototype pouch cell built with a pilot line service from an industrial manufacturer. These NCA//Nb_2O_5 prototype cells have demonstrated rapid 4C charge/discharge with limited self-heating and an extended cycle life with an industrially scaled weight loading, an optimal pairing ratio, and a reliable operating voltage range. These performance indicators have revealed the potential for adapting pseudocapacitive materials in commercial batteries for rapid charging, minimal heating, and increased safety.

4.2 Experimental Methods

Materials

The electrode materials used in this study are displayed in **Figure 4-1**. The Nb_2O_5-reduced graphene oxide (rGO) (Figure 4-1a) used as the negative electrode in full cells was synthesized using a solvothermal method followed by post-annealing under inner atmosphere.[35] Briefly, 0.582 g $C_4H_4NNbO_9 \cdot xH_2O$ (CBMM, Araxá, Brazil), 0.075 mL HCl (37% solution in water, Fisher Scientific), and 0.66 mL of graphene oxide solution (2 wt%, Graphenea, San Sebastián, Spain) were uniformly mixed in 50 mL water/ethanol (1:2 vol%) solution. The precursor solution, which was kept in a Parr reactor at 180 °C for the solvothermal synthesis, yields amorphous Nb_2O_5-rGO after 12 hours. The powder was retrieved by centrifugation (3000 rpm) and washed 3 times with ethanol (200-proof, Decon Labs, King of Prussia, PA) and dried in a 60 °C oven. To obtain T-phase Nb_2O_5-rGO, the amorphous powder was annealed at 550 °C for 12 hours under argon flow at 120 sccm. The X-ray diffraction pattern confirms the orthorhombic phase (JCPDS 30-873) of Nb_2O_5 with a Scherrer size of 32 nm.

The cathode material mesoporous lithium manganese oxide ($LiMn_2O_4$, LMO, Figure 4-1b) was synthesized using a sol-gel method incorporating a home-made polymethylmethacrylate (PMMA) microsphere suspension (55.3 mg mL^{-1}).[36] First, 2.2 mmol lithium nitrate ($LiNO_3$, MilliporeSigma, Burlington, MA) and 4 mmol manganese nitrate tetrahydrate ($Mn(NO_3)_2 \cdot 4H_2O$, Alfa Aesar, Tewksbury, MA) were completely dissolved in a 6.78 mL aqueous PMMA colloidal suspension by continuous stirring. The precursor suspension was pre-heated in an oil bath at 60˚C for 40 mins and poured into a petri dish kept at 25 ˚C with 20-28% humidity. After drying for 11 hours, a translucent gel formed, followed by calcination at 500 ˚C for 2 hours with a ramp rate of

2 ˚C/min to form the mesoporous LMO. The X-ray diffraction pattern confirms the spinel phase of LMO (JCPDS 35-0782) with a Scherrer size of 20 nm.

In addition to the synthesized materials, three other cathodes were also paired with the Nb_2O_5-rGO as a full cell: lithium iron phosphate nanoparticles ($LiFePO_4$, LFP, Figure 4-1c) with carbon coating was gifted by Professor William Chueh in the Department of Materials Science and Engineering at Stanford University,[37] and micron-sized lithium cobalt oxide ($LiCoO_2$, LCO, Figure 4-1d) and lithium nickel cobalt aluminum oxide ($LiNi_{0.8}Co_{0.15}Al_{0.05}O_2$, NCA, Figure 4-1e) were used as received from the MTI Corporation (Richmond, CA) and BASF Toda America (Battle Creek, MI), respectively. The LFP, NCA, and LCO powder were kept in an Ar-filled glovebox once received to minimize oxygen and moisture exposure.

Electrode Preparation

Active materials were blended with one or two types of conductive carbons in a designated binder solution, followed by doctor blading of slurry electrodes. Prior to mixing the slurries, conductive carbons including SuperP carbon black (Alfa Aesar, Tewksbury, MA), carbon nanofibers (CNF, D × L: 100 nm × 20-200 μm, MilliporeSigma, Burlington, MA), and carbon nanotubes (CNT, multiwall, OD: 5-15nm, purity > 95%, US Research Nanomaterials, Inc., Houston, TX) were heated in a vacuum oven at 110 ˚C. For the negative electrode, Nb_2O_5-rGO, SuperP and CNF were mixed in an aqueous binder solution of styrene-butadiene rubber (SBR, MTI Corporation) and carboxymethyl cellulose (CMC, Dow Chemical, Midland, MI) with a ratio of Nb_2O_5-rGO:SuperP:CNF:SBR:CMC = 90:2:2:3:3. For positive electrodes, a conductive binder of 15 g/L poly(3-hexylthiophene-2,5-diyl) (P3HT, MW 15000-30000, PDI = 1.6-1.8, regioregularity = 89-94%, Rieke Metals, Lincoln, NE) in o-xylene (99%, Extra Dry, ACROS Organics, Fair Lawn, NJ) was used to improve the electrode kinetics and effectively prevent the

parasitic reaction that occurs from overcharging.[38-40] Mesoporous LMO and LFP nanoparticle electrodes were prepared with a ratio of 90:5:5 (Active:SuperP:P3HT) and bulk-particle LCO and NCA electrodes were made with a ratio of 90:2.5:2.5:5 (Active:CNF:CNT:P3HT). Slurries were homogenized using a mortar and pestle and were cast manually onto copper (negative) and aluminum (positive) foils with controlled loadings by doctor blading. For building the prototype pouch cells, Nb_2O_5-rGO and NCA slurries were mixed using a slurry mixer (ARE-250 CE, THINKY, Laguna Hills, CA) and cast electrode tapes of 930 cm^2 using an automatic coater. The cast tapes (for both cell formats) were dried in an oven at 60 ˚C to remove visible solvents and were transferred to a vacuum oven at 110 ˚C for at least 12 hours for complete drying.

Full Cell Construction and Electrochemical Characterization

Development of the Nb_2O_5 full cells include three different stages: (1) study of full cell chemistries, (2) optimization of cell parameters and voltage, and (3) validation in a commercial prototype format. The first two stages were carried out using 2032-coin cells and the last stage was performed using pouch cells. To make the coin cells, vacuum-dried electrodes were punched into 0.71 cm^2 discs (~2 mg/cm^2, or ~0.3 mAh/cm^2) and were paired in 2032-coin cells with a Whatman GF/C separator soaked in 1.0 M $LiPF_6$ in EC/DMC/DEC (1:1:1 vol%). The active mass ratio of positive/negative (P/N) electrodes for LMO//Nb_2O_5, LFP//Nb_2O_5, LCO//Nb_2O_5, NCA//Nb_2O_5 was controlled at 1.73, 1.09, 1.14, and 0.85, respectively. These ratios were close to those determined by balancing the capacity between 150 mAh g^{-1} of Nb_2O_5 (10 wt%, rGO included) and the experimental nominal cathode capacity (Figure 4-2a), which is 85 mAh g^{-1} for LMO, 140 mAh g^{-1} for LFP, 131 mAh g^{-1} for LCO, and 174 mAh g^{-1} for NCA. Cyclic voltammetry (CV) and galvanostatic charge-discharge (GCD) were carried out using a VMP-3 potentiostat/galvanostat (Bio-Logic). For electrolyte wetting purposes, the as-prepared full cells were allowed to rest for 6

hours until a stable cell OCV was reached (~ -50 mV) before testing. The reported full cell capacity was normalized by the total weight of both active materials (g_{total}). Each cell was initiated by a CV measurement at 0.5 mV s^{-1} for 5 cycles to activate the P3HT binder in the positive electrode. The 1C-rate used in the GCD measurements was calculated from the cathode loading and the corresponding nominal capacity of the 5th cycle of the 0.5 mV s^{-1} CV.

A 1.2 Ah pouch cell of NCA//Nb_2O_5 was built by Battery Streak Inc. with a third-party contractor using a jelly-roll configuration (detailed in Table 4-1). Compared with the coin-cell electrodes, NCA electrodes gained ductility with additional 1 wt% of carbon (0.5 wt% each for CNF and CNT), which prevents visible crack formation during the rolling process. In addition, a polypropylene ceramic-coated separator (Targray) was used to replace the rigid glass fiber separator to meet the same manufacturing requirement. The as-cast cathode, anode, and electrolyte (1.0 M $LiPF_6$ in EC/DMC/DEC (1:1:1 vol%)) were assembled in cell pouches without further calendaring. For pouch cell testing, an 8-channel Bio-Logic potentiostat/galvanostat (BCS-815) capable of applying maximum 10 A was used for the GCD and electrochemical impedance spectroscopy (EIS) measurements. The as-made NCA//Nb_2O_5 pouch cells underwent three cycles

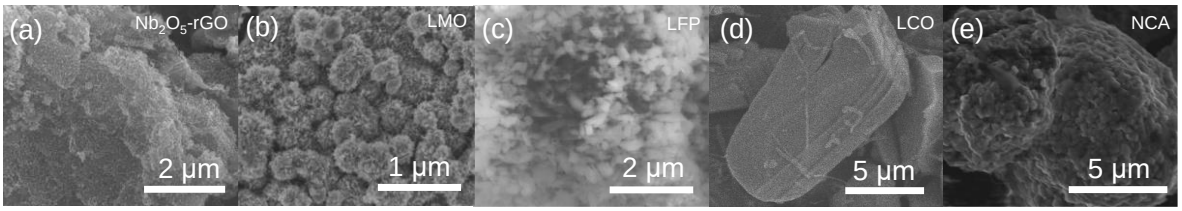

Figure 4-1. SEM morphologies for different electrode materials used in this study. (a) Nb_2O_5-rGO (b) Mesoporous $LiMn_2O_4$ (c) carbon-coated $LiFePO_4$ (d) commercial $LiCoO_2$ (e) commercial $LiNi_{0.8}Co_{0.15}Al_{0.05}O_2$.

of formation at a C-rate of C/10 between 2.9 V and 0.5 V using constant-current-constant-voltage (CCCV) charge protocol with a 50-mA cut-off current and constant-current (CC) discharge before any performance testing. Cell temperature measurements during fast charge/discharge were carried

out using an infrared thermometer (OS1327D-Series, Omega Engineering, Norwalk, CT) in a low-temperature oven (10GCE-LT, Quincy Lab Inc., Burr Ridge, IL) with a control accuracy of ±1 C°.

4.3 Results and Discussion

Rate Performance for Nb_2O_5-based Full cells

Galvanostatic charge-discharge measurements were used to determine the storage performance for four different Nb_2O_5-based full cells (**Figure 4-2**). The ideal voltage window of full cells can be determined by redox potentials of individual cathode half cells referenced to Nb_2O_5 in Figure 4-2a. Given the operating voltage range of Nb_2O_5 between 1.2 V and 2.5 V (vs. Li/Li^+), full cell voltages were adjusted according to the anticipated range, which is 1.5 V - 3 V for LMO//Nb_2O_5, 1 - 2.5 V for LFP//Nb_2O_5, 1 - 3V for LCO//Nb_2O_5, and 0.5 - 3 V for NCA//Nb_2O_5. Rate performance for the LMO//Nb_2O_5 cell was determined by the GCD measurement in Figure 4-2b. The LMO full cell has a relatively high nominal voltage of 2.3 V and demonstrated a capacity of 44 mAh g_{total}^{-1} at a rate of 2C and 33 mAh g_{total}^{-1} at 40C, illustrating a remarkable 75% capacity retention between a 30 min and 1 min charge/discharge. Figure 4-2c shows GCD performance for the LFP//Nb_2O_5 full cell between 0.5 V and 2.5 V, where the capacity stored at 1C (1 hour) was 65 mAh g_{total}^{-1} and gradually decreased to 50 mAh g_{total}^{-1} at 20C (140 sec). Due to the lower redox potential of LFP (3.4 V vs. Li/Li^+) compared to those of the other cathodes investigated, the nominal voltage for this full cell was also the lowest at 1.75 V. The LCO//Nb_2O_5 (Figure 4-2d) and NCA//Nb_2O_5 (Figure 4-2e) operated with an intermediate nominal voltage between that of LMO//Nb_2O_5 and LFP//Nb_2O_5 at 2.1 V. The LCO//Nb_2O_5 full cell stored a capacity of 70 mAh g_{total}^{-1} at 1C and retained 80% (56 mAh g_{total}^{-1}) of the capacity at 16 C, whereas the NCA//Nb_2O_5 showed the higher capacity of 80 mAh g_{total}^{-1} at 1C and retained a higher capacity of 60 mAh g_{total}^{-1} at 16 C. The rate performance for the full cells is best summarized by the Ragone plot in Figure

4-2f. Due to the higher nominal voltage, lower capacity, and better capacity retention, the LMO//Nb_2O_5 (94 Wh kg_{total}^{-1} at 1C) shares a similar power capability with the LFP//Nb_2O_5 (113 Wh kg_{total}^{-1} at 2C) by retaining a specific energy of 70 Wh kg_{total}^{-1} at the power of 5300 W kg_{total}^{-1}. The demonstrated performance is equivalent to 70% energy retention in a 45-sec charge/discharge, which makes these full cell chemistries ideal for high-power utilization. On the other hand, the LCO//Nb_2O_5 and NCA//Nb_2O_5 full cells have demonstrated a higher specific energy (> 150 Wh kg_{total}^{-1} at 1C) and retained more than 100 Wh kg_{total}^{-1} at the power of 3500 W kg_{total}^{-1}. This power capability is especially interesting since the micron-size LCO and NCA particles were subject to slow bulk diffusion that did not display fast operation in a half cell, implying that pairing with Nb_2O_5 was responsible for the improved performance.

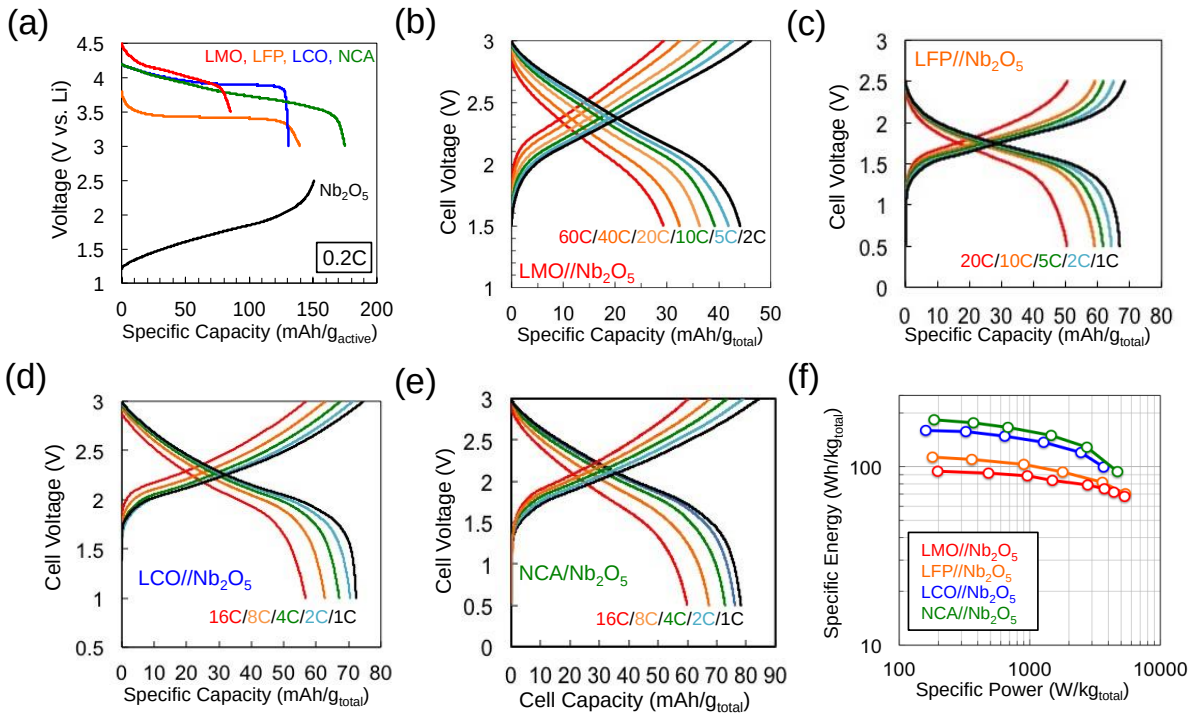

Figure 4-2. Galvanostatic profiles for (a) half cells of various electrode materials and full cells of (b) LMO//Nb_2O_5, (c) LFP//Nb_2O_5, (d) LCO//Nb_2O_5, and (e) NCA/Nb_2O_5. (d) Ragone plot comparing performance of different Nb_2O_5-based full cells.

Kinetic Analysis on Full Cells

The following kinetic analysis carried out using cyclic voltammetry (CV) on full cells aims to mechanistically explain the performance improvement observed upon pairing diffusion limited cathodes with pseudocapacitive Nb_2O_5. A modified *b-value* analysis, which uses the entire operating potential range instead of a single peak potential, was used to correlate different charge storage mechanisms with the sweep voltage, or the state of charge (*SOC*). The empirical correlation between the *SOC* and *b-value* can be derived by using the following equations:[41-43]

Equation 4-1

$$i(V) = av^{b(V)}$$

Equation 4-2

$$\text{CV-derived Capacity: } C(V) = \frac{1}{3.6}\int_{V_1}^{V_2}\frac{idV}{mv}$$

Equation 4-3

$$\text{SOC}(V) = \frac{C(V)}{C_{total}}$$

Equation 4-1 describes the *b-value* variation within the CV voltage range, where *i* is the current response corresponding to a specific voltage (*V*) and *v* is the sweep rate. The exponent *b* is a kinetic indicator which represents charge storage mechanisms from slow, diffusion-limited processes (*b*=0.5) to fast, surface-controlled processes (*b*=1). Equation 4-2 helps determine apparent capacity *C* (mAh) with a CV curve across a certain voltage range, where *m* is the active material loading and V_0 and V_1 are starting and final potentials, respectively. Equation 4-3 shows how we obtained the *SOC* as a function of cell voltage by normalizing the CV-derived capacity over total capacity of the full cell (C_{total}), which was itself derived from Equation 4-2 with the cell voltage limits ($V_0 = V_{min}$ and $V_1 = V_{max}$). Since the capacity derived from CV curves can decay

drastically due to polarizations at high sweep rates, the *C(V)* and C_{total} were derived from the CV curve of the slowest sweep rate. For example, C_{total} for LMO//Nb_2O_5 was 41 mAh g_{total}^{-1} derived from the LMO//Nb_2O_5 CV curve sampled at 1 mV s^{-1} in Figure 4-3a. The derived C_{total} was 65 mAh g_{total}^{-1} for LFP//Nb_2O_5, 68 mAh g_{total}^{-1} for LCO//Nb_2O_5, and 82 mAh g_{total}^{-1} for NCA//Nb_2O_5. These capacity values are consistent with the highest capacity determined by GCD for each chemistry (Figure 4-2). With these equations, dependence of *SOC* on charge storage mechanisms, or *b-value-SOC*, can now be determined with the CV curves for different chemistries. This can also serve as an empirical method for studying kinetics on a full cell, where the cell voltage varies rather than referencing a certain voltage or peak-current.

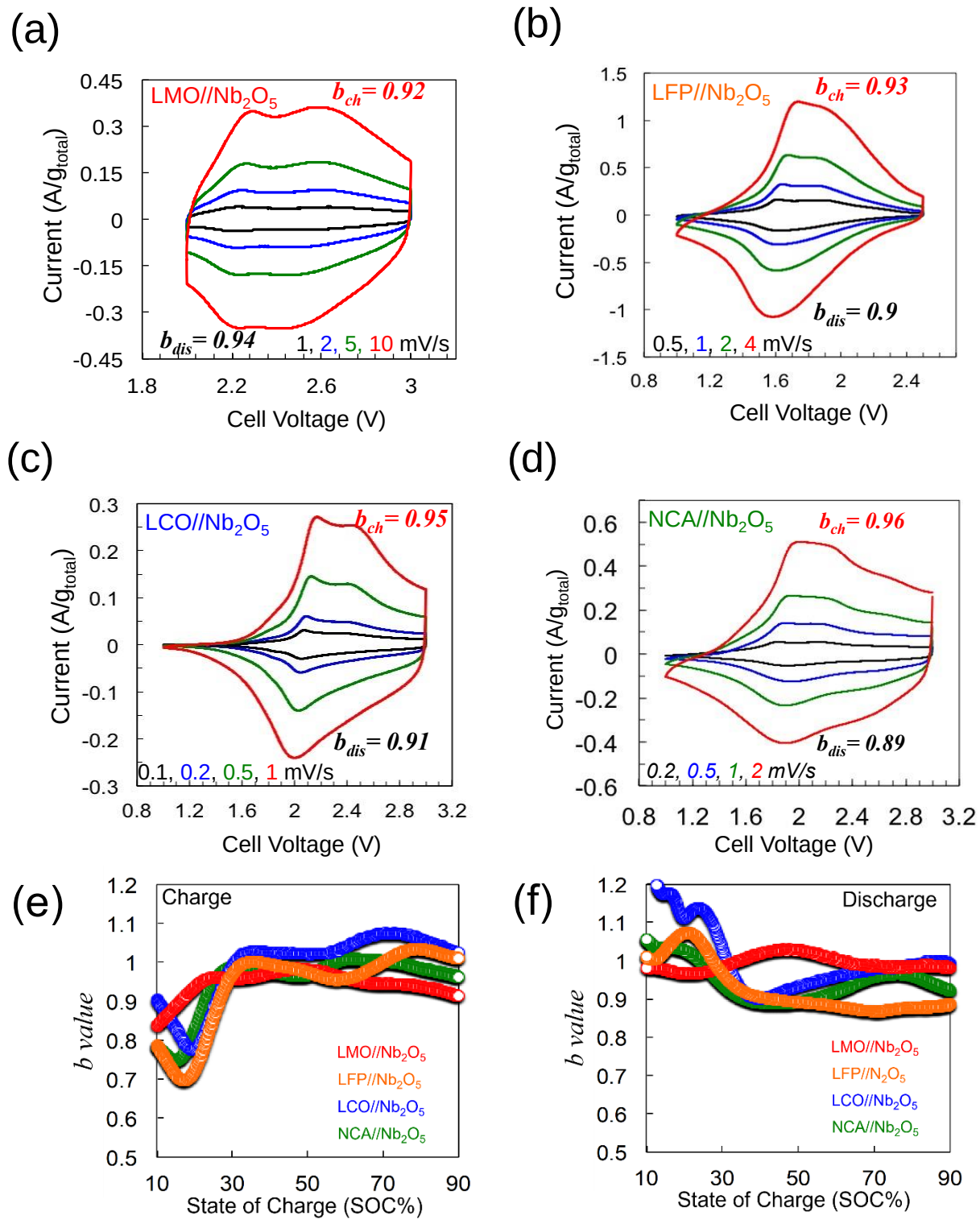

Figure 4-3. Full-cell CV curves for (a) $LMO//Nb_2O_5$, (b) $LFP//Nb_2O_5$, (c) $LCO//Nb_2O_5$, and (d) NCA/Nb_2O_5 for b-value analysis. The calculated peak current b-values are shown next to the corresponding peaks. The change in *b*-value with state-of-charge (SOC) during (e) charge and (f) discharge highlight the mostly surface-limited kinetics in full-cells where $b \approx 1$.

Figure 4-3a – d show CV curves for different full cell chemistries used in the analysis. Similar to the GCD measurement, the upper cut-off voltage is 3 V for the LMO//Nb_2O_5 (Figure 4-3a), LCO//Nb_2O_5 (Figure 4-3c), and NCA//Nb_2O_5 (Figure 4-3d) and 2.5 V for the LFP//Nb_2O_5 (Figure 4-3b). Regardless of the full cell chemistries, the peak potential difference for the paired redox peaks barely increased with the sweep rates. For example, the largest redox peak shifts found on the CV curves along the highest sweep rate was only 105 mV for the NCA//Nb_2O_5 and 160 mV for LMO, LFP, and LCO full cells, indicating that minimal polarization occurred with increasing sweep rates. The peak *b-value* for each chemistry was also derived and shown along the curves. Interestingly, most peak *b-value*s are higher than 0.9 regardless of charge or discharge process. This indicates that the storage mechanism for the cells was governed by fast surface-controlled processes. Although it is still unknown why the LFP//Nb_2O_5 and LCO//Nb_2O_5 demonstrated the unexpectedly high *b-values* with a diffusion-limited cathode,[44,45] the capacitor-like charge storage mechanism seems to explain the superior rate performance in Figure 4-2 and perhaps the synergistic effect that arises from pairing with an Nb_2O_5 anode.

By using the CV curves in Figure 4-3a – d, we derived cell-voltage-*SOC* correlation with Equation 4-2 and Equation 4-3. Similar to the GCD curves, voltage hysteresis has been found between the charge and discharge curves. The hysteresis existing at such a slow scan rate has been recognized as an indicator of entropy production, which causes efficiency loss for a device in the form of heat generation.[46-48] It is worthwhile to mention that the hysteresis in the LFP, LCO, and NCA full cells has been found to gradually decrease with increasing *SOC* while minimal hysteresis was demonstrated in the LMO full cell regardless of the *SOC*. The reduced hysteresis indicates that the charge/discharge process in the Nb_2O_5-paired full cells can be highly efficient through proper control of their *SOC*.

With the *b-values* derived from Figure 4-3a –d and the voltage-dependent *SOC*, we can obtain the *b-value-SOC* correlation for the full-cell charge and discharge stages shown in Figure 4-3e and Figure 4-3f, respectively. The correlation range from 0% to 10% *SOC* and 90% to 100% *SOC* were removed due to analysis deviation caused by current hysteresis at upper and lower voltage limits, thus only the *b-value* between 10% and 90% *SOC* is representative for each chemistry. For all full cells, the charging *b-value* remained below 0.9 between 10% and 30% *SOC* and gradually increased to 1 with minor fluctuation (±0.1) between 30% and 90% *SOC*. Thus, the first 20% *SOC* (10% to 30%) upon charge was considered to be where slow kinetics persisted and unfavorable for fast charging due to the lower *b-values*. The *b-value* variation within the kinetically limiting range also provides some insights. For example, the *b-value* dip, which has served as an indicator for localized ion starvation,[49] was observed in the analysis of LFP//Nb_2O_5, LCO//Nb_2O_5, and NCA//Nb_2O_5 full cells. The absence of a *b-value* dip in the analysis of the LMO full cell indicates that its mesoporous nanostructure has prevented localized electrolyte depletion in the electrode by effectively shortening the electrode-electrolyte distance. This was also observed in the superior galvanostatic rate performance of the LMO//Nb_2O_5 over the other cell chemistries (Figure 4-2).

In the discharge process, all of the cells retained a *b-value* above 0.9 between 90% and 30% *SOC*, whereas below 30% *SOC* again the cells demonstrated different discharge kinetics. While the LMO//Nb_2O_5 displayed $b \sim 1$ throughout the entire voltage range, the LFP//Nb_2O_5, LCO//Nb_2O_5, and NCA//Nb_2O_5 displayed $b > 1$ below 30% *SOC*. This deviation from $b \sim 1$ is consistent with the inability for fast charging below 30% *SOC* in the LFP//Nb_2O_5, LCO//Nb_2O_5, and NCA//Nb_2O_5. Overall, the *b-value-SOC* analysis helps to semi-quantify the capacitive *SOC* of the full cells as well as identify the capacity that is capable of fast charging. For example, a cell

charged to more than 30% *SOC* becomes more favorable for rapid charging than a completely discharged cell, except for the LMO//Nb_2O_5 cell chemistry. Although the LMO//Nb_2O_5 full cell has shown the most potential for high power applications, the material-based specific energy is lower than 100 Wh kg^{-1} (Figure 4-2f), making the device less desirable. The NCA//Nb_2O_5 cell, however, with a specific energy over 180 Wh kg^{-1} and a 60% of the *SOC* showing fast kinetics, is more suitable for high power prototype development.

Cell Optimization for NCA//Nb_2O_5 Full Cell

Before building a prototype cell, the effect of electrode loading, pairing ratio, and cell voltage range was studied to ensure the reliable utilization of the electrode materials. Although a cell built with higher mass-loading electrodes is expected to achieve a higher energy density, kinetic barriers caused by internal resistance and insufficient electrolyte percolation of a thick electrode should not be ignored.[50-53] **Figure 4**-4a shows the rate performance of NCA//Nb_2O_5 cells at various loadings between 4.9 and 13.3 mg cm^{-2}. Increasing the loading from 4.9 mg cm^{-2} to 13.3 mg cm^{-2} gradually deceased the slow-rate (0.5C) capacity from 150 mAh g_{NCA}^{-1} to 125 mAh g_{NCA}^{-1}, while the high-rate (16C) capacity dropped drastically from 95 mAh g_{NCA}^{-1} to 45 mAh g_{NCA}^{-1}. An intermediate loading of 7.5 mg/cm^2 seemed to be the optimal loading to retain over 90% of the 0.5C capacity (130 mAh g^{-1}) at 4C. Figure 4-4b re-plots Figure 4-4a as areal capacity versus operating current density. It is noted that regardless of electrode loadings, the capacity dropped rapidly with a current density higher than 10 mA cm^{-2}, indicating that the electrolyte mass transport has superseded the solid-phase diffusion within the electrode materials as the kinetically limiting factor. The current density where the initial areal capacity lost more than 20% was set as our cut-off current density, which is 5 mA cm^{-2} for a 13.3 mg (or 1.9 mAh) cm^{-2} loading, 7 mA cm^{-2} for 10.3 mg (or 1.4 mAh) cm^{-2}, and 10 mA cm^{-2} for 7.5 mg (or 1 mAh) cm^{-2}. The 7.5 mg cm^{-2} loading

was finally selected due to the ability to retain 80% of *SOC* under the current density of 10 mA cm^{-2}, which corresponds to a charging time of ~5 min (4 min 48 sec).

To study the effect of the pairing ratio on the NCA//Nb_2O_5 performance, 60 coin cells with average loading of 8.7 mg_{NCA} cm^{-2} were made and tested using GCD measurements. Figure 4-4c shows that the highest capacity was found at the P/N ratio close to 1 resulting in 150 mAh g_{NCA}^{-1}

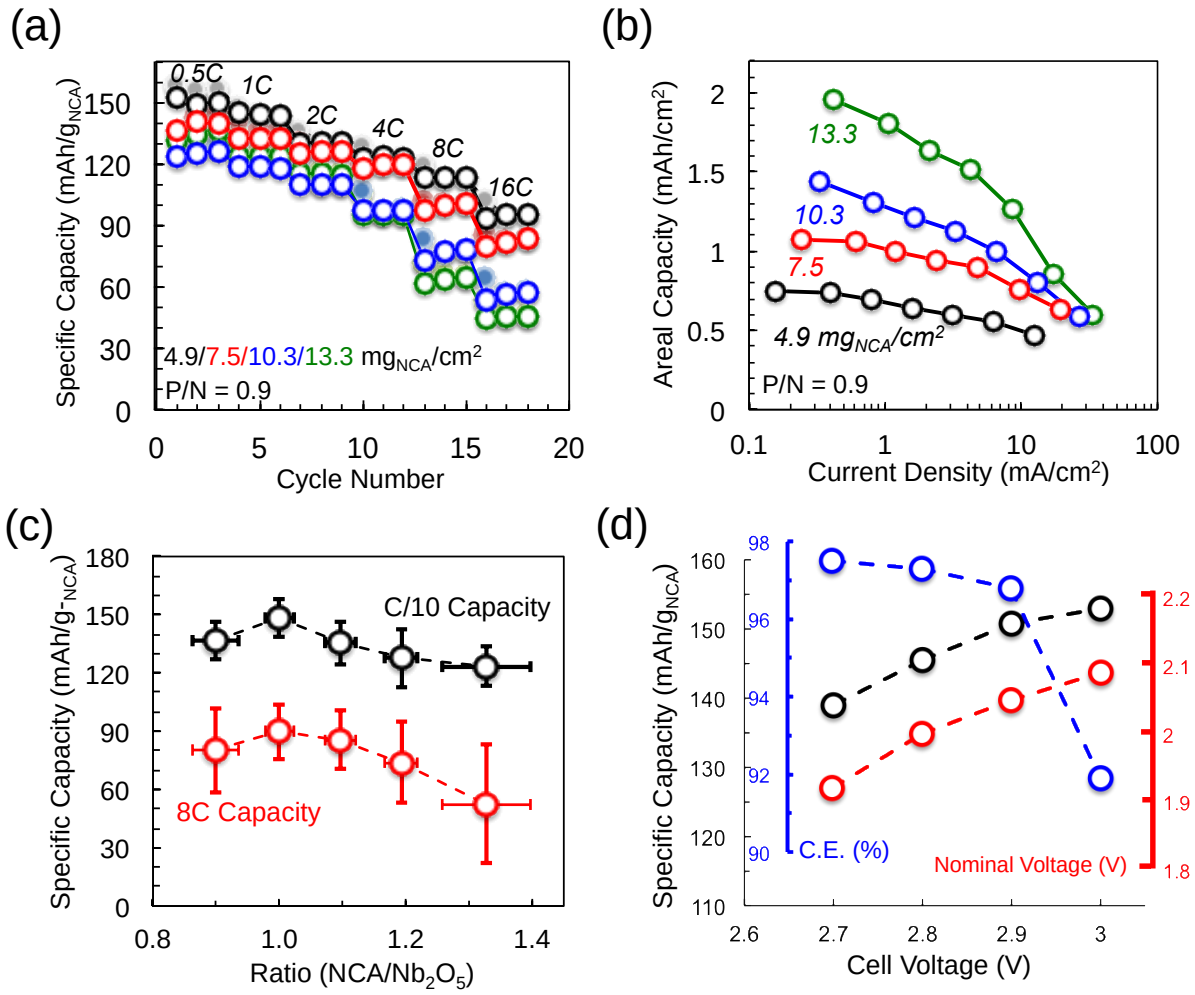

Figure 4-4. (a) Effect of areal loading on rate performance for NCA//Nb2O5 full cells. (b) Dependence of current density on areal capacity for the full cell at various loading. (c) Pairing ratio optimization with 60 coin cells (avg. 8.7 mg_{NCA} cm^{-2}) for higher specific capacity. (d) Effect of cell upper voltage on capacity, coulombic efficiency, and cell nominal voltage.

at C/10 and 90 mAh g_{NCA}^{-1} at 8C. Figure 4-4d shows cell voltage optimization based on capacity, coulombic efficiency (C.E.), and nominal voltage. The cells were charged using CCCV protocol with a C/3 C-rate and a cut-off current of C/20. The capacity and nominal voltage gradually increased when raising the upper voltage limit, however, the C.E. suddenly dropped to 92% at 3V, indicating that the cell was overcharged and prone to electrolyte breakdown. Thus, we have selected the following parameters for our prototype cell fabrication: 7.5 mg cm^{-2} as the target loading with a pairing ratio close to 1 as well as the cell upper voltage of 2.9 V to ensure a reasonable energy density and steady cycling efficiency.

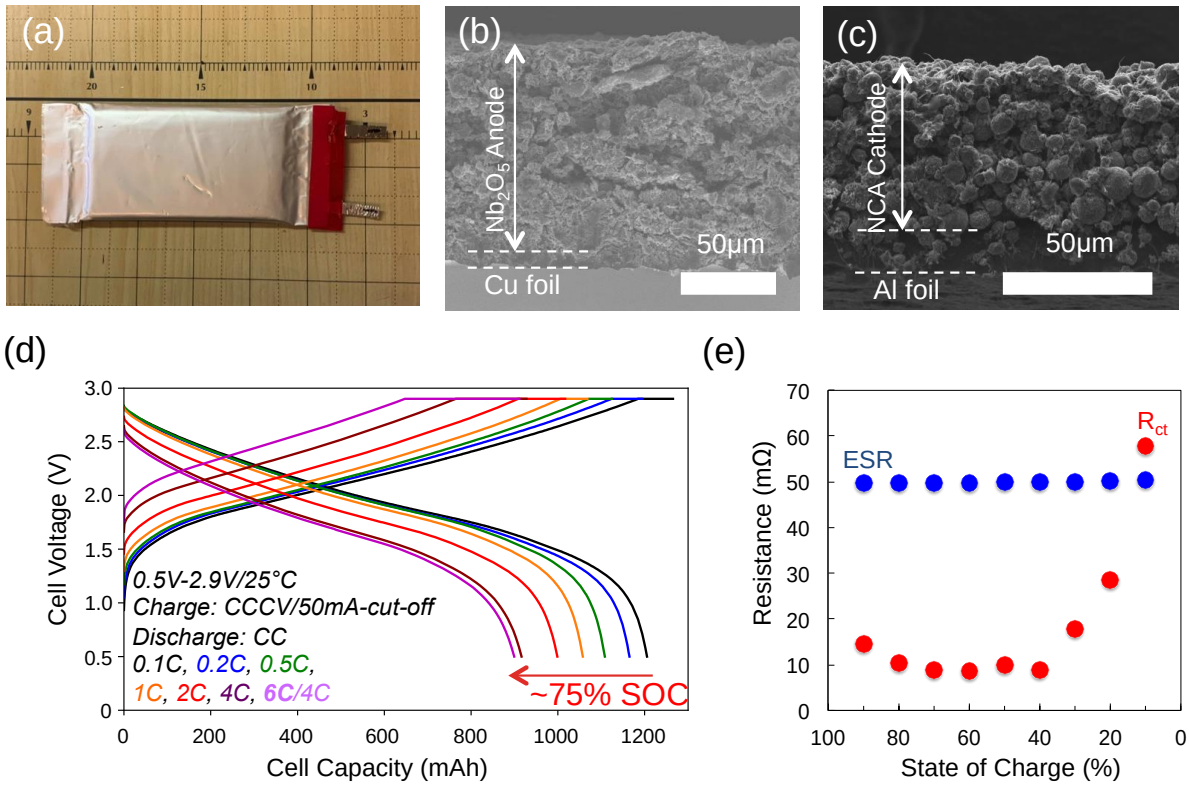

Figure 4-5. a) A photograph of 1.2 Ah NCA//Nb2O5 prototype cells. SEM images for **(b)** Nb_2O_5 anode and **(c)** NCA cathode used in the prototype cells. **d)** Rate performance for the prototype cell with various constant-current-constant-voltage (CCCV) protocols. **e)** Series resistance (ESR) and charge transfer resistance (R_{ct}) derived from impedance study at different cell state of charge (SOC).

Table 4-1. Cell Parameters of 1.2 Ah NCA//Nb_2O_5 Prototype Cell

Cell Specification	
Dimension (mm)	45 × 90 × 7
Max. Voltage (V)	2.9
Min. Voltage (V)	0.5
Nominal Voltage (V)	2.05
Capacity (C/10, mAh)	1200
Energy Density (Wh/L)	87
Nb_2O_5 Anode	
Active material loading	90%
Areal weight (mg/cm^2)	8.0
Areal capacity (mAh/cm^2)	1.1
Thickness (μm)	109
NCA Cathode	
Active material loading	89%
Areal weight (mg/cm^2)	7.8
Areal capacity (mAh/cm^2)	1.25
Thickness (μm)	56

Following the evaluation of lab-scale coin-cell devices which demonstrated the fast-charging capability and relatively stable operating window of a high mass loading NCA//Nb_2O_5 full-cell, a practical high-capacity pouch cell was developed. Table 4-1 details the specifications

for the NCA//Nb_2O_5 prototype cell (Figure 4-5a). The 1.2 Ah, 28 c.c. pouch cell operates between 0.5 V and 2.9 V (nominal voltage 2.05 V), leading to a cell energy density of 87 Wh/L. It should be noted that the energy density of pouch cells was significantly higher than that of coin cells because they were built with a thinner industrial-standard PE separator and a relatively low electrolyte-to-electrode weight ratio. Without further calendaring, the areal loading was controlled at around 8 mg/cm^2 for both electrodes and resulted in electrode thickness of 109-um for Nb_2O_5-rGO (Figure 4-5b) and 56-um for NCA (Figure 4-5c), respectively. Figure 4-5d shows charge-discharge curves for the prototype cell at different C-rates. With the CCCV-charge-CC-discharge protocol, the cell capacity was rated 1200 mAh at C/10 (black) and gradually decreased to 1060 mAh at 1C (orange) and 920 mAh at 4C (purple). Notably, the cell retained the 4C capacity with a 6C-CCCV charge protocol (pink), which enables the cell to store 100 mAh per minute up to 800 mAh.

Electrochemical impedance spectroscopy (EIS) measurements, shown in Figure 4-5e, confirm cell chemical stability at different *SOCs*. Before each measurement, the cell was charged at a 0.1C-rate to the associated *SOC*s, followed by a voltage hold for 1 hr. The EIS spectra were fit with an equivalent circuit model composed of an electronic series resistance of the electrolyte, separator, and both electrodes (ESR, real impedance intercept), SEI resistance (R_{SEI}, high-frequency semicircle), charge transfer resistance (R_{ct}, medium-frequency semicircle), constant phase elements (CPE-I & II), and a Warburg element (W_o, low-frequency tails). CPE-I and -II are attributed to morphological contributions from the nonplanar porous electrodes and W_o accounts for the slow diffusion processes which exists either in the solid-state or the bulk electrolyte. The R_{SEI} contribution was found to be negligible (< 1 mΩ), and the ESR and R_{ct} summarized in Figure 4-5e have shown quite different dependencies on the *SOC*. The cell ESR remained steady at 50

mΩ over the entire *SOC*, a good indicator for stable cycling without material degradation across the designed voltage range, whereas the R_{ct} dropped quickly below the ESR after reaching 20% *SOC* and remained consistently low at 10 mΩ until the end of charge. This indicates that the ESR above 20% *SOC* has become the limiting factor for fast charging and further cell processing is required to lower the series resistance, such as electrode calendaring.

Figure 4-6 shows reliability tests for the NCA//Nb_2O_5 prototype cell carried out with GCD measurements without a voltage hold. Figure 4-6a shows that with this protocol, the cell was still capable of storing 950 mAh at 0.5C and retained 700 mAh at 4C and 600 mAh at 6C. Figure 4-6 further demonstrates that the cell is capable of 4C long-term cycling with voltage cut-offs at 2.9 V and 1 V. On the first cycle, the cell demonstrated a capacity of 610 mAh which gradually decreased to 540 mAh at 1000^{th} cycle, and 485 mAh after 3000^{th} cycle, showing 80% retention of the fast-charge capacity with coulombic efficiency close to 100% (99.8%) throughout. After the many fast charging cycles, the cell still retained 880 mAh at 0.5C, leading to only 7% permanent capacity loss compared with the capacity at the same rate before the high rate cycling. EIS measurements were also carried out on the cycled cell. The fact that the EIS spectra before and after 3000 cycles were barely changed (ESR: 43 mΩ, R_{ct}: 20 mΩ) further confirms that there was no significant damage caused by the high power operation.

In addition to the long cycle life and high coulombic efficiency, minimal heat generation was also observed during the fast charge/discharge operation. The cell temperature variation under a 10-min charging protocol in Figure 4-6c further confirms minimal heat generation in the prototype. The cell temperature measured on the surface of the pouch was raised to 33 °C when the cell was charged up to 800 mAh with 6C-CCCV protocol (cut-off condition: 10-min/800 mAh) and cooled down naturally to 27 °C during its discharge with 3C (18 mins). Self-heating of

batteries is caused by reversible and irreversible heat generation upon operation. Reversible heat generation is observed in the form of a voltage hysteresis, which has been well-known to cause energy inefficiency in the form of waste heat and has led to the poor rate performance of existing

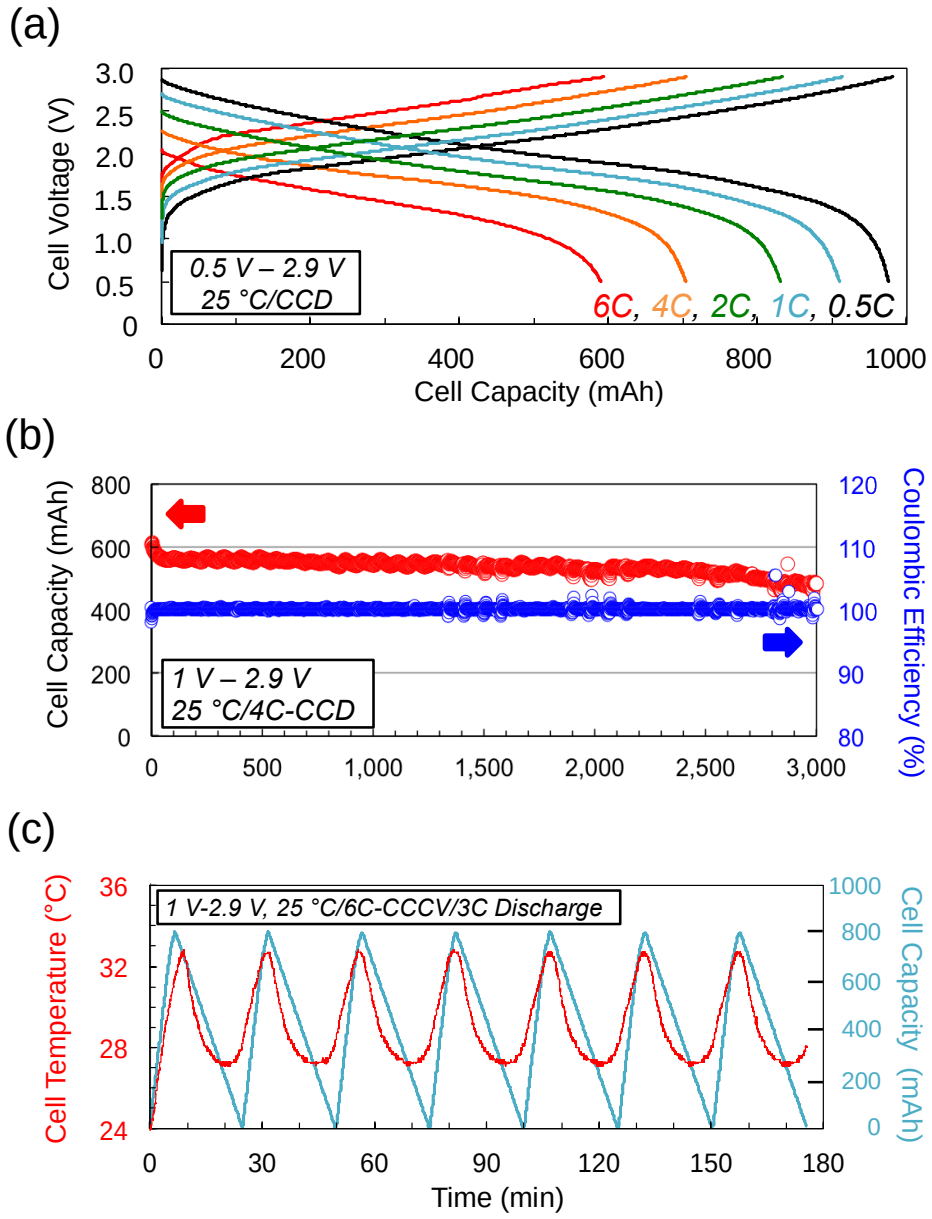

Figure 4-6. Reliability test for the NCA//Nb_2O_5 prototype cell. **a)** Rate performance with constant-current charge/discharge protocols. **b)** Capacity retention and coulombic efficiency for 300 cycles with 4C charge/discharge. **c)** Cell temperature variation with 6C-CCCV charge/3C discharge operation between 1 V and 2.9 V.

batteries.[46,48] Here, such voltage hysteresis was found to be minimal in LMO//Nb_2O_5 and reduced gradually for the other full-cell chemistries with increased *SOC* (> 30% *SOC*). Irreversible heat generation is defined as $Q_{irr} = -I^2R_i$,[47] where I is the applied charge/discharge current and R_i is the internal resistance or the sum of all polarization resistances which highly depends on the battery chemistries. **Table 4-2** lists cell resistances for commercial cells using different chemistries along with their maximum temperature change under fast charging. Although the ESR of our cell is at least 50% higher than the others, we have achieved a similar maximum temperature upon fast charge. This indicates that the heat generation contributed by polarization resistances in the NCA//Nb_2O_5 prototype cell was minimal. Therefore, with the reduced heat generation, the proposed cell could store more energy at high rates and retained good chemical stability during the fast-charging cycles.

Table 4-2. Comparison on different series resistance and maximum cell temperature under fast charge protocol for different cells.

Ref	Cell Chemistry	Cell Type	Format	Capacity (Ah)	Cell Voltage (V)	ESR (mΩ)	Protocol	T_{max} (°C)
53	Graphite//LFP	High-Power	Cylindrical	1.1	2 - 3.6	18	6C	35
45, 54	Graphite//LCO+ NMC	High-Power	Cylindrical	1.1	2.5 - 4.1	28	5C	33
55	LTO//NMC	High-Power	Pouch	5	1.5 - 2.8	3	4C	28
56	Graphite//NCA	High-Energy	Cylindrical	3	2.5 - 4.2	2	2.2C	53.2
57	SiC//NMC	High-Energy	Cylindrical	3.35	2.8 - 4.2	33	C/5	40
58	Graphite//NMC	High-Energy	Pouch	3.3	3 - 4.2	15	2C	32
	Nb_2O_5//NCA	**This Work**	**Pouch**	**1.2**	**1 - 2.9**	**50**	**6C**	**33**

4.4 Conclusions

Four different full-cell chemistries using a pseudocapacitive Nb_2O_5 anode and fast-kinetics cathodes (LMO, LFP, LCO, and NCA) were developed into 3 V batteries capable of fast charge/discharge cycling. The LMO//Nb_2O_5 and LFP//Nb_2O_5 full cells have demonstrated superior power capability, storing 70 Wh kg^{-1} over 5000 W kg^{-1}, whereas the LCO//Nb_2O_5 and NCA//Nb_2O_5 offered a higher specific energy of 100 Wh kg^{-1} with a comparable power of 3500 W kg^{-1}. Kinetic studies using *b-value-SOC* correlation were used to explain the rapid performance and suggest a surface-controlled storage contribution arises from paring diffusion limited cathodes with Nb_2O_5. This analysis has revealed that capacitor-like charging prevailed in the cells after being sufficiently charged over 30% *SOC*. The NCA//Nb_2O_5 chemistry, which achieved the highest energy density, was selected for further development of the chemistry into a practical prototype pouch cell after the electrode and cell voltage were optimization. The 1.2 Ah NCA//Nb_2O_5 prototype cell demonstrated two important fast charging features: (1) 4C constant current charge/discharge for over 3000 cycles and (2) maximum cell temperature at 33 °C with 6C-CCCV protocol. With the demonstration of high-rate stability and minimal joule heating, we believe the development of batteries using pseudocapacitive storage offers a potential solution to address fundamental thermal concerns of fast charging technologies.

4.5 References

[1] Nykvist, B.; Nilsson, M. Rapidly Falling Costs of Battery Packs for Electric Vehicles. *Nature Climate Change* **2015**, *5* (4), 329–332.

[2] Lu, J.; Chen, Z.; Ma, Z.; Pan, F.; Curtiss, L. A.; Amine, K. The Role of Nanotechnology in the Development of Battery Materials for Electric Vehicles. *Nature Nanotechnology* **2016**, *11* (12), 1031–1038.

[3] Van Noorden, R. The Rechargeable Revolution: A Better Battery. *Nature* **2014**, *507* (7490), 26–28.

[4] Manzetti, S.; Mariasiu, F. Electric Vehicle Battery Technologies: From Present State to Future Systems. *Renewable and Sustainable Energy Reviews* **2015**, *51*, 1004–1012.

[5] Lam, L. T.; Louey, R. Development of Ultra-Battery for Hybrid-Electric Vehicle Applications. *Journal of Power Sources* **2006**, *158* (2), 1140–1148.

[6] Rezvanizaniani, S. M.; Liu, Z.; Chen, Y.; Lee, J. Review and Recent Advances in Battery Health Monitoring and Prognostics Technologies for Electric Vehicle (EV) Safety and Mobility. *Journal of Power Sources* **2014**, *256*, 110–124.

[7] Etacheri, V.; Marom, R.; Elazari, R.; Salitra, G.; Aurbach, D. Challenges in the Development of Advanced Li-Ion Batteries: A Review. *Energy & Environmental Science* **2011**, *4* (9), 3243.

[8] Liu, Y.; Zhu, Y.; Cui, Y. Challenges and Opportunities towards Fast-Charging Battery Materials. *Nature Energy* **2019**, *4* (7), 540–550.

[9] Kim, D. S.; Kim, Y. E.; Kim, H. Improved Fast Charging Capability of Graphite Anodes via Amorphous Al2O3 Coating for High Power Lithium Ion Batteries. *Journal of Power Sources* **2019**, *422*, 18–24.

[10] Zaghib, K.; Dontigny, M.; Guerfi, A.; Charest, P.; Rodrigues, I.; Mauger, A.; Julien, C. M. Safe and Fast-Charging Li-Ion Battery with Long Shelf Life for Power Applications. *Journal of Power Sources* **2011**, *196* (8), 3949–3954.

[11] Tian, T.; Lu, L.; Yin, Y.; Li, F.; Zhang, T.; Song, Y.; Tan, Y.; Yao, H. Multiscale Designed Niobium Titanium Oxide Anode for Fast Charging Lithium Ion Batteries. *Advanced Functional Materials* **2020**, 2007419.

[12] Xiang, H. F.; Wang, H.; Chen, C. H.; Ge, X. W.; Guo, S.; Sun, J. H.; Hu, W. Q. Thermal Stability of LiPF6-Based Electrolyte and Effect of Contact with Various Delithiated Cathodes of Li-Ion Batteries. *Journal of Power Sources* **2009**, *191* (2), 575–581.

[13] Yi, J.; Wang, C.; Xia, Y. Comparison of Thermal Stability between Micro- and Nano-Sized Materials for Lithium-Ion Batteries. *Electrochemistry Communications* **2013**, *33*, 115–118.

[14] House, R. A.; Bruce, P. G. Lightning Fast Conduction. *Nature Energy* **2020**, *5* (3), 191–192.

[15] Li, Y.; Chen, H.; Lim, K.; Deng, H. D.; Lim, J.; Fraggedakis, D.; Attia, P. M.; Lee, S. C.; Jin, N.; Moškon, J.; Guan, Z.; Gent, W. E.; Hong, J.; Yu, Y.-S.; Gaberšček, M.; Islam, M. S.; Bazant, M. Z.; Chueh, W. C. Fluid-Enhanced Surface Diffusion Controls Intraparticle Phase Transformations. *Nature Materials* **2018**, *17* (10), 915–922.

[16] Augustyn, V.; Come, J.; Lowe, M. A.; Kim, J. W.; Taberna, P.-L.; Tolbert, S. H.; Abruña, H. D.; Simon, P.; Dunn, B. High-Rate Electrochemical Energy Storage through Li+ Intercalation Pseudocapacitance. *Nature Materials* **2013**, *12* (6), 518–522.

[17] Chen, D.; Wang, J.-H.; Chou, T.-F.; Zhao, B.; El-Sayed, M. A.; Liu, M. Unraveling the Nature of Anomalously Fast Energy Storage in T-Nb_2O_5. *Journal of the American Chemical Society* **2017**, *139* (20), 7071–7081.

[18] Meng, J.; He, Q.; Xu, L.; Zhang, X.; Liu, F.; Wang, X.; Li, Q.; Xu, X.; Zhang, G.; Niu, C.; Xiao, Z.; Liu, Z.; Zhu, Z.; Zhao, Y.; Mai, L. Identification of Phase Control of Carbon-Confined Nb_2O_5 Nanoparticles toward High-Performance Lithium Storage. *Advanced Energy Materials* **2019**, *9* (18), 1802695.

[19] Kong, L.; Zhang, C.; Wang, J.; Qiao, W.; Ling, L.; Long, D. Free-Standing *T* -Nb $_2$ O $_5$ /Graphene Composite Papers with Ultrahigh Gravimetric/Volumetric Capacitance for Li-Ion Intercalation Pseudocapacitor. *ACS Nano* **2015**, *9* (11), 11200–11208.

[20] Sun, H.; Mei, L.; Liang, J.; Zhao, Z.; Lee, C.; Fei, H.; Ding, M.; Lau, J.; Li, M.; Wang, C.; Xu, X.; Hao, G.; Papandrea, B.; Shakir, I.; Dunn, B.; Huang, Y.; Duan, X. Three-Dimensional Holey-Graphene/Niobia Composite Architectures for Ultrahigh-Rate Energy Storage. *Science* **2017**, *356* (6338), 599–604.

[21] Griffith, K. J.; Forse, A. C.; Griffin, J. M.; Grey, C. P. High-Rate Intercalation without Nanostructuring in Metastable Nb $_2$ O $_5$ Bronze Phases. *Journal of the American Chemical Society* **2016**, *138* (28), 8888–8899.

[22] Kim, J. W.; Augustyn, V.; Dunn, B. The Effect of Crystallinity on the Rapid Pseudocapacitive Response of Nb2O5. *Advanced Energy Materials* **2012**, *2* (1), 141–148.

[23] Budak, Ö.; Geißler, M.; Becker, D.; Kruth, A.; Quade, A.; Haberkorn, R.; Kickelbick, G.; Etzold, B. J. M.; Presser, V. Carbide-Derived Niobium Pentoxide with Enhanced Charge Storage Capacity for Use as a Lithium-Ion Battery Electrode. *ACS Applied Energy Materials* **2020**, *3* (5), 4275–4285.

[24] Chen, Z.; Li, H.; Lu, X.; Wu, L.; Jiang, J.; Jiang, S.; Wang, J.; Dou, H.; Zhang, X. Nitrogenated Urchin-like Nb $_2$ O $_5$ Microspheres with Extraordinary Pseudocapacitive Properties for Lithium-Ion Capacitors. *ChemElectroChem* **2018**, *5* (11), 1516–1524.

[25] Hemmati, S.; Li, G.; Wang, X.; Ding, Y.; Pei, Y.; Yu, A.; Chen, Z. 3D N-Doped Hybrid Architectures Assembled from 0D T-Nb2O5 Embedded in Carbon Microtubes toward High-Rate Li-Ion Capacitors. *Nano Energy* **2019**, *56*, 118–126.

[26] Lim, E.; Kim, H.; Jo, C.; Chun, J.; Ku, K.; Kim, S.; Lee, H. I.; Nam, I.-S.; Yoon, S.; Kang, K.; Lee, J. Advanced Hybrid Supercapacitor Based on a Mesoporous Niobium Pentoxide/Carbon as High-Performance Anode. *ACS Nano* **2014**, *8* (9), 8968–8978.

[27] Bloom, I.; Jansen, A. N.; Abraham, D. P.; Knuth, J.; Jones, S. A.; Battaglia, V. S.; Henriksen, G. L. Differential Voltage Analyses of High-Power, Lithium-Ion Cells. *Journal of Power Sources* **2005**, *139* (1–2), 295–303.

[28] Dubal, D. P.; Ayyad, O.; Ruiz, V.; Gómez-Romero, P. Hybrid Energy Storage: The Merging of Battery and Supercapacitor Chemistries. *Chemical Society Reviews* **2015**, *44* (7), 1777–1790.

[29] Srinivasan, V.; Newman, J. Design and Optimization of a Natural Graphite/Iron Phosphate Lithium-Ion Cell. *Journal of The Electrochemical Society* **2004**, *151* (10), A1530.

[30] Petzl, M.; Kasper, M.; Danzer, M. A. Lithium Plating in a Commercial Lithium-Ion Battery – A Low-Temperature Aging Study. *Journal of Power Sources* **2015**, *275*, 799–807.

[31] Goodenough, J. B.; Park, K.-S. The Li-Ion Rechargeable Battery: A Perspective. *Journal of the American Chemical Society* **2013**, *135* (4), 1167–1176.

[32] Xu, K. Electrolytes and Interphases in Li-Ion Batteries and Beyond. *Chemical Reviews* **2014**, *114* (23), 11503–11618.

[33] Aurbach, D.; Talyosef, Y.; Markovsky, B.; Markevich, E.; Zinigrad, E.; Asraf, L.; Gnanaraj, J. S.; Kim, H.-J. Design of Electrolyte Solutions for Li and Li-Ion Batteries: A Review. *Electrochimica Acta* **2004**, *50* (2–3), 247–254. 34.

[34] Scrosati, B.; Garche, J. Lithium Batteries: Status, Prospects and Future. *Journal of Power Sources* **2010**, *195* (9), 2419–2430.

[35] Lai, C.-H.; Ashby, D.; Moz, M.; Gogotsi, Y.; Pilon, L.; Dunn, B. Designing Pseudocapacitance for Nb_2O_5 /Carbide-Derived Carbon Electrodes and Hybrid Devices. *Langmuir* **2017**, *33* (37), 9407–9415.

[36] Lesel, B. K.; Cook, J. B.; Yan, Y.; Lin, T. C.; Tolbert, S. H. Using Nanoscale Domain Size To Control Charge Storage Kinetics in Pseudocapacitive Nanoporous $LiMn_2O_4$ Powders. *ACS Energy Letters* **2017**, *2* (10), 2293–2298.

[37] Li, Y.; Meyer, S.; Lim, J.; Lee, S. C.; Gent, W. E.; Marchesini, S.; Krishnan, H.; Tyliszczak, T.; Shapiro, D.; Kilcoyne, A. L. D.; Chueh, W. C. Effects of Particle Size, Electronic Connectivity, and Incoherent Nanoscale Domains on the Sequence of Lithiation in $LiFePO_4$ Porous Electrodes. *Advanced Materials* **2015**, *27* (42), 6591–6597.

[38] Lai, C.-H.; Ashby, D. S.; Lin, T. C.; Lau, J.; Dawson, A.; Tolbert, S. H.; Dunn, B. S. Application of Poly(3-Hexylthiophene-2,5-Diyl) as a Protective Coating for High Rate Cathode Materials. *Chemistry of Materials* **2018**, *30* (8), 2589–2599.

[39] Das, P.; Zayat, B.; Wei, Q.; Salamat, C. Z.; Magdău, I.-B.; Elizalde-Segovia, R.; Rawlings, D.; Lee, D.; Pace, G.; Irshad, A.; Ye, L.; Schmitt, A.; Segalman, R. A.; Miller, T. F.; Tolbert, S. H.; Dunn, B. S.; Narayan, S. R.; Thompson, B. C. Dihexyl-Substituted Poly(3,4-Propylenedioxythiophene) as a Dual Ionic and Electronic Conductive Cathode Binder for Lithium-Ion Batteries. *Chemistry of Materials* **2020**, *32* (21), 9176–9189.

[40] Pankow, R. M.; Thompson, B. C. The Development of Conjugated Polymers as the Cornerstone of Organic Electronics. *Polymer* **2020**, *207*, 122874.

[41] Ardizzone, S.; Fregonara, G.; Trasatti, S. “Inner” and “Outer” Active Surface of RuO2 Electrodes. *Electrochimica Acta* **1990**, *35* (1), 263–267.

[42] Wang, J.; Polleux, J.; Lim, J.; Dunn, B. Pseudocapacitive Contributions to Electrochemical Energy Storage in TiO_2 (Anatase) Nanoparticles. *The Journal of Physical Chemistry C* **2007**, *111* (40), 14925–14931.

[43] Babu, B.; Simon, P.; Balducci, A. Fast Charging Materials for High Power Applications. *Advanced Energy Materials* **2020**, *10* (29), 2001128.

[44] Pignanelli, F.; Romero, M.; Mombrú, D.; Téliz, E.; Díaz, V.; Castiglioni, J.; Zinola, F.; Faccio, R.; Mombrú, Á. W. Insights of Cobalt Doping on Carbon-Coated LiFePO4 Olivine Nanoparticles Prepared by Citric Acid Combustion Route as Cathodes for Lithium Batteries. *Ionics* **2019**, *25* (8), 3593–3601.

[45] Okubo, M.; Hosono, E.; Kim, J.; Enomoto, M.; Kojima, N.; Kudo, T.; Zhou, H.; Honma, I. Nanosize Effect on High-Rate Li-Ion Intercalation in $LiCoO_2$ Electrode. *Journal of the American Chemical Society* **2007**, *129* (23), 7444–7452.

[46] Assat, G.; Glazier, S. L.; Delacourt, C.; Tarascon, J.-M. Probing the Thermal Effects of Voltage Hysteresis in Anionic Redox-Based Lithium-Rich Cathodes Using Isothermal Calorimetry. *Nature Energy* **2019**, *4* (8), 647–656.

[47] Amietszajew, T.; McTurk, E.; Fleming, J.; Bhagat, R. Understanding the Limits of Rapid Charging Using Instrumented Commercial 18650 High-Energy Li-Ion Cells. *Electrochimica Acta* **2018**, *263*, 346–352.

[48] Srinivasan, R.; Carson Baisden, A.; Carkhuff, B. G.; Butler, M. H. The Five Modes of Heat Generation in a Li-Ion Cell under Discharge. *Journal of Power Sources* **2014**, *262*, 93–103.

[49] Girard, H.-L.; Dunn, B.; Pilon, L. Simulations and Interpretation of Three-Electrode Cyclic Voltammograms of Pseudocapacitive Electrodes. *Electrochimica Acta* **2016**, *211*, 420–429.

[50] Fuller, T.F., Doyle, M. and Newman, J., 1994. Simulation and optimization of the dual lithium ion insertion cell. *Journal of the Electrochemical Society, 141*(1), p.1.

[51] Ahmed, S.; Bloom, I.; Jansen, A. N.; Tanim, T.; Dufek, E. J.; Pesaran, A.; Burnham, A.; Carlson, R. B.; Dias, F.; Hardy, K.; Keyser, M.; Kreuzer, C.; Markel, A.; Meintz, A.; Michelbacher, C.; Mohanpurkar, M.; Nelson, P. A.; Robertson, D. C.; Scoffield, D.; Shirk, M.; Stephens, T.; Vijayagopal, R.; Zhang, J. Enabling Fast Charging – A Battery Technology Gap Assessment. *Journal of Power Sources* **2017**, *367*, 250–262.

[52] Gallagher, K. G.; Trask, S. E.; Bauer, C.; Woehrle, T.; Lux, S. F.; Tschech, M.; Lamp, P.; Polzin, B. J.; Ha, S.; Long, B.; Wu, Q.; Lu, W.; Dees, D. W.; Jansen, A. N. Optimizing Areal Capacities through Understanding the Limitations of Lithium-Ion Electrodes. *Journal of The Electrochemical Society* **2016**, *163* (2), A138–A149.

[53] Finegan, D. P.; Quinn, A.; Wragg, D. S.; Colclasure, A. M.; Lu, X.; Tan, C.; Heenan, T. M. M.; Jervis, R.; Brett, D. J. L.; Das, S.; Gao, T.; Cogswell, D. A.; Bazant, M. Z.; Di Michiel, M.; Checchia, S.; Shearing, P. R.; Smith, K. Spatial Dynamics of Lithiation and Lithium Plating during High-Rate Operation of Graphite Electrodes. *Energy & Environmental Science* **2020**, *13* (8), 2570–2584.

[54] Severson, K.A., Attia, P.M., Jin, N. *et al.* Data-driven prediction of battery cycle life before capacity degradation. *Nat Energy* **4,** 383–391 (2019).

[55] Notten, P.H., het Veld, J.O. Van Beek, J.R.G., Boostcharging Li-ion batteries: A challenging new charging concept. *J. Power Sources*, **145**, 89-94 (2005).

[56] Jaguemont, J., Omar, N., Abdel-Monem, M., Van den Bossche, P., Van Mierlo, J., Fast-charging investigation on high-power and high-energy density pouch cells with 3D-thermal model development. *Appl. Therm. Eng*, **128**, 1282-1296 (2018).

[57] Fleming, J., Amietszajew, T., Charmet, J., Roberts, A.J., Greenwood, D., Bhagat, R., The design and impact of in-situ and operando thermal sensing for smart energy storage. *J. Energy Storage*, **22**, 36-43 (2019).

[58] Sturm, J., Rheinfeld, A., Zilberman, I., Spingler, F.B., Kosch, S., Frie, F., Jossen, A., Modeling and simulation of inhomogeneities in a 18650 nickel-rich, silicon-graphite lithium-ion cell during fast charging. *J. Power Sources*, **412**, 204-223 (2019).

[59] Spingler, F.B., Wittmann, W., Sturm, J., Rieger, B. and Jossen, A., 2018. Optimum fast charging of lithium-ion pouch cells based on local volume expansion criteria. *J. Power Sources*, **393**,152-160 (2018).

5. Chapter 5. Anionic redox of amorphous tungsten and tantalum sulfides

5.1 Introduction

Energy storage devices have become a necessity for portable electronics, electric vehicles, and the integration of renewable energy technologies and will continue to gain in importance with the growing trend toward consumer devices in an interconnected network deemed the 'internet of things'. Within energy storage technology, lithium-ion (Li-ion) batteries have become the leading device for portable electronics. Over the past 50 years of Li-ion battery research, electrode material design has focused on the oxidation and reduction of metal cations to store and release charge.[1] Therefore, the amount of lithium that can be stored in an electrode is limited to the number of electrons that can be accepted by cations in the material (typically < 1 per transition metal). While some work has achieved multielectron redox in cationic redox materials, few have achieved substantially greater than 1 electron per metal outside of the families of Wadsley-Roth and bronze-phase niobium oxides,[2–4] reduced MoO_3,[5] and organic frameworks with ligands which have low gravimetric capacity even with multi-electron processes.[6] The anions that make up the rest of the electrode material structure are traditionally inactive and do not participate in charge storage. Thus, utilizing redox processes of anions can lead to a potentially large increase in Li-ion battery capacity and energy density helping to realize next-generation Li-ion battery materials.[7,8]

Recently, crystalline Li-ion electrode materials have been investigated for oxygen dimer ($2O^{-II}/(O_2)^{n-}$) and sulfur dimer ($2S^{-II}/(S_2)^{x-}$) redox activity as a route for breaking the ceiling of cation-limited capacity.[9–11] Therefore, there is a need to further probe the conditions in which anions will participate in lithium ion charge storage. Crystalline oxide materials investigated thus far have shown instabilities with lithium insertion, such as cation mixing and irreversible O_2 generation, and are limited in charge-discharge rate capability.[7] Sulfide materials are thought to be

more promising due to the covalent nature of sulfide bonding, which is important in designing stable anion redox behavior.[12,13] Another consideration is that of structure. In particular, amorphous materials present the opportunity for facile bond stretching and change of metal-ion coordination upon breaking of the S-S bonds in the polysulfide chains to reduce S_2^{x-} to $2S^{-II}$.[14–17] The disorder of amorphous active materials can offer better access for Li-ion insertion and thus the possibility of higher capacities.[15] The nature of increased anionic redox participation has also been investigated in relation to covalency of the anion, with S-S and Se-Se bonds being easier to break and reform than O-O bonds.[18] This behavior has been attributed to the smaller electronegativity difference between high-electronegativity anions and a given cation.[13,19]

Here, we present the Li-ion electrochemistry of amorphous and crystalline WS_2 conversion electrodes as well as amorphous WS_x (x = ~3) and TaS_y (y = ~2) insertion electrodes, deemed *a*-WS_x and *a*-TaS_y, respectively, which demonstrate multielectron redox per transition metal. The advantages of amorphous materials for anionic redox processes are highlighted in the comparison of crystalline and amorphous WS_2 and the comparison of tungsten sulfides with tantalum sulfide helps to further elucidate the relationship between anionic redox and covalency. In addition, the first pseudocapacitive, high-rate anionic redox material is presented, displaying reversible cycling redox at rates up to 60C (~1 min charge/discharge). This work provides an exciting path forward for multielectron, high-rate, high-capacity charge storage materials and a potential solution for battery materials with a both high energy density and high power density. The electrochemical lithiation of *a*-WS_x and *a*-TaS_y demonstrates exciting performance in terms of energy density and rate-capability while providing insight into the relationship between structure and electrochemical charge storage mechanisms.

Materials and Methods

Materials

Crystalline WS_2 [powder, 2 μm, 99% Sigma Aldrich] and tantalum metal [powder, ~325 mesh, 99.9% trace metal basis, Sigma Aldrich] were used as transition metal precursors as received and were stored in an Ar filled glove box. Sulfur (S_8) powder [reagent grade, purified by sublimation, ~100 mesh particle size, Sigma Aldrich] was used as a sulfur source and was dried at 60 ̊C on a Schlenk line before transferring into an Ar filled glove box for storage. Carbon black Super P [>99%, Alfa Aesar], polyvinylidene fluoride (PVDF) [Kynar HSV 900] binder, and Polytetrafluoroethylene (PTFE) [powder, Sigma] binder were used in composite electrodes and were dried under vacuum at 80 ̊C overnight before loading into the Ar-filled glovebox for use. The PVDF was then dissolved in 1-Methyl-2-pyrrolidone (NMP) [anhydrous, 99.5%, Sigma Aldrich] solvent, pre-dried over 3Å molecular sieves. Lithium hexafluorophosphate ($LiPF_6$) [99.8%, Oakwood chemicals] salt was used as received. Ethylene carbonate (EC) [anhydrous, 99%, Sigma Aldrich] and dimethyl carbonate (DMC) [anhydrous, > 99%, Sigma Aldrich] were dried over 3Å molecular sieves for 24h before use. Glass fiber separators [Grace GF/C, Whatman] were dried for 24h at 120 ̊C in vacuum before use. All materials were prepared and stored in an Ar-filled glove box (O_2 < 0.2 ppm).

Synthesis of amorphous sulfides

Amorphous sulfides were synthesized by chemomechanical synthesis in a planetary ball mill [Retsch PM100] in a 50 mL zirconia jar, ⅓-filled with 2mm zirconia milling media. Molar ratios of precursors totaling 1.5g were added to the jar in an Ar filled glove box which was sealed with a jar clamp to avoid oxidation during milling. Precursors were milled until X-ray amorphous at 500 rpm: 80 h for amorphous WS_2 40 h for amorphous WS_3 and 148 h for amorphous TaS_2.

Structural characterization

X-ray diffraction (XRD) was acquired of as-synthesized powders and *ex-situ* composite electrodes using a PANalytical X'PertPro diffractometer equipped with Cu Kα radiation (λ = 1.54 Å, 45 kV, 40 mA) in Bragg-Brentano geometry. *Ex-situ* electrode samples were sealed in Kapton to avoid oxidation. Raman spectroscopy was performed on a Renishaw inVia with a 785 nm laser at 0.1% laser power, 1200 gr/mm grating averaged over 3 scans with a 30 s acquisition time. All air-sensitive Raman samples were performed by sealing samples under a 0.2mm quartz window before measurement. Transmission electron spectroscopy (TEM) images and electron diffraction patterns were obtained on an FEI Technai G2 T20. X-ray photoelectron spectroscopy (XPS) [Kratos Axis Ultra] was performed to obtain the oxidation state of the transition metal and sulfur of the pristine materials as well as to determine the atomic ratio of transition metal to sulfur after synthesis. XPS was performed using a monochromatic aluminum X-ray source voltage of 10 kV and emission current of 10 mA (160 eV pass energy for survey spectra and 20eV pass energy for detailed scans). Peak calibration was performed using the adventitious carbon peak (284.8 eV). Analysis was performed in the CasaXPS software. W *4f* fittings were done with a Tougaard background and LA(1,1,400) peak shape while S 2p fittings were done with a Shirley background and LF(1,1,125,180) line shape as described in Ref X.[20] For quantification of XPS using peak ratios, only the higher eV peak was used in each doublet to avoid peak-overlap.

Electrochemical testing

The amorphous sulfide active materials were hand mixed with carbon black Super P and PVDF in NMP binder in an 80:10:10 mass ratio. Composite electrodes were cast onto Cu (*a*-TaS_y) or carbon coated Al (*a*-WS_x) with a doctor blade, resulting in an active material mass loading of

1-3 mg cm^{-2} and dried at 80℃ overnight. All electrodes were made in an Ar-filled glove box. 1M $LiPF_6$ EC: DMC 1:1 liquid electrolyte and a glass fiber separator were used in all experiments. Cyclic voltammetry (CV), galvanostatic (GV) cycling, and electrochemical impedance spectroscopy (EIS) measurements were performed on a VMP3 potentiostat/galvanostat [Bio-Logic] and a Land battery cycler [CT2001A]. EIS measurements were performed at open-circuit voltage with a sinusoidal signal in the frequency range from 1 MHz to 10 mHz at an amplitude of 10 mV. The simulation of the EIS experiments was carried out using ZFit software on EC-Lab (Biologic) using an equivalent circuit model of R1 + Q2/R2 + Q3/R3 + Q3 for coin-cell impedance. In situ EIS measurements were done by galvanostatic cycling to the desired voltage followed by a 30-min hold at that voltage to reduce the current to negligible levels before starting the EIS measurements.

C-rate calculations

To accurately portray the rate of galvanostatic experiments, C-rates were calculated post-cycling for each specific current (A g^{-1}). The C-rate was calculated by viewing the voltage-vs-time plots and obtaining the time to charge/discharge for the 3rd cycle. The time was then converted to a C-rate where 1C = 1 hr.

X-ray absorption spectroscopy

Tungsten LIII-edge X-ray absorption spectra were collected at beamline 4-1 at the Stanford Synchrotron Radiation Lightsource (SSRL), SLAC National Accelerator Laboratory. To prepare the samples, cast electrodes (1-2 mg cm^2) were cut into strips with dimensions of approximately 10 mm by 2 mm inside of an Ar-filled glovebox (O_2 < 0.1 ppm, H_2O < 0.1 ppm). Mylar tape was adhered to an aluminum 8-slot sample holder, and the electrode strips were placed in the gaps. The other side of the sample holder was also covered in Mylar tape to fully enclose the electrodes. The

sample holder was quickly transferred to a He-purged sample chamber. Data were acquired in transmission at the W L_{III}-edge using a using a Si-(220) $\phi = 0$ double-crystal monochromator with energy steps of 0.35 eV from 10184 eV to 10234 eV. The pre-edge was measured in steps of 10 eV from 9974 eV to 10174 eV. The EXAFS region was measured from k = 1.64 to k = 13.2 in steps of k = 0.05. All spectra are referenced to W foil measured simultaneously at the W L_{III}-edge (10207 eV), which was collected simultaneously, and 3 sweeps were averaged per sample. Background normalization, calibration and linear combination fitting were performed using the Demeter software, Athena.[21] W metal and WS_2 were used as standards to obtain the W oxidation states. EXAFS were extracted from the normalized absorption spectra by fitting a spline to the region between k = 0 and 13 $Å^{-1}$. EXAFS fittings were done with calculated structures resulting from DFT calculations (detailed below).

Tantalum LIII-edge X-ray absorption spectra were collected at beamline 4-1 at the Stanford Synchrotron Radiation Lightsource (SSRL), SLAC National Accelerator Laboratory. Sample preparation was consistent with the previously stated description. Transmission data were acquired at the Ta L_{III}-edge using a using a Si-(220) $\phi = 0$ double-crystal monochromator. All spectra were referenced to Ta foil measured simultaneously (9881.1 eV), and 3 sweeps were averaged per sample. Background normalization and calibration were performed using Athena. EXAFS were extracted from the normalized absorption spectra by fitting a spline to the region between k = 0 and 13 $Å^{-1}$.

Pair distribution function analysis

Ex-situ electrodes for PDF measurements were prepared as free-standing (current collector-free) electrodes in a ratio of 80:10:10 active material: PTFE binder: Super P in an Ar-filled glove box. The dry powders were hand mixed and pressed in a 13mm die to result in

electrodes with ~15-20 mg cm^{-2} loading. High mass loadings had no effect on the observed capacity. The *ex-situ* measurements were taken on ~100 mg of sample in a glass (neutron PDF) or Kapton tape (X-ray PDF) capillary, resulting in an average of 5-6 electrodes per measurement at each voltage. Neutron PDF measurements were performed on the Spallation Neutron Source (SNS)'s NOMAD beamline at Oak Ridge National lab with a Q_{max} of 28 $Å^{-1}$ (*a*-TaSy) and 30 $Å^{-1}$ (*a*-WS_x). X-ray PDF measurements were performed on the National Synchrotron Light Source II's PDF beamline 28-ID-1 The beam wavelength was 0.1664 Å and PDFs were measured a at ~210.3 mm sample-to-detector distance with Q_{max} of 22 $Å^{-1}$. PDF fittings were done on PDFgui software [22] and were calibrated using a Ni standard.

DFT calculations

Calculations were performed with density functional theory [23],[24] (DFT) using the Vienna *ab initio* simulation package[25] (VASP). The Perdew-Burke-Ernzerhof (PBE) functional[26] with D3 van der Waals correction[27] was used. All calculations were performed with a cutoff energy of 400 eV. The global optimization was done by the stochastic surface walking (SSW) method[28],[29], which is an unbiased potential energy surface exploration method.

For the global optimization process and Bader charge calculations, first order Methfessel-Paxton smearing with sigma value of 0.2 eV was used for Li-containing systems and gaussian smearing with sigma value of 0.1 eV was used for non-Li-containing systems (W_3S_{10} and Ta_4S_8 structures). For projected density of states (pDOS) calculations, the tetrahedron smearing method was used.

For the global optimization process, an automatic k-point mesh generated with R_k=15 Å was used for non-Li-containing systems (W_3S_{10} and Ta_4S_8 structures) and R_k=30 Å was used for Li-containing systems. For Bader charge and projected density of states (pDOS) calculations, we

further increased R_k to 50 Å. Test calculations were performed on the WS system (both for Li-containing and non-Li-containing structures) and no spin polarization was found. Therefore, calculations of the WS system were performed without spin polarization. Calculations of the TaS system were performed with spin polarization. For pDOS calculations, we also performed projections based on local orbital basis using the LOBSTER package, and the results were very similar to the projections made by VASP software, which is based on Wigner-Seitz radius. Therefore, the pDOS results done by VASP projection were shown. The XANES spectroscopy

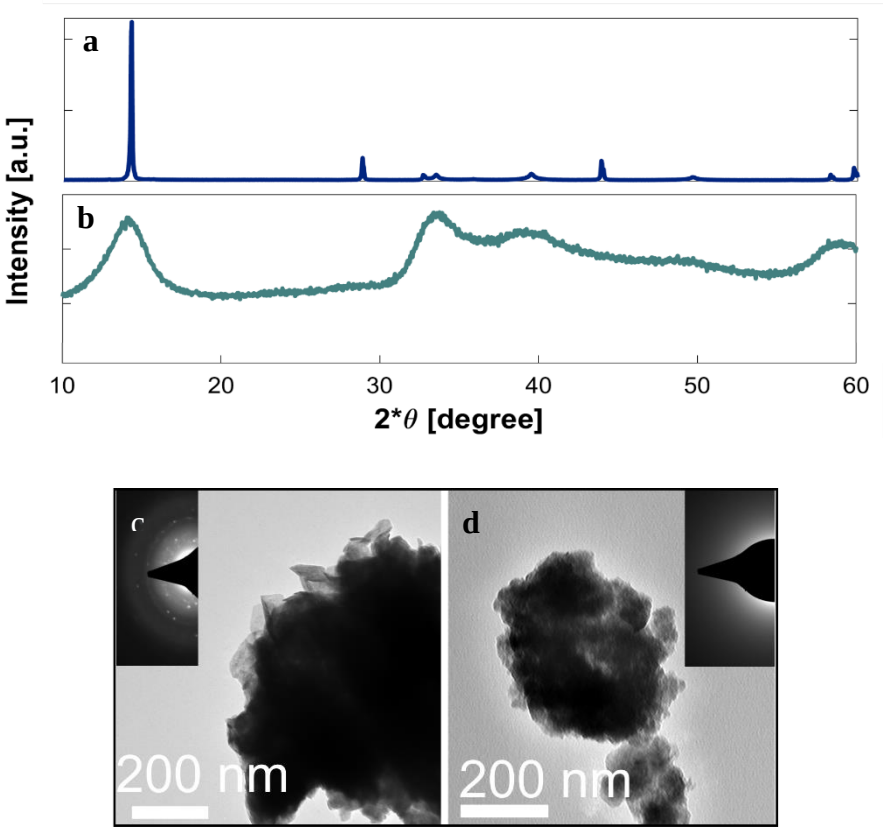

Figure 5-1. X-ray diffraction of **a)** crystalline vs **b)** amorphous WS_2 highlighting the X-ray amorphous structure of ball-milled WS_2 for 80h at 500 rpm. Transmission electron microscopy of **c)** crystalline and **d)** amorphous WS_2 showing a slight reduction in particle size after ball milling and amorphization. The electron-diffraction patterns shown in the insets also highlight the amorphous nature of the ball-milled powder without any long-range order, indicated by the diffuse diffraction region.

was simulated using the FDMNES software[30,31] based on the structures achieved in the global optimization. The finite difference method with a cutoff radius of 8 Å was used.

5.2 Lithiation of amorphous vs crystalline WS_2

In order to observe the effects of amorphization in the layered, 2H-WS_2 conversion material, the pristine material was ball milled in a planetary mill for 80h at 500 rpm under argon. The pristine crystalline and ball-milled WS_2 X-ray diffraction (XRD) patterns are shown in **Figure 5-1**a-b and highlight the broad, amorphous pattern of the ball-milled material. Transmission electron microscopy (TEM) images displayed a slight reduction in particle size after ball milling: ~500 nm and ~200 nm agglomerates in the crystalline and amorphous material, respectively (**Figure 5-1**c-d). The amorphization of the ball-milled powder can also be seen in the electron diffraction patterns, shown in the insets of the TEM images. The amorphous, ball-milled powder

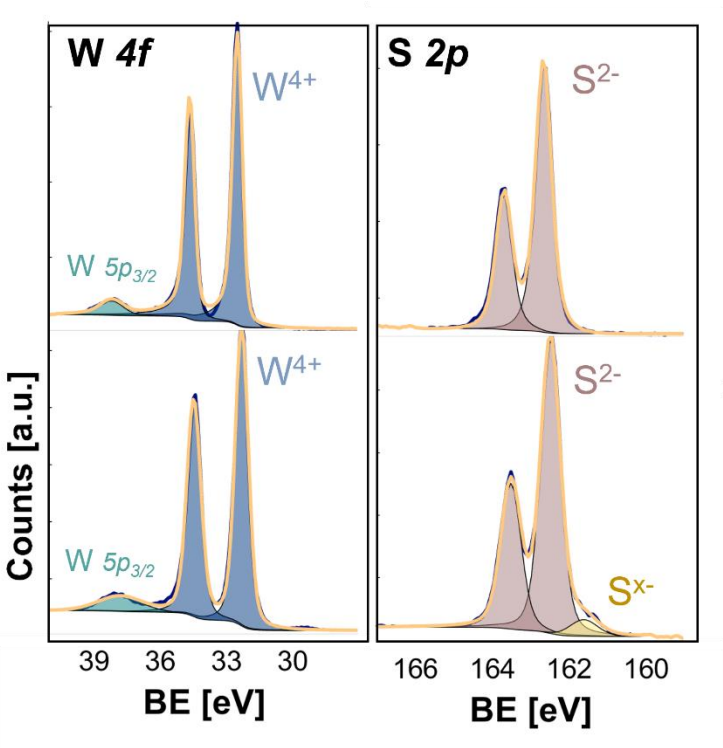

Figure 5-2. X-ray photoelectron spectroscopy detailed scans of crystalline (top) and amorphous (bottom) WS_2 in the W *4f* and S *2p* regions highlighting the similar surface oxidation states.

displayed a diffuse electron diffraction region while the crystalline phase displayed obvious crystallinity in the electron diffraction spots. X-ray photoelectron spectroscopy (XPS) displayed similar surface oxidation states of the pristine and amorphous material (**Figure 5-2**), suggesting amorphization did not significantly change the bonding on the surface of the material. Detailed scans of the W *4f* and S *2p* regions indicated W was in the 4+ state and S was the in 2- state in both WS_2 phases.

The advantage of Li-insertion into amorphous WS_2 over crystalline WS_2 was observed cyclic voltammetry (CV) vs Li-metal. When cycled in a composite electrode from 3 V to a sequentially lower voltage limit of 1, 0.8 and 0.6 V vs Li^+/Li at a scan rate of 0.1 mV s^{-1}, the cyclic voltammogram of the amorphous material displayed an onset of redox at higher voltages than that

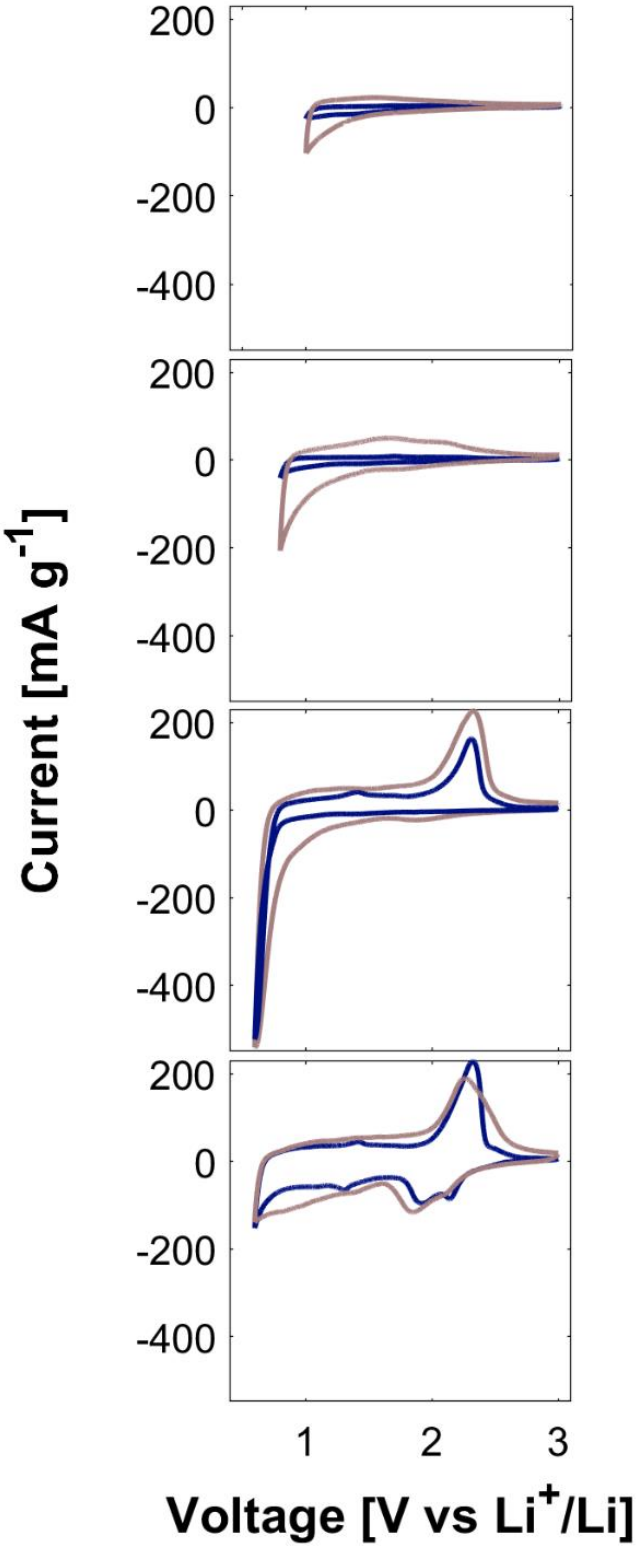

Figure 5-3. Cyclic voltammograms displaying the voltage window opening of amorphous (purple) and crystalline (blue) WS_2 showing the first cycle from **a)** 3.0 - 1.0 V, **b)** 3.0 – 0.8 V, **c)** 3.0 – 0.6V and **d)** the second cycle from 3.0 – 0.6V vs Li^+/Li. The difference in the current response highlights the higher lithiation voltage of the amorphous structure compared with that of the crystalline structure.

of

the crystalline material (**Figure 5-3**). There is near zero current obtained from the crystalline WS_2 material when cycled between 3.0 V and 0.8 V vs. Li^+/Li (**Figure 5-3**a-b) until the obvious conversion reaction at ~0.6 V shown in the negative current spike. In the amorphous material however, the onset of current upon lithiation begins earlier with a sloping current profile to 0.6 V upon lithiation instead of a dramatic current spike as observed in the crystalline material (**Figure 5-3**c). In the 2nd cycle to 0.6 V (**Figure 5-3**d), the amorphous material displayed broader, less well-defined defined redox peaks compared with those of the crystalline material, which may indicate a more gradual conversion reaction and Li-insertion process. In addition, the 2nd cycle of the amorphous WS_2 cycled to 0.6 V vs Li^+/Li offers a specific capacity of ~450 mAh g^{-1} while that of the crystalline material offers only ~300 mAh g^{-1} within the same voltage range. The ease of Li-insertion into amorphous WS_2 compared with that of crystalline WS_2 can also be seen in

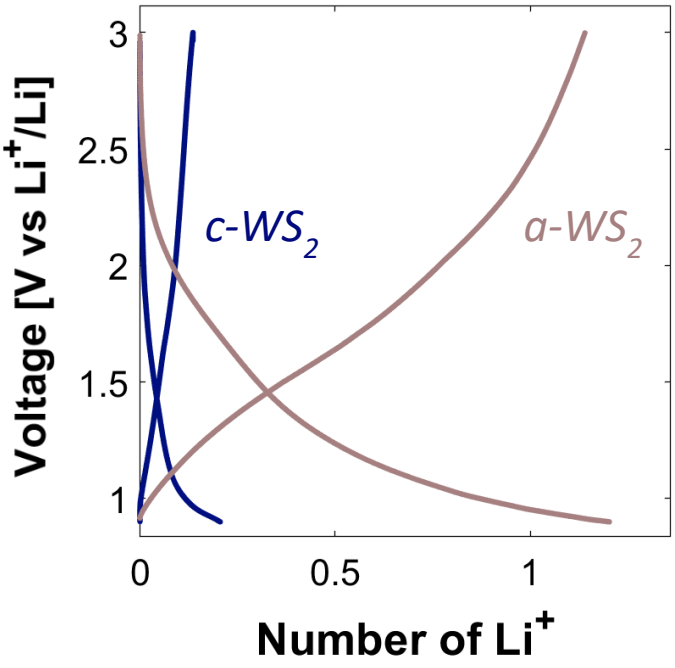

Figure 5-4. Galvanostatic cycling (2nd cycle) of composite electrodes of amorphous and crystalline WS_2 from 3.0 to 0.9 V vs Li^+/Li. The limited voltage cycling highlights the higher degree of lithium insertion (1.2 Li^+) into the amorphous phase compared with that of the crystalline phase (0.2 Li^+).

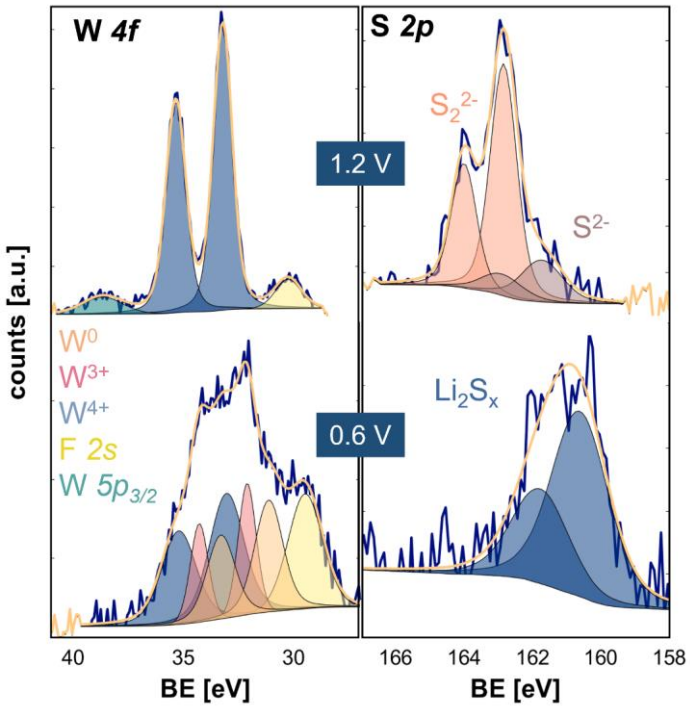

Figure 5-5. X-ray photoelectron spectroscopy (XPS) of ex-situ composite electrodes of amorphous WS_2 cycled to 1.2 V and 0.6 V vs Li^+/Li upon lithiation.

galvanostatic cycling between 3.0 and 0.9 V vs Li^+/Li at a C/5-rate (**Figure 5-4**). In the amorphous WS_2, 1.2 Li^+ (129 mAh g^{-1}) were reversibly inserted into the structure displaying a Coulombic efficient of 95%. In the crystalline WS_2, 0.2 Li^+ (22 mAh g^{-1}) were inserted within the same voltage range with a Coulombic efficiency of only 64%, indicating a much less reversible process than the amorphous WS_2.

XPS studies of lithiated crystalline and amorphous WS_2 also suggest Li-insertion into the amorphous material is easier than Li-insertion into crystalline WS_2. The ex-situ amorphous WS_2 composite electrode cycled to 1.2 V vs Li^+/Li on first lithiation displayed possible anionic redox before conversion (**Figure 5-5**) due to the formation of S_2^{2-} sulfur dimers on the surface and the surface W remaining in the W^{4+} state. Upon further lithiation to 1.2 V vs Li^+/Li (1^{st} cycle), the S *2p* region displayed conversion of the surface to Li_2S and the W 4f region displays reduction of

the W to fully reduced W-metal and W^{3+} with some remaining in the W^{4+} state. Thus, while the amorphous WS_2 still undergoes a conversion reaction, there is evidence of a possible Li-insertion mechanism before conversion to Li_2S and W^0. To further probe the lithiation activity of the amorphous and crystalline phases, chemical lithiation in n-butyllithium (1.6M in hexane) was performed by leaving the powder in the solution for 48h. This enables XPS to obtain the surface oxidation states without the interference of a solid-electrolyte interphase (SEI) formed in electrochemical cycling. Chemical lithiation in n-butyllithium is equivalent to electrochemical lithiation to ~1V vs Li+/Li,[32] which in CV appears to be where the lithiation of the amorphous phase has begun but there is still nearly zero current from the crystalline phase (**Figure 5-3**). After 48 h in n-butyllithium solution, XPS revealed successful chemical lithiation of the surface of the amorphous phase but not of the crystalline phase (**Figure 5-6**). In the W *4f* region, the amorphous WS_2 powder displayed doublets indicating fully reduced W-metal as well as some surface oxide species and unreacted WS_2. In the crystalline WS_2, however, the W remained in the W^{4+} state with some surface oxide species, probably due to exposure to hexane. Similarly, the S *2p* region of the amorphous WS_2 indicated conversion to Li_2S and Li_2S_n polysulfides while the crystalline WS_2 remained in the pristine S^{2-} state of WS_2.

The comparison of crystalline and amorphous WS_2 during chemical and electrochemical lithiation suggests that amorphous materials may offer some advantages over crystalline counterparts for Li-ion electrode materials. Here, the amorphous phase presented greater capacity within a given voltage range, earlier onset of lithiation, and the possibility of anionic redox behavior. Thus, amorphous materials may offer greater possibilities for improvement of Li-ion electrode systems compared with crystalline materials and a new field to explore for next-generation electrodes.

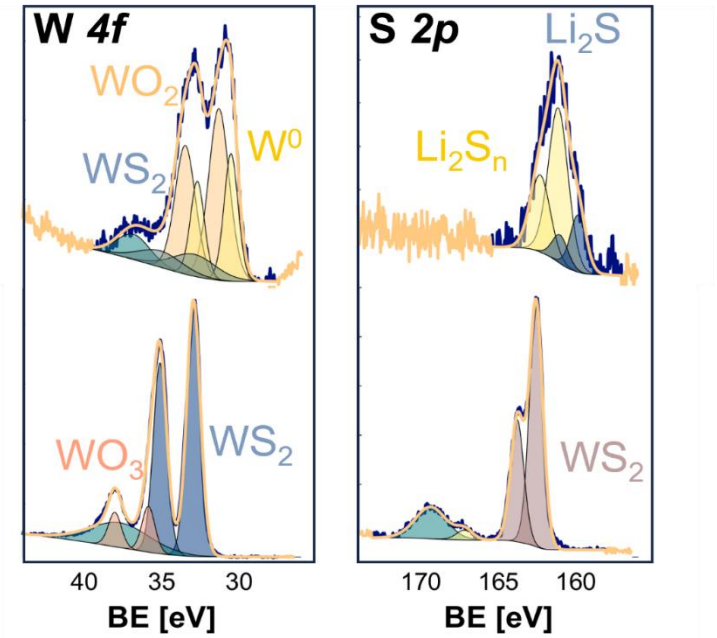

Figure 5-6. X-ray photoelectron spectroscopy (XPS) detailed scans of amorphous (top) and crystalline (bottom) WS_2 in the W *4f* and S *2p* regions after 48h in excess 1.6M n-butyllithium solution in hexane. displaying the lithiation of the amorphous phase but not of the crystalline phase to an electrochemical equivalence of ~1.0 V vs Li^+/Li.

5.3 Local structure of amorphous WS_x

Amorphous, sulfur-rich tungsten sulfide *a*-WS_x ($x \approx 3$) displayed a lack of long-range order after mechanochemical synthesis from crystalline WS_2 (*c*-WS_2) and S_8 powder precursors. X-ray diffraction (XRD) of the as-synthesized *a*-WS_x powder (**Fig. Appendix-1a (A-1a)**) displayed broad, poorly defined peaks, indicating the material is X-ray amorphous without long-range order. Transmission electron microscopy (TEM) images displayed *a*-WS_x particles that are 50-200 nm in size. Furthermore, the electron diffraction pattern (inset of **Fig. A-1b**) of *a*-WS_x had diffuse, poorly defined rings, further supporting the lack of long-range order. X-ray photoelectron spectroscopy (XPS) survey spectrum found the W:S ratio to be 1:2.9, slightly lower than added amounts during synthesis due to surface oxide species (**Fig. A-2a**). A detailed scan of the *a*-WS_x

W *4f* region (**Fig. 5-7a**) displayed tungsten in the W^{IV} formal oxidation state with one doublet at 32.2 eV binding energy (B.E.) and a W $5p_{3/2}$ peak at ~38 eV, despite being a sulfur-rich tungsten sulfide. Thus, redox balance for excess sulfur must be obtained by an incompletely reduced state of sulfur through the formation of S-S bonds. This was confirmed by the *a*-WS_x S *2p* XPS spectrum (**Fig. 5-7b**) which showed two prominent doublets with the S $2p_{3/2}$ peaks at 161.9 and 163.8 eV, that we attribute, respectively, to fully reduced, terminal isolated sulfur (S^T) and neutral, bridging polysulfides including S-S bonds (S^B), in a ~75:25 ratio (see Appendix 1 for further information on terminology). The Raman spectrum of the *a*-WS_x powder (**Fig. A-3**) also shows evidence of bridging polysulfides, consistent with results for other transition metal sulfides and earlier results for amorphous WS_3. [16,33,34]

Synchrotron X-ray absorption spectroscopy (XAS) of the W L_{III}-edge and neutron pair distribution function analysis (*n*PDF) were performed to better understand the transition metal and sulfur oxidation states of the pristine amorphous powders. Through X-ray absorption near-edge structure (XANES) analysis, the *a*-WS_x material was confirmed to be in the W^{IV} oxidation state with the same W L_{III}-edge energy as that of *c*-WS_2 (**Fig. A-4**). *n*PDF analysis is consistent with the XANES results as a peak at 2.08 Å, indicating S-S bonds are present in the *a*-WS_x material (**Fig. 5-7c, Fig. A-5**). The mixture of anion valence states in the pristine *a*-WS_x is unusual compared to most other transition metal sulfides which are composed of either purely terminal S in the formal reduced

state S^{-II}, such as observed in *c*-WS_2 (**Fig. A-6**), or purely bridging sulfur species, usually in S_2^{-II} dimers, such as in pyrite FeS_2.[12]

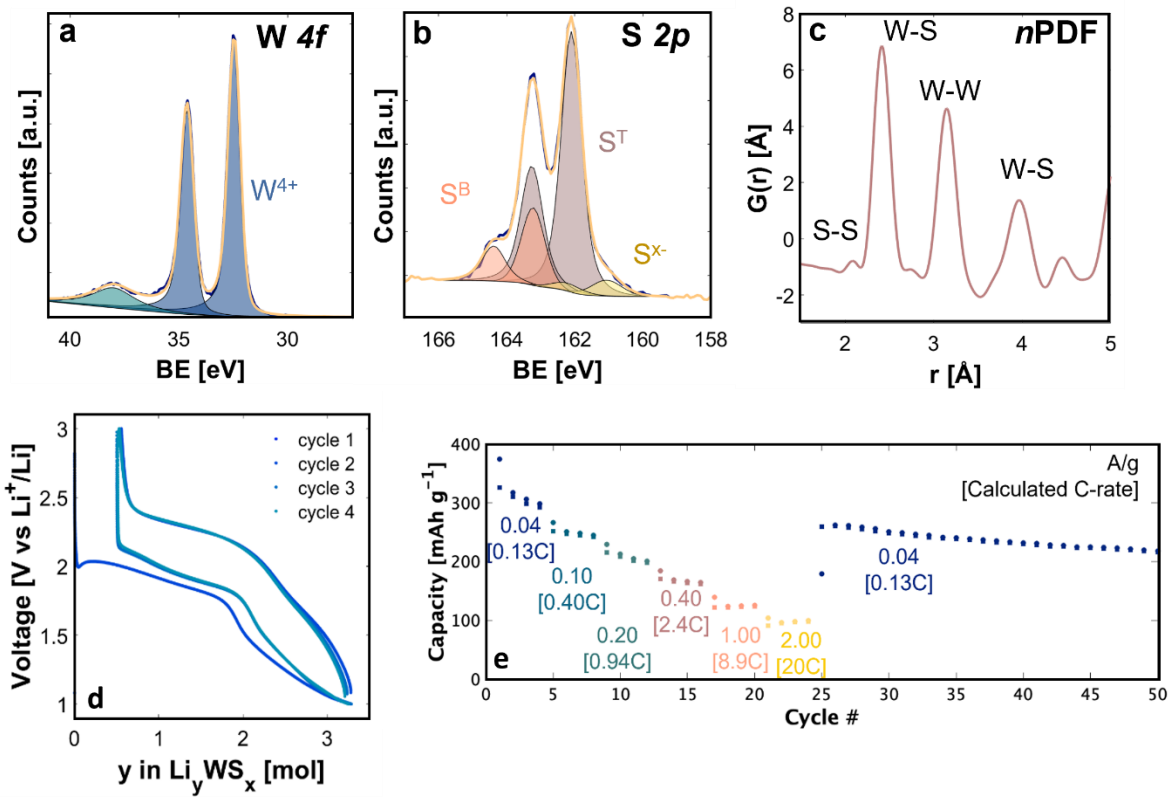

Figure 5-7. a-WS_x local structure and electrochemical lithiation. X-ray photoelectron spectroscopy (XPS) detailed scans of the **a)** W *4f* and **b)** S *2p* regions of *a*-WS_x, highlighting the complex sulfur anionic sates as a mix of bridging sulfur dimers and terminal S^{-II} species. **c)** Neutron pair distribution function analysis of *a*-WS_x powder from 1.5 to 5 Å showing the S-S bonds at 2.08 Å. Galvanostatic cycling of **d)** *a*-WS_x composite electrode from 3.0 to 1.0 V vs Li^+/Li at a specific current of 0.95 A g^{-1} highlighting the multielectron redox processes. **e)** Galvanostatic rate cycling from 0.04 to 2.0 A g^{-1}. See Appendix 1 for further experimental details.

5.4 Electrochemical lithiation of *a*-WS_x

The electrochemical properties of *a*-WS_x were investigated using traditional composite electrodes with conductive carbon and polymer binder. In a half-cell arrangement vs. Li-metal, cyclic voltammetry (CV) and galvanostatic (GV) cycling measurements displayed multielectron

redox (> 3 Li^+ inserted at slow rates) without signatures of conversion and relatively good performance at high rates, especially considering anionic redox participation.

In galvanostatic cycling of *a*-WS_x composite electrodes, the voltage profile displayed sloping 'S-curves' after the first lithiation (**Fig. 5-7d**). The 'S-curves' are characteristic of anionic redox materials where bonds in the polysulfide units are broken and reformed gradually throughout the voltage region.[7] The amorphous sulfide was able to reversibly accommodate 2.8 Li^+ per formula unit, corresponding to 261 mAh g^{-1} at a specific current of 0.95 A g^{-1}. Such a high number of lithium inserted per transition metal suggests that sulfur anions are indeed participating in the charge storage process. Reversible electrochemical cycling was demonstrated by the overlap of the GV curves after the first lithiation during the first four cycles (98% capacity retention, 98% Coulombic efficiency) shown in **Fig. 5-7d.** A combination of CV (**Fig. A-7**) measurements and *ex-situ* XRD (**Fig. A-8a**) helped to identify the intercalation region before conversion to W^0 and Li_2S.

Galvanostatic cycling of *a*-WS_x at different charge/discharge rates show that 30% capacity is retained when there is a 100× increase in specific current, from 0.02 to 2.0 A g^{-1} (**Fig. 5-7e**). While this is a relatively modest level of rate retention at high rate, the significant number of lithium inserted at slow rates (at 0.04 A g^{-1}, 312 mAh g^{-1}, or ~3 Li^+) results in a capacity of 97 mAh g^{-1} at 2.0 A g^{-1}, which is calculated to be a 20C-rate (see Materials and Methods for discussion of C-rate calculations). The kinetic behavior was further characterized in CV experiments in which the change in peak current with sweep rate was used to distinguish between diffusion limited and surface confined processes (**Fig. A-9a** and Appendix 1 for further information).

The favorable kinetics for *a*-WS_x lithiation occurred despite the existence of a voltage hysteresis. In the 4th cycle for *a*-WS_x (**Fig. 5-7d**) the voltage hysteresis between lithiation and

delithiation at 1 Li^+ inserted was 396 mV while the energy efficiency was calculated to be 82%. A combination of 'voltage window opening' GV experiments (**Fig. A-10**), galvanostatic intermittent titration technique (GITT) measurements (**Fig. A-11**), and *in-situ* electrochemical impedance spectroscopy (EIS) (**Fig. A-12)** demonstrated that there was no substantial change in kinetics or overpotential at various states of charge as commonly observed in the lithium kinetics of oxygen redox materials.[35,36] This highlights the advantage of sulfides for anionic redox over oxides, which

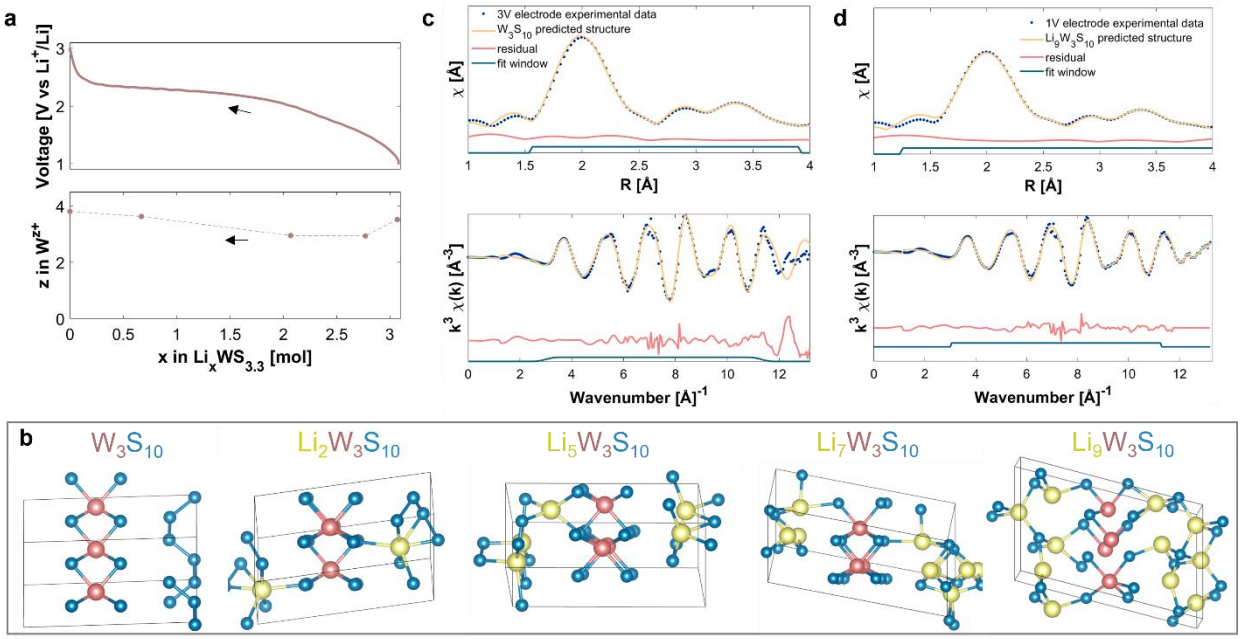

Figure 5-8. a-WS_x oxidation state with simulated $Li_xW_3S_{10}$ unit cells and W L_{III}-edge EXAFS fittings to predicted structures. a) W oxidation states of ex-situ a-WS_x electrodes from the XANES W L_{III} edge as a function of delithiation from linear combination fitting during the 1st delithiation. **b)** Lowest energy structures from DFT global optimization of a W_3S_{10} unit cell and the unit cell with 2, 5, 7, and 9 lithium inserted (W is red, S is blue, Li is yellow) shown in the c* orientation (of reciprocal space) for clarity. See **table S2** for simulated structure parameters. Corresponding EXAFS data for ex-situ electrodes cycled to **c)** 3 V (fully delithiated) and **d)** 1 V (fully lithiated) highlight the excellent representation of the local structure from 1.5 to ~4 Å (R-factor lower than 0.008 for all fittings). See **Table A-3** for EXAFS fitting parameters and **Fig. A-18** for EXAFS fittings of the intermediate structures $Li_2W_3S_{10}$ and $Li_7W_3S_{10}$.

can exhibit large changes in hysteresis, overpotential, and charge transfer resistance during cycling.

5.5 Electrochemical charge storage mechanisms in *a*-WS_x

The high number of Li inserted into the amorphous tungsten sulfide raises the tantalizing question of the charge storage mechanism responsible for accommodating 3 Li^+. XAS on the W L_{III}-edge was performed on *ex-situ* electrodes cycled to various degrees of lithiation to observe the change in transition metal oxidation state upon cycling (**Fig. A-13-S14, Table A-1**).

Fig. 5-8a displays the experimental oxidation states of W in *a*-WS_x as a function of lithium de-inserted at a specific current of 0.25 A g^{-1}. During delithiation of the *a*-WS_x electrode, there is a nonlinear change in W oxidation state as a function of lithium (**Table A-1**). The significant feature to note is that despite the insertion of 3 mol Li^+, the fully lithiated electrode (at 1.0 V vs. Li^+/Li) was found to contain W in nearly the same oxidation state as the fully delithiated electrode (at 3.0 V vs. Li^+/Li). This unusual transition metal redox behavior is made possible by the compensation of charge upon lithium insertion by the breaking and formation of sulfur bonds. XPS on *ex-situ* electrodes demonstrates the evolution of sulfur bonding in the S *2p* spectrum (**Fig. A-15**) from 93% bridging S-S bonds on the surface at 3.0 V to only 18% at 1.0 V vs Li^+/Li. The reduction of sulfur in S-S bonds to S^{-II} upon lithiation can also be observed in the *ex-situ* Raman spectroscopy measurements of *a*-WS_x electrodes (**Fig. A-16**). The bridging S-S bond peak at ~520 cm^{-1} is present in the fully delithiated 3.0 V electrode, as in the pristine *a*-WS_x material (**Fig. A-3**), while the Raman spectrum of the lithiated electrode at 1.2 V suggests few, if any, S-S bonds are present. Taken together, the XAS, XPS, and Raman spectroscopy suggest that anionic redox is responsible for the high capacity and lithium insertion capabilities of *a*-WS_x. Such a dynamic redox behavior of both the transition metal and sulfur bonds is not unprecedented and was observed

with Peierls distorted VS_4 [16,17] as well as amorphous Mo_3S_{11}.[37] However, the amount of redox-based charge storage, the cycling stability and electrochemical reversibility after the first cycle shown here are far superior to previously studied multi-electron, sulfur redox systems in liquid electrolyte.[14–17]

To further understand the charge storage mechanism in amorphous tungsten sulfide, computational simulations were performed with first principles global optimization methods to determine the lowest energy structure of a W_3S_{10} unit cell (**Fig. A-17**). The methodology and results of these calculations are detailed in the SI. The structural changes upon lithiation were further determined by calculating the structures of $Li_xW_3S_{10}$ for x = 2, 5, 7, and 9 (**Fig. 5-8b, Table A-2**). The optimized W_3S_{10} cell displayed alternating layers of trigonal prismatic W_3S_6 and S_4 neutral chains, with lithium incorporated into the $(S)_n$ chains upon lithiation.

The proposed structures were validated by fitting the experimental EXAFS and *n*PDF data to the calculated structures (**Fig. 5-8c-d, Fig. A-18-S19, Table A-3**). In addition, simulated XANES results were compared to experimental results (**Fig. A-20a-e**). Not only did the fully delithiated (3.0 V) and fully lithiated (1.0 V) *ex-situ* electrodes display excellent fittings to the W_3S_{10} and $Li_9W_3S_{10}$ local structures, but also the intermediate compositions, delithiated to 2.0 and 2.3 V, demonstrated excellent agreement with the $Li_7W_3S_{10}$ and $Li_2W_3S_{10}$ structures, respectively. Further details regarding the W_3S_{10} phase as related to the atomic configuration and atom-atom correlations are provided in the Appendix 1.

The lithiated structures demonstrate that sulfur bond breaking in the sulfur chains accommodated the majority of the stored lithium. Based on the simulated W_3S_{10} formula unit, a simple formal charge analysis suggests that 8 Li^+ are accommodated by the neutral S_4 chain reduction to $4S^{-II}$ and the W_3S_6 unit is reduced only by 1 electron to accommodate the final Li^+.

Accordingly, Bader charge (**Fig. A-21**) and projected density of states (pDOS) calculations (**Fig. A-22**) were used to confirm the associated electronic distribution (see Appendix 1 for details). While there are some differences in the details, the two approaches were in agreement that the first 8 electrons were accommodated by the neutral S_4 chain reduction and the W_3S_6 layer accommodated the 9th electron. This behavior is consistent with the results from the linear combination fitting in the XAS experiments. That is, after lithiation, W in the compound has a similar electronic structure to that of *c*-WS_2 and possesses a formal oxidation number of slightly less than W^{+IV} (**Fig. A-14, Fig. A-20**). Thus, the simulated structures are consistent with the experimental results for *a*-WS_x with anion redox having a central role in achieving the high capacity of *a*-WS_x, as S-S bond breaking and formation account for nearly all the observed charge storage properties.

5.6 Local structure of amorphous TaS_y

To further study the anionic redox capabilities of amorphous 5*d* transition metal sulfides, we investigated the structural and electrochemical properties of amorphous tantalum sulfide *a*-TaS_y ($y \approx 2$). After mechanochemical synthesis from Ta metal and S_8 precursors, the XRD pattern (**Fig. A-23a**) displayed broad peaks suggesting the lack of long-range order. TEM images (**Fig. A-23b**) displayed ~200-300 nm agglomerates with ~50 nm domains and electron diffraction, shown in the inset, displayed an entirely diffuse region indicating the absence of long-range order. Pressed pellets of *a*-TaS_y powder displayed semiconducting behavior although with a much greater electronic conductivity of ~1 S cm^{-1} as compared to *a*-WS_x (see Appendix 1 and **Fig. A-24**).

XPS also played a central role in establishing the chemistry and oxidation state of the *a*-TaS_y materials. The XPS survey spectrum (**Fig. A-2b**) resulted in a Ta:S ratio of 1:1.91, slightly lower than expected due to surface oxide species as observed in *a*-WS_x. XPS detailed scans of

pristine *a*-TaS_y suggest complex cation and anion valence states. In the Ta *4f* region (**Fig. 5-9a**), the two lower B.E. doublets with Ta $4f_{7/5}$ peaks at 23.9 and 24.4 eV B.E. were similar to those observed in 1T-TaS_2 where charge density waves and Peierls distortion create doublet splitting of the Ta^{4+} state.[38] Two doublets with the Ta $4f_{7/5}$ peaks at higher B.E. can be ascribed to surface oxide species, Ta_2O_{5-x} at 25.1 eV and Ta_2O_5 at 27.2 eV, and a Ta $5p_{3/2}$ peak at ~35 eV. The sulfur S *2p* spectrum (**Fig. 5-9b**) of *a*-TaS_y is similar to that of *a*-WS_x indicating a mix of reduced, terminal S^{-II} and neutral, bridging S-S bonds at 161.1 and 163.0 eV B.E. at a ratio of ~58:42, respectively. Further evidence of S-S bonds was displayed in the *a*-TaS_y powder *n*PDF spectrum by the S-S bond peak at 2.10 Å (**Fig. 5-9c**). The main peaks in *n*PDF spectrum at 2.48 and 3.30 Å can be ascribed to Ta-S and Ta-Ta bonds, respectively, and correspond well to crystalline TaS_2 phases and X-ray pair distribution function (*x*PDF) (**Fig. A-25).** [39,40]

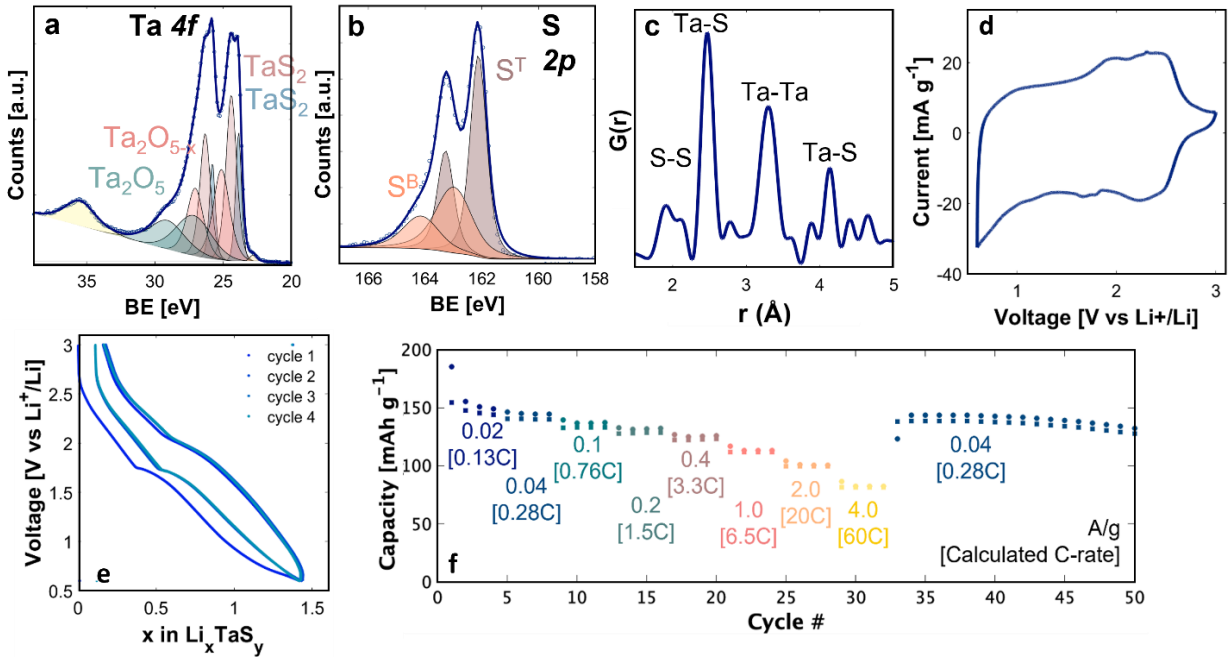

Figure 5-9. a-TaS_y local structure and electrochemical lithiation. XPS of the **a)** Ta 4f and **b)** S 2p regions of a-TaS_y, highlighting the complex sulfur anionic sates as a mix of bridging sulfur dimers and terminal S^{-II} species. **d)** nPDF analysis of a-TaS_y powder from 1.5 to 5 Å showing the S-S bonds at 2.08 Å.

d) Cyclic voltammetry of a-TaS_y composite electrode from 3.0 to 0.6 V vs Li+/Li at 0.1 mV s^{-1} showing the 3rd cycle. **e)** Galvanostatic cycling of the first 4 cycles of a-TaS_y composite electrode at a specific current of 0.1 A g^{-1} and **f)** galvanostatic-rate cycling demonstrating the high-rate capability of amorphous sulfides from 0.02 to 4 A g^{-1}. See Appendix 1 for further experimental details.

5.7 Electrochemical lithiation and charge storage mechanism of *a*-TaS_y

a-TaS_y not only demonstrates multielectron redox, it also exhibits rapid redox kinetics. Whereas materials with the possibility of anionic redox are typically characterized as sluggish and kinetically limited,[7] the electrochemical signatures in CV and GV measurements are characteristic of pseudocapacitive materials where the charge storage mechanism is surface-limited as opposed to diffusion-limited as in battery-like materials.[41] The GV curves were nearly linear with charge added incrementally with voltage, up to 1.3 Li^+ per formula unit at a specific current of 0.1 A g^{-1} (**Fig. 5-9e**). The insertion of more than one Li per transition metal suggests the sulfur anions are redox active and the overlap of the first four charge/discharge curves after the first cycle with 96% Coulombic efficiency demonstrates reversible cycling. In CV measurements, the lack of clearly defined peaks and a box-like CV, in contrast with CV cycling of *a*-WS_x, were also characteristic of surface-limited redox materials (**Fig. 5-9d**). The small features superimposed on the box-like CV may be due to tantalum redox or electron transfer between the tantalum and sulfur within the amorphous material.[17]

The fast kinetics of *a*-TaS_y are evident in the GV cycling experiments which reach specific capacities of 100 mAh g^{-1} at specific currents of 2.0 A g^{-1}, corresponding to approximately 30C (see Appendix 1). This high-rate capability in amorphous materials has also been observed in amorphous VO_2 [42], but has not been demonstrated thus far in amorphous transition metal sulfides. Further evidence of surface-limited redox behavior of Li insertion in *a*-TaS_y was displayed in the

b-value analysis derived from CV measurements (**Fig. A-9b**). This behavior highlights the excellent Li-ion diffusion kinetics of the *a*-TaS_y material despite the lack of long-range order and the apparent contribution of anion redox.

The voltage range of *a*-TaS_y before conversion was found to be larger than that of *a*-WS_x, with conversion to Ta^0 and Li_2S occurring at 0.4 V vs. Li^+/Li (**Fig. A-26**). CV measurements indicating that cycling to 0.6 V vs. Li^+/Li appeared to avoid conversion were supported by the lack of crystalline products in the XRD pattern of an *ex-situ* electrode cycled to 0.6 V (**Fig. A-8**). Although there was no conversion reaction upon insertion of up to 1.5 Li^+, the voltage hysteresis in GV cycling (**Fig. 5-9e**) was analogous to that observed in GV of *a*-WS_x. This hysteresis could represent slight structural relaxations or rearrangements within the amorphous structure to accommodate S-S bond breaking and formation, as previously reported.[11,43] The voltage hysteresis during cycling from 3.0 to 0.6 V vs Li^+/Li (**Fig. 5-9e**, 4th cycle) was found to be 442 mV at 1 Li^+ inserted while the energy efficiency was calculated to be 87%.

To evaluate the charge storage mechanism of *a*-TaS_y lithiation, *ex-situ* *n*PDF, *x*PDF and XPS analyses were performed on composite electrodes (**Fig. A-27-28**). Due to the negative and positive scattering lengths of lithium in neutron and X-ray total scattering, respectively, and the expected overlap of the Li-S atom distances upon lithium insertion (~1.9 – 2.3 Å) with the S-S bond distance (~2.1 Å), *n*PDF and *x*PDF serve as complementary techniques.[14,44,45] In *n*PDF analysis of *ex-situ* electrodes (**Fig. A-27a**), the *a*-TaS_y electrode lithiated to 0.7 V vs. Li^+/Li displayed an increase in the negative correlation Li-S peak at 2.0-2.3 Å, while the electrode delithiated to 3.0 V vs. Li^+/Li displayed an increase in the positive correlation S-S bond peak at ~2.0 Å. If Ta redox were solely responsible for charge storage, the S-S bond peak should not re-emerge upon delithiation. This suggests that S-S bonds are breaking upon lithiation to form Li-S

bonds and are reforming upon delithiation to reform S-S bonds. *x*PDF for the pristine *a*-TaS_y material and the *ex-situ a*-TaS_y composite electrodes at various stages of lithiation and delithiation (**Fig. A-27b**) show that a peak at ~2 Å remains constant. This is due to the positive scattering length of both S and Li in *x*PDF and the increase in Li-S upon lithiation and S-S upon delithiation. XPS detailed scans in the S *2p* region (**Fig. A-28**) of partially (1.8 V) and fully (3.0 V) delithiated *a*-TaS_y also demonstrate an increase in bridging sulfurs and a decrease in terminal sulfurs upon delithiation, indicating the formation of S-S bonds. Thus, the combined analysis of *x*PDF and *n*PDF with XPS suggests that the breaking and formation of S-S bonds during cycling is participating in the charge storage process for *a*-TaS_y. The charge storage mechanism of *a*-TaS_y contrasts with crystalline counterparts including 1T- and 2H-TaS_2 which display ~1 electron redox attributed to cation redox.[46,47] This behavior is not unexpected as the band structure of crystalline TaS_2 has been shown to evolve upon lithium uptake[47,48] and thus amorphization could readily produce band structures that are more favorable to anionic than cationic redox, as has been shown in other sulfide systems.[14,15]

Computational simulations of the *a*-TaS_y are able to provide additional insights for the charge storage mechanism. The global optimization approach found S-S bond formation, consistent with the experimental amorphous features, represented in a Ta_4S_8 unit cell (**Fig. 5-10a, Table A-4**). The structural changes upon lithiation were further determined by calculating the structures of $Li_xTa_4S_8$ where x = 3 and 6. The experimental Ta L_{III}-edge XAS and *n*PDF analysis data of the materials combined with the simulated XANES, EXAFS, and *n*PDF results exhibited excellent agreement between experimental data and simulated unit cells (**Fig. 5-10b-c, Fig. A-29-33**). That is, the Ta_4S_8 cell displayed a Ta_4S_6 bilayer and a S-S dimer (bond distance 1.89 Å), that does not interact with the Ta cations. The lithiated structures demonstrate the sulfur bond breaking

to accommodate the stored lithium and a limited interaction between lithium and the Ta_4S_6 bilayer, which remain relatively unchanged upon lithiation. A formal charge analysis suggests that upon lithiation 4 e^- are accommodated by the S-S dimer reduction and the Ta_4S_6 unit is only reduced by 2 e^- to accommodate 2 Li^+. This analysis is consistent with Bader charge (**Fig. A-33**) and pDOS calculations (**Fig. A-34**). Bader charge analysis suggested that the electrons were mainly

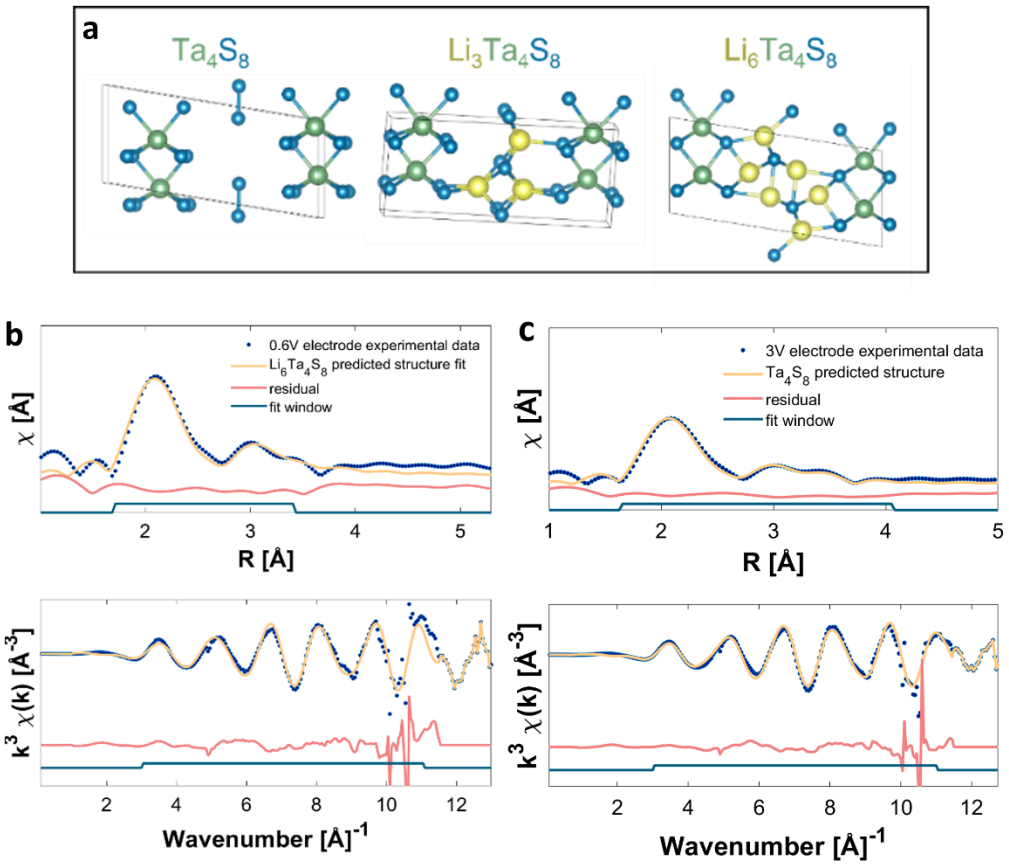

Figure 5-10. Simulated $Li_xTa_4S_8$ unit cells and Ta L_{III}-edge EXAFS fittings to predicted structures. a) Simulated structured of Ta_4S_8, $Li_3Ta_4S_8$ and $Li_6Ta_4S_8$ displaying for Ta_4S_8 a layered structure of alternating Ta_4S_6 and S_2 dimers, lithium being inserted into the S_2 layer to form $Li_3Ta_4S_8$ and $Li_6Ta_4S_8$. Structural parameters for predicted structures are shown in Table S3. EXAFS fittings of *ex-situ* electrodes fully lithiated to 0.6 V **(b)** and fully delithiated to 3.0 V **(c)** displaying excellent fits to the predicted structures. Fitting parameters are shown in **Table A-4.**

accommodated by reduction of the S atoms in the both the S_2 dimer and the Ta_4S_6 layer, and only a slight reduction of Ta atoms was involved, (**Fig. A-33**) while the pDOS results suggested that the 5th and 6th electrons reduced the Ta atoms in the Ta_4S_6 layer (**Fig. A-34)**. Thus, the simulated structures are consistent with the experimental results for *a*-TaS_y in that S-S dimer breaking and formation contribute significantly to the observed charge storage properties.

5.8 The advantage of amorphous, *5d* sulfide systems for anionic redox

The role of covalency in anionic redox has been discussed as advantageous to suppressing O_2 formation in the case of oxides and tuning the redox potential stability in the case of sulfides.[7,13] Recent studies, however, have shown that O_2 formation is still present in Li-rich layered oxides despite the increased covalency by 4*d* and 5*d* metal substitution.[49] Thus, it has proven difficult to design structurally rigid crystalline oxides with added capacity from anionic redox and good cyclability, regardless of the extent of covalent bonding. The more covalent nature of sulfide bonding, brought about by a rise in the sulfur anion *sp* band compared with that of oxides, is more likely to trigger hole formation in the top of the *sp* band, favoring anionic redox chemistries.[12,35] However, tuning the covalency of crystalline sulfides through anion substitution has revealed that increasing covalency may also lead to decreased stability.[13] Recently reported Li-rich layered sulfide $Li_{1.13}Ti_{0.57}Fe_{0.3}S_2$, a mixed anionic, cationic redox material, has shown promising cycle stability with a 78% capacity retention over 50 cycles at a C/2 rate.[11] However, fewer than 1 Li^+ per transition metal can be reversibly cycled into the structure indicating the limited participation of anionic redox in the charge-storage mechanism. Previously studied 3*d* and 4*d* amorphous transition metal sulfides, on the other hand, have shown quite high Li^+ insertion per transition metal (> 3), but with poor cycling stability and limited rate capability (< 20 mA g^{-1}).[14,15,37]

Here, 5*d* amorphous transition metal sulfides, based on electronegative (W) or weakly electropositive (Ta) metals to increase covalency, offer a route toward a combination of high-rate (> 20C cycling), multielectron (> 1 Li^+) redox processes with improved cyclability. Such excellent rate performance suggests an amorphous network can be advantageous for high-rate Li-insertion by S-S bond breaking and formation due to the lack of structural rigidity and an open architecture for Li^+ pathways.[42] These results also suggest that short-range order may be sufficient to support redox reactions and fast Li-ion diffusion as opposed to long-range channels or planes that are typically designed for Li-ion conducting electrodes.[41] Thus, the combination of multielectron redox and fast kinetics displayed in *a*-WS_x and *a*-TaS_y offers a pathway for designing new amorphous materials that enable high capacity for lithium, or other insertion ions, and high power in anionic redox systems.

5.9 References

1. Nitta, N., Wu, F., Lee, J. T. & Yushin, G. Li-ion battery materials: present and future. *Mater. Today* **18**, 252–264 (2015).
2. Griffith, K. J., Wiaderek, K. M., Cibin, G., Marbella, L. E. & Grey, C. P. Niobium tungsten oxides for high-rate lithium-ion energy storage. *Nature* **559**, 556–563 (2018).
3. Preefer, M. B. *et al.* Multielectron Redox and Insulator-to-Metal Transition upon Lithium Insertion in the Fast-Charging, Wadsley-Roth Phase PNb_9O_{25}. *Chem. Mater.* **32**, 4553–4563 (2020).
4. Kodama, R., Terada, Y., Nakai, I., Komaba, S. & Kumagai, N. Electrochemical and In Situ XAFS-XRD Investigation of Nb[sub 2]O[sub 5] for Rechargeable Lithium Batteries. *J. Electrochem. Soc.* **153**, A583 (2006).
5. Kim, H.-S. *et al.* Oxygen vacancies enhance pseudocapacitive charge storage properties of MoO3−x. *Nat. Mater.* **16**, 454–460 (2017).
6. Wada, K., Sakaushi, K., Sasaki, S. & Nishihara, H. Multielectron-Transfer-based Rechargeable Energy Storage of Two-Dimensional Coordination Frameworks with Non-Innocent Ligands. *Angew. Chem.* **130**, 9024–9028 (2018).
7. Assat, G. & Tarascon, J.-M. Fundamental understanding and practical challenges of anionic redox activity in Li-ion batteries. *Nat. Energy* **3**, 373–386 (2018).
8. Ji, H. *et al.* Ultrahigh power and energy density in partially ordered lithium-ion cathode materials. *Nat. Energy* **5**, 213–221 (2020).
9. Grimaud, A., Hong, W. T., Shao-Horn, Y. & Tarascon, J. M. Anionic redox processes for electrochemical devices. *Nat. Mater.* **15**, 121–126 (2016).

10. Zhao, C. *et al.* Review on anionic redox for high-capacity lithium- and sodium-ion batteries. *J. Phys. Appl. Phys.* **50**, 183001 (2017).
11. Saha, S. *et al.* Exploring the bottlenecks of anionic redox in Li-rich layered sulfides. *Nat. Energy* **4**, 977–987 (2019).
12. Rouxel, J. Anion-cation redox competition and the formation of new compounds in highly covalent systems. *Chem. - Eur. J.* **2**, 1053–1059 (1996).
13. Martinolich, A. J. *et al.* Controlling Covalency and Anion Redox Potentials through Anion Substitution in Li-Rich Chalcogenides. *Chem. Mater.* **33**, 378–391 (2021).
14. Doan-Nguyen, V. V. T. *et al.* Molybdenum polysulfide chalcogels as high-capacity, anion-redox-driven electrode materials for Li-ion batteries. *Chem. Mater.* **28**, 8357–8365 (2016).
15. Sakuda, A. *et al.* Amorphous Metal Polysulfides: Electrode Materials with Unique Insertion/Extraction Reactions. *J. Am. Chem. Soc.* **139**, 8796–8799 (2017).
16. Shimoda, K. *et al.* Structural characterization of an amorphous VS_4 and its lithiation/delithiation behavior studied by solid-state NMR spectroscopy. *RSC Adv.* **9**, 23979–23985 (2019).
17. Britto, S. *et al.* Multiple Redox Modes in the Reversible Lithiation of High-Capacity, Peierls-Distorted Vanadium Sulfide. *J. Am. Chem. Soc.* **137**, 8499–8508 (2015).
18. Hansen, C. J. *et al.* Multielectron, Cation and Anion Redox in Lithium-Rich Iron Sulfide Cathodes. *J. Am. Chem. Soc.* **142**, 6737–6749 (2020).
19. Rouxel, J. Some solid state chemistry with holes: Anion–cation redox competition in solids. *Curr. Sci.* **73**, 31–39 (1997).
20. Morgan, D. J. Core-level spectra of powdered tungsten disulfide, WS_2. *Surf. Sci. Spectra* **25**, 014002 (2018).

21. Ravel, B. & Newville, M. *ATHENA* , *ARTEMIS* , *HEPHAESTUS* : data analysis for X-ray absorption spectroscopy using *IFEFFIT*. *J. Synchrotron Radiat.* **12**, 537–541 (2005).
22. Farrow, C. L. *et al.* PDFfit2 and PDFgui: computer programs for studying nanostructure in crystals. *J. Phys. Condens. Matter* **19**, 335219 (2007).
23. Hohenberg, P. & Kohn, W. Inhomogeneous Electron Gas. *Phys. Rev.* **136**, B864–B871 (1964).
24. Kohn, W. & Sham, L. J. Self-Consistent Equations Including Exchange and Correlation Effects. *Phys. Rev.* **140**, A1133–A1138 (1965).
25. Kresse, G. & Hafner, J. *Ab initio* molecular dynamics for liquid metals. *Phys. Rev. B* **47**, 558–561 (1993).
26. Perdew, J. P., Burke, K. & Ernzerhof, M. Generalized Gradient Approximation Made Simple. *Phys. Rev. Lett.* **77**, 3865–3868 (1996).
27. Grimme, S., Antony, J., Ehrlich, S. & Krieg, H. A consistent and accurate *ab initio* parametrization of density functional dispersion correction (DFT-D) for the 94 elements H-Pu. *J. Chem. Phys.* **132**, 154104 (2010).
28. Shang, C. & Liu, Z.-P. Stochastic Surface Walking Method for Structure Prediction and Pathway Searching. *J. Chem. Theory Comput.* **9**, 1838–1845 (2013).
29. Shang, C., Zhang, X.-J. & Liu, Z.-P. Stochastic surface walking method for crystal structure and phase transition pathway prediction. *Phys Chem Chem Phys* **16**, 17845–17856 (2014).
30. Bunău, O. & Joly, Y. Self-consistent aspects of x-ray absorption calculations. *J. Phys. Condens. Matter* **21**, 345501 (2009).
31. Guda, S. A. *et al.* Optimized Finite Difference Method for the Full-Potential XANES Simulations: Application to Molecular Adsorption Geometries in MOFs and Metal–Ligand Intersystem Crossing Transients. *J. Chem. Theory Comput.* **11**, 4512–4521 (2015).

32. Whittingham, M. S. & Dines, M. B. n-Butyllithium—An Effective, General Cathode Screening Agent. *J. Electrochem. Soc.* **124**, 1387–1388 (1977).
33. Liang, K. S. *et al.* Amorphous MoS3 and WS3. *J. Non-Cryst. Solids* **42**, 345–356 (1980).
34. Chang, C. Infrared and Raman studies of amorphous MoS3 and poorly crystalline MoS2. *J. Catal.* **72**, 139–148 (1981).
35. Assat, G. *et al.* Fundamental interplay between anionic/cationic redox governing the kinetics and thermodynamics of lithium-rich cathodes. *Nat. Commun.* **8**, (2017).
36. Jiang, W. *et al.* Understanding the Discrepancy of Defect Kinetics on Anionic Redox in Lithium-Rich Cathode Oxides. *ACS Appl. Mater. Interfaces* **11**, 14023–14034 (2019).
37. Truong, Q. D. *et al.* Anionic redox in a-(Mo3S11)n polymer cathode for all-solid-state Li-ion battery. *Electrochimica Acta* **332**, 135218 (2020).
38. Zhao, R. *et al.* Stabilizing the commensurate charge-density wave in 1T-tantalum disulfide at higher temperatures *via* potassium intercalation. *Nanoscale* **11**, 6016–6022 (2019).
39. Zhao, R. *et al.* Tuning Phase Transitions in 1T-TaS_2 via the Substrate. *Nano Lett.* **17**, 3471–3477 (2017).
40. Jain, A. *et al.* Commentary: The Materials Project: A materials genome approach to accelerating materials innovation. *APL Mater.* **1**, 011002 (2013).
41. Choi, C. *et al.* Achieving high energy density and high power density with pseudocapacitive materials. *Nat. Rev. Mater.* **5**, 5–19 (2020).
42. Chao, D. *et al.* Amorphous VO_2: A Pseudocapacitive Platform for High-Rate Symmetric Batteries. *Adv. Mater.* 2103736 (2021) doi:10.1002/adma.202103736.

43. Saubanère, M., McCalla, E., Tarascon, J.-M. & Doublet, M.-L. The intriguing question of anionic redox in high-energy density cathodes for Li-ion batteries. *Energy Environ. Sci.* **9**, 984–991 (2016).

44. Ren, Y. & Zuo, X. Synchrotron X-Ray and Neutron Diffraction, Total Scattering, and Small-Angle Scattering Techniques for Rechargeable Battery Research. *Small Methods* **2**, 1800064 (2018).

45. Johnson, R. Computational Chemistry Comparison and Benchmark Database, NIST Standard Reference Database 101. (2002) doi:10.18434/T47C7Z.

46. Whittingham, M. S. Chemistry of intercalation compounds: Metal guests in chalcogenide hosts. *Prog. Solid State Chem.* **12**, 41–99 (1978).

47. Eibschutz, M., Murphy, D. W., Zahurak, S. & Waszczak, J. V. Electronic configuration of tantalum in 1T-LiTaS $_2$. *Appl. Phys. Lett.* **61**, 2976–2977 (1992).

48. Whittingham, M. S. Lithium incorporation in crystalline and amorphous chalcogenides: Thermodynamics, mechanism and structure. *J. Electroanal. Chem. Interfacial Electrochem.* **118**, 229–239 (1981).

49. House, R. A. *et al.* Covalency does not suppress O2 formation in 4d and 5d Li-rich O-redox cathodes. *Nat. Commun.* **12**, 2975 (2021).

50. Towns, J. *et al.* XSEDE: Accelerating Scientific Discovery. *Comput. Sci. Eng.* **16**, 62–74 (2014).

Appendix 1. Supplemental information: Anionic redox of amorphous tungsten and tantalum sulfides

Supplementary text

Electronic conductivity

To measure the electrical conductivity of the as-synthesized powder, electrochemical impedance spectroscopy (EIS) was performed on a pellet, dry pressed in 1.3 cm diameter die at pressure of 50 bar held for 30s, resulting ~0.1-0.2 cm thick pellets. The electrical conductivity of *a*-WS_x was found to be 5.6 x 10^{-5} S cm^{-1} at 23 ℃, displaying semiconducting behavior with an increasing electrical conductivity as a function of temperature (**Fig. A-24a**). While the electrical conductivity is lower than that of c-WS_2, it is reasonable for Li-ion battery electrode materials.(*13*),(*14*),(*15*) The electrical conductivity of *a*-TaS_y was larger than that of *a*-WS_x at 0.94 S cm^{-1} in a pressed dry pellet and again shows semiconducting electrical conductivity behavior as a function of temperature (**Fig. A-24b**).

Terminal sulfur vs bridging polysulfides

Here, the terms terminal sulfur S^T and bridging polysulfides S^B are used to distinguish between reduced sulfur and oxidized sulfur in the disordered structure. A terminal sulfur is a reduced, S^{2-} sulfur bonded to a metal cation. A bridging sulfur is an oxidized $(S\text{-}S)^x$ ($0 < x < -2$) bond that can be bonded to the disordered network, bonded to more $(S\text{-}S)^x$ bonds to form a sulfur chain, or left as an $(S\text{-}S)^x$ molecule within the disordered material. The two types of sulfur bonding, S^T and S^B, can be distinguished in XPS and Raman measurements as previously reported in literature.(*16*),(*17*),(*18*)

b-value analysis

The charge storage kinetics of an electrode material can be characterized as diffusion controlled (battery-like) or surface-controlled (capacitor-like). One method in which to qualitatively determine this is b-value analysis, described in detail elsewhere.(*19*) Briefly, the b-value can be determined from cyclic voltammetry as a function of sweep rate v and peak current i_p from the equation:

$$i_p = a \times v^b$$

where *a* is a constant and *b* is a power law exponent. When $b \approx 1$, the reaction mechanism is more capacitor-like and surface-controlled and when $b \approx 0.5$ the reaction mechanism is more battery-like and diffusion controlled. This analysis is only valid for intercalation or insertion materials (as opposed to conversion materials) and thus can be a mix of both diffusion- and surface-controlled resulting in *b*-values between 0.5 and 1.(*19*)

Electrochemical lithiation of a-WS_x

The first GV cycle displayed a voltage plateau at 2.1 V vs. Li^+/Li (also observed in CV measurements), with a slight overpotential at a specific current of 0.95 A g^{-1}. This behavior suggests an activated structural rearrangement upon initial lithiation, similar to that observed in crystalline 3R-WS_2 as it transforms to the 2H phase.(*20*) In CV measurements, a voltage range of 1.0 – 3.0 V vs. Li^+/Li was identified as the intercalation region before conversion to W^0 and Li_2S at 0.8 V vs. Li^+/Li.(*21*) Moreover, XRD measurements on an *ex-situ* electrode cycled to 1.0 V vs. Li^+/Li did not show the presence of crystalline conversion products within the 1.0 – 3.0 V vs. Li^+/Li range.

Using 'window opening' experiments to characterize GV cycling as a function of the voltage window (**Fig. A-10**), there was no substantial increase in voltage hysteresis at various states of charge. This behavior contrasts with reported behaviors of many oxygen redox materials including Li-rich NMC and highlights the difference of sulfur redox compared to that of oxygen.(*22*),(*23*) In Galvanostatic intermittent titration technique (GITT) experiments (**Fig. A-11**), the a-WS_x composite electrode displayed relatively stable overpotentials at ~100 mV as a function of lithiation. The voltage difference between charge and discharge at 1 Li^+ measured from the open circuit potential decreased to 295 mV, indicating a slight improvement at quasi-steady state. Despite the observed voltage hysteresis, the in-situ electrochemical impedance spectroscopy (EIS) results demonstrate minimal changes in ohmic, interfacial and charge storage resistance as a function of voltage (**Fig. A-12**). This highlights the advantage of sulfides for anionic redox over oxides, which exhibit large changes in charge transfer resistance during cycling.(*24*, *25*)

Electrochemical charge storage mechanisms in a-WS_x

For the *a*-WS_x electrode XAS measurements at the WL_{III}-edge, the oxidation states were calculated using linear combination fitting of the XANES spectra of pristine *a*-WS_x powder (W^{4+}) and tungsten metal foil (W^0) (**Fig. A-14, Table A-1**). The transition metal to sulfur ratio was set to W:S 1:3.3 based on maintaining a charge balance in the fully lithiated and delithiated states. Although this is a slightly higher ratio than obtained from XPS (1:2.9), it is not unreasonable considering the oxide species detected and the limited surface sensitivity of XPS.

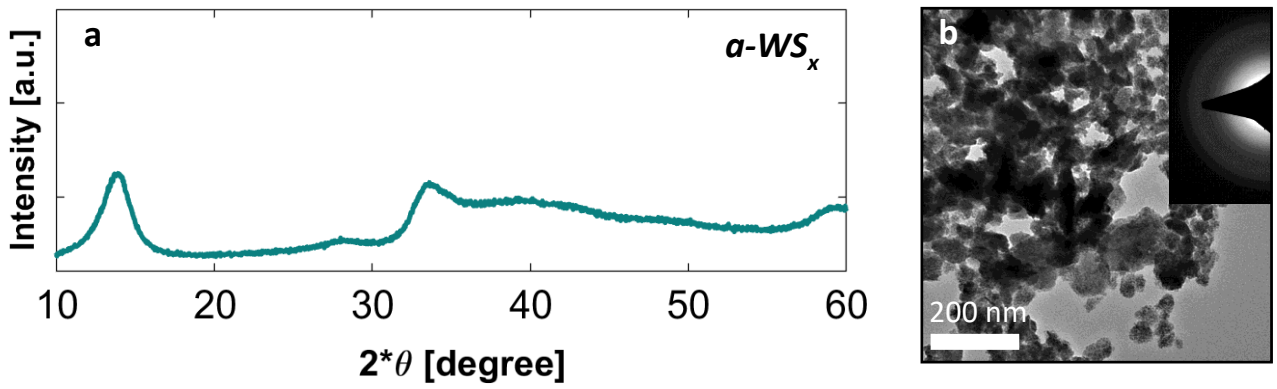

Fig. A-1. a) Powder X-ray diffraction (XRD) of a-WS_x displaying X-ray amorphous diffraction patterns. **b)** Transmission electron microscopy (TEM) images of a-WS_x with electron diffraction pattern shown in the inset. The disappearance of S_8 and *c*-WS_2 XRD peaks indicate the complete reaction of precursors in mechanochemical synthesis to form an amorphous metal sulfide.

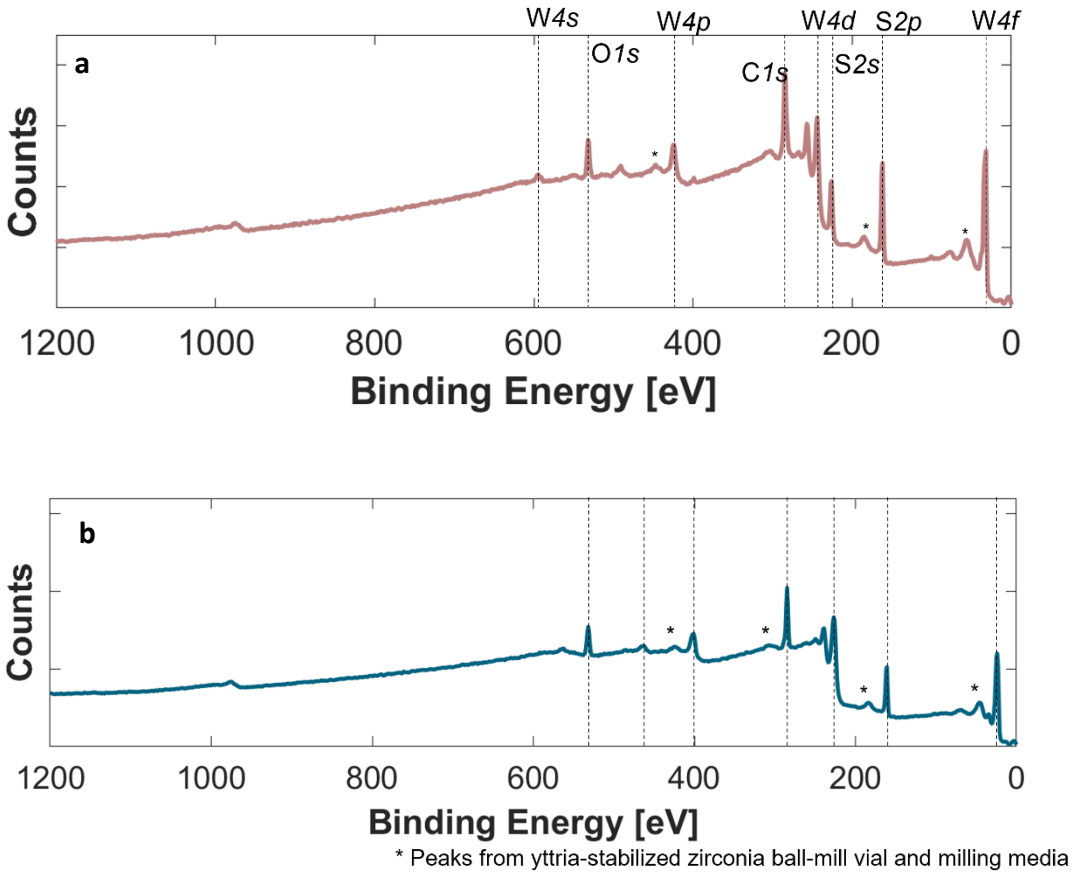

***Fig. A*-2.** X-ray photoelectron spectroscopy (XPS) survey spectra of **a)** a-WS_x and **b)** a-TaS_y used to quantify the surface composition of W:S 1:2.92 and Ta:S 1:1.91. Surface impurity peaks from the ball milling vail of ZrO_2 and Y_2O_3 are marked with an asterisk. Surface oxide species from sample transfer for XPS measurement resulted in transition metal: sulfur ratios slightly less than added experimentally.

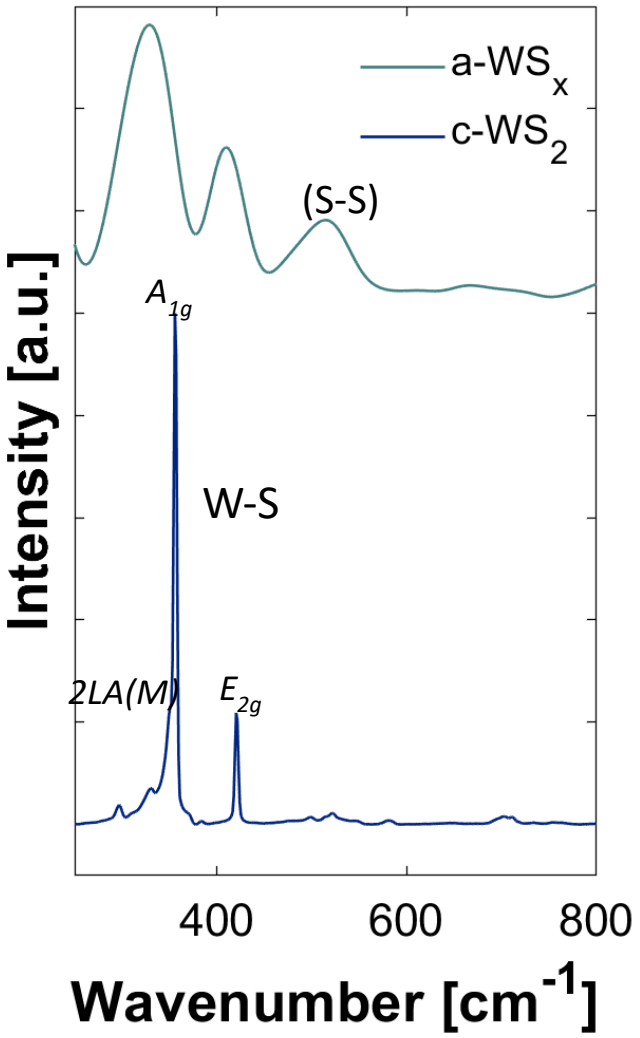

Fig. A-3. Raman spectroscopy of *a*-WS_x and c-WS_2 powders using a 785 nm laser. The Raman peaks characteristic of the LA(M) A_{1g} and E_{2g} modes of c-WS_2 were also present in the a-WS_x Raman spectrum, but more broad and diffuse compared with that of c-WS_2. This suggests local disorder in the amorphous material introduced by excess sulfur incorporation and amorphization.*(26),(27)* Due to the air sensitive nature of amorphous sulfides, the *a*-WS_x powder was sealed under a quartz window in an Ar-filled glove box for measurement.

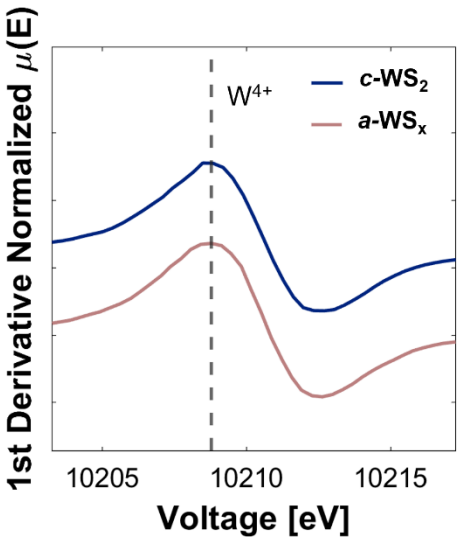

Fig. A-4. XANES spectra showing the normalized 1st derivative of crystalline WS_2 and *a*-WS_x indicating *a*-WS_x is in the same W^{4+} oxidation state as *c*-WS_2.

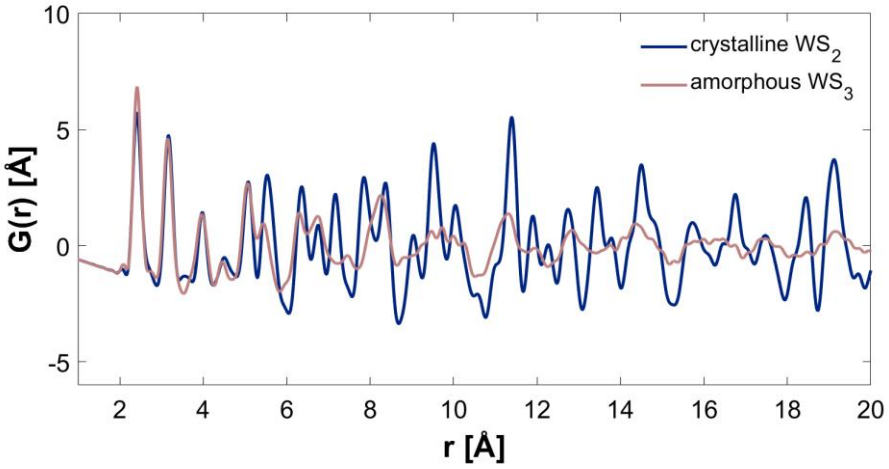

Fig. A-5. Neutron pair distribution function measurements of crystalline WS_2 and *a*-WS_x.

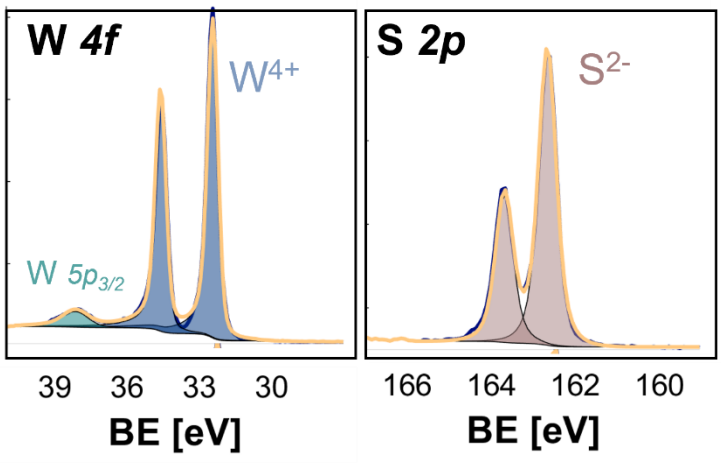

Fig. A-6. Detailed XPS scans of the W *4f* and S *2p* regions of crystalline WS_2 showing W in the 4+ state and S in the 2- state.

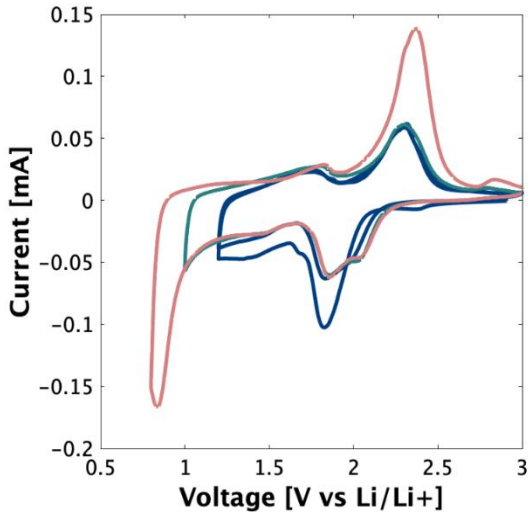

Fig. A-7. Cyclic voltammograms showing the first cycle window opening from 3 V vs Li^+/Li to progressively lower voltages in *a*-WS_x composite electrode coin-cell setups vs Li-metal at a sweep rate of 0.1 mV s^{-1}. The first cycle to 1.2 V shows the possible structure rearrangement at 1.8 V, also seen in galvanostatic cycling. Further lithiation to 0.8 V displays the conversion reaction to W^0 and Li_2S upon lithiation and the corresponding S_8 dissolution peak at 2.4 V vs Li^+/Li, commonly observed in literature.(*28*) Thus, a lower voltage limit of 1.0 V vs Li^+/Li was chosen for a-WS_x cycling.

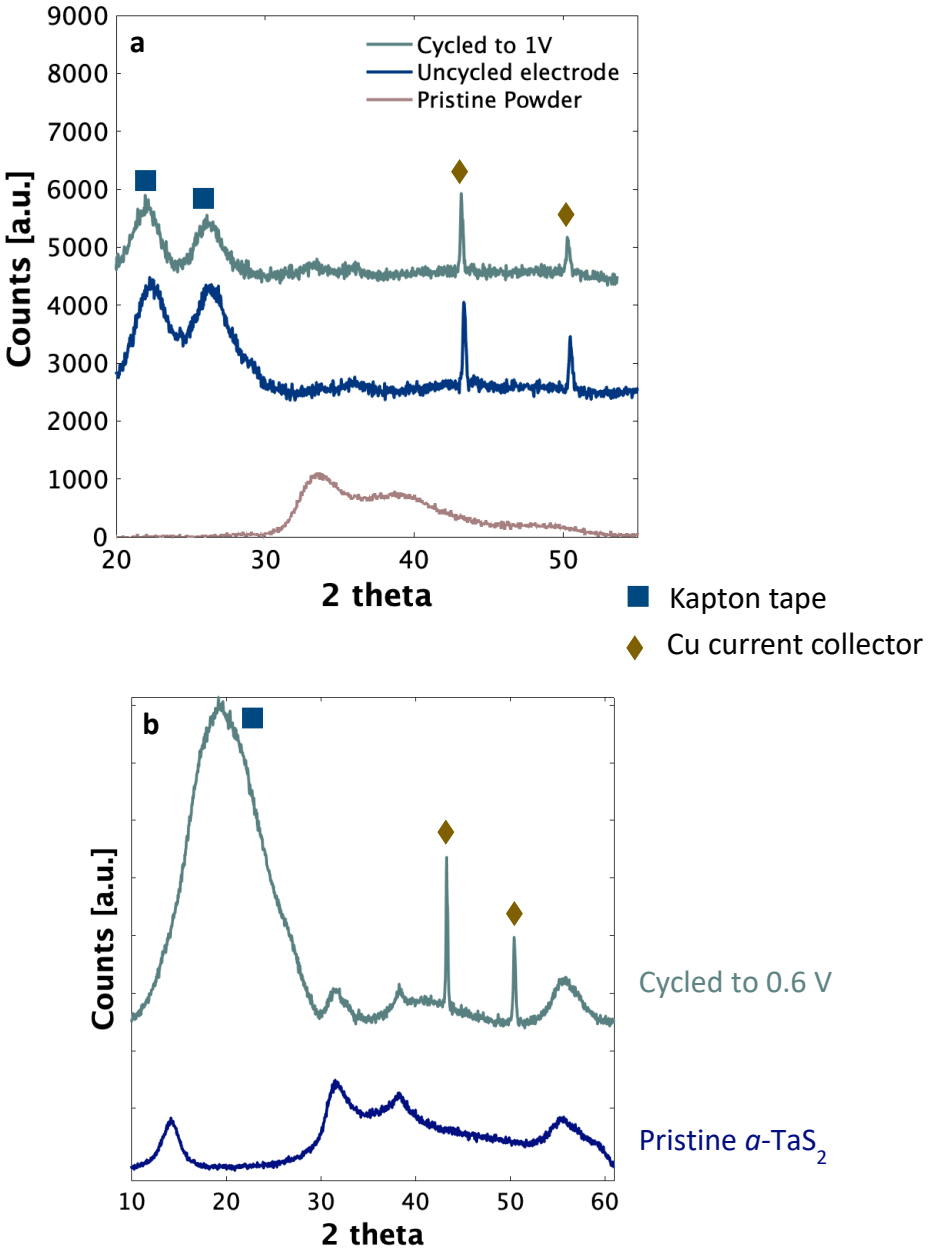

Fig. A-8. X-ray diffraction on ex-situ electrodes cycled at a C/5 rate to the lower voltage limit of 1.0 V vs Li+/Li for *a*-WS_x **(a)** and 0.6 V vs Li+/Li for *a*-TaS_y **(b)**. In both ex-situ electrodes, there were no new phases formed or the emergence of Li_2S peaks indicating that the conversion reaction to elemental metal and Li_2S was avoided.

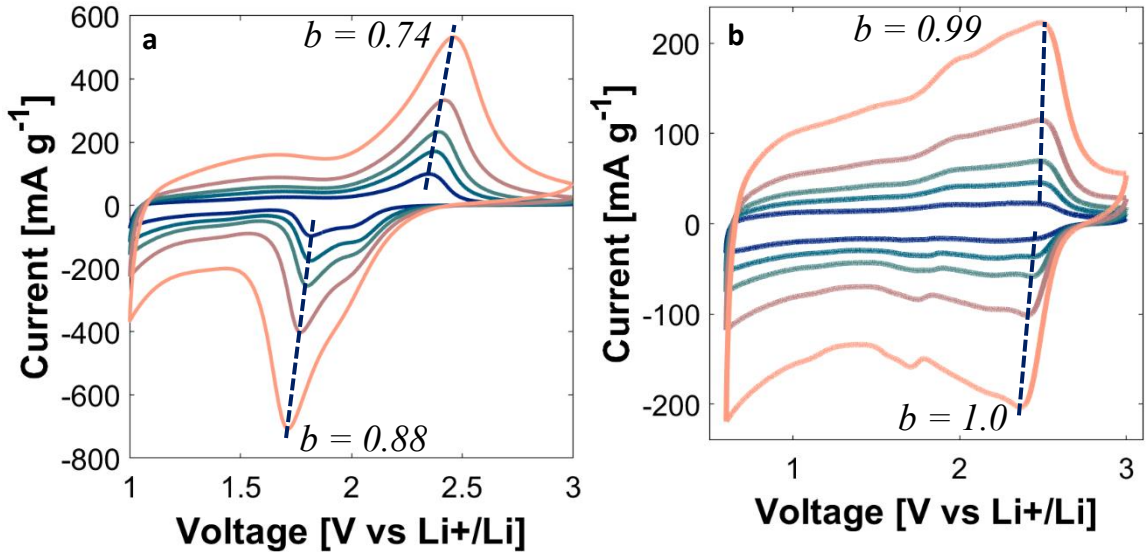

Fig. A-9. Cyclic voltammograms of **a)** *a*-WS_x and **b)** *a*-TaS_y at scan rates of 0.1, 0.2, 0.3, 0.5 and 1.0 mV s^{-1} with the calculated peak current b-values shown next to the corresponding peak.

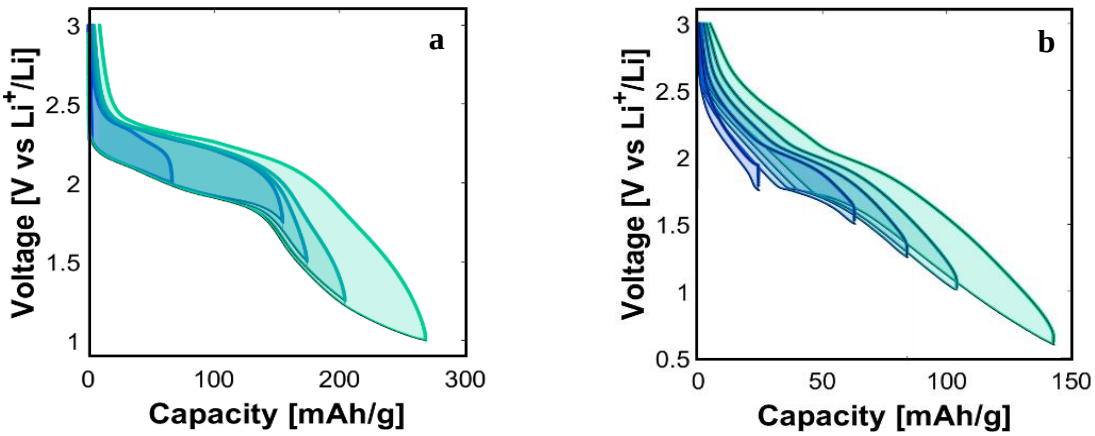

Fig. A-10. Galvanostatic window opening displaying the voltage hysteresis as a function of voltage window opening for **a)** *a*-WS_x from 3.0 – 1.0 V and **b)** a-TaS_y from 3.0 – 0.6 V vs Li^+/Li. The lack of a voltage region with significantly greater voltage hysteresis, as observed in some oxygen redox materials(22), suggests anionic redox is occurring throughout the voltage window instead of at a defined voltage.

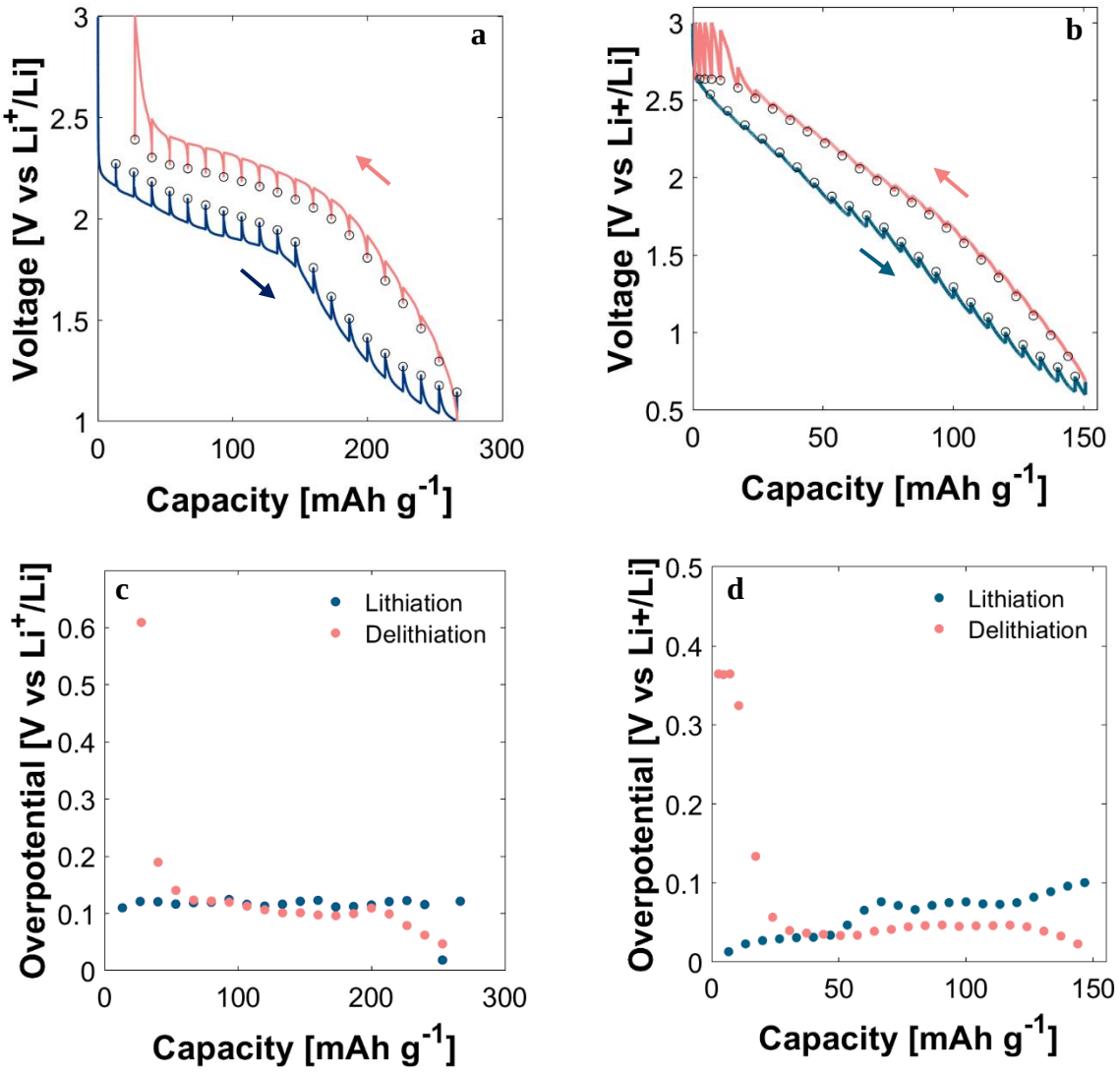

Fig. A-11. Galvanostatic intermittent titration technique (GITT) measurements on **a)** a-WS_x and **b)** a-TaS_y composite electrodes, both at a specific current of 0.4 A g^{-1} (a 0.13-C rate for a-WS_x and a 0.28C-rate for a-TaS_y) applied for 5 min followed by a 4-hour rest. The corresponding overpotential plots calculated from **c)** a-WS_x and **d)** a-TaS_y GITT measurement highlight the low polarization overpotential compared with other anionic redox electrode materials.*(29, 30)* Throughout the voltage window, a-TaS_y GITT measurements indicated that the overpotential was relatively constant at ~50 mV, highlighting the improved polarization and kinetics compared with those of a-WS_x.

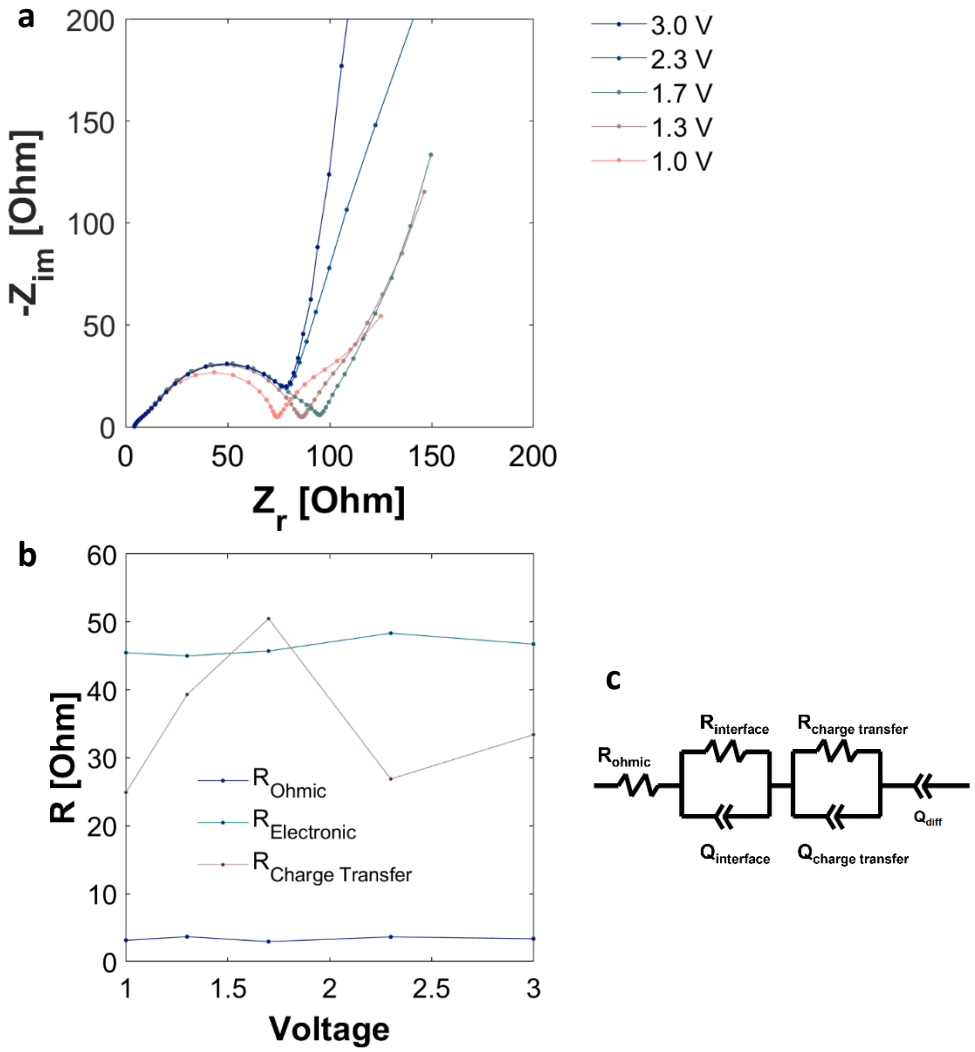

Fig. A-12. a) In-situ electrochemical impedance spectroscopy (EIS) during the 2nd lithiation of *a*-WS_x from 1 MHz to 10 mHz frequency. **b)** The ohmic resistance R_{ohmic}, electronic resistance $R_{electronic}$, and charge transfer resistance $R_{charge\ transfer}$ were calculated by fitting the EIS spectra to the circuit model shown in **(c)** consisting of a resistor, two RC elements, and a constant phase element. The circuit modeling demonstrates the negligible change in R_{ohmic} and the relatively small change $R_{charge\ transfer}$ throughout lithiation compared with oxygen redox, leading to superior kinetic performance.

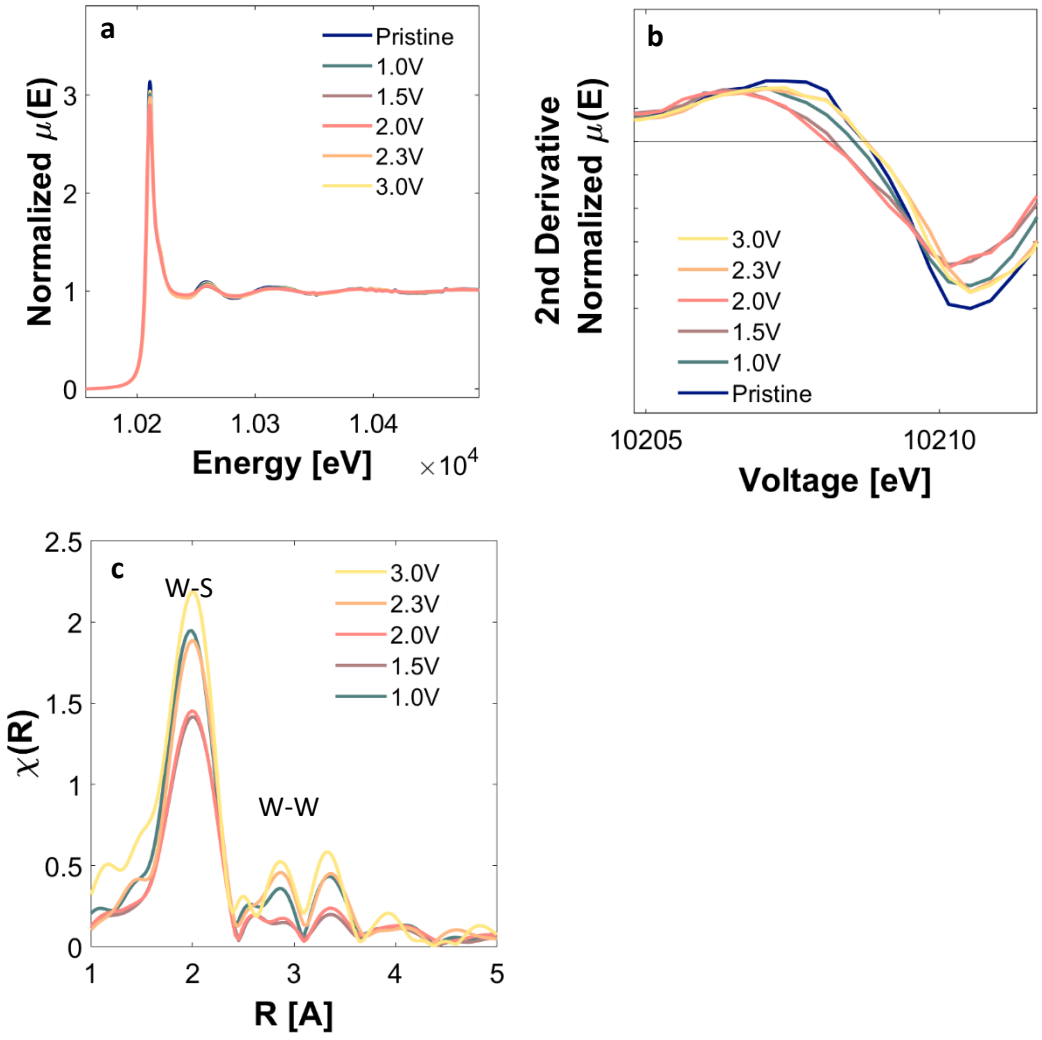

Fig. A-13. W L_{III}-edge XAS results on *a*-WS_x showing the XANES region of each composite electrode during delithiation from 1 to 3 V vs Li+/Li and the pristine *a*-WS_x powder displayed as **(a)** the white line spectrum and as **(b)** the normalized 2nd derivative. The y = 0 line is shown in black. **c)** The EXAFS spectra for each *a*-WS_x composite electrode during delithiation from 1 to 5 Å displaying the W-S and W-W atom distances in the first two peaks, respectively.

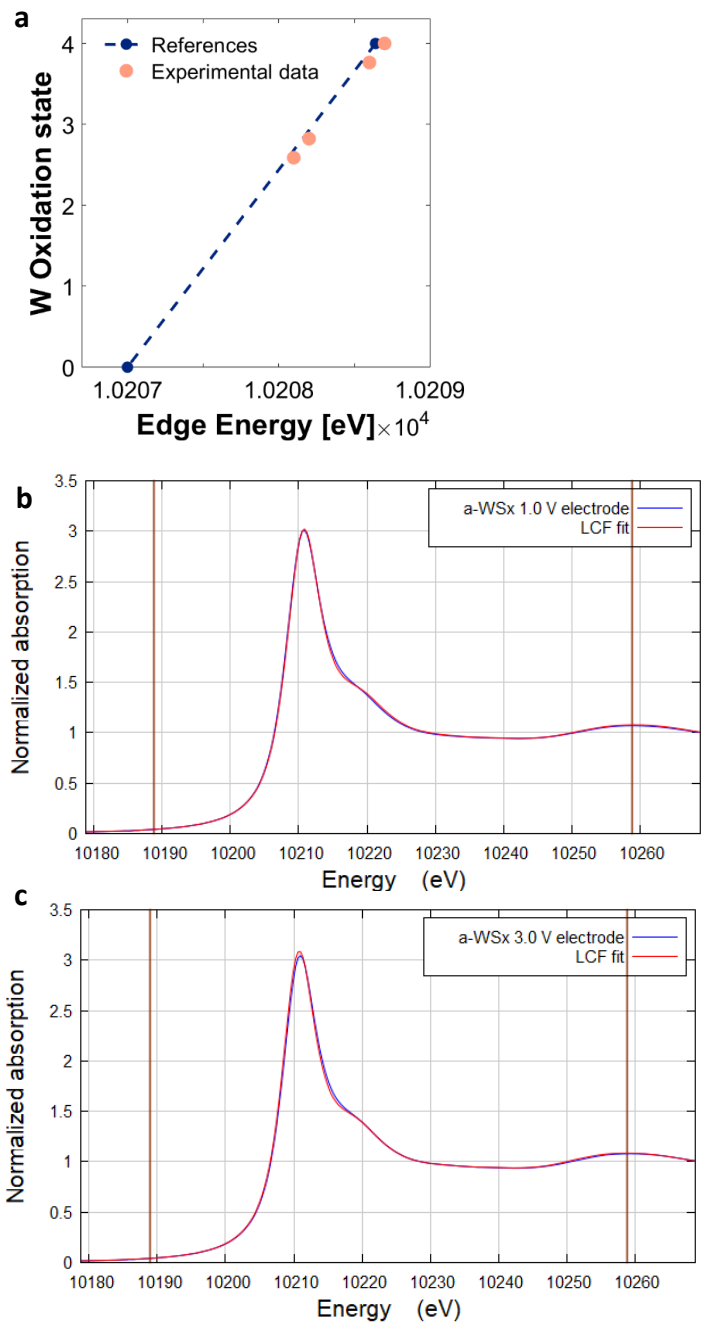

Fig. A-14. a) Extrapolation of XANES edge energy of ex-situ electrodes from tungsten foil (W^0) to crystalline WS_2 (W^{4+}) based on the 2nd derivative y = 0 crossing shown in Fig. S12b. **b-c)** Example linear combination fittings (LCF) of the fully lithiated 1.0 V electrode **(b)** and fully delithiated 3.0 V electrode **(c)**. The LCF fitting results of oxidation state, done in Athena software, and comparison to extrapolation results are shown in **Table A-1**.

Table A-1. W oxidation states from W L_{III}-edge XAS calculated from extrapolation of 2nd derivative (**Fig. A-13b, Fig. A-14a**) and from linear combination fittings (**Fig. A-14 b-c**).

Ex-situ electrode voltage [V vs Li^+/Li]	Number of Li inserted [mol]	Extrapolation Fitting	Linear Combination Fitting			
		W oxidation state	W oxidation state	a-WS3 powder weight (error)	W-foil weight (error)	R-Factor
1.0	3.1	3.8	3.5	0.88 (0.005)	0.12 (0.005)	0.0004
1.5	2.8	2.8	2.9	0.73 (0.008)	0.27 (0.008)	0.0011
2.0	2.1	2.6	2.9	0.74 (0.012)	0.26 (0.012)	0.0023
2.3	0.7	4	3.6	0.91 (0.013)	0.09 (0.013)	0.0030
3.0	0	4	3.8	0.95 (0.009)	0.05 (0.009)	0.0012

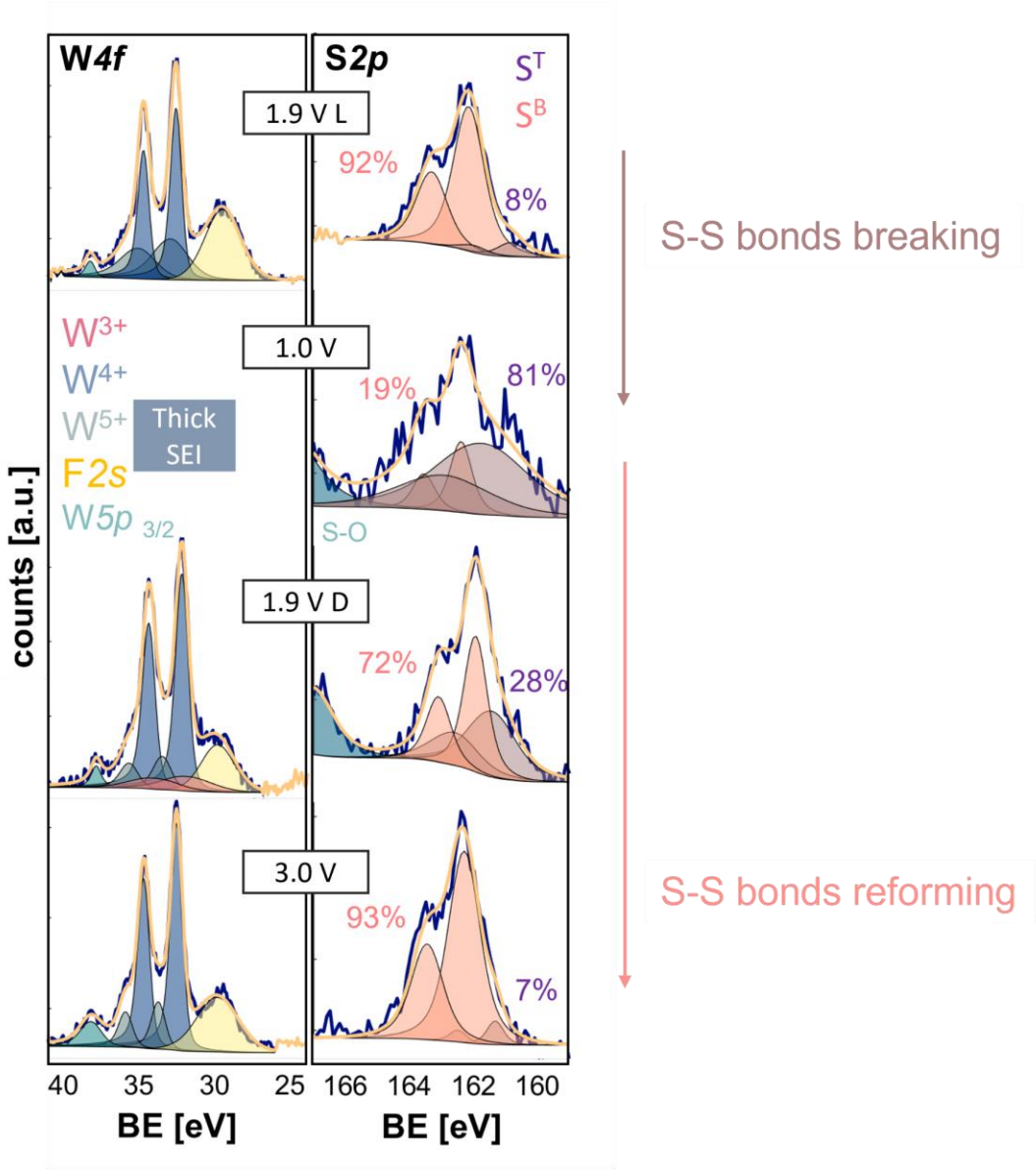

Fig. A-15. X-ray photoelectron spectroscopy detailed scans of *a*-WS_x ex-situ electrodes in the W *4f* and S *2p* regions. Ex situ electrodes were cycled to various degrees: 1.9 V during lithiation (1.9 L), fully lithiated to 1.0 V, delithiated to 1.9 V (1.9 D) and fully delithiated to 3.0 V. Although the W *4f* region overlaps with the F *2s* peaks from PVDF binder and $LiPF_6$ electrolyte complicating the XPS fitting, the electrodes can still be fit with various doublets indicating the W^{3+}, W^{4+}, and W^{5+} states. The S *2p* regions demonstrate an increase in terminal sulfur S^T bonds upon lithiation to 1.0 V and an increase in the bridging sulfur S^B bonds upon delithiation to 3.0 V.

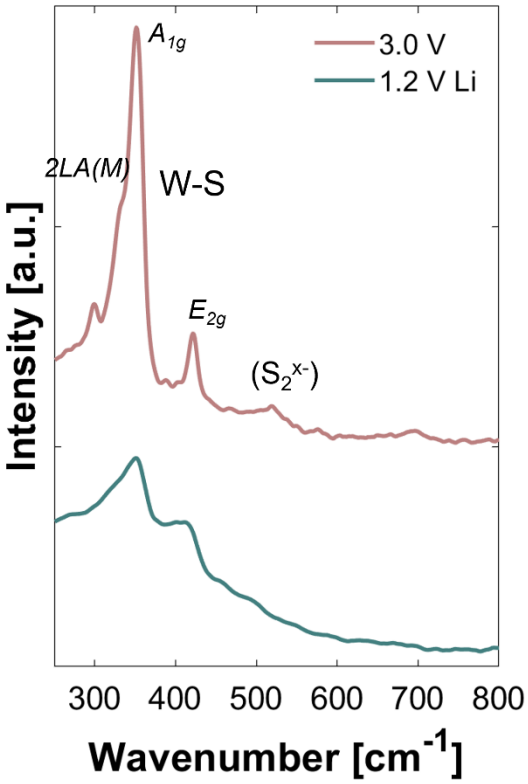

Fig. A-16. Raman spectroscopy on ex-situ *a*-WS_x composite electrodes in the fully delithiated (3.0 V) and almost fully lithiated (1.2 V Li) state taken on a 785 nm laser and sealed under quartz windows for air-free measurements. An electrode lithiated to 1.2 V instead of 1.0 V vs Li+/Li was measured to avoid large SEI effects on the Raman spectrum at lower voltages. The Raman spectra also confirm the lack of crystalline Li_2S or S_8 formation, which would be observed by peaks at 380 and 475, respectively.*(31),(32)*

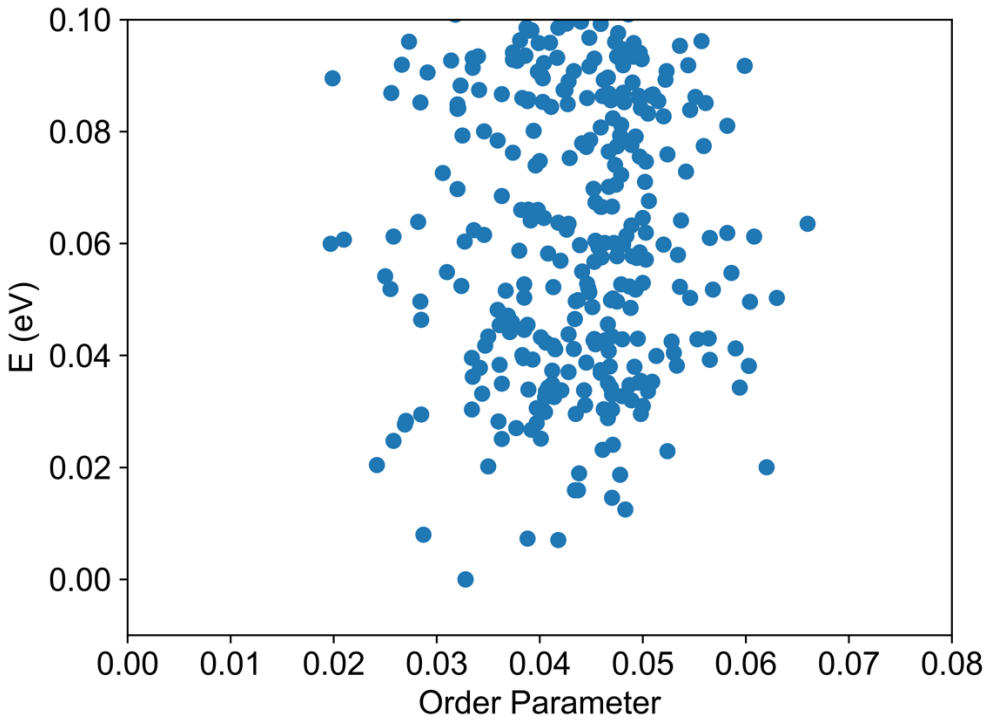

Fig. A-17. Local minima visited within 0.1 eV energy window with respect to the lowest energy structure, agreeing with the amorphous feature. The Steinhardt-type order parameter was used to further distinguish the structures visited on the global potential energy surface, shown as the x axis.

Fig. A-2. Structural properties of the predicted lowest energy structure of $Li_xW_3S_{10}$ shown in **Fig. 5-8.**

W_3S_{10}		**$Li_2W_3S_{10}$**		**$Li_5W_3S_{10}$**		**$Li_7W_3S_{10}$**		**$Li_9W_3S_{10}$**	
Space Group									
P 1		P 1		P 1		P 1		P 1	
Lattice constant (Å)									
a	11.09580	a	11.29460	a	12.36770	a	13.32020	a	13.56770
b	5.45396	b	5.47000	b	5.40037	b	5.51995	b	8.21728
c	5.49657	c	5.41745	c	5.40419	c	5.50720	c	3.42316
Angles (°)									
α	119.6790	α	60.3704	α	62.2846	α	119.8390	α	78.1747
β	90.7384	β	88.3963	β	94.9738	β	90.6456	β	86.0495
γ	88.2480	γ	82.2360	γ	90.1740	γ	100.8550	γ	104.8100
Unit cell volume ($Å^3$)									
V	288.8578	V	287.9730	V	318.0470	V	342.3310	V	358.1590

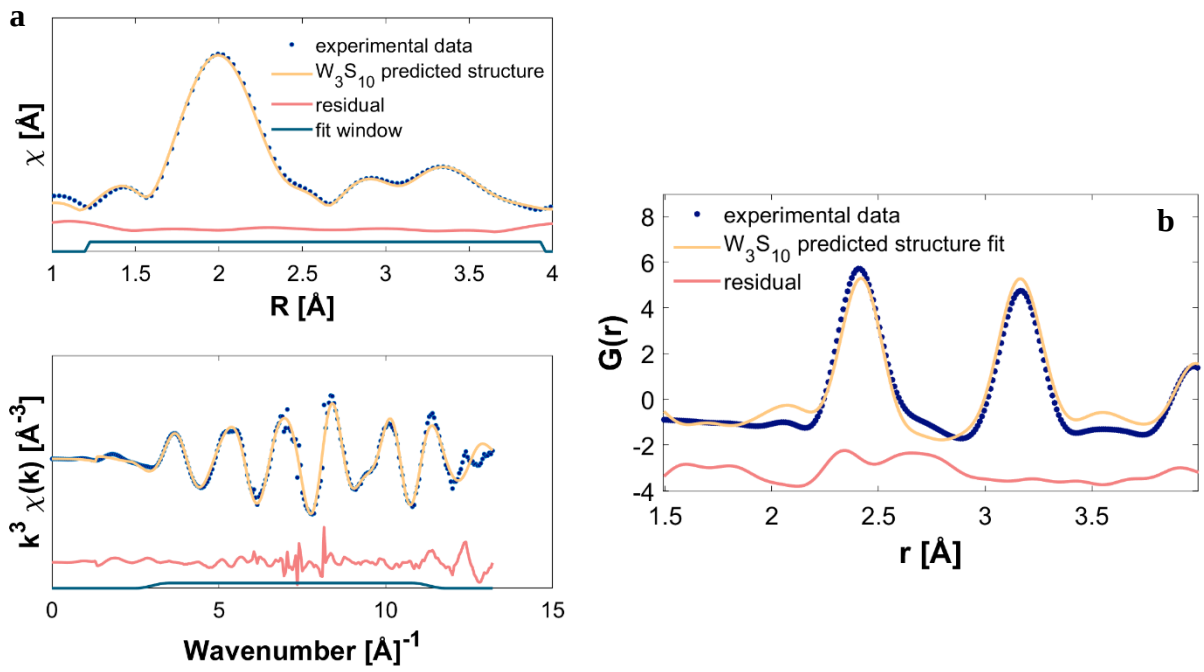

Fig. A-18. Pristine W_3S_{10} powder a) EXAFS and b) neutron PDF (nPDF) fit to the calculated lowest energy structure of W_3S_{10}. EXAFS fittings were done in Artemis and nPDF fittings were done in PDFgui.(*2, 3*) It is worth mentioning that for the delithiated W_3S_{10} phase, the atomic configuration around W atoms in the obtained layer structure fit extremely well to the proposed structure from ~1.5 to 4 Å in the EXAFS spectrum of the W L_{III}-edge **(*Fig. A*-18a and Fig. 5-8c**).

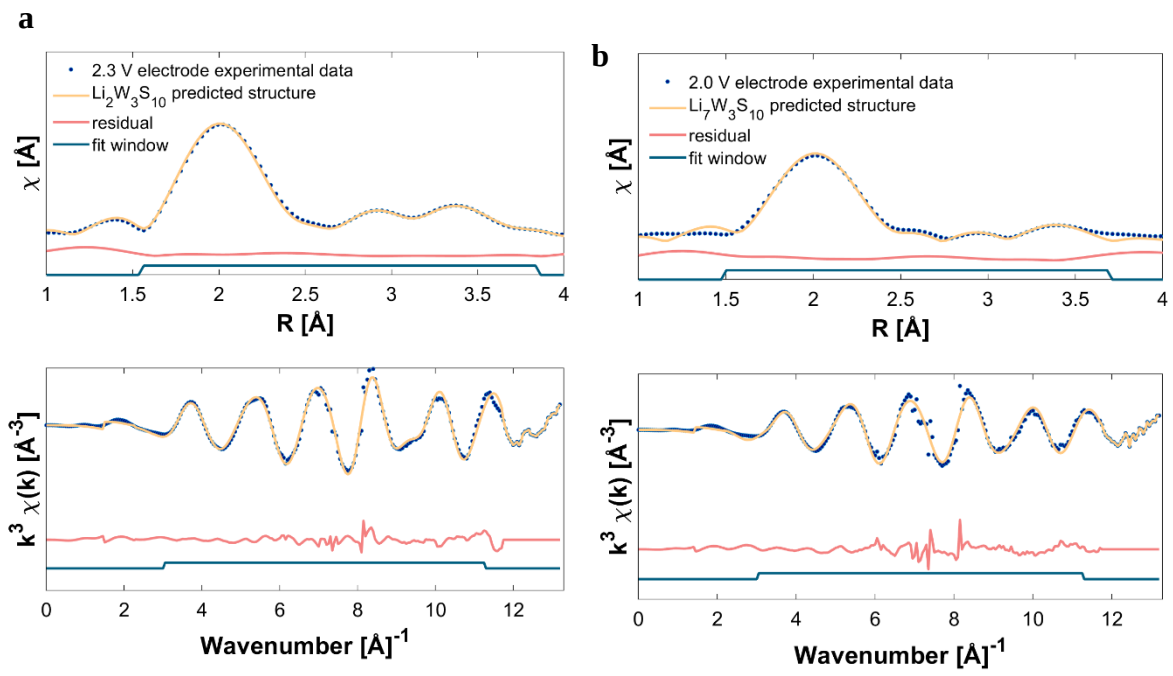

Fig. A-19. EXAFS fittings of ex-situ electrodes fit to predicted lithiated structures. **a)** $Li_2W_3S_{10}$ predicted structure fit to the EXAFS spectrum of an ex-situ electrode delithiated to 2.3V vs Li^+/Li. **b)** $Li_7W_3S_{10}$ predicted structure fit to the EXAFS spectrum of an ex-situ electrode delithiated to 2.0V vs Li^+/Li.

Table A-3. EXAFS fitting parameters for W_3S_{10}.

	Bond	**N**	**S_0^2**	**σ^2 [Å^2]**	**e_0 [eV]**	**ΔR [Å]**	**R_{eff} [Å]**	**R [Å]**	**R-factor**
W_3S_{10} fit to pristine *a*-WS_x powder fit to	S3.1	6	0.883	0.00342	6.825	-0.00541	2.4124	2.40699	0.0025
	W2.1	5	0.883	0.00737	2.17	-0.03038	3.1626	3.13222	
	S9.2	4	0.883	0.00348	0.744	-0.10951	3.9918	3.88229	
	Bond	**N**	**S_0^2**	**σ^2 [Å^2]**	**e_0 [eV]**	**ΔR [Å]**	**R_{eff} [Å]**	**R [Å]**	**R-factor**
$Li_0W_3S_{10}$ fit to 3.0 V delithiated electrode	S3.1	6	0.814	0.0036	7.17	-0.00953	2.4124	2.40287	0.0023
	W2.1	5	0.814	0.00743	2.016	-0.02245	3.1626	3.14015	
	S9.2	4	0.814	0.003	1.284	-0.1015	3.9918	3.8903	
	Bond	**N**	**S_0^2**	**σ^2 [Å^2]**	**e_0 [eV]**	**ΔR [Å]**	**R_{eff} [Å]**	**R [Å]**	**R-factor**
$Li_2W_3S_{10}$ fit to 2.3 V on delithiation electrode	S2.1	6	0.704	0.00382	8.337	0.00468	2.4088	2.41348	0.0012
	W3.1	4	0.704	0.00448	-1.519	-0.02513	3.1388	3.11367	
	W2.3	2	0.704	0.00129	19.638	0.44409	3.1691	3.61319	
	S2.2	3	0.704	0.00538	-2.668	-0.15106	3.9445	3.79344	
	S9.2	3	0.704	0.02779	12.587	0.27565	3.9844	4.26005	
	Bond	**N**	**S_0^2**	**σ^2 [Å^2]**	**e_0 [eV]**	**ΔR [Å]**	**R_{eff} [Å]**	**R [Å]**	**R-factor**
$Li_7W_3S_{10}$ fit to 2.0 V on delithiation electrode	S9.1	6	0.594	0.00456	7.075	0.0014	2.4163	2.4177	0.0087
	W2.1	5	0.594	0.01337	-8.803	-0.11131	3.1828	3.07149	
	S9.2	6	0.594	0.0141	-1.417	-0.12092	3.9986	3.87768	
	Bond	**N**	**S_0^2**	**σ^2 [Å^2]**	**e_0 [eV]**	**ΔR [Å]**	**R_{eff} [Å]**	**R [Å]**	**R-factor**
$Li_9W_3S_{10}$ fit to 0.6 V lithiated electrode	S1.1	2	0.721	0.0011	4.946	-0.08172	2.3856	2.30388	0.0058
	S9.1	4	0.721	0.00031	4.934	-0.01541	2.4385	2.42309	
	W3.1	3	0.721	0.00468	-2.003	-0.10465	3.2136	3.10895	
	W2.2	1	0.721	0.00449	19.796	0.42744	3.2444	3.67184	
	W1.1	2	0.721	0.00227	19.451	0.15844	3.4232	3.58164	
	S2.2	2	0.721	0.00819	-11.742	-0.45152	4.1472	3.69568	

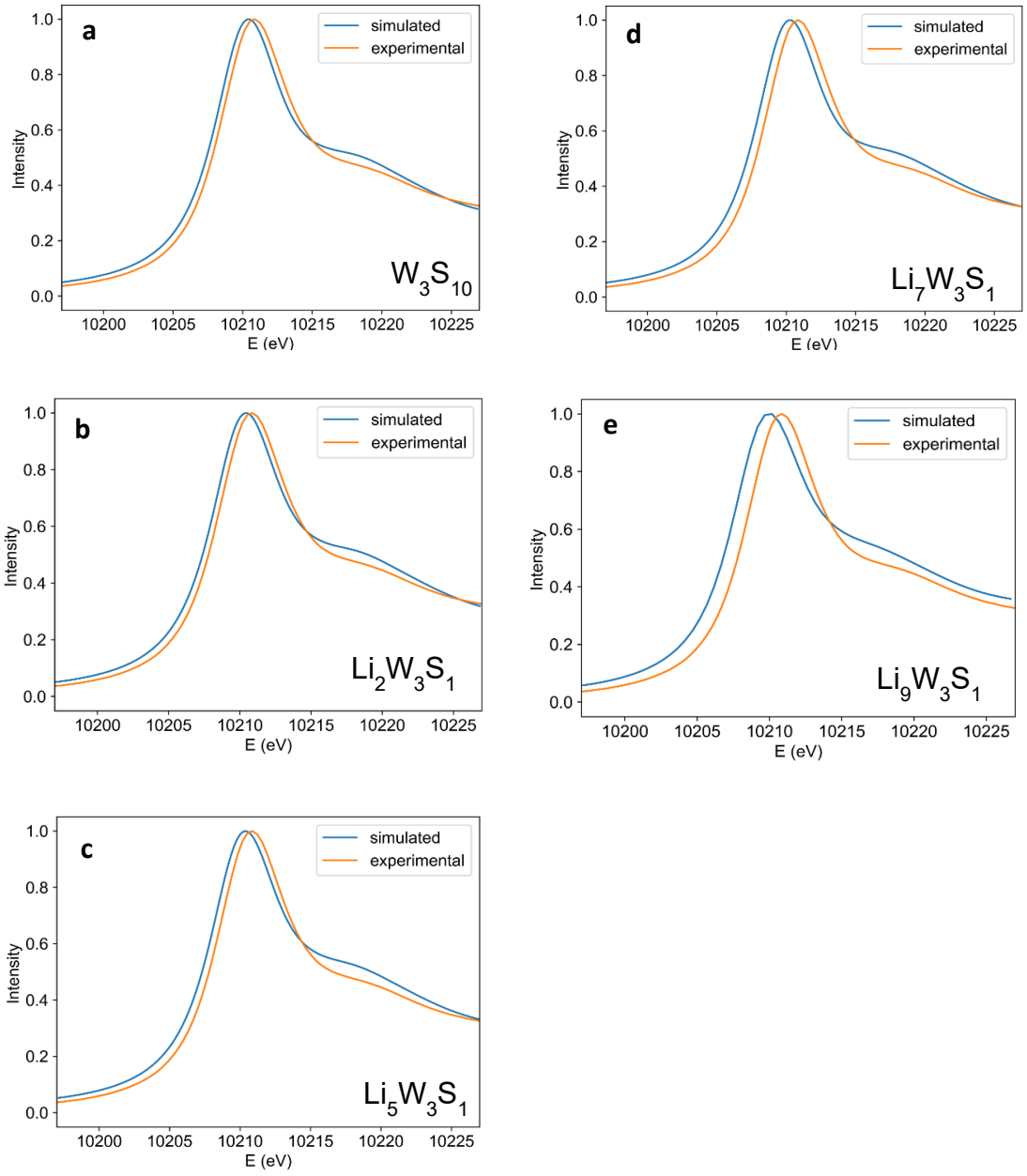

***Fig. A*-20.** XANES calculations of simulated structures at various degrees of lithiation compared with experimental results from W L_{III}-edge XAS measurements for $Li_xW_3S_{10}$ x = 0, 2, 5, 7, and 9.

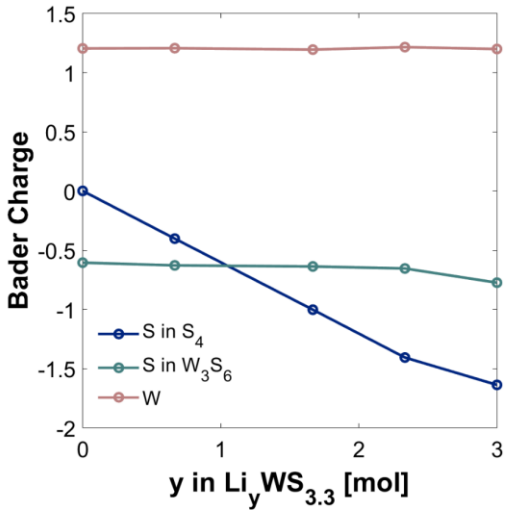

***Fig. A*-21.** Average Bader charge values of W and S atoms in W_3S_6 layers and S atoms in S_4 chains calculated for the structures shown in **Fig. 5-8b**. One should first note that W has a high electronegativity, 2.36, only 0.22 less than S, so that the electronic structure has an iono-covalent character, with fractional charges. Bader charge analysis suggests that the first 8 electrons are accommodated by S and the 9th electron led to further reduction of the partially negatively charged S atoms in the W_3S_6 layer

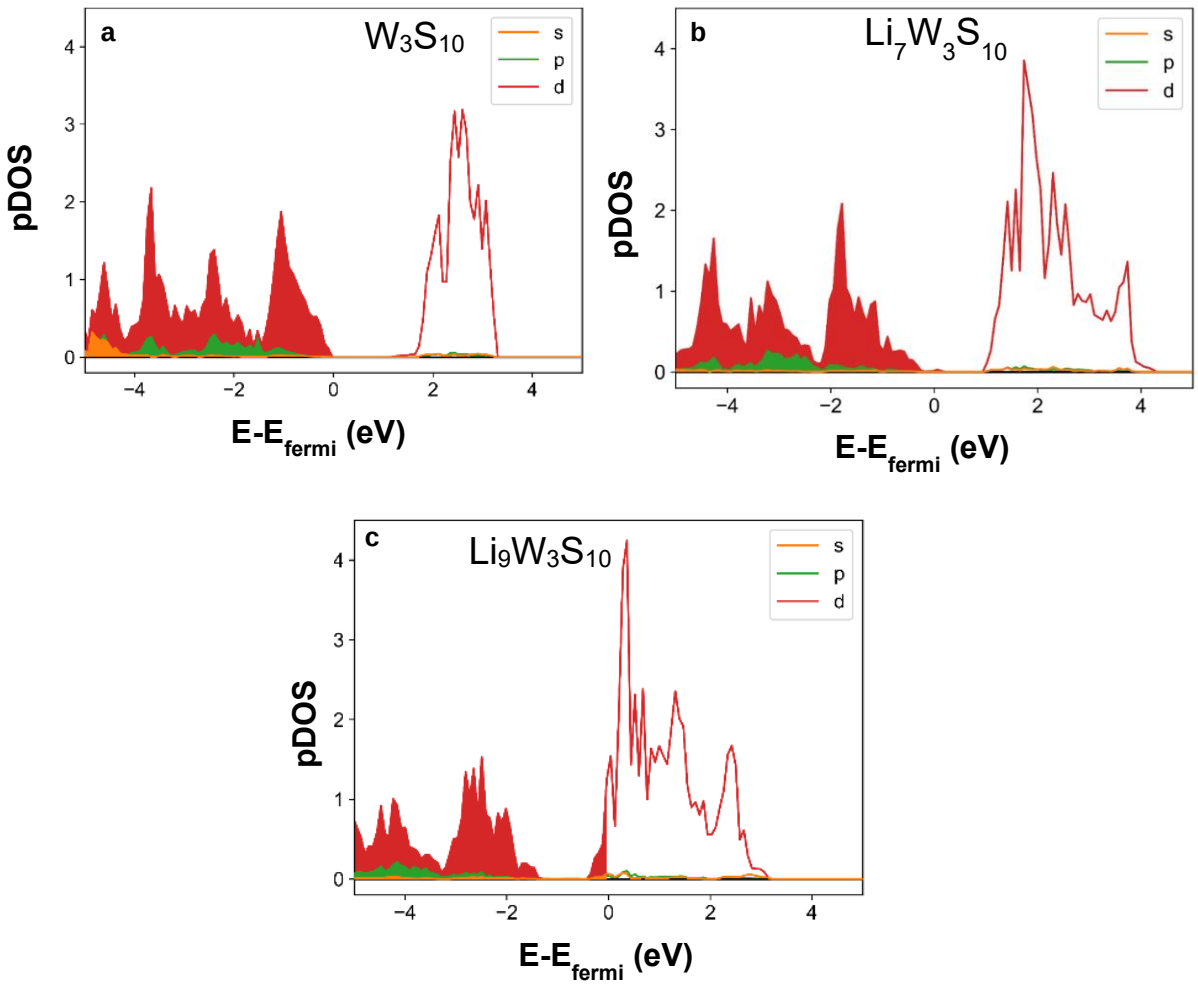

Fig. A*-22.** Projected density of states (pDOS) on W atoms in the **a)** nonlithiated W_3S_{10} structure **b)** the intermediate lithiated $Li_7W_3S_{10}$, displaying no major change in the W band structure compared with the W_3S_{10} delithiated structure and **c)** the fully lithiated $Li_9W_3S_{10}$ structure. Compared with Bader charge calculations (Fig. A*-21**), the two approaches agreed that the first 8 electrons were accommodated by the neutral S_4 chain reduction and the W_3S_6 layer accommodated the 9th electron. pDOS results suggest that the 9th electron reduced the W atoms in the W_3S_6 layer (c). In any case, the reduction level of the W_3S_6 unit upon the lithiation process is very modest, with only one electron per 3 transition metals, and a fraction of this electron goes on the S atoms.

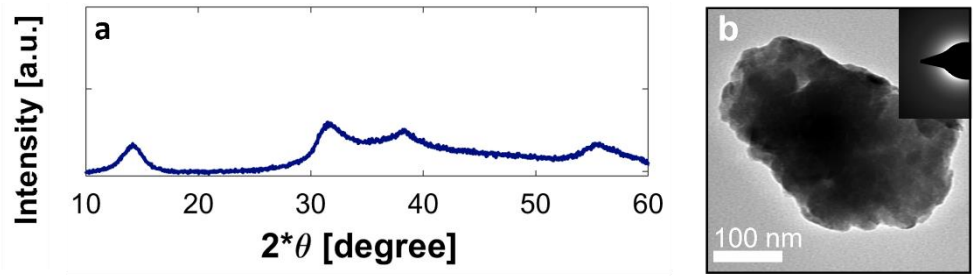

***Fig. A*-23.** The *a*-WS_x XRD pattern **(a)** displays an X-ray amorphous structure and **(b)** *a*-WS_x TEM imaging shows ~200-300 nm particles with an amorphous electron diffraction pattern (shown in the inset).

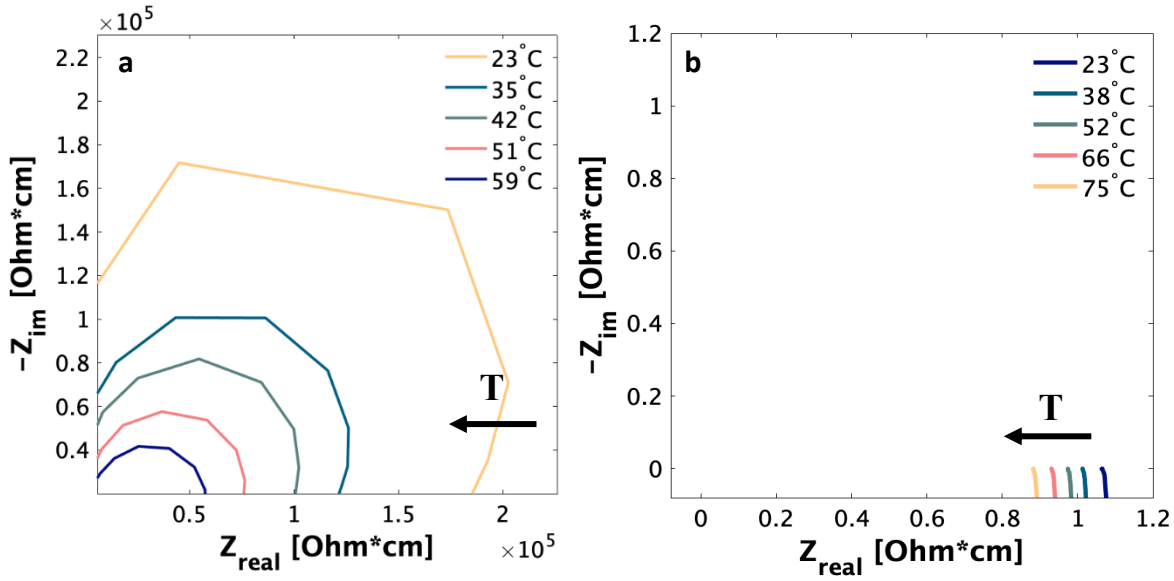

Fig. A-24. Electrochemical impedance spectroscopy (EIS) measurements on pristine **a)** *a*-WS_x and **b)** *a*-TaS_y as a function of temperature. Powders were dry pressed in 1.3 cm diameter die at pressure of 50 bar resulting 0.11 and 0.23 cm thick pellets for *a*-WS_x and *a*-TaS_y, respectively. The high frequency arc in (a) is due to the experimental setup; only the x-intercept is used for analysis.

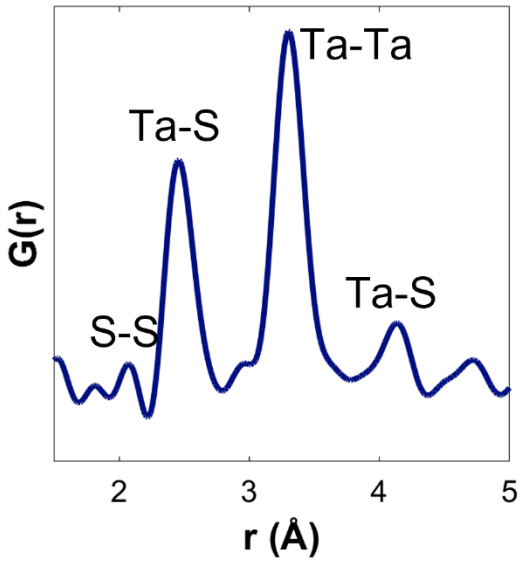

Fig. A-25. X-ray pair distribution function of *a*-TaS_y powder displaying S-S dimers at 2.08 Å and Ta-S and Ta-Ta atoms at distances which correspond to the neutron PDF spectrum (**Fig. 5-9c**).

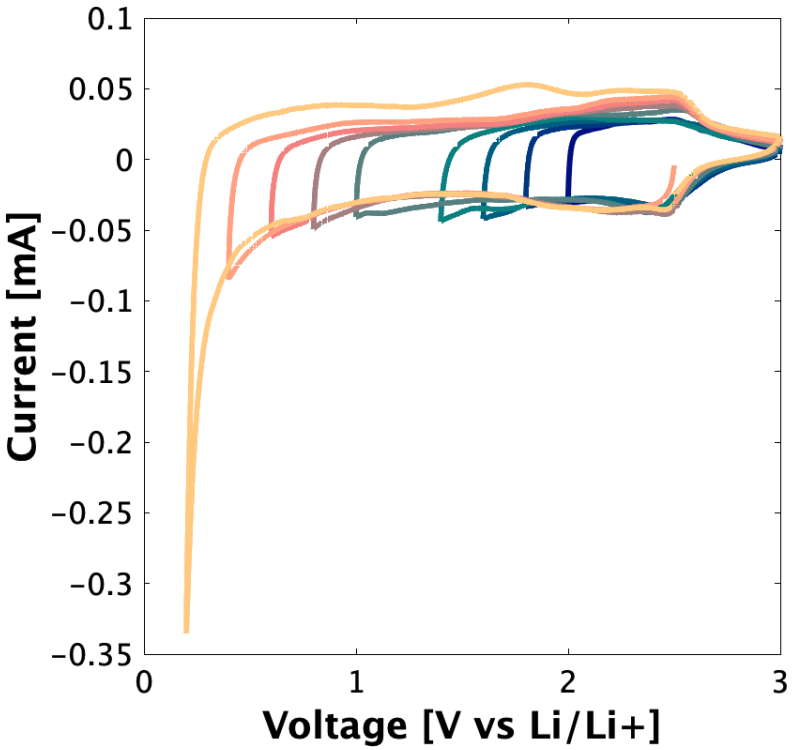

***Fig. A*-26.** Cyclic voltammetry voltage window opening of a-TaS_y composite electrode in a half-cell experiment vs Li-metal from 3.0 V to 0.2 V vs Li+/Li, highlighting the conversion to Ta^0 and Li_2S at 0.4 V Li+/Li. Thus, opening the window from 3 V to a lower voltage limit of 0.6 V avoided the conversion reaction during lithiation.

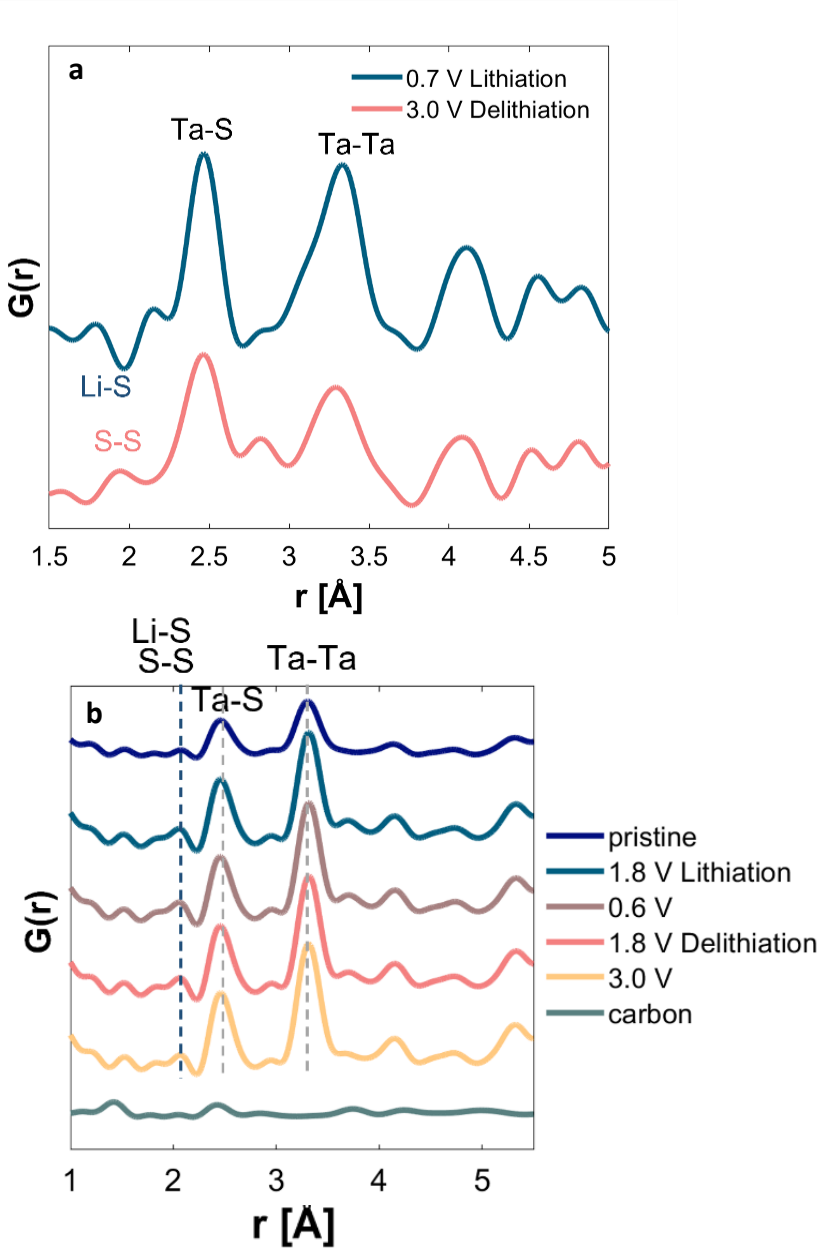

***Fig. A*-27. a)** Neutron pair distribution function (nPDF) analysis of composite a-TaS_y electrodes lithiated to 0.7 V vs Li^+/Li and delithiated to 3.0 V vs Li^+/Li displaying the negative correlation peak of Li-S upon lithiation and positive correlation. **b)** X-ray pair distribution function (xPDF) analysis of pristine and ex-situ electrodes cycled to various degrees of lithiation and delithiation displaying similar spectra regardless of the degree of lithiation due to the positive scattering lengths of both S and Li in xPDF. All electrodes for PDF were cycled in 2-electrode Swagelok setups vs Li-metal with 1M $LiPF_6$ EC:DMC 1:1 electrolyte at a specific current of 0.25 A g^{-1} and a mass loading of 15-20 mg cm^{-2}.

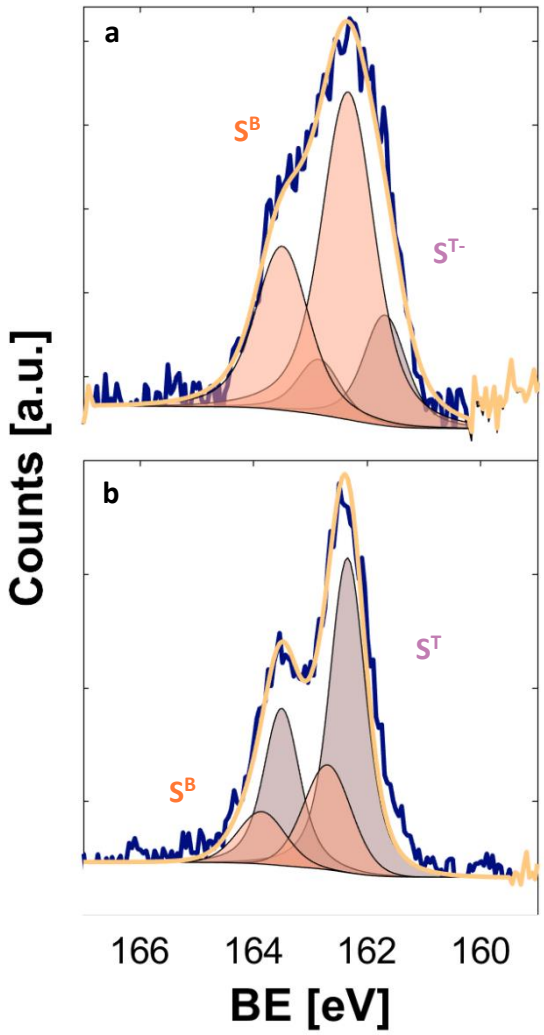

Fig. A-28. Detailed XPS scans in the S *2p* region of ex-situ *a*-TaS_y composite electrodes in the **a)** fully delithiated state at 3.0 V and **b)** partially delithiated to 1.8 V vs Li^+/Li displaying the change in mixed anion valence state during cycling. In the fully delithiated electrode **(a)** the majority of surface sulfur consists of oxidized, bridging sulfur bonds while the partially delithiated electrode **(b)** is mostly terminal in the reduced S^{2-} state.

Table A-4. Structural properties of the predicted lowest energy structure of $Li_xTa_4S_8$ shown in **Fig. 5-10.**

Ta_4S_8		**$Li_3Ta_4S_8$**		**$Li_6Ta_4S_8$**	
Space Group					
P 1		P 1		P 1	
Lattice constant (Å)					
a	12.98810	a	13.24810	a	13.47600
b	5.70561	b	5.64026	b	5.89903
c	3.25369	c	3.31963	c	3.40660
Angles (°)					
α	90.2080	α	90.0295	α	89.9983
β	95.7292	β	90.8680	β	90.0559
γ	99.2315	γ	89.1052	γ	98.9061
Unit cell volume ($Å^3$)					
V	236.7557	V	247.9931	V	267.5436

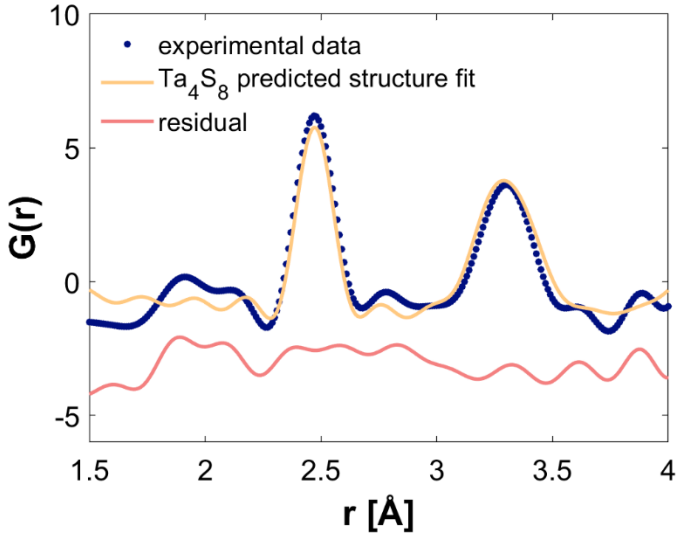

***Fig. A*-29.** Neutron PDF fitting of pristine *a*-TaS_y powder to the simulated Ta_4S_8 structure (**Table A-3**). Fitting was performed in PDFgui software.

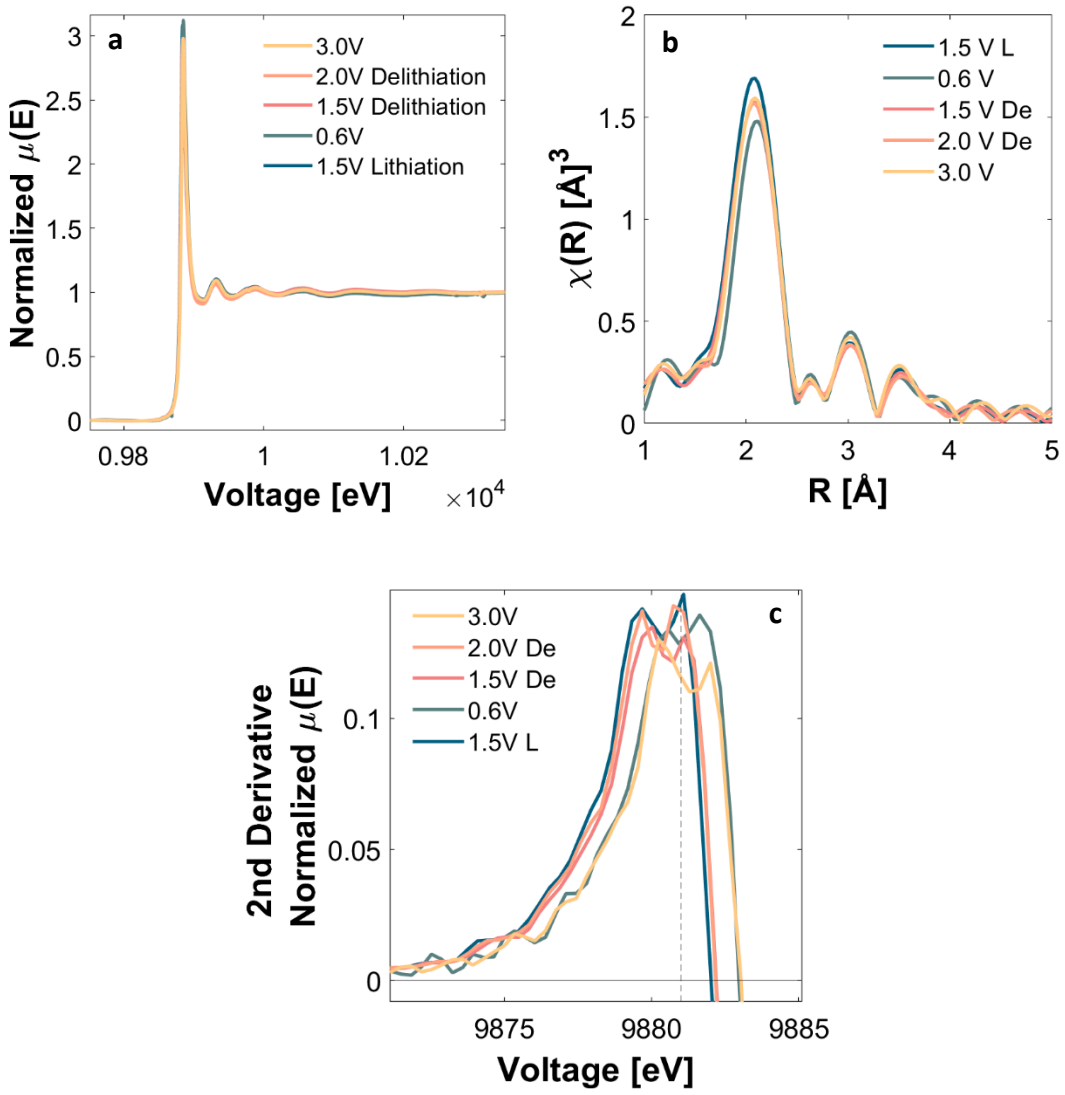

***Fig. A*-30.** X-ray absorption spectroscopy at the Ta L_{III}-edge displaying **a)** the white line spectra, **b)** the EXAFS spectra and **c)** the zero-point crossing of the 2nd derivative of the white line spectra for ex-situ electrodes cycled to 3.0 V, 2.0 V and 1.5 V on delithiation (De), 1.5 V on lithiation (L) and 0.6 V. Data processing was performed in Athena.

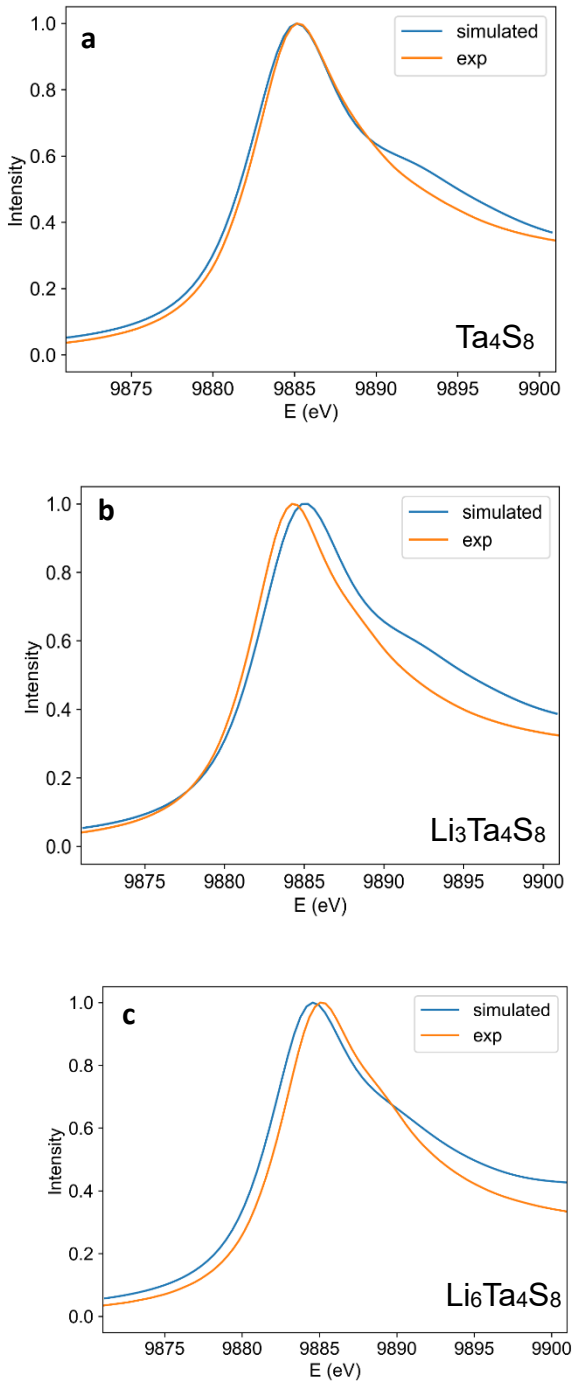

***Fig. A*-31.** XANES simulations of $Li_xTa_4S_8$ for x = 0, 3, and 6 compared with the experimental results from Ta L_{III}-edge XAS measurements.

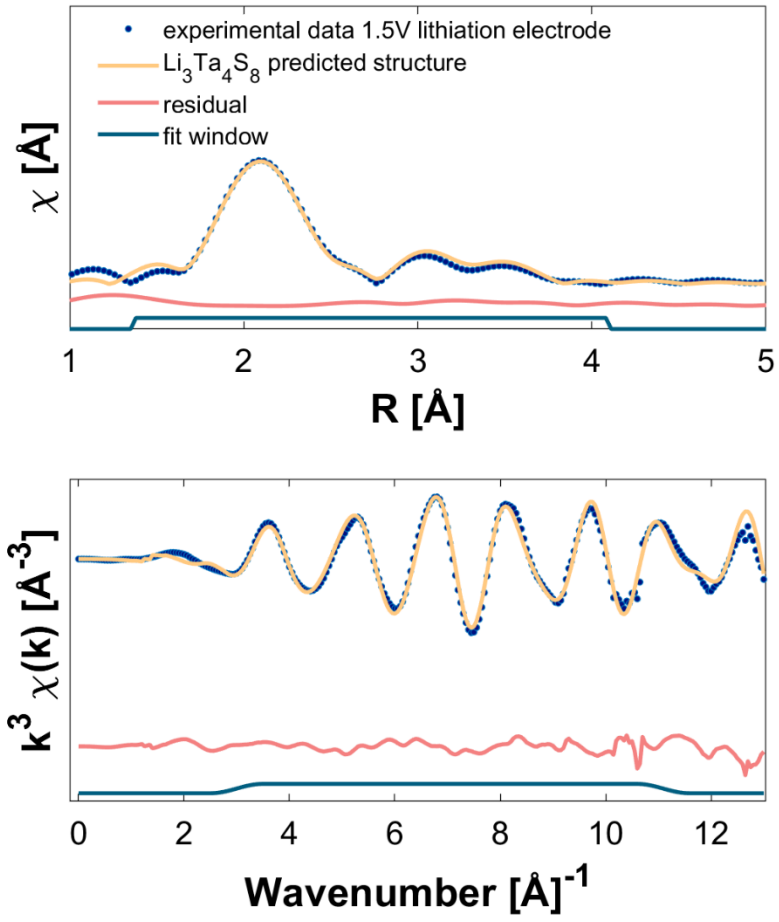

***Fig. A*-32.** EXAFS fitting of *a*-TaS_y ex-situ electrode cycled to 1.5 V on lithiation fit to the simulated structure of $Li_3Ta_4S_8$.

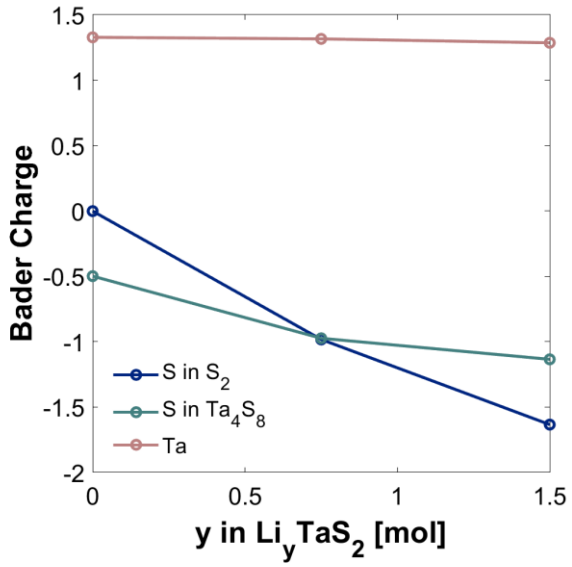

***Fig. A*-33.** Average Bader charge values of Ta atoms/S atoms in Ta_4S_6 layers/S atoms in S_2 dimers calculated for the structures shown in **Fig. 5-10a**. Ta electronegativity is 1.5, hence lower than that of W, but still close enough to that of S to provide significant iono-covalent character. Bader charge analysis suggested that the all the electrons were mainly accommodated by reduction of the S atoms in the both the S_2 dimer and the Ta_4S_6 layer, and only a slight reduction of Ta atoms was involved

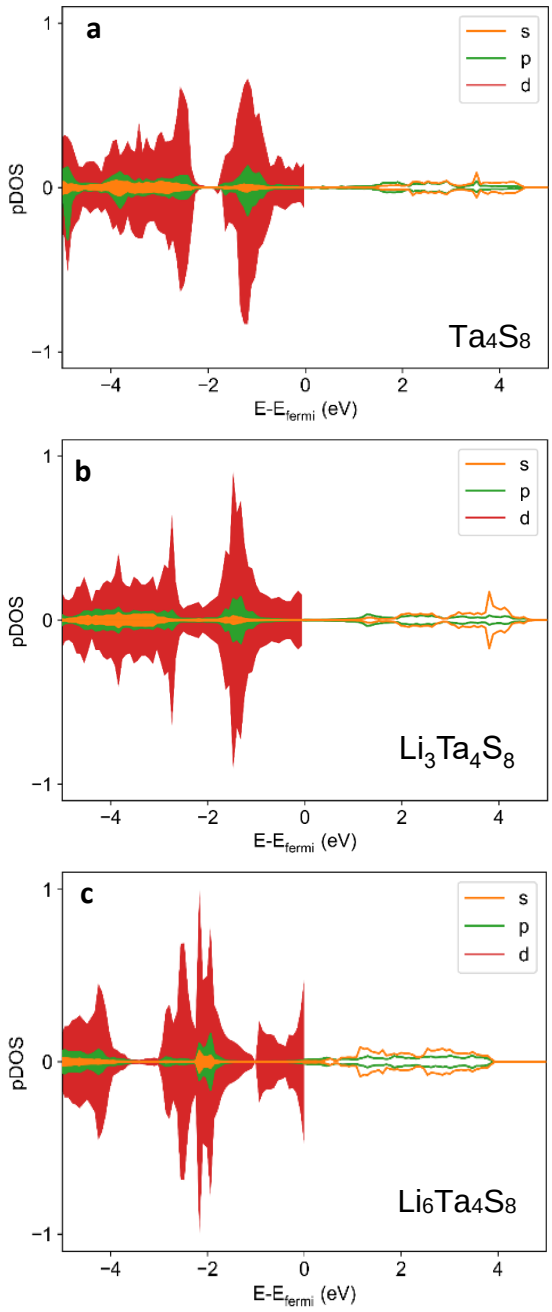

Fig. A-34. Projected density of states (pDOS) on Ta atoms in the **a)** nonlithiated Ta_4S_8 structure, **b)** intermediate lithiated state $Li_3Ta_4S_8$, displaying no major change in the Ta band structure compared with the Ta_4S_8 delithiated structure in (a) and **c)** the fully lithiated $Li_6Ta_4S_8$ structure. The pDOS results suggested that the 5th and 6th electrons reduced the Ta atoms in the Ta_4S_6 layer.

Table A-5. EXAFS fitting parameters for simulated Ta_4S_8, $Ta_3Ta_4S_8$, $Li_6Ta_4S_8$ structures fit to electrodes cycled to 3.0V, 1.5 V on lithiation, and 0.6 V, respectively.

	Bond	**N**	**S_0^2**	**σ^2 [Å^2]**	**e_0 [eV]**	**ΔR [Å]**	**R_{eff} [Å]**	**R [Å]**	**R-factor**
Ta_4S_8 fit to 3.0 V delithiated electrode	S6.1	3	0.502	0.00049	2.766	0.02245	2.4576	2.48005	0.0066
	S5.1	3	0.502	0.00235	2.126	-0.03411	2.5122	2.47809	
	Ta1.1	4	0.502	0.00292	1.172	0.03379	3.2663	3.30009	
	Ta3.2	3	0.502	0.00437	8.025	0.18835	3.2976	3.48595	
	S2.2	2	0.502	0	-4.401	-0.05087	4.0805	4.02963	
	S1.2	3	0.502	0.01175	6.176	0.16429	4.1176	4.28189	

	Bond	**N**	**S_0^2**	**σ^2 [Å^2]**	**e_0 [eV]**	**ΔR [Å]**	**R_{eff} [Å]**	**R [Å]**	**R-factor**
$Li_3Ta_4S_8$ fit to 1.5 V on lithiation electrode	S2.1	3	0.701	0.00586	7.116	-0.01599	2.4646	2.44861	0.0055
	S1.1	3	0.701	0.00142	5.869	-0.00941	2.5081	2.49869	
	Ta3.1	2	0.701	0.00227	4.477	0.06424	3.2458	3.31004	
	Ta2.1	3	0.701	0.01311	10.097	0.1446	3.2913	3.4359	
	Ta1.1	2	0.701	0.01156	3.972	-0.09374	3.3196	3.22586	
	S2.3	4	0.701	0.0106	1.331	-0.06039	4.1417	4.08131	

	Bond	**N**	**S_0^2**	**σ^2 [Å^2]**	**e_0 [eV]**	**ΔR [Å]**	**R_{eff} [Å]**	**R [Å]**	**R-factor**
$Li_6Ta_4S_8$ fit to 0.6 V lithiated electrode	S2.1	6	0.5	0.0013	3.84	-0.03417	2.5224	2.48823	0.0129
	Ta3.1	6	0.5	0.00478	2.561	-0.08818	3.4063	3.31812	
	Ta4.1	1	0.5	0	14.442	0.40989	3.187	3.59689	

Appendix 1. References

1. D. J. Morgan, Core-level spectra of powdered tungsten disulfide, WS_2. *Surf. Sci. Spectra*. **25**, 014002 (2018).
2. B. Ravel, M. Newville, *ATHENA* , *ARTEMIS* , *HEPHAESTUS*: data analysis for X-ray absorption spectroscopy using *IFEFFIT*. *J. Synchrotron Radiat.* **12**, 537–541 (2005).
3. C. L. Farrow, P. Juhas, J. W. Liu, D. Bryndin, E. S. Božin, J. Bloch, T. Proffen, S. J. L. Billinge, PDFfit2 and PDFgui: computer programs for studying nanostructure in crystals. *J. Phys. Condens. Matter*. **19**, 335219 (2007).
4. P. Hohenberg, W. Kohn, Inhomogeneous Electron Gas. *Phys. Rev.* **136**, B864–B871 (1964).
5. W. Kohn, L. J. Sham, Self-Consistent Equations Including Exchange and Correlation Effects. *Phys. Rev.* **140**, A1133–A1138 (1965).
6. G. Kresse, J. Hafner, *Ab initio* molecular dynamics for liquid metals. *Phys. Rev. B.* **47**, 558–561 (1993).
7. J. P. Perdew, K. Burke, M. Ernzerhof, Generalized Gradient Approximation Made Simple. *Phys. Rev. Lett.* **77**, 3865–3868 (1996).
8. S. Grimme, J. Antony, S. Ehrlich, H. Krieg, A consistent and accurate *ab initio* parametrization of density functional dispersion correction (DFT-D) for the 94 elements H-Pu. *J. Chem. Phys.* **132**, 154104 (2010).
9. C. Shang, Z.-P. Liu, Stochastic Surface Walking Method for Structure Prediction and Pathway Searching. *J. Chem. Theory Comput.* **9**, 1838–1845 (2013).
10. C. Shang, X.-J. Zhang, Z.-P. Liu, Stochastic surface walking method for crystal structure and phase transition pathway prediction. *Phys Chem Chem Phys*. **16**, 17845–17856 (2014).

11. O. Bunău, Y. Joly, Self-consistent aspects of x-ray absorption calculations. *J. Phys. Condens. Matter*. **21**, 345501 (2009).
12. S. A. Guda, A. A. Guda, M. A. Soldatov, K. A. Lomachenko, A. L. Bugaev, C. Lamberti, W. Gawelda, C. Bressler, G. Smolentsev, A. V. Soldatov, Y. Joly, Optimized Finite Difference Method for the Full-Potential XANES Simulations: Application to Molecular Adsorption Geometries in MOFs and Metal–Ligand Intersystem Crossing Transients. *J. Chem. Theory Comput.* **11**, 4512–4521 (2015).
13. B. Vikram Babu, K. Vijaya Babu, G. Tewodros Aregai, L. Seeta Devi, B. Madhavi Latha, M. Sushma Reddi, K. Samatha, V. Veeraiah, Structural and electrical properties of Li4Ti5O12 anode material for lithium-ion batteries. *Results Phys.* **9**, 284–289 (2018).
14. M. Park, X. Zhang, M. Chung, G. B. Less, A. M. Sastry, A review of conduction phenomena in Li-ion batteries. *J. Power Sources*. **195**, 7904–7929 (2010).
15. J. Balach, J. Linnemann, T. Jaumann, L. Giebeler, Metal-based nanostructured materials for advanced lithium–sulfur batteries. *J. Mater. Chem. A.* **6**, 23127–23168 (2018).
16. J. Heo, J. S. Sanghera, J. D. Mackenzie, A structural investigation of As2S3□Tl2S glasses by XPS. *J. Non-Cryst. Solids*. **101**, 23–30 (1988).
17. H. Nasu, R. M. Almeida, J. Heo, J. S. Sanghera, J. D. Mackenzie, XPS studies of sulfide and selenide glasses. *J. Non-Cryst. Solids*. **95–96**, 351–358 (1987).
18. V. V. T. Doan-Nguyen, K. S. Subrahmanyam, M. M. Butala, J. A. Gerbec, S. M. Islam, K. N. Kanipe, C. E. Wilson, M. Balasubramanian, K. M. Wiaderek, O. J. Borkiewicz, K. W. Chapman, P. J. Chupas, M. Moskovits, B. S. Dunn, M. G. Kanatzidis, R. Seshadri, Molybdenum Polysulfide Chalcogels as High-Capacity, Anion-Redox-Driven Electrode Materials for Li-Ion Batteries. *Chem. Mater.* **28**, 8357–8365 (2016).

19. C. Choi, D. S. Ashby, D. M. Butts, R. H. DeBlock, Q. Wei, J. Lau, B. Dunn, Achieving high energy density and high power density with pseudocapacitive materials. *Nat. Rev. Mater.* **5**, 5–19 (2020).
20. C. M. Julien, Lithium intercalated compounds. *Mater. Sci. Eng. R Rep.* **40**, 47–102 (2003).
21. R. Chen, T. Zhao, W. Wu, F. Wu, L. Li, J. Qian, R. Xu, H. Wu, H. M. Albishri, A. S. Al-Bogami, D. A. El-Hady, J. Lu, K. Amine, Free-Standing Hierarchically Sandwich-Type Tungsten Disulfide Nanotubes/Graphene Anode for Lithium-Ion Batteries. *Nano Lett.* **14**, 5899–5904 (2014).
22. G. Assat, J.-M. Tarascon, Fundamental understanding and practical challenges of anionic redox activity in Li-ion batteries. *Nat. Energy*. **3**, 373–386 (2018).
23. S. Saha, G. Assat, M. T. Sougrati, D. Foix, H. Li, J. Vergnet, S. Turi, Y. Ha, W. Yang, J. Cabana, G. Rousse, A. M. Abakumov, J.-M. Tarascon, Exploring the bottlenecks of anionic redox in Li-rich layered sulfides. *Nat. Energy*. **4**, 977–987 (2019).
24. G. Assat, D. Foix, C. Delacourt, A. Iadecola, R. Dedryvère, J.-M. Tarascon, Fundamental interplay between anionic/cationic redox governing the kinetics and thermodynamics of lithium-rich cathodes. *Nat. Commun.* **8** (2017), doi:10.1038/s41467-017-02291-9.
25. W. Jiang, C. Yin, Y. Xia, B. Qiu, H. Guo, H. Cui, F. Hu, Z. Liu, Understanding the Discrepancy of Defect Kinetics on Anionic Redox in Lithium-Rich Cathode Oxides. *ACS Appl. Mater. Interfaces*. **11**, 14023–14034 (2019).
26. K. Shimoda, K. Koganei, T. Takeuchi, T. Matsunaga, M. Murakami, H. Sakaebe, H. Kobayashi, E. Matsubara, Structural characterization of an amorphous VS_4 and its lithiation/delithiation behavior studied by solid-state NMR spectroscopy. *RSC Adv.* **9**, 23979–23985 (2019).

27. C. Chang, Infrared and Raman studies of amorphous MoS3 and poorly crystalline MoS2. *J. Catal.* **72**, 139–148 (1981).

28. M. Agostini, B. Scrosati, J. Hassoun, An Advanced Lithium-Ion Sulfur Battery for High Energy Storage. *Adv. Energy Mater.* **5**, 1500481 (2015).

29. B. Li, M. T. Sougrati, G. Rousse, A. V. Morozov, R. Dedryvère, A. Iadecola, A. Senyshyn, L. Zhang, A. M. Abakumov, M.-L. Doublet, J.-M. Tarascon, Correlating ligand-to-metal charge transfer with voltage hysteresis in a Li-rich rock-salt compound exhibiting anionic redox. *Nat. Chem.* **13**, 1070–1080 (2021).

30. S. Nagarajan, S. Hwang, M. Balasubramanian, N. K. Thangavel, L. M. R. Arava, Mixed Cationic and Anionic Redox in Ni and Co Free Chalcogen-Based Cathode Chemistry for Li-Ion Batteries. *J. Am. Chem. Soc.* **143**, 15732–15744 (2021).

31. M. Hagen, P. Schiffels, M. Hammer, S. Dörfler, J. Tübke, M. J. Hoffmann, H. Althues, S. Kaskel, In-Situ Raman Investigation of Polysulfide Formation in Li-S Cells. *J. Electrochem. Soc.* **160**, A1205–A1214 (2013).

32. J.-T. Yeon, J.-Y. Jang, J.-G. Han, J. Cho, K. T. Lee, N.-S. Choi, Raman Spectroscopic and X-ray Diffraction Studies of Sulfur Composite Electrodes during Discharge and Charge. *J. Electrochem. Soc.* **159**, A1308–A1314 (2012).

Appendix 2. Plasma enhanced atomic layer deposition of thin film $Li_{1+x}Mn_{2-x}O_4$ for realization of all solid-state 3D lithium-ion micro batteries.

JVST A
Journal of Vacuum Science & Technology A
ARTICLE
avs.scitation.org/journal/jva

Plasma enhanced atomic layer deposition of thin film $Li_{1+x}Mn_{2-x}O_4$ for realization of all solid-state 3D lithium-ion microbatteries

Cite as: J. Vac. Sci. Technol. A 39, 012408 (2021); doi: 10.1116/6.0000644
Submitted: 17 September 2020 · Accepted: 23 November 2020 ·
Published Online: 21 December 2020

Ryan Sheil,[1,a)] Danielle Butts,[2,a)] Katherine Jungjohann,[3] Jinkyoung Yoo,[4] Bruce Dunn,[2] and Jane P. Chang[1,b)]

AFFILIATIONS

[1]Department of Chemical and Biomolecular Engineering, UCLA, Los Angeles, California 90095
[2]Department of Material Science and Engineering, UCLA, Los Angeles, California 90095
[3]Center for Integrated Nanotechnologies, Sandia National Laboratory, Albuquerque, New Mexico 87185
[4]Center for Integrated Nanotechnologies, Los Alamos National Laboratory, Los Alamos, New Mexico 87545

Note: This paper is part of the 2021 Special Topic Collection on Atomic Layer Deposition (ALD).
[a)]**Contributions:** These authors contributed equally.
[b)]**Electronic mail:** jpchang@ucla.edu

ABSTRACT

The plasma enhanced atomic layer deposition (PEALD) process for MnO_2 was demonstrated, exhibiting self-limiting growth as well as stable composition and stable growth rate over a temperature window of 205–265 °C. The PEALD process for MnO_2 was combined with the thermal ALD process for LiOH to synthesize $Li_{1+x}Mn_{2-x}O_4$ thin film cathodes, where the stoichiometry was effectively controlled to allow for crystallization in the electrochemically active spinel phase. A 3D nanostructure consisting of an $Li_{1+x}Mn_{2-x}O_4$ cathode layer, ALD $Li_xAl_ySi_zO$ solid electrolyte, and SiGe nanowire anode was fabricated and characterized via TEM. The $Li_{1+x}Mn_{2-x}O_4$ thin films maintained 66% of the areal capacity upon a 100× increase in the rate (4–360 μA cm^{-2}) as well as 97% capacity retention over 100 cycles at ~5C. The ALD $Li_{1+x}Mn_{2-x}O_4$ thin films exhibited a volumetric capacity of 52 μAh cm^{-2} μm^{-1} at a C-rate of ~0.5C and, coupled with the high operating voltage (4.0 V), offer some of best areal energy densities for ALD thin film cathodes, making it a viable material for integration with 3D lithium-ion microbatteries.

I. INTRODUCTION

Lithium-ion batteries have been a truly transformative technology enabling mobile electronics and electric vehicles due to their superior energy density over other battery chemistries. Due to safety and cycle life limitations, a much-concerted effort is under way toward the development of all-solid-state Li-ion batteries. Li-ion batteries are also being developed for miniaturized power sources, on the millimeter to micrometer scale, for applications such as sensors for IoT and biomedical applications, wireless communication devices, flexible electronics, and on-chip power.[1–4] Thin film batteries are the leading candidate to power these small-scale devices, where complex 3D architectures are needed for high areal energy densities. One of the first all-solid-state 3D Li-ion batteries fabricated utilized Si micropillars [aspect ratio (AR) ~2] where subsequent layers of the current collector, cathode, electrolyte, and anode were deposited sequentially via physical vapor deposition. The 3D structure was found to perform worse than its 2D planar counterpart at higher rates, which was suggested to be due to inhomogeneous cathode and electrolyte coating (nonconformal along the micropillar structure) as well as the low ionic conductivity of the electrolyte.[5]

In order to combat these issues, a more recent work utilized atomic layer deposition to deposit all the layers (current collector, anode, electrolyte, and cathode) on high aspect ratio etched Si pores (AR = 10), which significantly outperformed its 2D planar counterpart—with the areal capacity increasing with increasing aspect ratio of the host structure.[2] Atomic layer deposition (ALD) offers the ability to synthesize high quality, pinhole free, conformal thin films on high aspect ratio structures due to its non-line-of-sight nature. However, the slow growth rates limit the scope of

ALD to films less than 100 nm thick. Improvement in film growth rates can be achieved through transitioning from a traditional ALD process to a spatial atomic layer deposition (SALD) process. SALD for 3D battery applications was recently explored for the optimization of precursor dose to assess conformality on high aspect ratio structures.[1] The high surface area/large aspect ratio structures required of 3D thin film microbatteries (3D TFMB's) produces a trade-off: high surface area is advantageous in that it corresponds to larger deposits of active material per ALD cycle, but a large aspect ratio has a deleterious effect in that it may require much larger precursor exposure times to ensure complete surface reaction. Thus, a balance between surface area and aspect ratio must be struck to achieve optimal 3D TFMB processing conditions.

A crucial component of 3D TFMB processing is the ability to deposit cathode materials with optimal interfacial properties to ensure homogeneous active material utilization, adequate cycle life, and high rate performance. Several thin film cathode materials have been synthesized via ALD such as $LiCoO_2$, $Li_xV_2O_5$, Li_xVO_2, $LiFePO_4$, and $LiMn_2O_4$.[2,6–11] $Li_{1+x}Mn_{2-x}O_4$ is of great interest due its high rate capability and high voltage range versus Li^+/Li. $LiMn_2O_4$ synthesis has been demonstrated using a thermal ALD process, where lithium *tert*-butoxide (LiOtBu) and Li(thd) were found to directly react with manganese oxide to preferentially form $Li_{1+x}Mn_{2-x}O_4$.[12] Furthermore, reduction of thickness has shown to dramatically increase the rate performance in PVD thin film $LiMn_2O_4$.[12] Nonstoichiometric lithium-rich manganese oxide spinels, $Li_{1+x}Mn_{2-x}O_4$, where $x \leq 0.33$, also exhibited improved performance as compared to $LiMn_2O_4$. This can be attributed to lithium substitution in the octahedral Mn sites, which promote increased cycling stability due to suppression of both the Jahn–Teller distortion upon deep discharge as well as the Mn^{3+} disproportionation reaction. Cycling stability improvements with lithium substitution, however, must be weighed against the decrease in theoretical capacity in the 4.0 V region as the manganese ions become tetravalent to maintain charge neutrality (theoretical capacity of 154 mAh/g for $x = 0$).[13] Therefore, an optimal composition for $Li_{1+x}Mn_{2-x}O_4$ is desired that achieves high stability without significantly sacrificing capacity. This suggests that ALD is an ideal method for $Li_{1+x}Mn_{2-x}O_4$ thin film synthesis due to its ability to control the degree of Li substitution for optimizing electrochemical performance.

Here, we report the development of a plasma enhanced ALD (PEALD) process for $Li_{1+x}Mn_{2-x}O_4$ with tunable stoichiometry. First, the PEALD process of MnO_2 is discussed utilizing O_2 plasma and $Mn(thd)_3$, which, although previously reported, has not been extensively characterized.[14,15] Li incorporation was achieved through utilization of a lithium *tert*-butoxide/H_2O thermal ALD process. The structural and electrochemical properties were probed as a function of ALD cycle ratio, where the $Li_{1+x}Mn_{2-x}O_4$ thin films demonstrated good rate performance and cycle stability. The development and characterization of thin film electrode and electrolyte materials as well as their integration in 3D solid-state batteries present the opportunity to better understand material-specific properties applicable to batteries of all length scales as well as to study the unique phenomena that may arise during utilization in a complex geometry.

II. EXPERIMENT

A. Atomic layer deposition of lithium manganese oxide and lithium aluminum silicate

ALD of $Li_xMn_yO_z$ was carried out in a home-built hot-wall vacuum chamber, which was maintained at a base pressure of 35 mTorr. The metal-organic precursors, tris(2,2,6,6-tetramethyl-3,5-heptanedionato)manganese(III) [$Mn(thd)_3$] (99.9%, Strem Chemicals, Inc.) and LiOtBu (99.9%, Strem Chemicals, Inc.), were utilized as the Mn and Li sources, respectively. $Mn(thd)_3$ was held at 130 °C, and LiOtBu was held at 140 °C to provide adequate vapor flux. All precursors were delivered to the chamber via a heated gas-line held at 150 °C. H_2O was utilized as the oxidant source for deposition of $LiOH/Li_2O$ and was held at room temperature. O radicals were utilized as the oxidant source for deposition of MnO_x utilizing a coaxial waveguide microwave radical beam source operated at 25 W power as previously described.[16–18] A constant flow of ~1 SCCM of O_2 was delivered to the chamber during the depositions. O_2 was not found to react with any of the precursors at the temperatures tested. The chamber was purged for 75 s following LiOtBu and H_2O pulse, 50 s for $Mn(thd)_2$, and 30 s post O radical exposure. A typical deposition sequence was as follows: $[a[Mn(thd)_3/O] + b(LiOtBu/H_2O)]$, where a and b were altered to tune the composition of the resulting thin films.

ALD of $Li_xAl_ySi_zO$ was carried out in a home-built hot-wall vacuum chamber, maintained at a base pressure of 50 mTorr as described elsewhere.[19] The metal-organic precursors trimethyl aluminum, LiOtBu, and tris-tertbutoxy silanol were utilized for Al, Li, and Si incorporation, respectively, all utilizing H_2O as the oxidant. The ALD cycle consisted of a deposition sequence of $5 \times [10(Al_2O_3)–6(LiOH)–1(SiO_2)]$, deposited at 225 °C. The sample was exposed to ambient for a short period and then loaded for the $Li_{1+x}Mn_{2-x}O_4$ deposition. The sample was then rapid thermal annealed at 750 °C for 1 min.

B. Materials and electrochemical characterization

Si(001) wafers cut 1×1 cm^2 were utilized as substrates for all growth characterization, and platinized silicon (purchased from MEMS Exchange) consisting of the stack structure of $Pt(100\text{ nm})/TiO_2(10\text{ nm})/SiO_2(300\text{ nm})/Si$ was utilized as the substrate for electrochemical characterization. Film thicknesses were estimated with a J.A. Woollam M-88 spectroscopic ellipsometer (SE) with wavelengths of 280–760 nm cross-checked with scanning electron microscope (SEM) imaging utilizing an FEI Nova 600 SEM/FIB. X-ray photoelectron spectroscopy (XPS, Kratos Axis Ultra) spectra were collected using monochromatic Al Kα x-ray radiation. Energy referencing was based on the C 1s peak of adventitious carbon, set to a binding energy of 284.8 eV. A pass energy of 160 eV was utilized for survey spectra, while a pass energy of 40 eV was utilized for the detailed (high-resolution) XPS scans. Specific XPS fitted values can be seen in Table S1 (Ref. 31) and corresponding literature values in Table S2.[31] Depth profile XPS was performed *in situ* through sputtering with a 4 keV Ar^+ beam. The crystal structure was characterized utilizing an X'pert Pro powder x-ray diffractometer (XRD) using Cu kα radiation. Crystallization of the thin films were performed via rapid thermal

annealing for 1–5 min at temperatures of 550–750 °C under an O_2 environment, utilizing an AccuThermo AW 610 RTP furnace. Atomic force microscopy measurements were performed using a Bruker Fast-Scan Scanning Probe Microscope with ScanAsyst using Bruker ScanAsyst-Air probes.

All electrochemical measurements were performed in a flooded three electrode cell in an Ar-filled glovebox (less than 1 ppm O_2/H_2O), where lithium metal foil was utilized as the counter and reference electrode. 1M $LiClO_4$ in a 1:1 by volume solution of ethylene carbonate and dimethyl carbonate was utilized as the liquid electrolyte. The $LiMn_{2-x}O_4$ thin films deposited on Pt-Si wafers were connected via an alligator clip for electrical connection, where the active area was calculated for only the area exposed to liquid electrolyte. The defined area for liquid electrolyte contact was calculated from optical images and a custom MATLAB script. Volumetric capacities for 2D samples were calculated based on SE/SEM determined thicknesses and the active area exposed to liquid electrolyte. Gravimetric capacities for C-rate calculations were estimated based on the bulk density of $LiMn_2O_4$. All electrochemical measurements were performed via a Bio-Logic VMP-3 potentiostat. Cyclic voltammetry and galvanic cycling were performed over the voltage range of 4.5–3.5 V.

C. Fabrication of nanowire batterylike structure and TEM characterization

Single crystalline SiGe nanowires were synthesized by gold (Au) catalyzed vapor-liquid-solid method in a chemical vapor deposition (CVD) reactor. To prepare Au catalysts Au nanoparticles whose diameter was 100 nm were dispersed on germanium (111) substrates. Prior to dispersion of Au nanoparticles, the Ge substrates were cleaned by a piranha solution. The cleaned substrates were immersed in 2% HF solution for 1 s before loading into the CVD chamber. Silane diluted in hydrogen (50% SiH_4 in H_2) and germane diluted in hydrogen (30% GeH_4 in H_2) were the precursors for silicon (Si) and germanium (Ge), respectively. The typical pressure of the CVD reactor was 3 Torr. The ratio of the SiH_4 flow rate to the GeH_4 flow rate was 3. The growth temperature was in the range of 450 and 550 °C. Next, ALD $Li_xAl_ySi_zO$ was coated on the SiGe nanowires and Si wedge structure utilizing the chemical precursors of lithium *tert*-butoxide, trimethyl aluminum, and tris-tertbutoxy silanol as reported here[19,20] at a deposition temperature of 225 °C. Post $Li_xAl_ySi_zO$ deposition, ALD of $Li_{1+x}Mn_{2-x}O_4$ was deposited and the resulting structure was rapid thermal annealed at 750 °C for 1 min with a ramp rate of 50 °C/s. TEM characterization was performed on FEI Tecnai F30 TEM operating at 300 kV utilizing a Nanofactory STM-TEM holder.

III. RESULTS AND DISCUSSION

A. ALD process characterization of the individual oxides: MnO_2 and LiOH/Li_2O

First, to confirm self-limiting growth, precursor saturation behavior was tested. A stable growth rate was observed for the ALD MnO_2 process at dose times of 50 s for $Mn(thd)_3$ and 10 s for the O_2 plasma dose as shown in Fig. 1(b). It was previously reported that saturation behavior for $Mn(thd)_3/O_2$ plasma couple could not be achieved due to inhomogeneous film deposition for O_2 plasma dose times as long as 120 s.[14] The apparent discrepancy could stem from a wide range of processing conditions such as differences in the plasma source [remote RF source (300 W) versus microwave source (25 W) reported here], which could affect both the composition of plasma species present as well as their energies, in addition to the deposition temperature (180 vs 205–265 °C reported here). The growth rate behavior for MnO_2 characterized at 225 °C was found to exhibit two features: an initial regime of higher growth rate, potentially indicative of a nucleation or island growth regime (<100 cycles) (with the y-intercept forced to zero), and a second regime with a linear fit to yield a growth rate of ~0.2 Å/cycle as shown in Fig. 1(a). The ALD temperature window and saturation behavior of the LiOtBu/H_2O process was not characterized here as it was described extensively elsewhere,[21,22] but the measured growth was 1.0 Å/cycle determined via *ex situ* spectroscopic ellipsometry as shown in Fig. 1(a). The LiOtBu/H_2O ALD process has successfully been implemented in a wide range of complex oxides[19,20,23,24] but presents challenges as LiOH/Li_2O films are air-reactive as well as hygroscopic leading to the potential of CVD-type growth.

The growth rate of the MnO_2 films was relatively constant over the range of temperatures tested, but slightly increased with the deposition temperature as shown in Fig. 1(c). High-resolution XPS was utilized to confirm the composition of the deposited films as a function of the deposition temperature as shown in Fig. S1,[31] where the Mn $2p_{3/2}$ and Mn $2p_{1/2}$ binding energies were 642.0–642.4 eV and 653.6–653.9 eV, respectively, for the deposition temperatures tested. The Mn $2p_{3/2}$ peak binding energy is most likely indicative of the Mn^{4+} oxidation state corresponding to MnO_2, but Mn_2O_3 could not be ruled out.[25,26] Over the deposition temperature range of 205–265 °C, the carbon content was measured to be between 20% and 25%, where most of the carbon content is assumed to be that of adventitious carbon on the sample surface due to the *ex situ* nature of the measurement as shown in Fig. 1(d). The O:Mn atomic ratios of the as-deposited films varied between 2.2 and 2.7, most likely indicating an MnO_2 stoichiometry, where some oxygen can be contributed to adventitious carbon species. Due to no discernable change in composition across the temperature range, the most likely observable change in the ellipsometry determined growth rate was due to a change in material density or surface roughness. This was confirmed via atomic force microscopy where the root mean square surface roughness increased (0.44–1.83 nm) with increasing deposition temperature (205–265 °C), as shown in Fig. 1(c).

B. ALD growth, composition, and structural characterization of $Li_{1+x}Mn_{2-x}O_4$

Depositions of $Li_{1+x}Mn_{2-x}O_4$ films were carried out with the following ALD supercycle sequence: $n[a[Mn(thd)_3/O_2$ Plasma$]$-b(LiOtBu/H_2O)], which was then repeated to deposit a film of the desired thickness. Samples referred to as (a:b) correspond to the MnO_2 to LiOH ALD cycle ratio; for instance (50:1) refers to a deposition sequence of [50[$Mn(thd)_3$]-1(LiOtBu/H_2O)]. First, the composition was characterized as a function of deposition sequence (Fig. 2) for various cycle ratios: $n[a(MnO_2)$-b(LiOH)], where n was

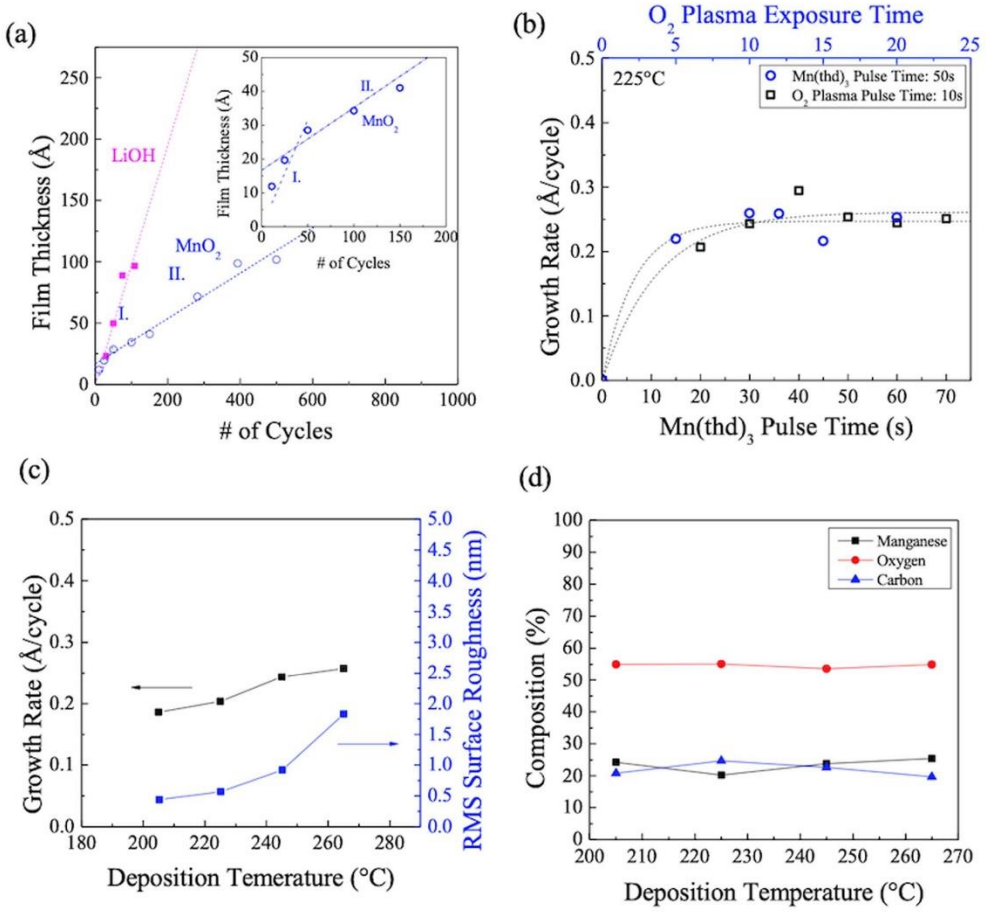

FIG. 1. Growth characterization for PEALD of MnO_x and ALD of LiOH. (a) Growth thicknesses for LiOH (square) and MnO_x (circle) measured via spectroscopic ellipsometry with a calculated growth rate of 0.6 and 0.2 Å/cycle, respectively. The growth rate appeared to follow two regimes changing near 100 ALD cycles for ALD MnO_x more clearly seen in the zoomed-in inset. (b) The growth rate as a function of precursor pulse time for $Mn(thd)_3$ and O_2 plasma demonstrating self-limiting behavior. Characterization of precursor saturation of the $Mn(thd)_3$ and O_2 plasma was performed with 350 cycles for each process condition. (c) The growth rate and surface roughness as a function of deposition temperature for MnO_2 films deposited on Si(001) and the corresponding surface composition (d) as quantified via XPS.

chosen to make the total number of cycles near 800. Remarkably, lithium-rich films were observed for samples deposited with ALD cycles ratios between: [15(MnO_2)-1(LiOH)] to [200(MnO_2)-1(LiOH)], corresponding to 6.25%–0.5% LiOH ALD cycles of the total supercycle [i.e., $b/(a+b)$ in ALD supercycle: $a(MnO_2)$-b(LiOH)]. This behavior is similar to that observed for a previous ALD study, where LiOtBu was proposed to directly react with MnO_2 to form $LiMn_2O_4$.[12] Although films were lithium-rich, the growth rate did not increase significantly with an increasing fraction of LiOH subcycles, where a growth rate of ~0.4 Å/cycle was observed. An SEM cross section image of an $Li_{1+x}Mn_{2-x}O_4$ thin film consisting of three supercycles of [250(MnO_2)-1(LiOH)] is

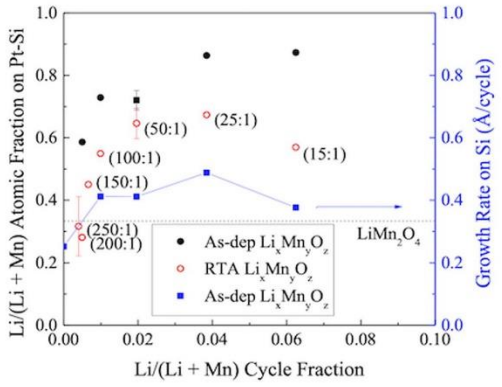

FIG. 2. Composition and growth rate vs ALD cycle sequence for $Li_{1+x}Mn_{2-x}O_4$. The incorporation of Li (determined via XPS) vs ALD cycle ratio for Li_xMn_yO as-deposited (solid circle) and after rapid thermally annealing at 750 °C (open circle) both deposited on $Pt/TiO_2/SiO_2/Si$ substrates is high at low ALD cycle fractions. The growth rate of Li_xMn_yO vs increasing LiOH subcycle ratios (as-deposited) was characterized on Si(001) substrates using spectroscopic ellipsometry is shown in square symbols. Silicon substrates were utilized to simplify ellipsometry fitting.

shown in Fig. S2.[31] The growth rate agrees well with spectroscopic ellipsometry measured growth rates exhibiting a growth rate of 100 Å per supercycle and 0.4 Å/cycle calculated dividing the thickness by the total number of subcycles.

Due to the surface-sensitive nature of XPS, there can always be added complexity due to different chemical states near the upper-most surface, especially when samples are characterized *ex situ*. For stoichiometric $LiMn_2O_4$, there should be an equal ratio of Mn^{4+} and Mn^{3+} cations. Li substitution in the spinel structure ($Li_{1+x}Mn_{2-x}O_4$) is commonly observed, where for every Li^+ substitution, an Mn^{3+} is oxidized to maintain charge neutrality up to the extreme of $Li_{4/3}Mn_{5/3}O_4$ ($Li_4Mn_5O_{12}$) in which all Mn exist in the Mn^{4+} oxidation state. It follows that if the $Li_xMn_yO_z$ is in the spinel structure (which has been verified and is discussed below), then the ratio of the Mn^{4+} to the Mn^{3+} oxidation state should be a measure of the degree of lithium substitution—highly relevant to the corresponding electrochemical properties. XPS detailed spectra (Mn 2p, O 1s, C 1s, and Li 1s/Mn 3p) for several $Li_xMn_yO_z$ samples as well as ALD MnO_x as a comparison, are shown in Fig. 3. There is an emphasis on the post-rapid thermal annealing samples due to their relevance to electrochemical testing. First, in comparison to the (15:1) before and after rapid thermal annealing, the presence of C1s signal at high binding energy (>289 eV) attributed to lithium carbonate is observed in the as-deposited sample, but not after rapid thermal annealing. Changes are also evident in the O 1s spectra, where the ratio of the two fit peaks is attributed to more metal bound oxygen post rapid thermal annealing. Furthermore, an increase in the Mn 2p signal is observed, and the Li 1s shifts to lower binding energy, most likely indicative of more lithium oxide compared to that of lithium carbonate surface composition. In a previous ALD study involving the synthesis of lithium titanate, a lithium- and carbon-rich surface formed upon atmosphere exposure as lithium hydroxide can react to form lithium carbonate;[27] this reaction could be occurring in the $Li_xMn_yO_z$ thin films. Next, in comparing the C1s XPS spectra of rapid thermal annealed samples deposited with various ALD sequences, the majority of the C 1s signal is attributed to sp^3 carbon with the large majority expected to be adventitious carbon from ambient exposure. In fitting the Mn 2p spectra, four peaks (two for $2p_{3/2}$ and two for $2p_{1/2}$) with constrained *fwhm*, peak splitting, and peak area (2:1 for $2p_{3/2}$:$2p_{1/2}$) were utilized. Across the samples, there was not a significant change clearly evident in the Mn 2p, where the Mn $2p_{3/2}$ peak near 642.5 eV was attributed to Mn(IV)-O, and a shoulder at 641.8 eV was attributed Mn(III)-O. Slightly more clear are the changes observed in the Mn 3p spectra, where, in comparing the (15:1) to the (100:1 and 250:1) samples, the ratio of the two fit peaks attributed to the Mn(IV) and Mn(III) oxidation states decreases with fewer LiOH ALD cycles. This could be indicative of a high lithium content spinel ($Li_{1+x}Mn_{2-x}O_4$) but due to the surface-sensitive nature of XPS cannot be fully confirmed.

To further assess the bulk composition versus surface composition, *in situ* Ar^+ ion beam etching was performed in conjunction with XPS. It should be noted that Ar^+ etching is a physical process that can alter the surface, especially due to varying sputtering rates for different atomic weights and chemical bonding. Figure 4(a) shows the relative compositions as a function of etch time (depth within film). After the first etch step (180 s), the carbon content decreased from ~25% to around 5%, which potentially is the amount of carbon incorporated within the film due to precursor decomposition or incomplete ligand exchange. After the first etch step, the lithium content decreases, while manganese and oxygen content increased. After 360 s etch time, the film composition remained stable (within 1%–2%) with a relative composition of Li: 13%, Mn: 31%, O: 51%, and C: 5%. Figure 4(b) shows the Li/(Li + Mn) atomic fraction as well as Mn 3s exchange splitting as a function of etch time. After 360 s, the Li/(Li + Mn) decreases to a constant value of about 0.3 slightly less than what would be expected for $LiMn_2O_4$. The Mn 3s exchange splitting increases significantly after the first etch step (4.5–5.3 eV), then steadily increases to 5.6 eV, indicative of a lower Mn oxidation state. Photoelectron transitions for the 3s valence state have two possible final states ($3s^13p^63d^x$) from an initial state ($3s^23p^63d^x$), where x = 3, 4, and 5 for the oxidation states of Mn^{4+}, Mn^{3+}, and Mn^{2+}, respectively, where in one final state, the 3s electron is correlated with the 3d electrons of parallel spin and the other antiparallel.[28] The effect of Ar^+ etching aside, there is a significant variance in surface versus bulk composition (more lithium and carbon rich). The relatively stable Li/(Li + Mn) ratio after the first etch step could be indicative of a more uniform composition as well as a coupling of the two elements, where the individual oxides would be expected to have varying sputtering rates.

The $Li_xMn_yO_z$ thin film crystal structure was probed as a function of rapid thermal annealing treatment. Thin films with ALD cycle sequences ranging from (15:1) to (250:1) were amorphous as deposited but crystallized upon rapid thermal annealing

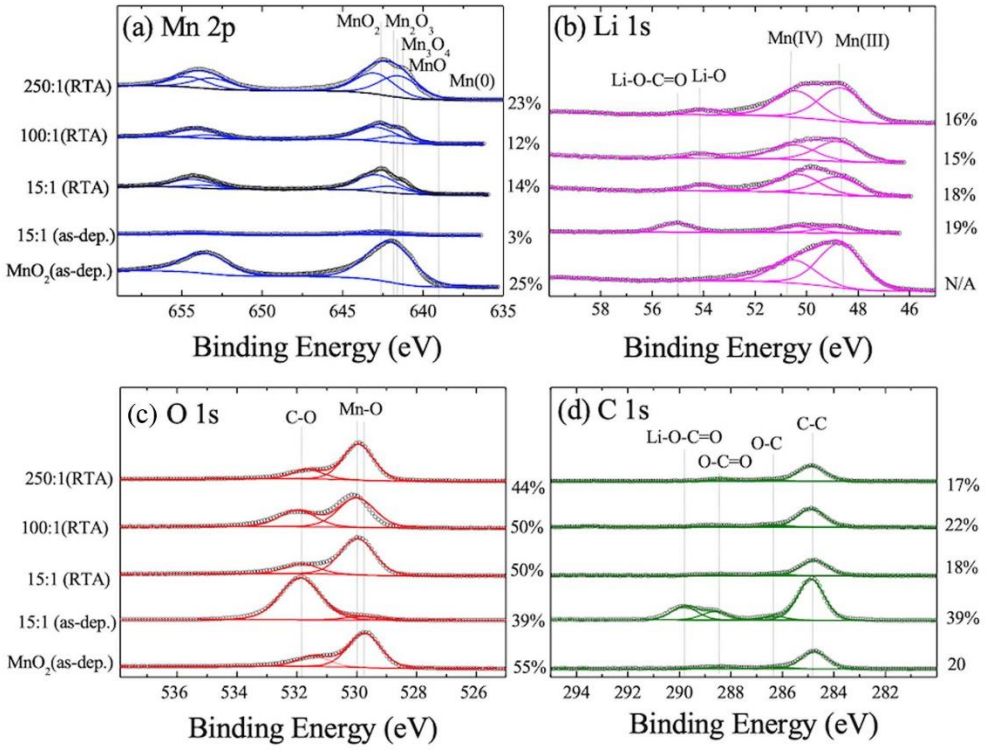

FIG. 3. XPS detailed scans of three representative $Li_xMn_yO_z$ samples deposited with cycle sequences of 15(MnO_2)-1(LiOH) (as-dep, RTA), 100(MnO_2)-1(LiOH)(RTA), 250 (MnO_2)-1(LiOH)(RTA), and MnO_2, where the spectra for the Mn 2p, Li 1 s, O 1 s, and C1 s, are shown in parts (a)–(d), respectively. In the as-deposited state, the surface was carbon-rich and manganese deficient as can be seen in comparing the 15(MnO_2)-1(LiOH) sample before and after rapid thermal annealing, where reduction of lithium carbonate can be observed in the C 1s detailed scan shown in (d).

into the spinel structure as shown in Fig. 5(a). Figure 5(b) shows XRD spectra of two films with ALD deposition sequence [50(MnO_2)-1(LiOH)] and [250(MnO_2)-1(LiOH)] in both the as-deposited state as well as after rapid thermal annealing at 750 °C. The measured lattice spacing for the (111) reflection was 4.72 and 4.75 Å for the 50:1 and 250:1, respectively, as compared to 4.76 Å (JCPDS reference pattern 00-004-0802) reported in the literature. A shift to a lower value of the (111) reflection is indicative of a compressed unit cell. Lithium-substituted spinels ($Li_{1+x}Mn_{2-x}O_4$, $x \leq 0.33$) have been observed to have a decreased lattice constant with increased lithium substitution.[13] Comparing the shift in the XRD spectra further suggests an increase in lithium-substituted $Li_{1+x}Mn_{2-x}O_4$ with a higher percentage of LiOH ALD subcycles.

An all-solid-state nanowire battery-like structure was fabricated to assess the structure properties of the $Li_{1-x}Mn_2O_4$ films deposited on a 3D structure. An SiGe nanowire was utilized as a substrate/current collector/anode, where the alloy composition was determined to be $Si_{0.51}Ge_{0.50}$ from the selected area electron diffraction image shown in Fig. S3(a).[31] Next, an ALD $Li_xAl_ySi_zO$ layer was deposited on the SiGe nanowire to act as a solid electrolyte layer with composition $Li_{0.16}Al_{0.2}Si_{0.64}O_{2.7}$ (XPS spectra shown in Fig. S4).[31] A conformal thin $Li_xAl_ySi_zO$ film coated SiGe film is shown in the TEM image in Fig. S3(b),[31] where the (i) denotes carbon deposition, (ii) the SiGe nanowire, (iii) the $Li_xAl_ySi_zO$ layer, and (iv) the gold nanoparticle utilized for SiGe growth. Next, an ~20 nm $Li_{1+x}Mn_{2-x}O_4$ film was deposited on the $Li_xAl_ySi_zO$ coated SiGe nanowire to act as a cathode material. The nanostructure was

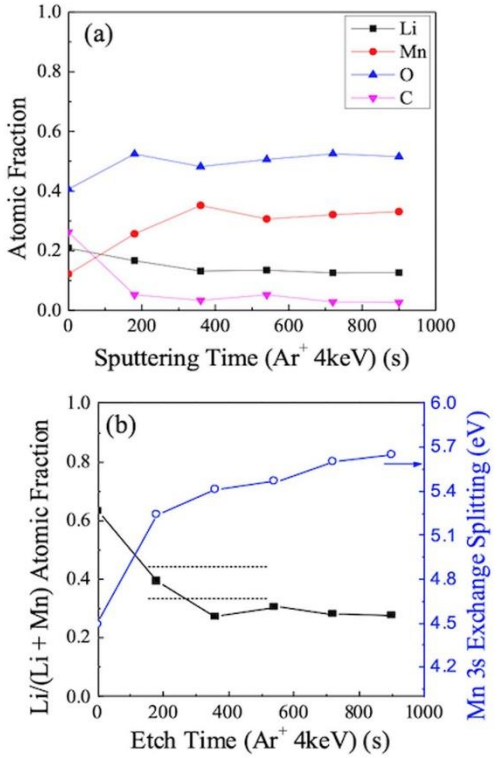

FIG. 4. *In situ* depth profiling XPS of a [50(MnO_2)-1(LiOH)] thin film. (a) Relative composition of the $Li_{1+x}Mn_{2-x}O_4$ thin films as a function of sputtering time. (b) Li/(Li + Mn) atomic fraction vs sputtering time (square) and Mn 3s exchange splitting (circle). The upper horizontal dashed line refers to the $Li_4Mn_5O_{12}$ stoichiometry, whereas the bottom horizontal dashed line refers to the $LiMn_2O_4$ stoichiometry.

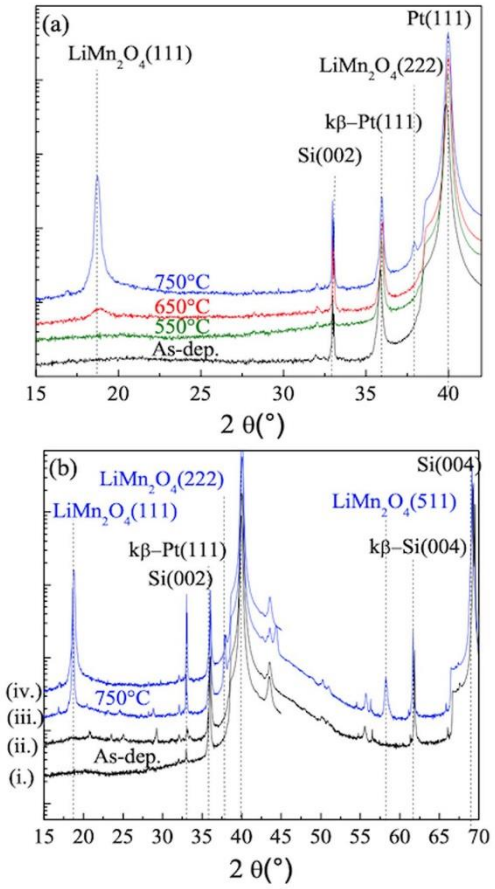

FIG. 5. (a) XRD spectra of a LixMnyOz thin film deposited with the cycle sequence 50(MnO_2)-1(LiOH) for various rapid thermal annealing treatments (As-dep, 550, 650, and 750 °C). (b) XRD of samples grown at different cycle sequences: (50:1) denoted as (ii and iv) and (250:1) denoted as (i and iii) in the as-deposited state and post rapid thermal annealing.

then rapid thermally annealed for 1 min at 750 °C to crystallize the $Li_{1+x}Mn_{2-x}O_4$ film into the electrochemically active spinel phase. A TEM image of the final structure is shown in Fig. S3(c),[31] and bright field (BF) and dark field (DF) STEM of another nanowire is shown in Fig. S3(d).[31] Immediate observation is that the Au tip has broken and diffused down the length of the nanowire (dark regions in BF and light regions in DF) during the annealing process. The edges are rough due to $Li_{1+x}Mn_{2-x}O_4$ crystallite formation along the surface of the nanowire. Selected area electron diffraction is shown in Fig. S3(e),[31] where polycrystalline rings are observed corresponding to the $Li_{1+x}Mn_{2-x}O_4$ phase. The *d* spacing associated with the (113) set of planes was measured to be 0.247 nm as compared to the 0.249 nm value as measured in the literature for $LiMn_2O_4$ (JCPDS reference pattern 00-035-0782). Finally, HRTEM of one of the nanowire samples is shown in Fig. S3(f),[31] where 0.47 nm lattice spacing was observed associated with the (111) planes of $LiMn_2O_4$ as well as various regions exhibiting Moiré diffraction patterns most likely arising from overlap of rotated $Li_{1+x}Mn_{2-x}O_4$ lattices.

C. Electrochemical characterization of $Li_{1+x}Mn_{2-x}O_4$ thin films

Lithium-rich manganese oxide spinels, $Li_{1+x}Mn_{2-x}O_4$, where $x \leq 0.33$, exhibit improved performance as compared to $LiMn_2O_4$.[29] For lithium manganese oxide spinels of stoichiometry $Li_4Mn_5O_{12}$ ($Li_{1.33}Mn_{1.67}O_4$), no lithium can be extracted at 4 V since all Mn ions are tetravalent. $Li_4Mn_5O_{12}$ can be lithiated in a reversible two-phase reaction at 3 V, up to $Li_{4+x}Mn_5O_{12}$, where $x \leq 2.5$.[30] In this section, electrochemical characterization of $Li_xMn_yO_z$ thin films with various ALD cycle ratios was assessed and compared to the compositional analysis of Sec. III B. First, cyclic voltammetry was utilized to determine the redox activity of the rapid thermal annealed $Li_xMn_yO_z$ thin films. For samples deposited with cycle sequences with more than 0.66% LiOH subcycles [150(MnO_2)-1(LiOH)], the $Li_xMn_yO_z$ was not electrochemically active in the 4 V region—indicative of the $Li_4Mn_5O_{12}$ phase. Cyclic voltammograms of the $Li_xMn_yO_z$ deposited with fewer than 0.66% LiOH subcycles [250(MnO_2)-1(LiOH)] are shown in Fig. 6, displaying the distinct doublet redox peak at 4.0 V associated with a two-step delithiation/lithiation process of $LiMn_2O_4$. The 4.0 V region is associated with insertion or removal of Li-ion from 8a tetrahedral sites, where the ~150 mV splitting between peaks is due to the preferential ordering in one half of the available tetrahedral sites.[30]

Next, galvanostatic charge/discharge cycling was performed on a sample deposited with the cycle sequence 12[250(MnO_2)-1(LiOH)] to assess the rate capability as well as cycle stability. Theoretical charge-discharge rates were estimated assuming theoretical density of $LiMn_2O_4$ and the predicted thickness from the ellipsometry determined growth rate. Due to the difficulty in assessing the exact film thickness, all capacities are reported in areal capacities. In order to confirm electrochemical stability when cycled up to 4.5 V, galvanostatic rate testing was performed, increasing the upper voltage cutoff from 4.3 to 4.5 V at various charge/discharge rates (Fig. S5).[31] The galvanostatic charge/discharge curves at various specific currents and a 4.5 V cutoff were found to be stable, with minimal Mn ion dissolution and electrolyte breakdown, and are shown in Fig. 7(a). The rate capability was assessed by measuring the capacity for the third charge/discharge cycle at increasing currents (3.6 to 360 $\mu A\,cm^{-2}$) corresponding to approximate C-rates of C/2, C, 2.5C, 5C, 10C, 15C, 25C, 40C, and 50C and then returning back to the lowest applied current, 3.6 $\mu A\,cm^{-2}$. At the lowest rate (3.6 $\mu A\,cm^{-2}$), the areal capacity was measured to be 5.2 $\mu Ah/cm^2$. Increasing the current 20-fold (36 $\mu A/cm^2$) resulted in a capacity of 4.4 $\mu Ah/cm^2$ and a 100-fold rate increase resulted in a capacity of 3.9 $\mu Ah/cm^2$ corresponding to a 66% capacity retention at a specific current of 360 $\mu A/cm^2$. Furthermore, after cycling at 360 $\mu A/cm^2$, the current was then reduced back to 3.6 $\mu A\,cm^{-2}$ to assess any damage from high rate cycling. In these experiments, 98% of the initial capacity remained. To assess cycling stability the sample was cycled at a constant rate of 5C (36 $\mu A\,cm^{-2}$) for 100 cycles (190 total cycles) as shown in Fig. 7(b). The columbic efficiency and discharge capacity on the first cycle were 94.6% and 4.7 $\mu Ah/cm^2$, respectively, and 98.7% and 4.6 $\mu Ah/cm^2$ after the 100th cycle. High columbic efficiency becomes increasingly important for integration in thin film batteries as there is a limited lithium reservoir due the ultrathin nature of the electrolyte layer. The demonstrated cycling stability and capacity retention (~97% over 100 cycles) at high specific currents suggest that Li substitution from ALD synthesis was sufficient to prevent Mn ion dissolution at high voltage and stabilize the thin film surface without sacrificing areal capacity.

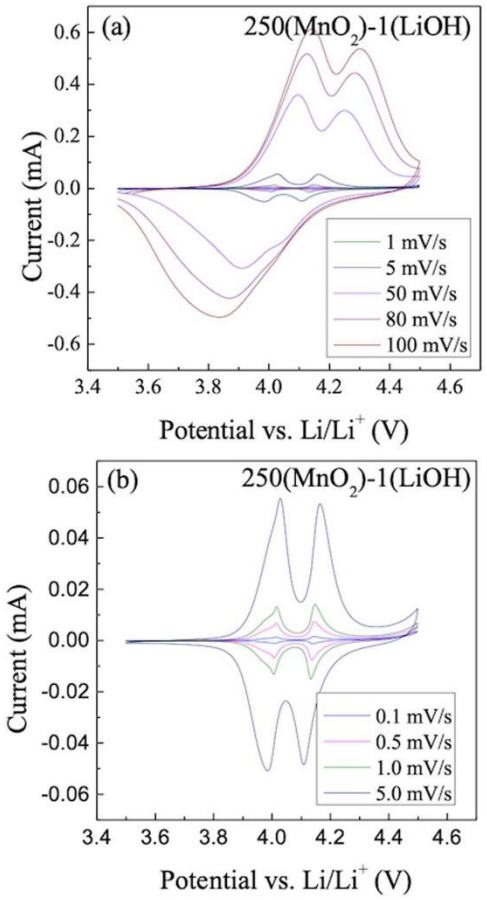

FIG. 6. Cyclic voltammetry of an $Li_{1+x}Mn_{2-x}O_4$ thin film deposited with a ALD cycle sequence of 250(MnO_2)-1(LiOH) at various rates (0.1–100 mV/s) with a voltage window of 3.5–4.0 V. All measurements were performed in a three neck flask setup in 1M $LiClO_4$ in 1:1 EC:DMC. Part (a) shows sweep rates from 1 to 100 mV/s and part (b) shows sweep rates from 0.1 to 5.0 mV/s.

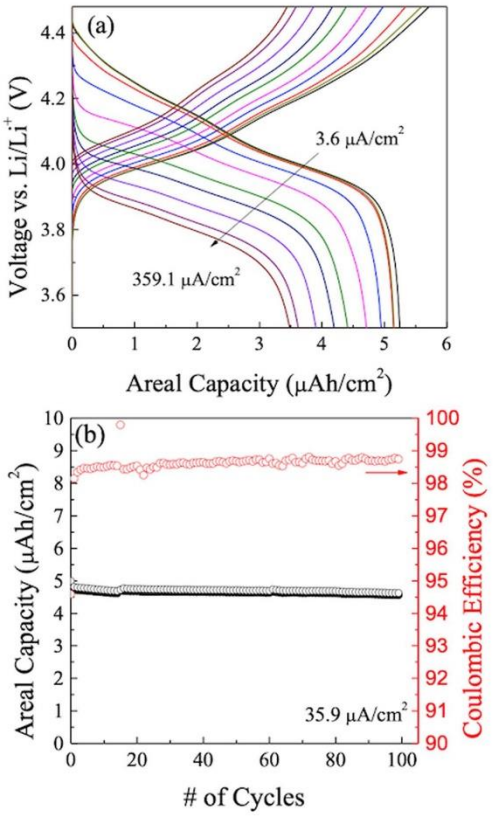

FIG. 7. Galvanostatic cycling from 3.5 to 4.5 V vs Li/Li^+ of $Li_{1+x}Mn_{2-x}O_4$ thin film with ALD cycle sequence of 250(MnO_2)-1(LiOH). (a) Charge/discharge curves of the third cycle at each current density ranging from 3.6 to 360 $\mu A\,cm^{-2}$ roughly corresponding theoretically calculated rates of C/2, C, 2.5C, 5C, 10C, 15C, 25C, 40C, and 50C based on the estimated thickness and bulk density. (b) Charge/discharge capacity and columbic efficiency as a function of cycle number at a specific current of 36 $\mu A\,cm^{-2}$ (~5C).

IV. SUMMARY AND CONCLUSIONS

In this work, the ALD process for MnO_2 and $LiMn_2O_4$ was demonstrated. The stoichiometry of ALD $Li_{1+x}Mn_{2-x}O_4$ was effectively controlled to allow for crystallization in the electrochemically active $Li_{1+x}Mn_{2-x}O_4$ phase. The $Li_{1+x}Mn_{2-x}O_4$ thin films exhibited great rate capability and capacity retention—maintaining 66% of the areal capacity upon increasing the specific current by a factor of 100 as well as ~97% capacity retention over 100 cycles at 36 $\mu A/cm^2$ (~5C). The research presented here shows that due to the inherent control over composition, atomic layer deposition is a unique tool to explore various compositions not accessible via other synthesis techniques that could provide insight into the development of high-performance materials. The continued development of 3D thin film batteries with high areal energy densities will require the realization of optimized high aspect ratio current collector/electrode architectures in conjunction with the development of spatial ALD or hybrid ALD/CVD processes for improved growth rates.

ACKNOWLEDGMENTS

The authors thank Jon Lau and Chris Choi for insightful discussions and helping with initial electrochemical characterization. The authors thank Xia Sang for his work in editing the final manuscript. The authors would also like to acknowledge the Nanoelectronics Research Facility (NRF) and the use of the Integrated Systems Nanofabrication Cleanroom (ISNC) at the California NanoSystems Institute (CNSI) in UCLA. Portions of this research were carried out at the Stanford Synchrotron Radiation Lightsource, a national user facility operated by Stanford University on behalf of the U.S. Department of Energy (DOE), Office of Basic Energy Sciences. This work was performed, in part, at the Center for Integrated Nanotechnologies, an Office of Science User Facility operated for the U.S. Department of Energy, Office of Science by Los Alamos National Laboratory (Contract No. 89233218CNA000001) and Sandia National Laboratories (Contract No. DE-NA-0003525). Sandia National Laboratories is a multimission laboratory managed and operated by National Technology & Engineering Solutions of Sandia, LLC, a wholly owned subsidiary of Honeywell International, Inc., for the U.S. DOE's National Nuclear Security Administration under Contract No. DE-NA-0003525. The views expressed in the article do not necessarily represent the views of the U.S. DOE or the U.S. Government. D.B. and B.D. were supported by the Office of Naval Research (No. N00014-19-1-2113). R.S. and J.C. were supported by the Office of Naval Research (No. N00014-13-1-0466).

DATA AVAILABILITY

The data that support the findings of this study are available within the article and its supplementary material.[31]

REFERENCES

[1]S. Moitzheim, B. Put, and P. M. Vereecken, Adv. Mater. Interfaces **6**, 1900805 (2019).
[2]A. Pearse *et al.*, ACS Nano **12**, 4286 (2018).
[3]S. Ferrari, M. Loveridge, S. D. Beattie, M. Jahn, R. J. Dashwood, and R. Bhagat, J. Power Sources **286**, 25 (2015).
[4]T. S. Arthur *et al.*, MRS Bull. **36**, 523 (2011).
[5]A. A. Talin, D. Ruzmetov, A. Kolmakov, K. McKelvey, N. Ware, F. El Gabaly, B. Dunn, and H. S. White, ACS Appl. Mater. Interfaces **8**, 32385 (2016).
[6]M. E. Donders, W. M. Arnoldbik, H. C. M. Knoops, W. M. M. Kessels, and P. H. L. Notten, J. Electrochem. Soc. **160**, A3066 (2013).
[7]F. Mattelaer, K. Geryl, G. Rampelberg, J. Dendooven, and C. Detavernier, ACS Appl. Mater. Interfaces **9**, 13121 (2017).
[8]F. Mattelaer, K. Geryl, G. Rampelberg, T. Dobbelaere, J. Dendooven, and C. Detavernier, RSC Adv. **6**, 114658 (2016).

[9]E. Østreng, K. B. Gandrud, Y. Hu, O. Nilsen, and H. Fjellvåg, J. Mater. Chem. A **2**, 15044 (2014).
[10]X. Chen, E. Pomerantseva, P. Banerjee, K. Gregorczyk, R. Ghodssi, and G. Rubloff, Chem. Mater. **24**, 1255 (2012).
[11]J. Liu, M. N. Banis, Q. Sun, A. Lushington, R. Li, T.-K. Sham, and X. Sun, Adv. Mater. **26**, 6472 (2014).
[12]V. Miikkulainen, A. Ruud, E. Østreng, O. Nilsen, M. Laitinen, T. Sajavaara, and H. Fjellvåg, J. Phys. Chem. C **118**, 1258 (2014).
[13]R. J. Gummow, A. de Kock, and M. M. Thackeray, Solid State Ionics **69**, 59 (1994).
[14]F. Mattelaer, P. M. Vereecken, J. Dendooven, and C. Detavernier, Chem. Mater. **27**, 3628 (2015).
[15]J. H. Choi, C. Pham, J. Dorman, T. Kim, and J. P. Chang, J. Magn. Magn. Mater. **498**, 166146 (2020).
[16]C. D. Pham, J. Chang, M. A. Zurbuchen, and J. P. Chang, Chem. Mater. **27**, 7282 (2015).
[17]T. T. Van and J. P. Chang, Surf. Sci. **596**, 1 (2005).
[18]J. P. Chang and H. H. Sawin, J. Vac. Sci. Technol. A **15**, 610 (1997).
[19]J. Cho, T. Kim, T. Seegmiller, and J. P. Chang, J. Phys. Chem. C **120**, 11837 (2016).
[20]Y.-C. Perng, J. Cho, S. Y. Sun, D. Membreno, N. Cirigliano, B. Dunn, and J. P. Chang, J. Mater. Chem. A **2**, 9566 (2014).
[21]A. S. Cavanagh, Y. Lee, B. Yoon, and S. George, ECS Trans. **33**, 223 (2010).
[22]A. C. Kozen, A. J. Pearse, C.-F. Lin, M. A. Schroeder, M. Noked, S. B. Lee, and G. W. Rubloff, J. Phys. Chem. C **118**, 27749 (2014).
[23]E. Kazyak *et al.*, Chem. Mater. **29**, 3785 (2017).
[24]B. Wang, Y. Zhao, M. N. Banis, Q. Sun, K. R. Adair, R. Li, T.-K. Sham, and X. Sun, ACS Appl. Mater. Interfaces **10**, 1654 (2018).
[25]V. Di Castro and G. Polzonetti, J. Electron Spectrosc. Relat. Phenom. **48**, 117 (1989).
[26]B. J. Tan, K. J. Klabunde, and P. M. A. Sherwood, J. Am. Chem. Soc. **113**, 855 (1991).
[27]V. Miikkulainen, O. Nilsen, M. Laitinen, T. Sajavaara, and H. Fjellvåg, RSC Adv. **3**, 7537 (2013).
[28]A. J. Nelson, J. G. Reynolds, and J. W. Roos, J. Vac. Sci. Technol. A **18**, 1072 (2000).
[29]G. Xu, Z. Liu, C. Zhang, G. Cui, and L. Chen, J. Mater. Chem. A **3**, 4092 (2015).
[30]M. M. Thackeray, Prog. Solid State Chem. **25**, 1 (1997).
[31]See supplementary material at https://doi.org/10.1116/6.0000644 for the XPS spectra of MnO_x thin films deposited at various deposition temperatures, SEM image of an example ALD $LiMn_2O_4$ thin film, TEM of a nanobattery like structure, XPS spectra of ALD $Li_xAl_ySi_zO$, example galvanostatic charge/discharge curves for ALD $LiMn_2O_4$, and specific details of XPS fitting for manganese oxides.